University of Southampton

Faculty of Engineering and Physical Sciences
School of Physics and Astronomy

Testing Precession of Super-Eddington Flows in Ultraluminous X-ray sources

Norman Khan
MPhys
ORCiD: 0000-0002-3955-0697

A thesis for the degree of Doctor of Philosophy

September 2022

Abstract

This thesis presents the results of my PhD research into the subset of accreting compact objects known as ultraluminous X-ray sources (ULXs). Studies of ULXs suggest that they may exist in a distinct supercritical accretion state, differing from that found in galactic stellar-mass black hole binaries, resulting in higher observed luminosities due to anisotropic emission. Long-term studies of many ULXs also reveal modulations of their X-ray light curves which has be interpreted as a form of precession of the super-critical accretion flow. The combination of these factors at the population level may make it possible to make broader predictions about ULXs such as the underlying black hole to neutron star ratio and the possible observational bias that may be present in these systems.

The first chapter in this thesis provides an theoretical introduction to compact objects and the physics of accretion in the sub-critical and supercritical regime. I explain some physical mechanisms that lead to the formation of the accretion disc and the the emergent spectrum. The chapter concludes with a short overview of some of the precession mechanisms that could be present in X-ray binaries.

The second chapter is an explanation of ULXs from an observational perspective, these are bright X-ray sources found away from the centre of galaxies that were first discovered in the late 1970s. The chapter will commence with a brief chronological history of the ULX field to the current day, then in subsequent sections I will cover several predicted phenomena in ULXs and their observational evidence.

The third chapter of this thesis builds on previous work in the field and seeks to answer the questions of how the observed population of ULXs may be affected by the combination of anisotopic emission and precession. This chapter combines stellar population synthesis codes with a geometrical ULX model to obtain estimates of what the ULX population may resemble under a variety of scenarios. This work has appeared in (Khan et al., 2022).

Chapter four contains an observational study of a sample of approximately forty ULXs using the *Swift* observatory. We make predictions for relative UV/Optical to X-ray emission under different inclinations and mass accretion rate and subsequently search for first order linear correlations between the long-term light curves in the different energy bands.

Conclusions are provided in the sixth and final chapter, as well as suggestions for future work.

In an attempt to eliminate the ambiguity of astrophysical source names, I have taken the care to provide SIMBAD (Wenger et al., 2000) identifiers for source names mentioned in this thesis, these are available via hyperlinks in the PDF version of this document.

Contents

List of Figures

List of Tables

Declaration of Authorship

I, Norman Khan, declare that this thesis and the work presented in it is my own and has been generated by me as the result of my own original research.

I confirm that:

1. This work was done wholly or mainly while in candidature for a research degree at this University;
2. Where any part of this thesis has previously been submitted for a degree or any other qualification at this University or any other institution, this has been clearly stated;
3. Where I have consulted the published work of others, this is always clearly attributed;
4. Where I have quoted from the work of others, the source is always given. With the exception of such quotations, this thesis is entirely my own work;
5. I have acknowledged all main sources of help;
6. Where the thesis is based on work done by myself jointly with others, I have made clear exactly what was done by others and what I have contributed myself;
7. Parts of this work have been published in:
   Khan et al. 2022

Signed:..... Date: 27/09/2022

Chapter 1

An Introduction to Accretion Physics

Accretion is a term used by astronomers to describe the gravitational infall of matter onto a compact object. This process is thought to be among the most efficient at converting gravitational potential energy into radiation in the universe, and much of the theoretical and observational understanding has come about in the last fifty years.

In this chapter, I will provide an introduction to compact objects and X-ray binaries (XRBs). I begin by explaining the physics of mass transfer in binary star systems and how this leads to the formation of an accretion disc. I show how radiative processes in the disc lead to the creation of the emergent X-ray spectrum. I additionally show how depending on the mass accretion rate, competing forces within the accretion disc may result in different geometry from the standard thin disc model. The chapter concludes with an introduction to precession in the context of XRBs.

1.1 Compact Objects

The term compact object (CO) is primarily used to refer to one of three stellar objects: black holes (BH), neutron stars (NS) and white dwarfs (WD). This thesis does not cover the latter of these.

1.1.1 Black Holes

BHs were the first type of CO to be predicted, originally in the classical regime by English clergyman John Michell (Michell, 1784) as a star sufficiently dense that its escape velocity would exceed the speed of light $\sqrt{\frac{2GM}{r}} \geq c$, this idea would later be formalised under Einstein's framework of general relativity (Einstein, 1916) by Karl Schwarzschild (Schwarzschild, 1916) who found solutions to the Einstein field equations for a static and spherically symmetric body. One mathematical peculiarity of these Schwarzschild black holes was to be found at $r = 0$ and at $r_s = \frac{2GM}{c^2} = 2R_{\rm G} \approx 3(\frac{M}{M_\odot})$ km at these points the solution would become singular, the first singularity at $r = 0$ is considered to be a gravitational singularity, a

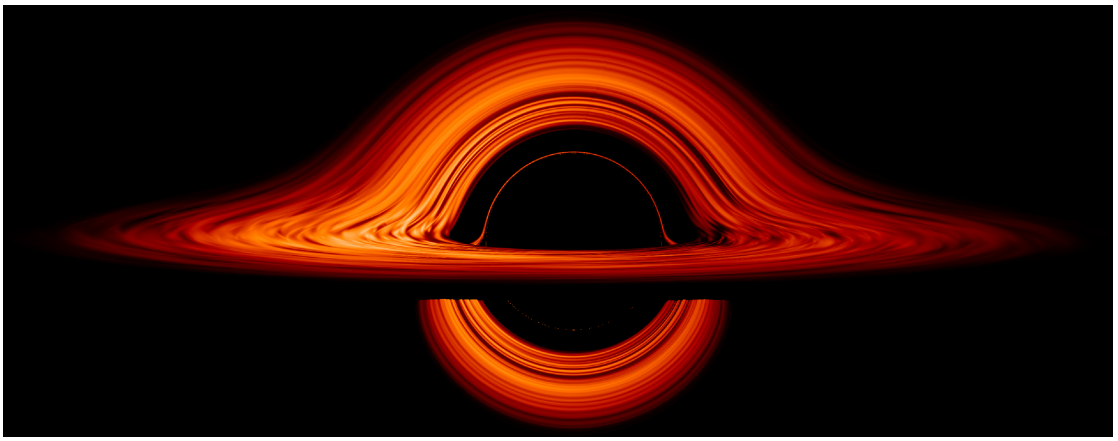

Figure 1.1: Simulation of a black hole by NASA's Goddard Space Flight (Schnittman, 2021). The strong gravitational lensing results in distortion of the light meaning that we are able to see light that arises from behind the black hole.

region of infinite spacetime curvature, while the second, commonly known as the Schwarzschild radius denotes the boundary of the event horizon beyond which no matter or radiation may escape the gravitational field. In the above equations, G is the gravitational constant, M the mass of the black hole, c the speed of light, $R_{\rm G}$ is known as the gravitational radius $M_\odot$ is the mass of the Sun. The most abundant BHs are the stellar mass $1-100\ M_\odot$ BHs, believed to be formed after the gravitational collapse of massive $>25\ M_\odot$ stars (Heger et al., 2003). At $100-100,000\ M_\odot$ we have the illusive intermediate mass BHs (IMBHs), the strongest convincing evidence for their existence comes from the gravitational wave GW190521 (Abbott et al., 2020a) caused by the merger of two BHs with masses $\sim$ 85 and $\sim$ 66 resulting in an IMBH of 142 $M_\odot$. Finally, in the range $10^5-10^9\ M_\odot$ we have the super-massive BHs (SMBHs), these are primarily thought to reside at the centre of almost all[1] galaxies, however their formation still remains of open debate, one suggestion is that they may be formed by the direct collapse of matter in dark matter halos in the early universe (Begelman et al., 2006), another suggestion is that accretion onto extremely massive stars formed from metal-free gas in the early universe could serve as progenitors (Milosavljević & Merritt, 2001).

The addition of angular momentum leads to solutions to the Einstein field equations known as Kerr or, in the case of a non-zero electric charge, Kerr-Newman BHs. These solutions require a second dimensionless number known as the spin (a or a_*) and is given by $a_* = cJ/GM^2$ where J is the magnitude of the BH angular momentum. The spin parameter is dimensionless and bounded between -1 and 1. Many efforts have been made to measure the spin of BHs in the universe, for a review on observational constraints on the value of BH spin (see Reynolds 2021).

[1]The nearby galaxy M33 is thought to not contain a SMBH (Gebhardt et al., 2001)

1.1.2 Neutron Stars

The existence of NSs was proposed in Baade & Zwicky 1934; they suggested that supernovae could represent the transition of an ordinary star to a star composed of mostly neutrons. These NSs would be capable of reaching higher densities than ordinary stars and would be a strong source of observed cosmic rays. PSR B1919+21 was the first NS discovered in 1967 (Hewish et al., 1968) via radio observations showing recurring pulses of a period $P \sim 1.337$ s, these pulsating neutron stars are known as pulsars. The ATNF pulsar catalogue v1.67 (Hobbs et al., 2004) counts 3320 pulsars, most of which have been discovered in the radio bands in our own galaxy or in the dwarf satellite galaxies SMC and LMC. NSs are expected to have masses in the range of $\sim 1.4 - 3.0\ M_{\odot}$ and radii of around ~ 10 km. Unlike BHs, which have very weak magnetic fields[2], NSs may have dipolar or higher order magnetic field, with strengths of B $\sim 10^{8-15}$ G, these fields, have the ability to strongly impact the star and its immediate surroundings, significantly increasing the complexity of modelling these systems. An unsolved problem with regard to neutron stars is finding a thermodynamic description of key state variables e.g. density, pressure, and temperature as a function of radius, the so-called 'equation of state', while much progress has been made in recent years, there is still much debate as to what the internal structure of neutron stars may resemble.

1.2 Binary Systems and Mass Transfer

It is thought that the majority of stars exist in binaries or higher order systems, and that more than 70% of all massive stars will exchange mass with a companion at some point in their lifetime (Abt & Levy, 1976; Sana et al., 2012). XRBs are systems composed of a normal star and a compact object, and through the process of accretion, gravitational energy is converted into radiation. It is common to subclassify XRBs based upon the relative masses of the stars in the binary, high mass X-ray binaries (HMXBs) are those systems where the companion star is more massive than the CO, such that the mass ratio $q = M_1/M_2 > 1$, while low mass X-ray binaries (LMXBs) have mass ratios of $q < 1$, this is not a strict definition and others exist such as companions of less than $< 1.5\ M_{\odot}$ for LMXBs, and $> 10\ M_{\odot}$ for HMXBs (van den Heuvel, 1993).

Broadly speaking, there are two ways in which accretion onto a compact object may occur; these are shown in figure 1.2. The first is known as Bondi accretion and is particularly relevant for systems with early-type companions (namely O or B type stars, see section 3.2.1). The stellar wind of these early type stars is highly supersonic with velocities of order $v \sim \sqrt{2GM/R} \sim 1000$ km s^{-1} with mass loss rates of around $\dot{\mathrm{M}}_{\mathrm{W}} \sim 10^{-6} - 10^{-5}$ M$_{\odot}$ yr^{-1}. Accretion occurs as the orbiting compact object travels through the radiatively driven stellar wind produced by the massive star, this process is thought to be present in the eclipsing binary M33 X-7. The second method is accretion via Roche lobe overflow (RLOF), which I will describe in the following section.

[2]The event Horizon Telescope estimate the SMBH in M87 to have a field strength of B $\sim 1 - 30$ G.

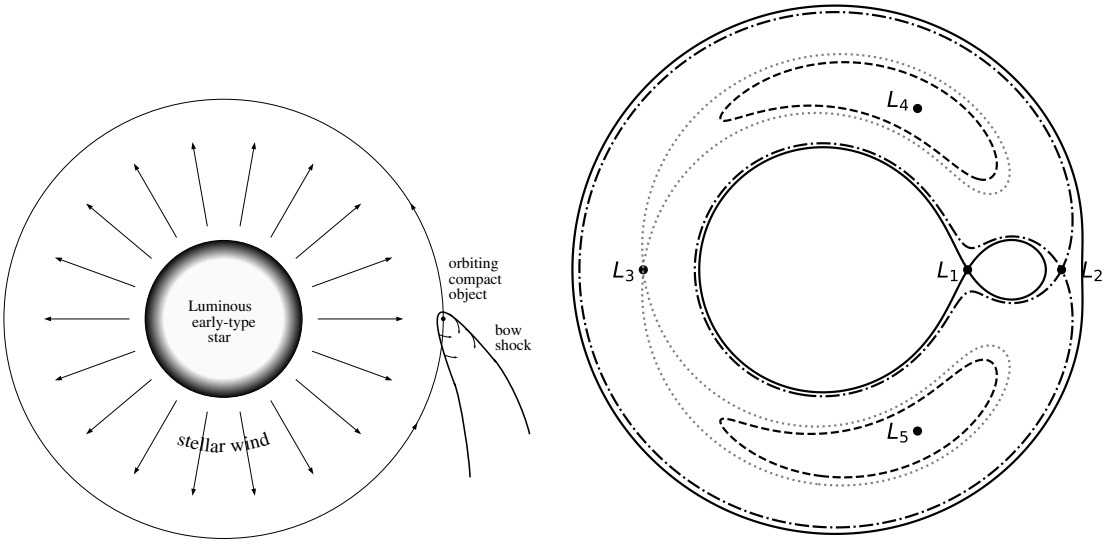

Figure 1.2: The two main methods of accretion in binary systems. Left: Schematic for Bondi accretion from a stellar wind. (Figure from Frank et al. 2002) Right: Roche potentials for a mass ratio $q = M_1/M_2 = 20/1 = 20$. The Lagrangian points L_1 - L_5 are labelled.

1.2.1 Roche Lobe Overflow

The term 'Roche lobe' describes a teardrop-shaped equipotential surface surrounding a star in which material is bound to the star by gravity. The right panel in Figure 1.2 shows the Roche potentials for a binary system with a mass ratio of $q = M_1/M_2 = 20$, the Roche lobe is represented by the inner solid figure-of-eight shaped line with the intersection occurring at the point of gravitational equilibrium known as the inner Lagrange point L_1. Matter from one star, large enough to fill its Roche-lobe, will more easily 'overflow' via the inner Lagrange point into the potential basin of the other star's lobe. A consequence of mass transfer via L_1 is that the transferred material will possess significant orbital angular momentum, which is important for the formation of the accretion disc (see section 1.3).

A useful estimation of the size of the Roche lobe, accurate to 1% may be given by the Eggleton Formula eq 1.1 (Eggleton, 1983):

$$r_1 = \frac{0.49a(M_1/M_2)^{2/3}}{0.6(M_1/M_2)^{2/3} + \ln(1 + (M_1/M_2)^{1/3})} \tag{1.1}$$

Where a is the orbital separation, M_1 and M_2 the mass of the two stars, and r_1 the radius of the sphere whose volume approximates the Roche lobe of mass M_1.

1.2.2 Characteristic timescales in astrophysics

Three characteristic timescales are often used when referring to stellar evolution and or mass transfer in binary systems, the shortest of the three is known as the **dynamical timescale**, $\tau_{\rm dyn}$ (eq 1.2), and is a measure of the timescale on which

a star would expand or contract if the balance between pressure gradients and gravity were suddenly disrupted (and is the same as the free-fall timescale).

$$\tau_{\rm dyn} = \sqrt{\frac{R^3}{2GM}} \tag{1.2}$$

In the case of HMXBs as the massive star accretes onto the CO, its star's radius and Roche lobe will shrink; if the radius of the Roche lobe becomes smaller than the thermal equilibrium radius of the star of the same mass, then the secondary can no longer stay in thermal equilibrium and mass transfer will proceed on a **thermal timescale**, $\tau_{\rm th}$ (eq 1.3).

$$\tau_{\rm th} \approx \frac{GM^2}{RL} \tag{1.3}$$

Finally, we define the **nuclear timescale**, $\tau_{\rm nuc}$ (eq 1.3), as the timescale on which the star will exhaust its supply of nuclear fuel.

$$\tau_{\rm nuc} = \frac{qXM \times 6 \times 10^{18} \text{ erg g}^{-1}}{L} \tag{1.4}$$

In the above equations L is the luminosity, q is the fraction of fuel available for burning in the core ($q_\odot \sim 0.1$) and X the hydrogen mass fraction ($X_\odot \sim 0.7$), the factor of 6×10^{18} erg g^{-1} is the energy released from fusing 1 gram of hydrogen to helium.

These three characteristic timescales are useful to bear in mind when discussing binary evolution and are related by $\tau_{\rm dyn} < \tau_{\rm th} < \tau_{\rm nuc}$, calculating these values for the sun gives approximately 1100 s $< 3 \times 10^7$ yr $< 7 \times 10^9$ yr.

1.3 Accretion Discs

Accretion discs are gravitationally bound structures composed of gas and dust in orbit around a central mass. Ubiquitous in astrophysics, these discs occur around a variety of objects such as black holes, white dwarfs and protostars. Accretion discs are formed if the specific angular momentum of the in-falling material passing through L_1 or accreting from the wind is able to be efficiently removed (Frank et al., 2002). This is commonly the case for close binary systems undergoing Roche-lobe overflow (see sec. 1.2.1).

A test particle in orbit around a central mass in the absence of dissipative forces will remain on a fixed orbit, for the radius of the orbit to move inwards a torque is required to remove some of the angular momentum. The mechanism for this torque was initially unknown but was presumed to arise from a variety of physical effects including turbulence and molecular viscosity. Shakura & Sunyaev 1973 ascribed a constant (α) to describe the bulk processes involved in angular momentum redistribution, and specifically related the kinematic viscosity (υ) to the pressure and torque. It is now thought that the primary mechanism responsible for viscosity is the magnetorotational instability (MRI) (Balbus & Hawley, 1991, 1998), a useful analogy for this process is that of a spring connecting two particles in orbit at slightly different radii around a central mass. The inner mass closer to

the central body will have a higher angular velocity than the outer mass, the spring connecting the two masses will then pull the inner mass back while at the same time pull the outer mass forward, each particle thus receives an opposite signed torque meaning that the inner particle falls further in while the outer mass moves further out. Observational evidence suggests a typical range of $\alpha \sim 0.1 - 0.4$ while numerical estimates for α suggest values that are an order of magnitude smaller (King et al., 2007)

1.3.1 The Eddington Limit

The Eddington luminosity, $L_{\rm Edd}$, describes the maximum luminosity a body of mass M can achieve under the effect of steady spherically symmetrical accretion. It assumes that the matter exists in hydrostatic equilibrium where the force from radiation pressure is balanced by the gravitational force.

In accretion physics, the Eddington luminosity is sometimes given in the form:

$$L_{Edd} = \frac{4\pi GMc}{\kappa} = \frac{GM\dot{M}_{\rm Edd}}{2R_{\rm in}} \approx 1.26 \times 10^{38} \left(\frac{M}{M_\odot}\right) \text{erg s}^{-1} \tag{1.5}$$

Where $\kappa = 0.2(1 + X) = 0.34$ cm^2 g^{-1} is the Thompson opacity, and X the hydrogen mass fraction (for solar $X_\odot = 0.7$). $R_{\rm in} = 3R_{\rm s}$ is the inner disc radius (for $a_* = 0$). Where m_p is the mass of the proton and σ_T the Thompson cross-section. The above form assumes that the gas is composed entirely of hydrogen and has a constant opacity dominated by electron scattering.

The corresponding Eddington accretion rate may be given by:

$$\dot{M}_{\rm Edd} = \frac{48\pi GM}{c\kappa} = \frac{L_{\rm Edd}}{\eta c^2} \approx 2 \times 10^{18} \left(\frac{M}{M_\odot}\right) \text{ g s}^{-1} \tag{1.6}$$

where η is the efficiency of gravitational energy release, which for Schwarzschild BHs is of the order ~ 0.06 but for Kerr BHs may be as high as ~ 0.4 (Shakura & Sunyaev, 1973). η in the case of NSs is around ~ 0.1 the main difference being that the presence of a surface means that energy is not ultimately lost as it is never able to reach the event horizon which lies inside the NS.

1.3.2 Thin Accretion Discs

For accretion rates in the range $\dot{M} \sim 0.01 - 0.3\ M_{\rm Edd}$ the accretion disc is able to cool efficiently via black body emission[3] and so the optically thick ($\tau \gg 1$) plasma and becomes geometrically-thin with a height to radius ratio of $H/R \ll 1$ Reynolds (2021).

An analytic solution was presented in (Shakura & Sunyaev, 1973), this seminal work provided equations describing three distinct regions based upon the dominant pressure force and opacity (see fig 1.3). In the inner region, the flow is expected to be dominated by radiation pressure and the light-matter interaction occurs predominantly with charged particles via Thompson scattering. The middle region

[3]Inverse Compton Scattering (Comptonization) and cyclotron radiation (in the case of magnetic fields) are additional cooling mechanisms.

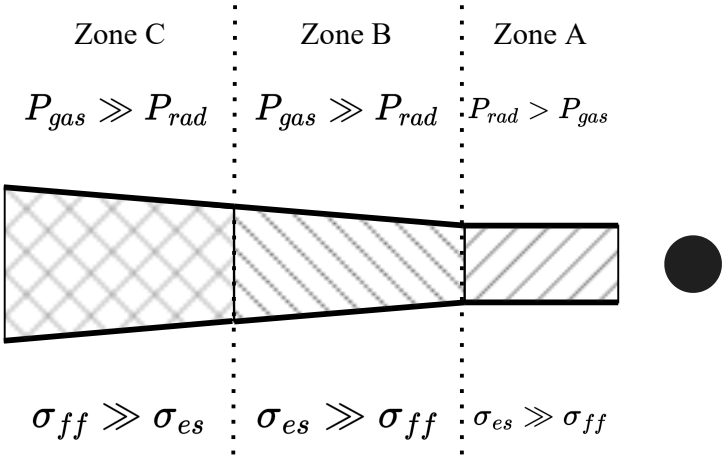

Figure 1.3: The three regions presented in Shakura & Sunyaev 1973 with their dominant forms of pressure and opacity. P_{gas} and P_{rad} are the gas and radiation pressure respectively. The (Thompson) is σ_{es}, while σ_{ff} is the free-free (Bremsstrahlung) cross-section.

is also dominated by electron (Thompson) scattering however is expected to be gas pressure dominated, while the outermost regions of the disc are also gas pressure dominated but the opacity is dominated by free-free (Bremsstrahlung) processes.

The Thin Disc Spectrum

The model presented by Shakura & Sunyaev 1973 assumes a thin ($H/R \ll 1$), axially symmetric and stationary ($\partial/\partial t = 0$) disc. The model allows for the description of the spectra that would be obtained from such a disc; here I will present a simplified version of the derivation for the radial flux and temperature relations. Under this model, the fluid viscosity v is driven by turbulent forces in the disc and given by:

$$v = \alpha c_s H \tag{1.7}$$

where α is the viscosity parameter (see 1.3), c_s the sound speed in the disc and H the scale height of the disc.

The presence of viscous torques on particles in Keplerian orbit leads to dissipation of the mechanical energy with the torque defined as:

$$\tau_\phi(R) = 2\pi R v \Sigma R^2 \Omega' \tag{1.8}$$

where v is the kinematic velocity, Σ is the surface density and $\Omega' = \mathrm{d}\Omega/\mathrm{d}r$ i.e. rate of change of angular velocity between two annuli in the disc of width $\mathrm{d}r$.

By considering dissipation across both faces of the disc ($2 \times 2\pi R \mathrm{d}R$), the amount of mechanical heat loss is given by $\tau_\phi \Omega' \mathrm{d}r$, providing a heat loss per unit area $D(R)$ of:

$$D(R) = \frac{\tau_\phi \Omega'}{4\pi R} = \frac{1}{2} v \Sigma R^2 \Omega'^2 \tag{1.9}$$

Since the matter in the accretion disc is essentially a fluid, it is subject to differential rotation; by setting the angular velocity to the Keplerian angular velocity $\Omega_K = \sqrt{\frac{GM}{R^3}}$ the dissipation per unit face area can be shown to be:

$$D_K(R) = \frac{9vGM\Sigma}{8R^3} \tag{1.10}$$

by imposing the conservation of mass $\dot{M} = -2\pi R\Sigma v$, where $\dot{M}$ is the mass accretion rate, and the boundary condition that the torque goes to 0 at the inner edge of the disc ($\Omega' = 0$) it can be shown that

$$v\Sigma = \frac{\dot{M}}{3\pi}\left[1 - \left(\frac{R_{in}}{R}\right)^{1/2}\right] \tag{1.11}$$

by combining equations 1.10 and 1.11 we obtain the commonly quoted form of the viscous dissipation per unit disc face area (i.e. flux) (eq 2.6 in Shakura & Sunyaev 1973)

$$D(R) = \frac{3GM\dot{M}}{8\pi R^3}\left[1 - \left(\frac{R_{in}}{R}\right)^{1/2}\right] \tag{1.12}$$

To obtain the total luminosity from the disc we integrate between $R_{\rm in}$ and the outer edge which for our purposes as $R_{\rm out} \gg R_{\rm in}$ may assume exists at infinity which yields:

$$L = \int_{R_{\rm in}}^{\infty} D(R) 4\pi R \mathrm{d}R = \frac{12}{8} GM\dot{M} \int_{R_{\rm in}}^{\infty} \frac{1}{R^2}\left[1 - \left(\frac{R}{R_{\rm in}}\right)^{-1/2}\right] \mathrm{d}R \tag{1.13}$$

$$= \frac{12}{8} GM\dot{M}\frac{1}{3R_{\rm in}} = \frac{GM\dot{M}}{2R_{\rm in}} = \dot{m}L_{\rm Edd} \tag{1.14}$$

Here we have used equations 1.5 and 1.6 and defined the dimensionless accretion rate as $\dot{m} = \dot{M}/\dot{M}_{\rm Edd}$. Using the Stefan-Boltzmann law $D(R) = \sigma T_{\rm eff}^4$ we can also obtain the radial temperature profile of the disc:

$$T_{\rm eff}(R) = \left\{\frac{3GM\dot{M}}{8\pi R^3\sigma}\left[1 - \left(\frac{R_{in}}{R}\right)^{1/2}\right]\right\}^{1/4} \tag{1.15}$$

Equation 1.15 implies that the temperature profile for thin discs goes as $T(R) \propto R^{-p} \propto R^{-3/4}$ where $p = 3/4$. For stellar mass BHs and NSs the inner regions of the disc are expected to reach temperatures of > 0.3 keV ($\sim 10^7$ K).

It is common to define a factor $f_{\rm col} \geq 1$ called the colour temperature correction such that $T_{\rm max} = f_{\rm col}T_{\rm eff}$, this correction provides the amount of deviation from a blackbody and serves to increase the observed peak temperature of the disc and likely depends on the vertical structure of the disc.

The observed spectrum may be obtained by first assuming that each annulus of the disc radiates at its characteristic temperature $T(R)$, following Planck's law of black-body radiation (eq 1.16)

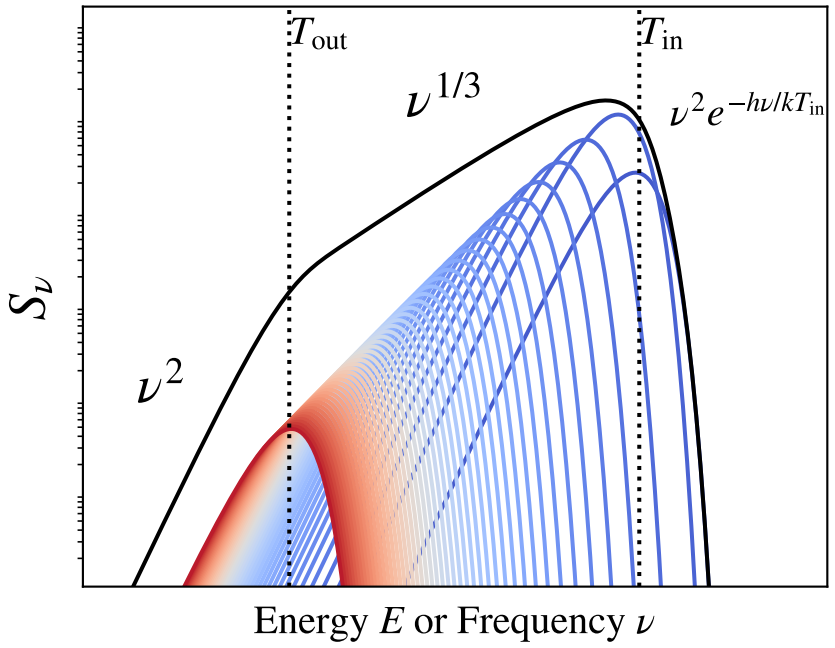

Figure 1.4: Diagram of the thin disc spectra (black line) from Shakura & Sunyaev 1973 showing the blackbody contribution from 50 annuli, cooler annuli appear in redder colours, while hotter annuli appear in bluer colours.

$$B_\nu(R) = \frac{2h}{c^2} \frac{\nu^3}{e^{h\nu/k_B T(R)} - 1} \tag{1.16}$$

$B_\nu(R)$ is the spectral radiance at a given radius per unit frequency (ν), h is Planck's constant, k_B the Boltzmann constant.

Next, we can integrate the specific intensities over the entire disc to obtain the emergent spectrum:

$$S_\nu(\nu) = \frac{cos(i)}{D^2} \int_{R_{in}}^{R_{out}} B_\nu[T(R)] 2\pi R dR \propto \nu^{1/3} \int_0^{h\nu/kT_0} \frac{x^{5/3}}{e^x - 1}\, dx \tag{1.17}$$

Here, i is the inclination to the disc and D is the distance to the observer.

Equation 1.17 gives rise to a characteristic spectrum, at low frequencies (energies) the spectrum is the Rayleigh-Jeans tail from the cool outer edge of the accretion disc with a slope of $S_\nu \propto \nu^2$, at intermediate frequencies the spectra follows a slope of $S_\nu \propto \nu^{1/3}$ while at high frequencies the spectrum falls away exponentially as $\propto \nu^2 e^{-h\nu/hT_{\rm in}}$ where $T_{\rm in}$ is the temperature of the inner disc see figure 1.4.

1.3.3 Supercritical Accretion Discs

In close binaries, it is possible that the mass inflow rate in the outer regions of the disc, may significantly exceed the Eddington rate $\dot{m} \gg 1$.

One way this may occur is if the donor star is in the (or evolving to) red giant phase, the so-called "case B" evolution (Kippenhahn & Weigert, 1967). As

the donor moves through the Hertzsprung gap in the HR diagram, the star no longer burns hydrogen in the core and so expands, massive mass transfer may subsequently occur provided that the initial mass ratio is $q_i \lesssim 1$, this leads to an expansion of the binary during mass transfer, which occurs on a thermal timescale (King & Ritter, 1999).

In HMXBs with mass ratios of $q \gg 1$, super-Eddington mass transfer via Roche-Lobe overflow was generally disregarded, as the high mass ratio is thought to render the process unstable. However, models invoking steep H/He gradients in the layers beneath the giant stars' surface can enable super-Eddington mass transfer on nuclear timescales ($\sim 0.15 - 0.5$ Myr) for both NS and BH accretors (Quast et al., 2019). This regime is often called the super-critical or super-Eddington regime and several models have been put forward to explain how accretion may occur under such conditions, these models may be divided into two broad categories. In the first category of models, all of the supplied gas eventually reaches the CO, models of this kind include the 'Polish Doughnut' and the 'slim disc' sometimes known as the optically thick advection-dominated accretion flow (ADAF[4]) (Jaroszynski et al., 1980; Abramowicz et al., 1988). These models were developed in the late 1970s and early 1980s for constructing a perfect fluid equilibria of matter orbiting around a Kerr black hole.

In the second set of models, only a small fraction of the input gas may end up reaching the CO as most of the gas ends up being blown away by radiation pressure, one example of such a model includes the supercritical accretion disc presented in Shakura & Sunyaev 1973.

Both of these models predict fairly similar radial temperature distributions and luminosities, where they diverge however is due to the presence of a strong wind which can block and reprocess the emission, leading to an observational appearance that strongly depends on the inclination angle (i) to the line of sight. However, it is likely that the reality will lie in a balance between these two models, this was explored in the model put forward by Poutanen et al. 2007 which I will discuss in this section.

The Disc Vertical Structure

The scale height (H/R) for a super-critical accretion disc is determined by the balance between two competing forces acting in the vertical axis of the disc. Gravity will act to pull matter towards the compact object, and so has a vertical component that acts to flatten the disc, while acting in the opposite direction is the force arising from radiation pressure which serves to puff up the disc, this balance is encapsulated by equation 1.18 (Shakura & Sunyaev, 1973).

$$\frac{H}{R} = \dot{m}_0 \frac{3}{r}(1 - r^{-1/2}) \tag{1.18}$$

Equation 1.18 is plotted for three values of $\dot{m}_0$ in figure 1.5 from 0 to 10 $R_{\rm in}$, it can be seen as the mass accretion rate increases, the maximum scale height (H/R) of the disc also increases. At critical value of $\dot{m}_{\rm cr} = 9/4 = 2.25$ the disc

[4]Note that this ADAF is distinct from the optically *thin* ADAF thought to occur at very low accretion rates ($\dot{m} \ll 0.1$) (Narayan & Yi, 1994)

height ratio first reaches unity at a characteristic radius known as the spherisation radius $R_{\rm sp}$. It is at this radius from which an outflow forms, as there is no effective gravity and so the matter is unbound, meaning that it may be accelerated and expelled via any amount of radiative or centrifugal force, this outflow serves as an additional mechanism for the removal of angular momentum from the system.

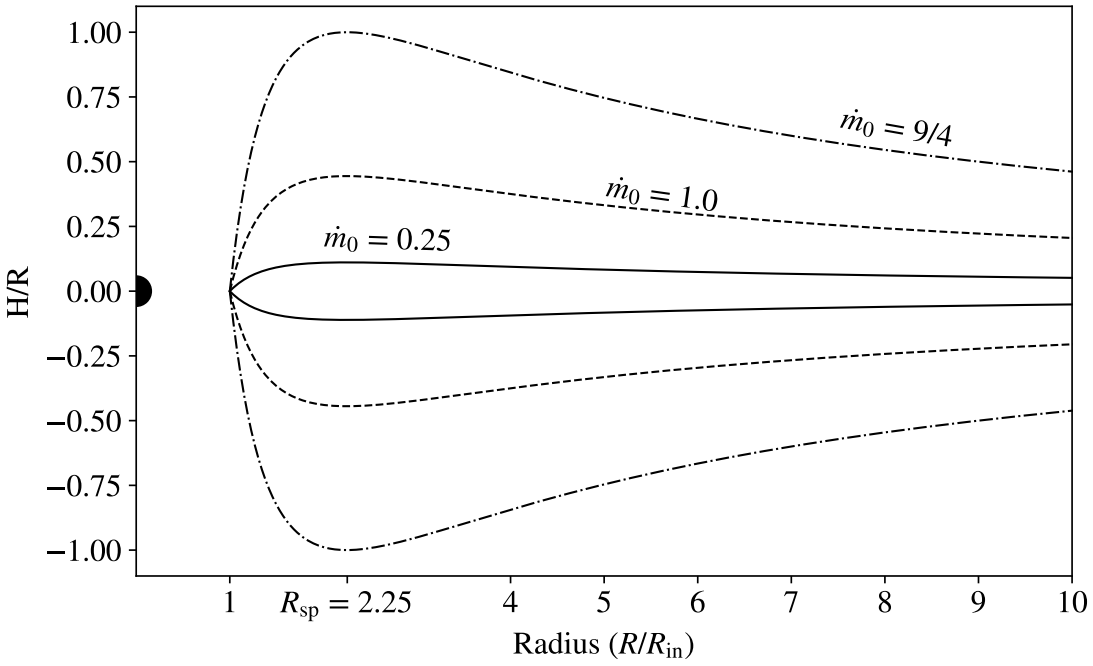

Figure 1.5: The height ratio of the disc (H/R) shown for three different mass accretion rates $\dot{m}_0 = 0.25$ (solid) 1.0 (dashed) and $9/4 = 2.25$ (dash-dot) where the disc first reaches a scale height of unity at the spherisation radius $R_{\rm sp}$, the size of CO is not to scale.

It can be seen from figure 1.5 that the geometry of the supercritical disc differs from the sub-critical accretion disc where the matter distribution follows $H/R \ll 1$. For radiation pressure supported discs, the disc can have a scale height of order unity $HR \sim 1$ which can create a funnel close to the central regions and lead to anisotropic emission.

Flux, Luminosity and Spectrum

Due to the high accretion rate, the energy-conversion efficiency η is substantially decreased, this is due to the photon diffusion timescale and the infall time being approximately equal, which leads to advective energy transport dominating over radiative cooling. In order to accelerate the outflow (wind) a certain amount of the radiative energy must be supplied, this fraction is denoted as $\epsilon_{\rm w}$. The addition of the wind results in a modification of the conservation of angular momentum of the system (see Lipunova 1999 for details) which leads to a radial energy flux of the form $Q_{\rm rad} \propto R^{-2}$.

$$Q_{\rm rad}(R) \approx \frac{GM\dot{M}(R)}{8\pi R^3} \approx \frac{GM\dot{M}_0 R}{8\pi R^3 R_{\rm sp}} \propto R^{-2} \tag{1.19}$$

Here $Q_{\rm rad}(R)$ is the radiative flux from one of the two accretion-disc surfaces. In the absence of advection, we can assume that the mechanical energy due to viscosity is equal to the energy radiated $Q_{\rm rad} = Q^+$. However, accounting for advection leads to $Q_{\rm rad} = Q^+ - Q_{\rm adv}$. We have used $\dot{M}(R) = \dot{M}_0 R/R_{\rm sp}$ where $\dot{M}_0$ is the matter supply rate to the disc, i.e. the accretion rate at the largest radii of the disc.

Integrating $Q_{\rm rad}$ between the inner radius and the photon trapping radius $R_{\rm tr}$ (where photon diffusion and accretion timescales are equal) then results in a logarithmic dependence for the luminosity on the mass accretion rate.

$$L \propto \int_{\rm in}^{\rm tr} Q_{\rm rad}(R) R {\rm d}R \propto \int_{R_{\rm in}}^{R_{\rm out}} R^{-1} {\rm d}R = \ln\left(\frac{R_{\rm tr}}{R_{\rm in}}\right) \approx L_{\rm Edd}\left(1 + \frac{3}{5}\ln \dot{m}_0\right) \tag{1.20}$$

The supercritical disc is radiation pressure supported as opposed to gas pressure supported for a thin disc (except in the inner regions), this fact, combined with the geometrically thick nature and the domination of electron scattering opacity leads to a temperature profile scaling as $T \propto R^{-1/2}$ (as compared to $\propto R^{-3/4}$ for thin discs) (Watarai et al., 2000). This difference in the radial temperature profile means that the characteristic spectra show a different slope in the mid-frequency ranges with $\nu S_\nu \propto \nu^{4/3}$ for standard thin discs and $\nu S_\nu \propto \nu^0$ in the high accretion rate advection-dominated accretion flow (ADAF). The difference between thin accretion discs and slim discs is shown in figure 1.6, I have plotted the `XSPEC` models `diskbb` for various inner disc temperatures in the range $T_{\rm in} = 1 - 5$ keV while a relativistic model for a stationary slim accretion disc `slimbh` (Sadowski, 2011) has been plotted for various inclinations in the range $i = 0° - 85°$.

1.3.4 Precession

Lense-Thirring Precession

So far, the accretion discs I have mentioned have all had the property that matter moves in an approximately circular orbit around the CO and the CO's spin axis is also perpendicular to the plane of rotation of matter in the disc. It is thought however that if the orbiting matter is not in line with the equatorial plane of the rotating mass, potentially due to asymmetries in the supernova process, then the orbiting matter will precess in a prograde fashion around the angular momentum axis of the rotating object resulting in precessions of the longitude of the ascending node (Ω) and the argument of periapsis (ω). This effect is known as Lense-Thirring precession, named after Lense & Thirring 1918 who first derived the effect in the weak field limit. This effect was confirmed to exist experimentally by measuring its extremely weak presence in the Earth's magnetic field using the Gravity probe-B experiment (Everitt et al., 2011), which measured the geodetic and frame-dragging drift that changed by ~ 6.6 arcseconds per year.

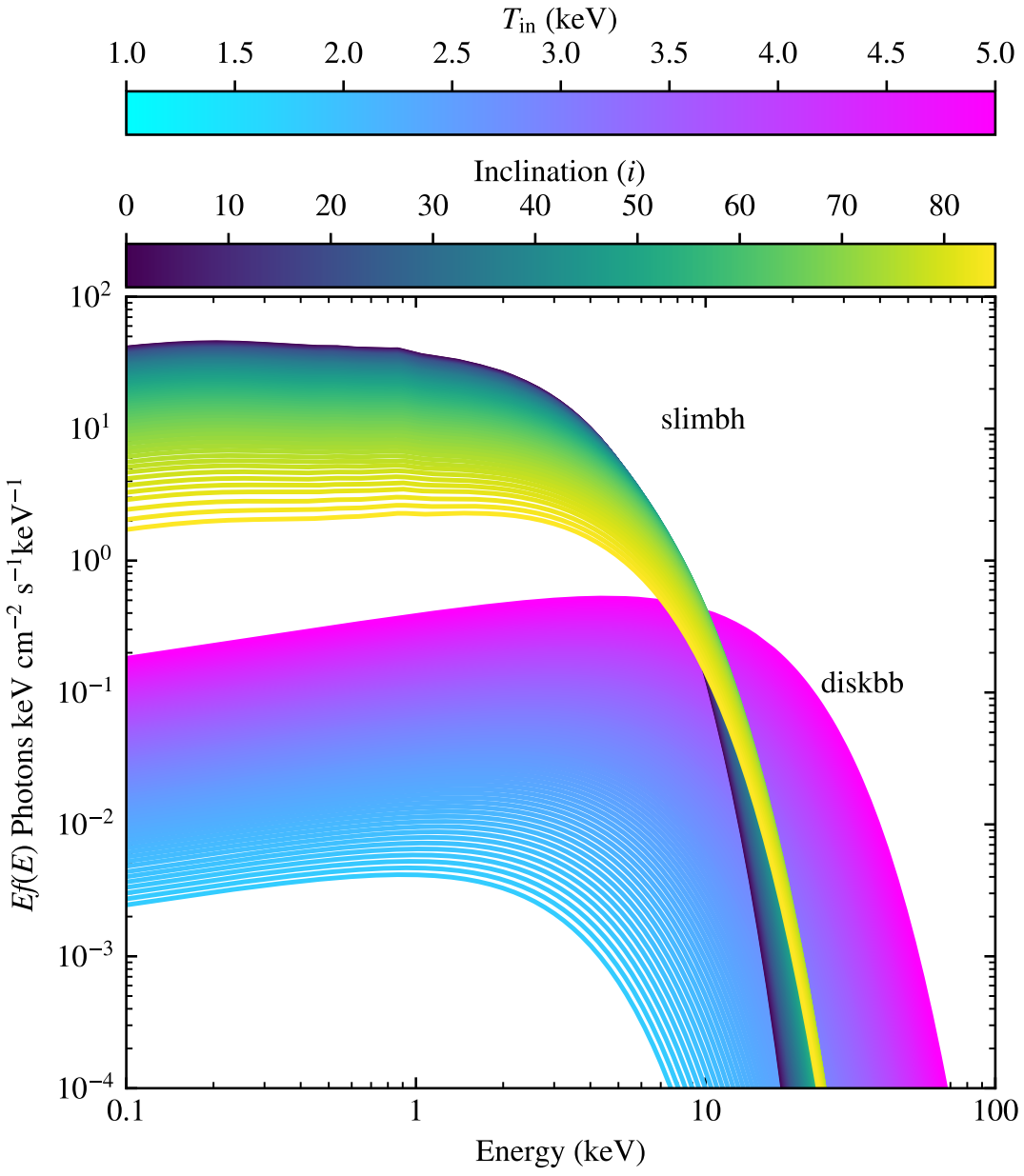

Figure 1.6: Unabsorbed spectra for a variety of thin accretion discs (`diskbb`) at different temperatures in the range $T \sim 1-5$ keV, as well as several slim accretion discs (`slimbh`) in different inclinations in the range $i \sim 0-85°$.

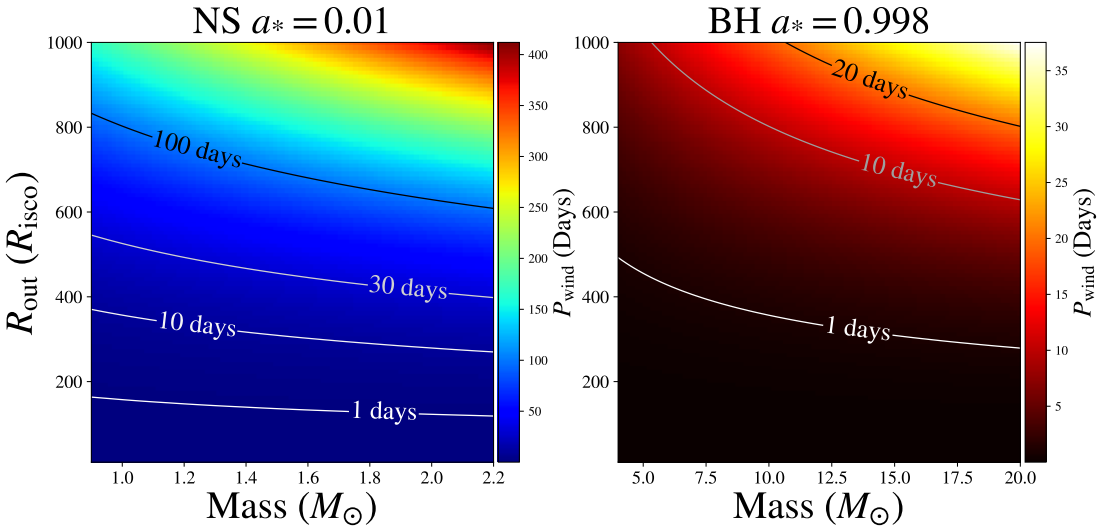

Figure 1.7: Values for $P_{\rm wind}$ represented by the color (eq 1.21) plotted for values of $R_{\rm in} = 10 - 1000\ R_{\rm isco}$ (y-axis). The left panel shows NS with masses in the range $0.9 - 2.2$ M$_\odot$ with spin values of $a_* = 0.01$, while the right panel shows BHs with high values spin $a_* = 0.998$ with masses in the range $4 - 20$ M$_\odot$. Contours are shown for a variety of timescales.

The Lense-Thirring precession frequency can self-consistently explain the origin of quasi-periodic oscillations (QPOs) in LMXBs with BH donors (Stella & Vietri, 1998). The nodel precession frequency is given by $\nu_{\rm LT} = GMa/(\pi c^3 r^3)$ and since the frequency scales with the inverse cube of the radius, it can be shown that orbits closer to the rotating object will experience a stronger torque and attempt to re-align with the CO's spin axis.

In the case of supercritical accretion discs where the disc and wind in the inner regions can reach large scale $H/R \geq 1$, Lense-Thirring precession may cause the inner flow to precess. (Ichimaru, 1977; Esin et al., 1997; Poutanen et al., 1997; Fragile et al., 2007)

Middleton et al. 2018 derived the precession period for a supercritical accretion disc following Fragile et al. 2007 and is given in equation 1.21:

$$P_{\rm wind} = \frac{GM_a M_\odot \pi}{3c^3 a_*} r_{\rm out}^3 \frac{1 - \left(\frac{r_{isco}}{r_{out}}\right)^3}{\ln\left(r_{out}/r_{isco}\right)}\ \text{(s)} \tag{1.21}$$

In the above equation $r_{\rm isco}$ is the innermost stable circular orbit and $r_{\rm out}$ is the outer photospheric radius (the radius at which the wind becomes optically thin). Poutanen et al. 2007 determined this radius to be approximately:

$$r_{\rm out} \approx \frac{3\epsilon_{\rm w}}{\beta\zeta} \dot{m}_0{}^{-3/2} r_{\rm isco} \tag{1.22}$$

where $\epsilon_{\rm w}$ is the fraction of radiative energy powering the outflow, β and $\zeta = \cos(\theta)$ are parameters relating to the outflow velocity and opening angle respectively.

Figure 1.7 shows equation 1.21 plotted for NS with masses in the range $0.9 - 2.2$ $M_\odot$ with spins of $a_* = 0.01$, as well as black holes with high spin $a_* = 0.998$ and masses in the range $4 - 20$ $M_\odot$. Both plots are shown for values of $R_{\rm out} = 10 - 1000$ $R_{\rm isco}$ and contours are overlaid to highlight several timescales. It can be seen that the higher values of spin result in much lower values of $P_{\rm wind}$.

Although Lense-Thirring precession is commonly invoked to explain certain observational signatures, it is worth noting that there are several other processes that may also induce similar effects, I will briefly cover some of them in the following section.

Other Precession Mechanisms

The Slaved Disc: Under this model, it is assumed that if the material is transferred through the accretion disc at relatively rapid speeds, then the disc normal will follow the precessing secondary spin axis. This model has been used to explain the 164-day periodicity in the galactic microquasar SS433 (Whitmire & Matese, 1980) requiring the secondary's rotation rate to be approximately half the corotation value. It has also been used to explain the periodic $\sim$ 35 day transient pulsations observed in Her X-1 (Roberts, 1974).

Radiative Warps Although the precession in Her-X-1 was initially, interpreted as a slaved disc more recent studies suggest that this may actually be due to a twisted accretion disc caused by a radiative warp (Pringle, 1992). In this process, a geometrically thin, optically thick disc may become warped due to non-axisymmetric forces, one governing shear within the plane of the disc and the other governing the shear perpendicular to the disc; the resulting torque acts to modify the warped disc and change its structure over time (Maloney et al., 1996).

Freely precessing neutron stars: Neutron stars are thought to consist of an inelastic crust containing a compressible liquid core, as a result, it is possible that the NS becomes oblate due to centrifugal forces or stresses of the crystalline solid. The core of the star will couple in a frictional way to the crust, and the resulting precession will be far more complicated than that of a rigid body (Jones & Andersson, 2001). An interesting recent result from LIGO that could shed doubt on this scenario however is the constraint on the equatorial ellipticities of several pulsars being less than $\epsilon < 10^{-8}$ (Abbott et al., 2020b).

Magnetic Warping: If the accretion disc surrounds a rotating magnetized central star (e.g. NS, WD or T Tauri star) then the disc can be subject to magnetic torques that can induce warping and precession in the disc. This model has been used to explain several phenomena such as the spin evolution of X-ray pulsars, QPOs and super-orbital periods in XRBs. (Lai, 1999)

1.4 The Swift Telescope

The Neil Gehrels *Swift* Observatory (Gehrels et al., 2004) is a multi-wavelength space observatory launched in 2004; while originally designed for the detection and rapid follow-up of Gamma Ray Bursts (GRBs), *Swift* has been used for many other subfields of study.

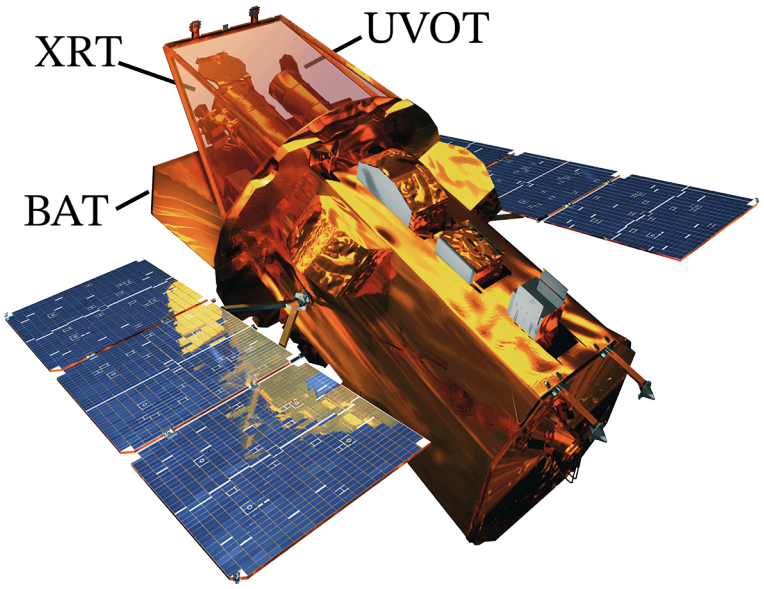

Figure 1.8: A 3D model of the *Swift* with the three telescopes labelled.

Aboard the observatory are three instruments: BAT, XRT and UVOT; these are labelled in figure 1.8. The Burst Alert Telescope (BAT) (Barthelmy et al., 2005) is the primary instrument used for locating GRBs and so is sensitive to photons with energies in the range $15 - 150$ keV and has an extremely large field of view (FoV) of ~ 1.4 sr which corresponds to approximately $1.4/4\pi \approx 10\%$ of the sky. After locating a GRB with BAT, *Swift* adjusts its position via a rapid slew (usually of order tens of seconds) and is able to search for afterglows using its X-ray telescope (XRT). The XRT (Burrows et al., 2005) is sensitive to X-rays in the $0.2 - 10$ keV energy range. The architecture of the telescope uses a Wolter-I design whereby photons are reflected at shallow angles by 12 concentric gold-coated nickel mirrors before landing on the silicon-based charge-coupled device (CCD) to create a 600x600 pixel image, meaning that each pixel corresponds to 2.36 arcseconds. The XRT has a FoV of 23.6 x 23.6 arcminutes (for reference the moon subtends about 30 arcminutes) and a point source will be spread by ~ 20 arcseconds, meaning that *Swift* XRT positions are roughly accurate to 1-3 arcseconds. The telescope is capable of operating in three modes: imaging, photon-counting and windowed timing, the first two of these are fairly similar, measuring the position, energy and time on the CCD of an incident photon, while window timing (WT) mode which only registers events along a single spacial dimension, but allows a temporal resolution of 1.8 ms.

The final instrument on *Swift* is the Ultraviolet and Optical Telescope (UVOT) (Roming et al., 2005). The modified Ritchey-Chrétien telescope is co-aligned and observes simultaneously with the XRT, the original reason for its inclusion was to capture the early (~ 1 minute) UV and optical photons from GRBs in the 170-600 nm band. Similar to the XRT in photon counting mode, the UVOT telescope is capable of recording both the arrival time and position of individual photons to sub-arcsecond. The UVOT has a slightly smaller FoV than the XRT with only 17x17 arcminutes, this means that it is possible to detect a source in the XRT without being able to image the same location with the UVOT. The final

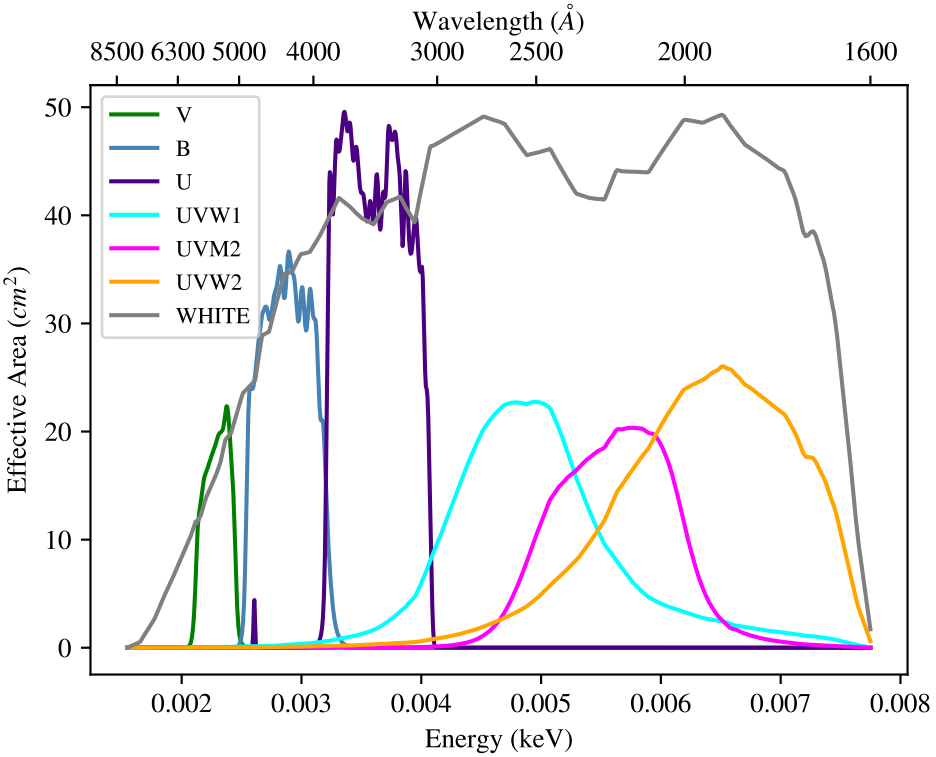

Figure 1.9: *Swift-UVOT* effective areas created from *Swift* response files.

images produced by the UVOT are 2048 squared pixels, meaning that each pixel corresponds to roughly 0.5 arcseconds, while the PSF is comparable to that of the XRT at 2.5 arcseconds. The UVOT hosts a total of seven filters, three in the optical (V, B, U), three in the UV (UVW1, UVM2, UVW2) and one broadband filter (WHITE), a plot of each of these bands effective areas is shown in figure 1.9. What is notable is that the photometric system used by UVOT and its close relative the Optical Monitor aboard *XMM-Newton* allow for the study of energies in the 1600 - 3000Å range, which would be strongly impeded at ground level.

Chapter 2

Ultraluminous X-ray Sources

Ultraluminous X-ray sources (ULXs) are the primary target of study in this thesis. The most common definition for ULXs is that they are point-like X-ray sources with observed luminosities that exceed 10^{39} erg s^{-1} with the specific requirement that they are not located in the centre of galaxies (off-nuclear) (e.g., Roberts 2007).

This chapter provides an introduction to ULXs from an observational perspective. I begin by proving a historical timeline of ULXs since their discovery in the late 1970s, and how the understanding of their nature has evolved over time. I then review some of the broad population-level studies that have been conducted on ULXs before covering the various pieces of spectral and temporal observational evidence that can signal the nature of the CO, companion star, accretion flow and its geometry. The chapter ends by briefly mentioning some other phenomena that although may initially appear similar in luminosity to ULXs are a result of different mechanisms to the standard picture.

2.1 A Short Chronological History

2.1.1 1979 - 1989 : First Detections and Early Theories

The Einstein Observatory (HEAO-2) (Giacconi et al., 1979) launched in November 1978 and operated for around two and a half years before exhaustion of the satellite's thruster fuel supply rendered the telescope inoperable in April 1981. Despite its short lifetime, the scientific contribution of the telescope should not be understated. Some key discoveries made with Einstein include: providing evidence that diffuse X-ray background, first observed in 1962, is created at least in part by a summation of observed X-ray sources (Tananbaum et al., 1979), the existence of X-ray jets observed in Centaurus A and M87 (Schreier et al., 1979, 1982), and confirming that all stars produce X-rays to some degree (Pallavicini et al., 1981).

Being the first X-ray instrument capable of image resolution, Einstein discovered approximately $\sim$ 5000 X-ray sources during its operation, $\sim$ 16 (0.3%) of which were considered to be ULX candidates above 10^{39} erg s^{-1} Helfand (1984); Fabbiano (1989)

The source M33 X-8 (Long et al., 1981) was among the first sources identified as being above the ULX threshold ($\sim 1.1 \times 10^{39}$ erg s^{-1}) and despite the authors suspecting that the source was a low-luminosity AGN (not helped by its proximity

to the galactic centre), they noted that the source exhibited several notable differences to typical AGN. It was observed that the size, brightness, and star formation rate of the nuclear region of M33 closely resembled those found in globular clusters. Early population synthesis models (O'Connell, 1983) predicted that perhaps around 160,000 neutron stars could have been produced in the nuclear region of the galaxy; could it be possible that the summed emission of binaries in the nuclear region could be responsible for this source, which at the time was a factor of three brighter than the most massive binary known SMC-X1 (Schreier et al., 1972) but simultaneously far dimmer than any known AGN (Kriss & Canizares, 1982)?

This theory was quickly ruled out by follow-up observations of M33 X-8 (Markert & Rallis, 1983) which showed that the source was strongly variable on the timescale of months, showing changes in luminosity by a factor of 40%. This behaviour would have to be caused by a single object, or as Robert W. O'Connell summarised in 1983: "The X-ray emission in the nucleus is unlikely to originate from a massive binary in the young population. If a massive compact object is involved, it is unusually quiescent at other wavelengths. Intermediate mass binaries may provide a type of X-ray source in M33's nucleus which is not common in other environments." – O'Connell 1983

These intermediate mass binaries, more commonly referred to as intermediate mass black holes (IMBHs) are systems where the black hole mass is expected to be in the region of $10^2 - 10^5$ $M_\odot$ and became strong contenders for the possible powering source for ULXs.

It is worth noting that at least one NS-OB star system, known as early as 1986, was known to have reached ULX luminosities. The flaring source A0538-66 was observed to have a maximum luminosity of 1.2×10^{39} erg s^{-1} and a period of 0.069 s (Stella et al., 1986) thus demonstrating that XRBs containing NS accretors could reach, albeit for a short time, luminosities in excess of ten times their Eddington luminosity.

2.1.2 1990 - 1999 : The ROSAT era

The launch of the Röntgensatellit (*ROSAT*) in June 1990 marked a turning point for X-ray astronomy and the study of ULXs. Sensitive to soft X-rays with energies $0.1-2.4$ keV *ROSAT* was the first X-ray satellite to conduct an all-sky survey, the associated bright source catalogue contained 18,811 sources and covered around 92% of the sky (Voges et al., 1999). With *ROSAT* came an abundance of bright X-ray sources as well as the birth of the term ultraluminous X-ray source (ULX) appearing first in the literature in Mizuno et al. 1999.

Colbert & Mushotzky 1999 used *ROSAT* and *ASCA* data of 13 ULXs, in 39 nearby face-on spiral galaxies to try to identify the nature of the accretor, they provided four plausible explanations: 1) The sources could be low-luminosity AGN, potentially due to low black hole masses or low accretion rates 2) IMBH binaries in the soft (high) state with masses in the range 3) superluminal X-ray sources similar to the galactic sources GRS 1915+105 and GRO J1655-40 which show evidence of bipolar superluminal outflows in their radio images. 4) young X-ray supernovae similar to SN 1978K in NGC1313, which has remained X-ray

bright with $L > 10^{38}$ erg s^{-1} for over 30 years (Schlegel, 2017).

2.1.3 2000 - Present : The *Chandra* and *XMM-Newton* era

The 2000s were marked by the idea that ULXs were binaries undergoing super-critical accretion as proposed by King et al. 2001. One proposition was that the observed luminosities of ULXs could be explained via a form of beaming, either geometrical, whereby anisotropy of the X-ray emission could lead to higher observed luminosities (King et al., 2001), or by relativistic beaming whereby one views the source directly along relativistic jets (Körding et al., 2002). Support for this idea came in the form of optical observations of several ULXs made by Pakull & Mirioni 2002, who identified optical nebulae associated with at least seven ULXs, many of which appeared to show bubble-like structures centred on the ULX position with radii $\sim$ 100 pc (much larger than supernovae remnants), possibly suggesting the presence of a powerful outflow driving the gas outwards, many more nebulae have since been found around ULXs (see section 2.6), and could be similar in nature to the W50 nebula powered by SS 433.

Following detailed studies of ULX spectra (see section 2.3) made possible by the high throughput of *XMM-Newton* and *Chandra* the theory that ULXs were accreting IMBHs would slowly begin to lose its foothold. Stobbart et al. 2006 showed that simple models assuming a multicolour disc were not adequate to explain the curvature between $3-10$ keV seen in many of the observed ULX spectra, meaning it was unlikely that they were just scaled up XRBs. Gladstone et al. 2009 performed further investigations proposing canonical ULX states distinct from those found in sub-Eddington XRBs.

Despite this, there are some ULXs that do show strong similarities to the sub-Eddington XRBs, the most notable example is the hyper-luminous X-ray source (HLX defined as $\geq 10^{41}$ erg s^{-1}) ESO243-49 HLX-1 (Farrell et al., 2009). The source shows the traditional hysteresis cycle seen in XRBs as well as radio jet emission as it transitions from the low/hard to the high/soft state (Webb et al., 2012), and with a maximum luminosity of 1.2×10^{42} erg s^{-1} is a prime candidate for an intermediate mass black hole with a mass of $\sim 10^3 - 10^4$ M$_\odot$ (Davis et al., 2011).

As monitoring campaigns on ULXs continued, it was revealed that some ULXs appeared to show long-term modulation of their X-ray light curves such as the 62-day periodicity found in M82 ULX-1 (Kaaret et al., 2006), these so called super-orbital periods would appear to be pervasive among the ULXs (see section 2.5).

A major milestone in the field came from the detection of pulsations with a using *NuSTAR* in M82 X-2, (Bachetti et al., 2014). A key feature of the pulsations was a large negative spin derivative, indicative of linear spin-up which could not be possible with in the case of a BH accretor that without a solid surface would not be able to provide the necessary accretion torque the source was thus the first unambiguously identified NS ULX.

Since then, more than a dozen ULXs have also been found to host NS accretors (see section 2.4.1) which has brought into question what the actual ULX demographic might be, and which up until this point had been widely considered to be

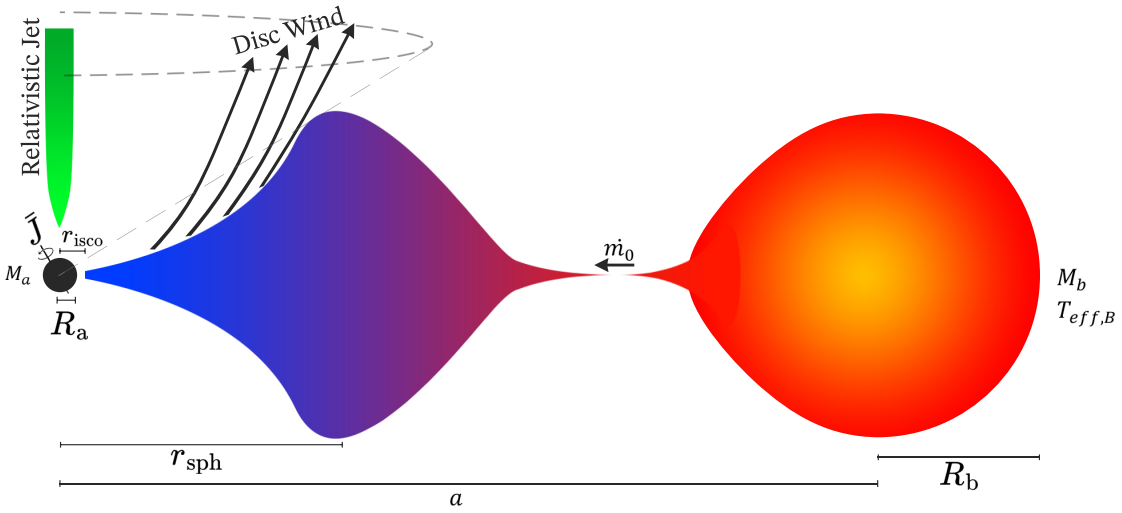

Figure 2.1: Diagram of a binary system undergoing supercritical accretion. R_a is the radius of the primary, R_b, the radius of the companion star with an effective temperature of $T_{\rm eff,B}$. The objects are separated by the semi-major axis a, $r_{\rm isco}$: the innermost stable circular orbit, $r_{\rm sph}$: the spherization radius. The CO spin axis which has been drawn misaligned from the disc axis is denoted by $\bar{J}$. Finally, the mass transfer rate in units of Eddington at the outer radius of the disc is labelled as $\dot{m}_0$.

BH accretors.

The gradual accumulation of new data provided sufficient evidence that many ULXs are indeed sources with supercritical accretion discs, and the discovery of neutron stars only further increased confidence in this theory. The field today now has a canonical picture of ULXs (see figure 2.1), however, many open questions still exist.

2.2 Population Characteristics

2.2.1 Catalogues

In the last 20 years, several attempts have been made to catalogue ULXs, one of the main considerations of which is completeness. Completeness refers to the fact that low-luminosity sources become increasingly more difficult to detect with increasing distance, which introduces a bias towards brighter sources at large distances, which may hamper studies of ULX population properties. One method to correct for this bias is to define a 'complete' sub-sample of sources that are within a certain distance $D_{\rm max}$ that are above a specified luminosity threshold $L_{\rm min}$, if $L_{\rm min}$ is significantly below the luminosity of the sources one is interested in (10^{39} erg s^{-1}) one can be somewhat sure that we are not biased by missing any sources below or near the luminosity threshold.

Table 2.1 lists some major efforts by various authors to catalogue ULXs made over the last $\sim$ 20 years, the majority have been compiled using data from *Chandra*

Catalogue	N_{ULX}	N_{gal}	N_{ULX}/N_{gal}
Humphrey et al. (2003)	22	13	1.69
Swartz et al. (2004)	154	82	1.88
Liu & Bregman (2005)	109	313	0.35
Liu & Mirabel (2005)	229	85	2.69
Swartz et al. (2011)	107	127	0.84
Mineo et al. (2012)	89	29	3.07
Earnshaw et al. (2019)	384	305	1.26
Kovlakas et al. (2020)	629	309	2.04
Walton et al. (2022)	1843	951	1.94
Bernadich et al. (2022)	779	517	1.51
Scott Barrows et al. (2022)	259	237	1.09

Table 2.1: Summary of ULX catalogues showing the number of ULXs N_{ULX}, host galaxies N_{gal} and ULXs per galaxy N_{ULX}/N_{gal}.

while some more recent catalogues have also included *XMM-Newton* Earnshaw et al. (2019) and also *Swift* data (Walton et al., 2022). I have summarised the number of ULXs in the catalogue and the number of galaxies they were detected in, it can be seen that the average *observed* number of ULXs per galaxy is roughly around $\sim 1-2$, the reason for a higher abundance in Mineo et al. 2012 is due to their focus on star forming galaxies, which are known to have an over-abundance of ULXs see: Zezas et al. 1999; Roberts & Warwick 2000; Humphrey et al. 2003. More specifically it was found that ULXs were preferentially associated with star forming regions in the arms of spiral galaxies and less likely to appear in low star forming elliptical galaxies (Liu & Bregman, 2005), this observation makes sense as ULXs and HMXBs are thought to have short evolutionary time-scales of order $\lessapprox 10^7$ yr, and so their X-ray emission is thought to promptly follow the episode of star formation. In contrast, LMXBs and SMBHs have much longer evolutionary timescales and so their presence can not be strongly correlated with star formation, this actually means that ULXs and HMXBs can serve as a useful probe for recent star forming activity in a given galaxy, which may be compared to other methods such as 60-μm I-band flux of the galaxy (Grimm et al., 2003; Mineo et al., 2012).

Kovlakas et al. 2020 used the *Chandra* Source Catalogue 2.0 to locate 629 ULXs in 309 galaxies within < 40 Mpc, with a 20% contamination from background AGN or foreground stars, they re-confirm the relation between ULXs and SFR, but extend the relation to include the stellar mass of the galaxy. The same authors found that low metallicity galaxies show an excess of ULXs, an observation that had been previously made by several authors (see: Pakull & Mirioni 2002; Soria et al. 2005; Mapelli et al. 2010; Prestwich et al. 2013; Brorby et al. 2014; Tzanavaris et al. 2016). Stellar evolution predicts that the more massive stars are formed if the metallicity (Z) of the progenitor gas is low. The outer layers of massive stars are thought to have reduced wind-loss rates due to lower opacities, leading to more massive cores which subsequently collapse into more massive BHs (Maeder, 1992), this explanation may explain why ULXs are associated with low-Z regions.

Bernadich et al. 2022 catalogued 779 ULXs in 517 galaxies by combining the 4XMM-DR9 catalogue with the Heraklion Extragalactic CATaloguE (HECATE),

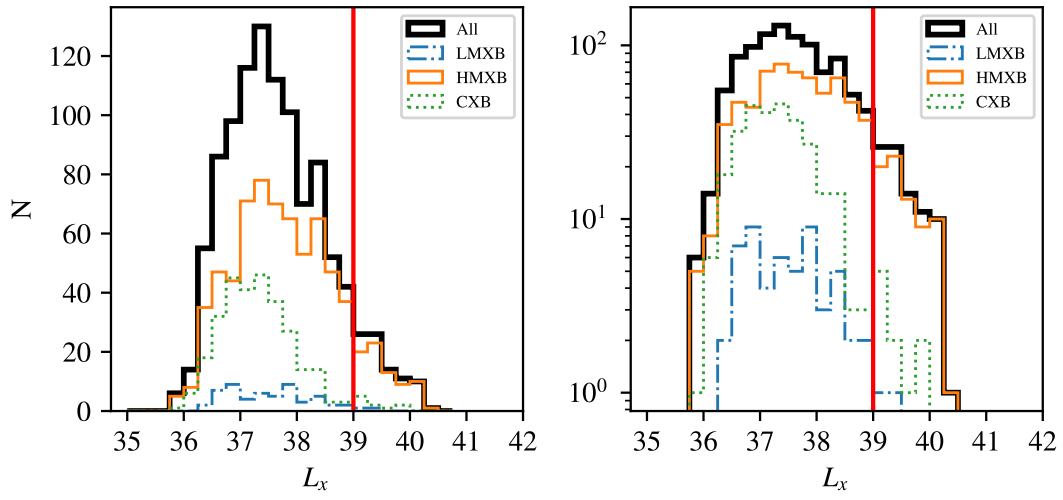

Figure 2.2: X-ray luminosity function (XLF) created for 1055 sources from (Mineo et al., 2012), showing the contribution from HMXB, LMXB and the cosmic X-ray background (CXB), 89 (8.44%) of the sources are above the 10^{39} erg s^{-1} luminosity (red line). The left and right plots show unlogged and logged y-axis respectively.

a massive catalogue of 204733 galaxies within 200 Mpc. An interesting analysis was conducted into the level of intra-observation variability for a subset of 147 ULXs by using the Gregory-Loredo variability probability, (Gregory & Loredo, 1992) which gives the probability of the source light curve not being created from a source with a constant flux. On average, they found that there is an 18% chance that a ULX is not variable, meaning that 82% of ULXs are likely to be variable. The variability is found to be highest for the subset of ULXs in late spirals with 90% of ULXs likely to be variable and minimised for lenticular galaxies with 74% of ULXs being variable. The bright ULXs, defined as sources with $L \geq 5 \times 10^{40}$ erg s^{-1}, appear to show lower levels of variability with average variability probabilities of 42% meaning that 58% of sources are likely to be variable within an observation.

Scott Barrows et al. 2022 collated a sample of 259 ULXs over the redshift range $z = 0.002 - 0.51$ ($\sim$ 10 Mpc$-$ $\sim$ 2000Mpc), this makes it the deepest ULX catalogue ever assembled. The catalogue was constructed via cross-matching galaxies from the Sloan Digital Sky Survey with the *Chandra* Source Catalogue. A key conclusion of their study is that the Occupation Fraction (the fraction of galaxies that host at least one ULX candidate) of ULXs is positively correlated with redshift. The authors also estimate the contribution to the cosmic X-ray background (CXB) at $z = 1$ to be around $\sim 1\%$, meaning that ULXs are therefore likely to contribute significantly to the overall ionising radiation from galaxies (see Fragos et al. 2013b).

We are rapidly approaching the point where the upper end of the luminosity range is no longer dominated by low statistics. Hyperluminous X-ray sources (HLXs) with luminosities $L \geq 10^{41}$ erg s^{-1}, will soon warrant their own catalogue, in fact, a catalogue of 72 HLXs is currently being prepared by (A. D. A. Mackenzie,

et al., in preparation).

The yet unreleased ULX catalogue that will be provided by *eROSITA* is expected to have a profound effect on our view of the ULX population. The *eROSITA* all-sky survey, *eRASS*, will scan half of the sky every six months for a period of four years and will probe previously unexplored depths, Bernadich et al. 2022 extrapolated the number of ULXs candidates found per unit sky area and providing a flux cut at the *eROSITA* sensitivity predicted that $\sim$ 2000 ULXs would be found in the first cycle of *eRASS*.

2.2.2 Population Synthesis Simulations

I have previously alluded to the forms of bias created from survey completeness (section 2.2.1), sometimes called the Malmquist bias (Malmquist, 1922, 1925), and the anisotropic nature of beamed emission, the combination of these two effects means that the *observed* population will be different from the *intrinsic* population. Stellar population synthesis models can provide a tool to better understand the intrinsic population and the evolution of systems on astrophysical timescales inaccessible to observation. In Chapter 3 I make extensive use of results from stellar population synthesis models, and so I will provide an explanation of their application to ULXs here.

Wiktorowicz et al. 2017 performed binary population synthesis calculations using `StarTrack` (see section 3.2.1) with the goal of trying to explain the evolutionary history of the ULX class. The simulation starts by specifying initial mass functions (IMF) of the form $\varepsilon(m) = m^{-\alpha}$ for both the primary and secondary, the IMF of the primary M_a was sampled from a power-law with index $\alpha = 2.7$ in the range $6 - 150$ M$_\odot$ motivated by observations of young and populous star clusters (Kroupa & Weidner, 2003), while the mass of the secondary was sampled from the range $0.08 - 150$ M$_\odot$ chosen to preserve a uniform mass-ratio distribution.

Distributions for the initial binary separations are given by $P(a) \sim 1/a$, while the eccentricity of the binaries follows the thermal eccentricity distribution first derived by Jeans (1919) the distribution function, $f(e)$, in terms of the eccentricity, e, is given by $f(e)\ de = 2e\ de$, this result implies that the eccentricities will be distributed linearly and nearly circular orbits will be rare. The median eccentricity of such a distribution is $e = 1/\sqrt{2}$; this derivation makes the assumption that all the stars in the sample have interacted many times and have reached statistical equilibrium, a result that remains somewhat contested observationally (see Geller et al. 2019).

Half of the stars with masses below 10 M$_\odot$ were set to be in binary systems, while stars greater than this mass were always in binary systems. For each simulation, 20 million (2×10^7) binary systems were evolved, from which their total mass was calculated ($M_{\rm sim}$) and used to calculate a scaling factor by dividing the mass of all the systems by the mass of the Milky Way: $SF = M_\star / M_{\rm sim}$ where $M_\star \sim 6 \times 10^{10}$ M$_\odot$ (Licquia & Newman, 2015).

A variety of simulations were carried out, for a range of metallicities: ($Z = 0.02, 0.002$ and 0.0002) as well as two different scenarios describing star formation, 1) a constant star formation rate (SFR) of 6 M$_\odot$ yr^{-1} for a period of 10 Gyr and 2) a burst star formation rate of 600 M$_\odot$ yr^{-1} for a duration of 100 Myr.

To calculate the source luminosity, the logarithmic dependence of bolometric luminosity on the mass accretion rate $L_{\rm x,iso} \sim L_{\rm Edd}[1 + \ln(\dot{m}_0)]$ (Poutanen et al., 2007) was used and subsequently beamed by a factor $L_x = L_{\rm x,iso}/b$ (King et al., 2001). The beaming prescription involves two cones with half opening angles $\theta/2$ located at opposite ends of the compact object. If one assumes a cone with half opening angle $\theta/2$, one can easily find that the ratio of solid angles of a cone to a sphere is given by:

$$\Omega = \int_0^{2\pi} \int_0^{\theta/2} \sin(\theta) d\theta d\phi = 2\pi \left[1 - \cos(\theta/2)\right] \tag{2.1}$$

Since there are two cones, we multiply the above number by two and divide by the solid angle of a sphere (4π).

$$\frac{2 \times 2\pi \left[1 - \cos(\theta/2)\right]}{4\pi} = 1 - \cos(\theta/2) = b$$

for a random distribution of binary inclinations, b is the "probability" of looking down a cone as a function of θ. e.g. a half opening angle of 90° would correspond to a beaming factor of 1 and observational probability of 100%.

The binaries created in the simulation were evolved from their starting positions on the zero-age main sequence (ZAMS). Wiktorowicz et al. 2017 find that ULXs containing NS accretors may be found as early as 6 Myr after star formation. The authors find that ULXs containing BH accretors are a minority as compared to the NS ULXs, but would appear to dominate at early epochs in the constant SFR model, they also find that BHs dominate the HLX class with luminosities $> 10^{41}$ erg s^{-1}. Two formation pathways for a typical young NS and BH ULX system from the simulations are illustrated in figure 2.3.

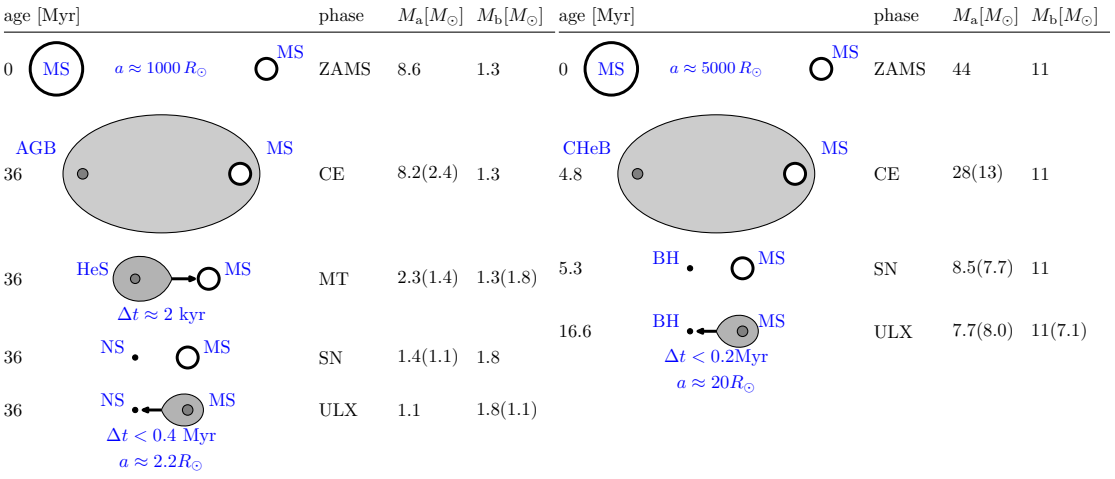

Figure 2.3: Schematic representation of the dominant NS ULX evolutionary route for young systems (left) and the dominant route for BH ULX evolution in star forming regions (right). The age and mass values reflect those in a typical system. (Wiktorowicz et al., 2017)

In Wiktorowicz et al. 2019 the authors expanded upon their previous work by investigating how anisotropic emission of radiation affects the observed sample of

ULXs. Their simulations are largely similar to those found in Wiktorowicz et al. 2017 with some small differences such as the sampling of initial distributions of eccentricities $P(e) \sim e^{-0.42}$ and orbital periods $P(\log P) \sim (\log P)^{-0.55}$. As in Wiktorowicz et al. 2017 the authors again emphasize that the total number of NS ULXs is significantly higher than the total number of BH ULXs, however the addition of the anisotropic emission causes the observational populations to be comparable, this is because the BH accretors are typically found to be emitting isotropically with $b \sim 1$ and undergo nuclear timescale mass transfer, while the NS accretors are predominantly beamed with $b \sim 0.07 - 0.2$ and have typical mass transfer on a thermal timescale. They predict that the observed NS population represent only 20% of the total NS population.

2.3 Spectral Characteristics

Studies of the HMXB Cygnus X-1 (Tananbaum et al., 1972) showed that the source displayed two distinct spectral states: a high luminosity state with a soft spectrum without radio emission, and a low-luminosity state with a hard spectrum accompanied by radio emission. These states are found with near-ubiquity in XRBs (along with several other sub-states see Esin et al. 1997) and are thought to correspond to different modes of accretion onto the compact object. These state transitions occur during outbursts, likely caused by the thermal-viscous instability (see Lasota 2001), which can be traced out in the hardness vs count rate parameter space commonly called the hardness-intensity diagram (HID) which traces out a q-shaped path that travels in the anti-clockwise direction. Despite these state transitions being known for over 50 years, their exact physical nature remains an open question. XRBs spend their time in a quiescent state between outbursts. The hard state then follows quiescence, in this state, the spectra are dominated by a thermal component peaking at $\sim$ 100 keV, one model that may explain for this state is that of a truncated accretion disc where the central regions have been replaced with a hot inner-flow meaning that few seed photons are able to illuminate the optically thick accretion flow (Done et al., 2007), from the hard state, state the source moves to the soft state. In the soft state, the spectra appear dominated by thermal emission, thought to be due to a geometrically thin, optically thick accretion disc extending down to the ISCO (Shakura & Sunyaev, 1973), for this reason, it is sometimes referred to as the thermal state. The soft state may also have a non-thermal component, modelled as a power-law that extends to high energies ($\sim$ 100 keV - 1 MeV) the origin of this high energy emission is thought to be due to scattering in optically thin material composed of a mix of both thermal and non-thermal electrons that are probably in a region above the disc surface sometimes referred to as the corona (Zdziarski & Gierliński, 2004).

One of the main distinguishing features of ULXs is that the vast majority appear to not display transitions between the canonical 'hard' and 'soft' states seen in sub-Eddington sources[1]. Gladstone et al. 2009 extracted high resolution spectra for 12 ULXs with $> 10,000$ counts and were able to rule out single component

[1]Some HLXs do appear to share this hysteresis cycle, further justifying their subclassification from the ULX regime (see: Godet et al. 2009; Servillat et al. 2011; Webb et al. 2012)

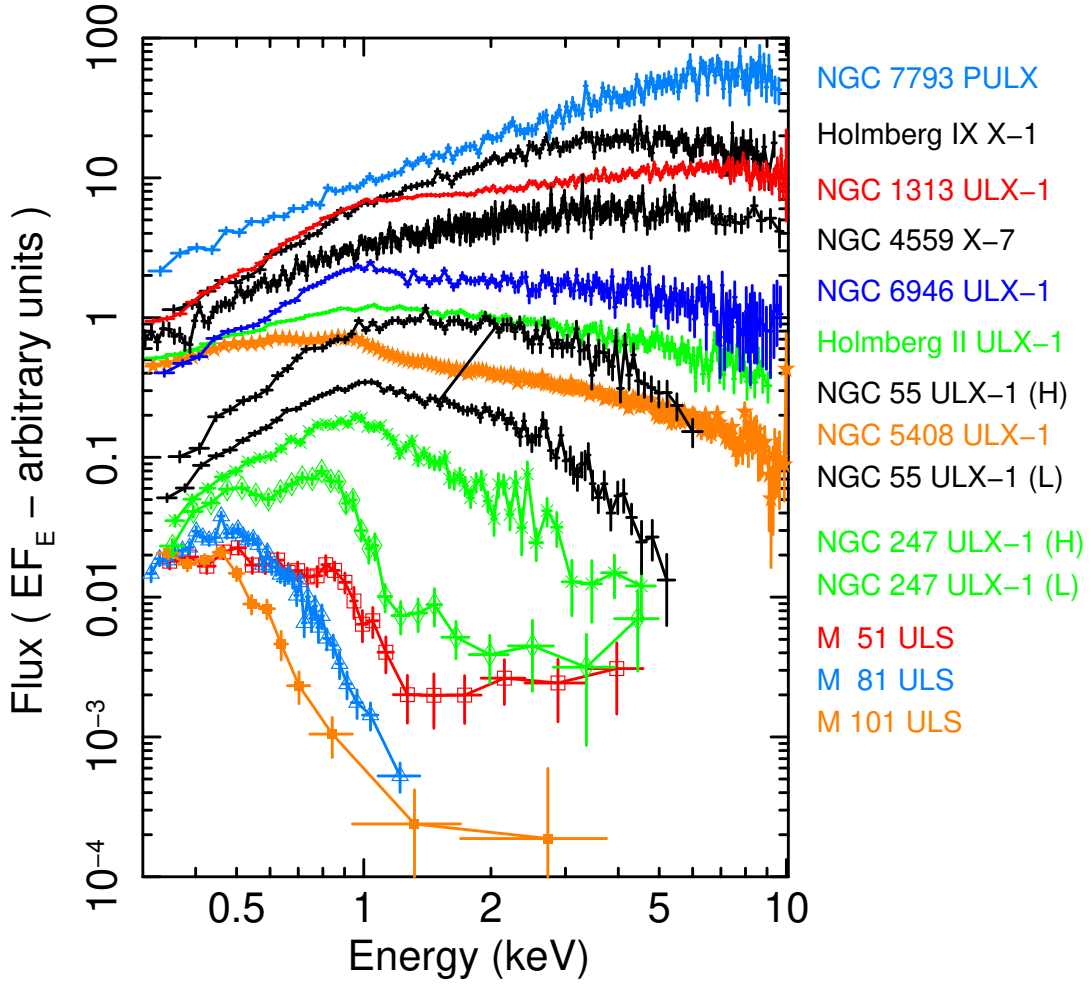

Figure 2.4: X-ray spectra of some of the brightest ULXs with the increasing hardness ratio from the bottom to top. Figure taken from (Barra et al., 2022)

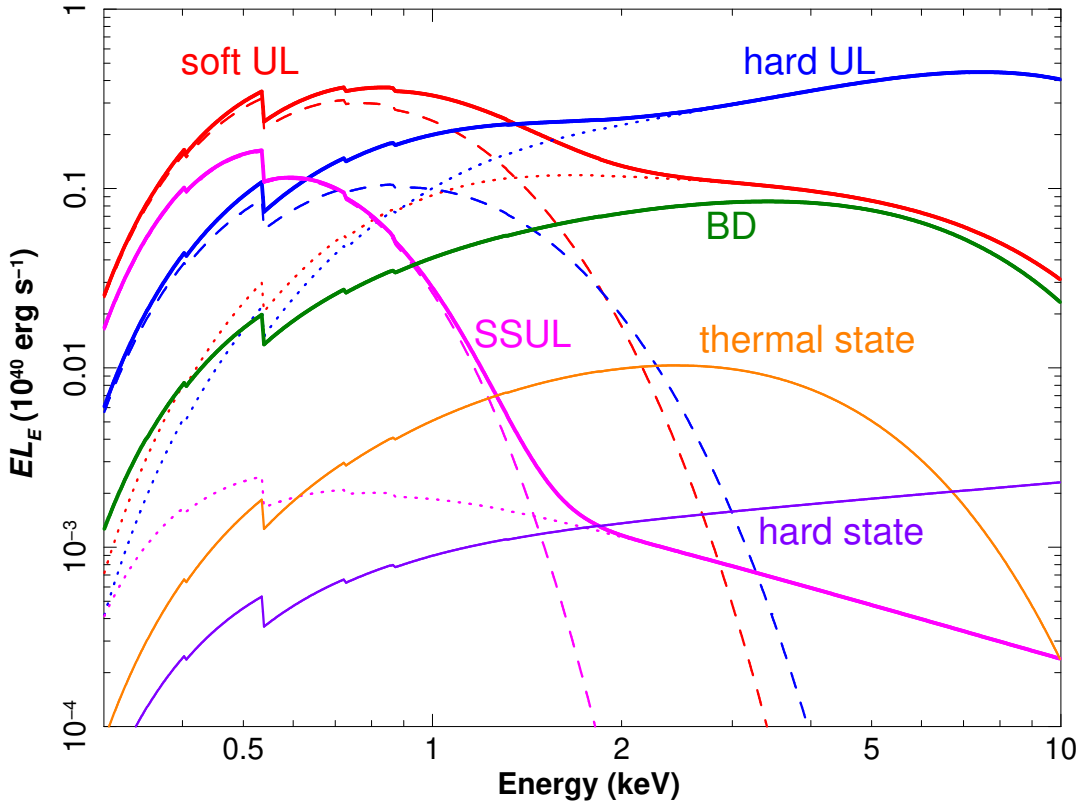

Figure 2.5: A diagram showing the two canonical XRB spectra thermal (soft) and hard states as well as four various states proposed to exist in ULXs: soft and hard ultraluminous; SSUL: supersoft ultraluminous; BD: broadended disc; figure taken from (Kaaret et al., 2017)

power-law continuum and multicolour disc (MCD) black body models, both of these models had previously been used to infer the existence of IMBHs from lower-quality spectra assuming thin sub-Eddington accretion discs of temperatures of $0.1-0.2$ keV (see: Colbert & Mushotzky 1999; Miller et al. 2004). Gladstone et al. 2009 found that combining the power-law and MCD models provided significantly better fits to the data, but still failed to describe the 'rollover' found ubiquitously in ULX spectra above 3 keV. Gladstone et al. 2009 suggested that ULXs could instead be modelled as an optically thick corona that blocks the inner part of the disc, such that the visible part of the disc has a much lower temperature.

The second feature in ULX spectra is a large contribution of flux at energies below < 1 keV, known qualitatively as the soft-excess. This was proposed by Gladstone et al. 2009 to be the sources of the seed photons that would then be inverse Compton scattered in the optically thick corona, providing the higher energy emission. Gladstone et al. 2009 dubbed this model the ultraluminous state and suggested that all these sources were in a super-Eddington accretion state.

Sutton et al. 2013 expanded on the work of Gladstone et al. 2009 and proposed three empirical classifications based upon the best fit values for a doubly absorbed MCD plus power-law spectral model. The three classifications were given the names: broadened disc (BD) and soft and hard ultraluminous; figure 2.5 shows the relative shapes of these spectra as well as the shapes of the soft and hard states in classical X-ray binaries, figure 2.4 shows a variety of ULX spectra obtained from (Barra et al., 2022), it may be seen that sources near the top are consistent with the hard UL shape, moving down they become softer, more consistent with the soft UL state, while the sources at the bottom are consistent with the super-soft (SS) state.

Some ULXs have been found to evolve through these aforementioned phenomenological spectral classifications (Middleton et al., 2015a; Luangtip et al., 2016). An explanation is that depending on the source inclination, the observed ULX spectra can be divided into three cases (see figure 2.6). At low inclinations ($i < \theta/2$) the spectra may appear as hard UL as the central hard emission can be seen directly. If the view of the central region changes, which could occur due to precession of the inner regions of the disc, or an increase or decrease in the accretion rate changing the funnel opening angle, (Middleton et al., 2015a) the wind could enter the line-of-sight leading to softer spectra since the central hard photons are either scattered out of the line-of-sight resulting in soft UL spectra. Alternatively, the wind could remain out of the line-of-sight (especially the case for low inclinations) and the central hard photons are increasingly beamed up the funnel. Theoretically, ULXs viewed at mid-inclinations should display soft UL spectra, increasing the accretion rate for these inclinations result in increasingly softer spectra as one looks through a greater amount of the wind. For edge-on inclinations, the spectra are predicted to be extremely soft in X-rays giving rise to super soft sources and sources which even may peak in the UV (see Kaaret et al. 2010).

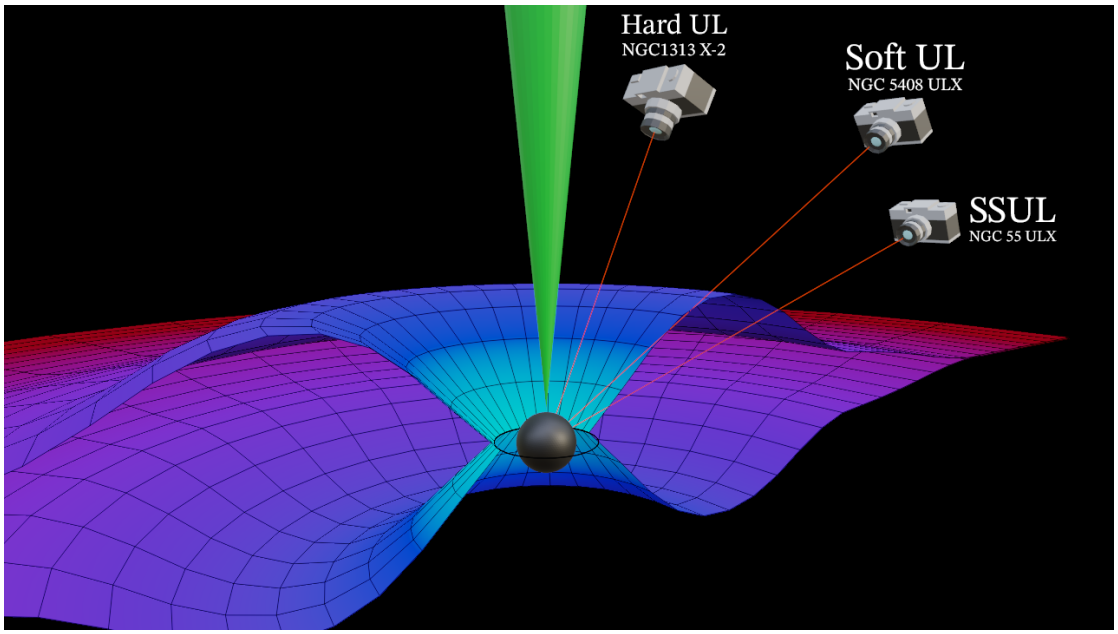

Figure 2.6: A diagram of the possible scenarios giving rise to three types of ULX spectra. At low inclinations, it is possible to see the hard emission down the funnel created by the supercritical disc, resulting in harder spectra. At mid-inclinations, one loses the view of the central regions and observes the cooler emission arising from the outer-photosphere. At very high inclinations one is looking through a large amount of the disc, much of the central region is occluded by strong winds and much of the observed emission arises from the cool outer regions of the wind (Poutanen et al., 2007).

2.3.1 Outflows

One of the main predictions of the super-critical model of accretion is the presence of fast-moving, mass loaded outflows (Poutanen et al., 2007; Abolmasov et al., 2009). Two methods exist observationally for confirming the existence of these outflows in ULXs, the first is presence of Doppler broadened spectral lines in high-resolution X-ray spectra, the second method is estimating the kinematic power of the outflow by observing the emission signature of the interaction with its surrounding environment.

The first hint of broadened lines came from Middleton et al. 2014 who re-interpreted soft residuals in the spectra of NGC 5408 X-1 and NGC 6946 X-1 as the presence of an optically thin plasma outflowing into the line-of-sight and ionized by the central source, as noted by the authors however the line profile was not resolved (Middleton et al., 2015b; Walton et al., 2016a).

The first confirmed detection ($> 5\sigma$) of X-ray Doppler shifted lines was found by Pinto et al. 2016 (see also Walton et al. 2016a), and came from highly ionized iron, oxygen and neon found in the sources NGC 1313 X-1 and NGC 5408 X-1 using exposures $\sim$ 100 ks from the *XMM-Newton* Reflection Grating Spectrometer (RGS). Specifically, they found that the *absorption* lines confirmed the existence of a photoionized gas within a wind moving with velocities of at least

$\sim 66,000$ km s^{-1} or equivalently, $\sim 0.2c$, meaning that the gas is moving at relativistic speeds. Ultrafast outflows have subsequently been detected in two PULX sources: NGC300 ULX-1 (Kosec et al., 2018b) and Swift J0243.6+6124 (van den Eijnden et al., 2019), as well as in NGC 55 ULX (Pinto et al., 2017b) and NGC 4395 ULX1 (Ghosh et al., 2022). The first large-scale search for ionised emission and absorption features (Kosec et al., 2021) has revealed that outflowing winds appear to be common among the ULX class.

M101 ULX-1 was confirmed to be a BH - Wolf-Rayet binary with a orbital period of 8.2 days via optical spectroscopy by Liu et al. (2013). Based on the orbital period and nature of the companion, a BH mass of $5 \leq \mathrm{M} \leq 20 - 30$ M$_\odot$ is proposed. Shen et al. (2015) performed modelling of M101 ULX-1 and find that an optically thick outflow from the BH with an outflow rate of around $\dot{\mathrm{M}} \sim (0.4 - 2) \times 10^{-4}$ M$_\odot$ yr^{-1} may be able to explain the X-ray emission of the source.

Soria et al. 2014 detected a radio-optical structure powered by M83 ULX-1, ascribed to emission from a radio bubble or radio lobes inflated by the mechanical power of the BH. They found that optical-infrared line emission implied an average kinetic power of 3×10^{40} erg s^{-1}, inferring an expansion age of 16,000 years with a velocity of $v_s \sim 200 - 310$ km s^{-1}.

2.4 Neutron star ULXs

2.4.1 Pulsating ULXs

A number of ULXs are known to exhibit pulsations signalling NS accretors. Sometimes called PULXs, a dozen or so pulsating ULXs are given in table 2.2, which includes a few sources that are not commonly mentioned.

One explanation for these systems is that they are magnetars, that is to say, neutron stars with very large dipole fields with $B \sim 10^{13-15}$G. The large magnetic field could result in a reduction of the electron scattering cross-section (Canuto et al., 1971) below the Thompson value, allowing for super-Eddington luminosities in certain directions. (Tong, 2015; Eksi et al., 2015; Mushtukov et al., 2015; Dall'Osso et al., 2016)

Another explanation for the sources is that they are powered by neutron stars with relatively normal dipole field strengths (10^{11-13} G) but the X-rays are beamed due to the outflow from the supercritical accretion disc (King & Lasota, 2019).

One process that should be only present in systems with neutron star accretors is the intermittent accretion caused by infalling matter having to overcome a centrifugal barrier created by the interaction of the rotating NS magnetic field with the accretion disc. The process can be explained via the relation between two characteristic radii: the first is the corotation radius $r_{\mathrm{co}} \equiv (GMP^2/4\pi^2)^{1/3}$, which is the radius at which the angular velocity of the star matches the Keplerian velocity of the disc, the second is the magnetospheric radius R_{m}, defined as the radius at which the magnetic pressure balances the ram pressure of the accretion flow. An estimate of the magnetospheric radius for a super-Eddington accretion flow may be given by equation 2.2:

$$R_{\mathrm{m}} \approx 4.2 \times 10^7 B_{12}^{4/9} \ (\mathrm{cm}) \tag{2.2}$$

Source Name	L_x (erg s^{-1})	P (s)	$\dot{P}$ (s^{-1})	Ref
GRO J1744-28	$\sim 10^{40}$	~ 0.42	$+1.7 \times 10^{-12}$	1
CXOU J073709.1+653544	$\sim 10^{39}$	~ 18	-1.1×10^{-7}	2
XMMU J031747.5-663010	$\sim 1.6 \times 10^{40}$	~ 765.6	-	3
M82 X-2	1.8×10^{40}	~ 1.37	-2.7×10^{-10}	4
NGC 7793 P13	$\sim 10^{40}$	~ 0.43	-3×10^{-11}	5, 6
NGC 5907 ULX-1	$\sim 10^{41}$	~ 1.1	-8×10^{-10}	7
SMC X-3	2.5×10^{39}	~ 7.8	-7.4×10^{-10}	8
SWIFT J0243.6+6124	$\sim 2 \times 10^{39}$	~ 9.8	-2.2×10^{-8}	9, 10
NGC 300 ULX-1	4.7×10^{39}	~ 31.5	-5.6×10^{-7}	11
M51 ULX-8	4.8×10^{39}	-	-	12
NGC 1313 X-2	6×10^{39}	~ 1.5	-3.3×10^{-8}	13
M51 ULX-7	7×10^{39}	~ 2.9	-2.4×10^{-10}	14
RX J0209.6-7427	$\sim 2 \times 10^{39}$	~ 9.3	-1.75×10^{-8}	15
NGC 7793 ULX-4	$\sim 3.4 \times 10^{39}$	~ 0.4	-3.5×10^{-8}	16

Table 2.2: 14 ULXs that have been proven or are suspected based on cyclotron lines to contain neutron star accretors. L_x : luminosity, P : Spin period $\dot{P}$: Spin period derivative References: 1 : Sazonov et al. (1997) 2 : Trudolyubov et al. (2007) 3 : Trudolyubov (2008) 4 : Bachetti et al. (2014) 5 : Fürst et al. (2016) 6 : Israel et al. (2017b) 7 : Israel et al. (2017a) 8 : Tsygankov et al. (2017) 9 : Jenke & Wilson-Hodge (2017) 10 : Doroshenko et al. (2018) 11 : Carpano et al. (2018) 12 : Brightman et al. (2018) 13 : Sathyaprakash et al. (2019) 14 : Rodríguez Castillo et al. (2020) 15 : Chandra et al. (2020) 16 : Quintin et al. (2021) See also A0538-66 : Stella et al. (1986) ($L_{\max} \sim 1.2 \times 10^{39}$ erg s^{-1})

where B_{12} is the magnetic field strength in units of 10^{12} G. (Middleton et al. 2022 in prep)

If $R_{\rm co} > R_{\rm m}$, accretion occurs as matter arrives at the magnetospheric radius from which it is assumed to free-fall onto the NS magnetic poles. However, if $R_{\rm co} < R_{\rm m}$, the centrifugal force created by the rapidly rotating magnetosphere leads to the matter being propelled away, rather than being accreted; this so-called 'propeller effect' (Illarionov & Sunyaev, 1975). In systems where $R_{\rm co} \approx R_{\rm m}$, it is thought that these two radii may repeatedly cross, resulting in periods of accretion and periods of quiescence within the magnetospheric radius. Observationally, the propeller effect has been invoked to explain bi-modal luminosity distribution in a few ULXs (Tsygankov et al., 2016; Earnshaw et al., 2018; Vasilopoulos et al., 2021)

2.4.2 Cyclotron Lines

Absorption lines have been detected in two ULXs: M51 ULX-8 (Brightman et al., 2018) and NGC 300 ULX1 (Walton et al., 2018) (although the latter of these is disputed see Koliopanos et al. 2019). These lines have been interpreted as cyclotron lines, also called cyclotron scattering resonance features (CRSF) and are thought to be due to the resonant scattering of charged particles in a strong magnetic field. A useful feature of these lines is that their shape and strength allow

for estimations of the magnetic field strength. The estimate is higher if the line feature is produced by protons as compared to electrons. Assuming electrons for NGC 300 ULX1 points to a field of order $B \sim 10^{12}$ G and for M51 ULX-8 implies $B \sim 10^{9-15}$ G depending on whether the feature is due to protons or electrons.

2.5 Periods & Super-Orbital Periods

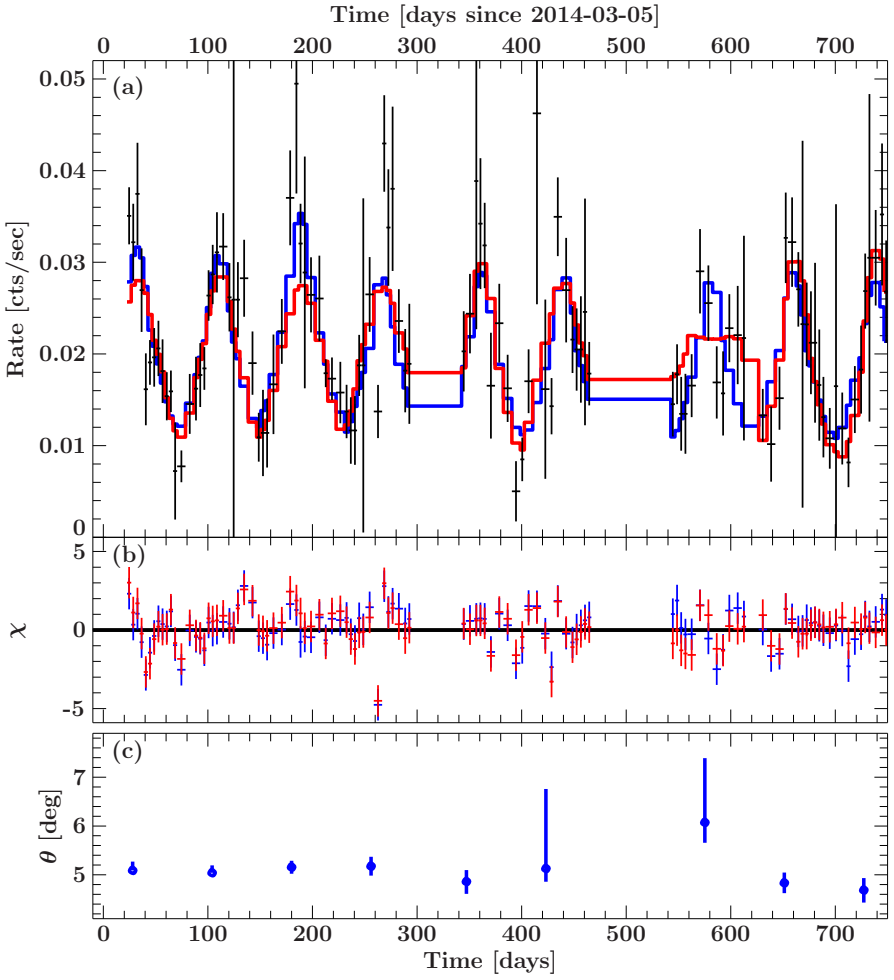

Figure 2.7: The $0.3 - 10$ keV *Swift* XRT light curve of NGC 5907 ULX-1, binned to 4 d. The model with a fixed opening angle is shown in red, while the model with variable opening angle is shown in blue. (b) Residuals of the model fits depicted in the same colours. (c) The half-opening angles θ of the best-fitting model with a fixed intrinsic luminosity. The half-opening angle is around 5°. Figure from Dauser et al. 2017.

Studies of SS 433 (Abell & Margon, 1979) showed that in addition to the ~ 13 day orbital periodicity, a much longer period of ~ 163 days was also detected. This super-orbital period has been explained as precession of relativistic ($\sim 0.2c$) jets due to a slaved disc (see section 1.3.4).

Various periods are known to exist in a number of ULXs with various interpretations. In table 2.3 I have summarised many of these periods and whether they

have been interpreted as being orbital or super-orbital.

Source Name	Period (days)	Nature	Citation
A0538-66	16.64	Orbital	White & Carpenter (1978)
A0538-66	421	Super	McGowan & Charles (2003)
SS 433	13	Orbital	Abell & Margon (1979)
SS 433	163	Super	Abell & Margon (1979)
M33 X-8	106	Super	Dubus et al. (1997)
M82 X-1	62	Orbital	Kaaret et al. (2006)
NGC 1313 X-2	6.12	Orbital	Liu et al. (2009)
NGC5408 X-1	2.65	Orbital	An et al. (2016)
NGC5408 X-1	115	Super	Strohmayer (2009)
NGC5408 X-1	189	Super	An et al. (2016)
7793 P13	64	Orbital	Motch et al. (2014)
M82 X-2	2.5	Orbital	Bachetti et al. (2014)
M82 X-2	55	Super	Kong et al. (2016)
NGC5907 ULX-1	5	Orbital	Walton et al. (2016b)
NGC5907 ULX-1	78.1	Super	Fürst et al. (2017)
NGC 4395 ULX-1	62.8	?	Vinokurov et al. (2018)
M51 ULX-7	2	Orbital	Rodríguez Castillo et al. (2020)
M51 ULX-7	38	Super	Brightman et al. (2020b)
NGC 925 ULX-3	127	?	Earnshaw et al. (2022)

Table 2.3: Various periods and their inferred nature in ULXs.

A figure of the superorbital period found in NGC5907 ULX-1 may be seen in figure 2.7, the light curve has been fit with the model from Dauser et al. 2017.

A linear relationship was found between the orbital period and superorbital period in ULXs, akin to what is seen in disc-fed neutron star supergiant X-ray binary and Be/X-ray binary systems by Townsend & Charles 2020. A linear fit between the two periods yielded $P_{\rm sup} = 22.9 \pm 0.1\ P_{\rm orb}$, although the authors do not provide any physical basis on the origin of the superorbital period, they make use of the relation and its similarity of the relation to what is seen in sub-ULX sources to argue that ULX pulsars may be supergiant X-ray binary and Be/X-ray binary systems accreting at super-Eddington accretion rates.

The nature of the super orbital periods observed in ULXs is still of open debate, however, some kind of precession is often touted as being responsible. Lense-Thirring precession of the supercritical accretion disc remains a popular explanation for several sources, however, there exist other possibilities (see section 1.3.4). A recent study made by Sridhar et al. 2021 provided an analytic relation between the Lense-Thirring (see section 1.3.4) period and the orbital period that also appears to follow a straight line in log-log space, similar to what was observed by Townsend & Charles 2020.

2.6 Optical Counterparts

In the last 20 years, much research has focused on identifying optical counterparts to ULXs. The suspected companion star has identified in many studies, and are often found to be O or B stars (see Liu et al. 2002; Roberts et al. 2001; Goad et al. 2002; Liu et al. 2004; Kuntz et al. 2005; Ptak et al. 2006; Roberts et al. 2008; Liu et al. 2007; Feng & Kaaret 2008; Motch et al. 2011; Grisé et al. 2011, 2012; Jonker et al. 2012; Gladstone et al. 2013; Wang et al. 2015; Vinokurov et al. 2018; Allak et al. 2022), or in some cases red supergiants or asymptotic giant branch stars (see Liu & Di Stefano 2008; Heida et al. 2015, 2016; López et al. 2017; Heida et al. 2019), it is worth noting however that there is an observational bias in detecting these large and bright stars in external galaxies and so it could be that the association of these types may be somewhat over-represented, this is especially true when large-scale searches often fail to identify clear counterparts, meaning that many companions are below the detection threshold.

Fabrika et al. 2015 using the 8.2 m *Subaru* telescope acquired optical spectra for four ULXs: Holmberg II X-1, Holmberg IX X-1, NGC4559 X-7, and NGC 5204 X-1. All the spectra show bright He II λ4686, Hα, Hβ emission lines, the lines are broad with widths corresponding to velocities of $500 - 1500$ km s^{-1}. These He-II lines are not typically associated with stellar mass black holes but have been detected in SS 433 and some systems with late nitrogen Wolf-Rayet stars as donors. The relative strength of the He II λ4686 lines compared to the hydrogen lines however are not seen in the spectra of these hot stars and so the authors suggest that the spectra are produced from the wind that must be even hotter and more ionized than the stellar winds found in Wolf-Rayet or Luminous-Blue variable stars, and therefore must come from the accretion disc.

UV Counterparts

A small amount of research has been conducted in the UV with regard to ULXs; since most light in the UV range ($10 - 320$ nm) is absorbed by the Earth's atmosphere, studies in this wavelength must use space-based observatories. Kaaret et al. 2010 used the Hubble Space Telescope (HST) in the far UV (FUV) (1533 Å) to analyse the source NGC 6946 ULX3. The authors conclude that the UV flux is consistent with a blackbody spectrum of $T \sim 30,000$ K that is possibly from a companion star, however in order to account for the nebular He-II flux across the broad-band spectrum (FUV, B, V, I bands and He-II flux), a truncated multi-colour disc with an outer disc temperature of $T \sim 16,000$ K provide adequate fits to produce the ionising radiation. Tao et al. 2011 analysed 13 ULXs using HST and find that both magnitude and colour variation is detected in these sources on the order of days to years. Additionally, they suggest that the optical spectrum of NGC 2403 X-1 which includes the near-UV F330W filter ($\sim$ 3300Å) is potentially consistent with a standard MCD model.

Sonbas et al. 2019 using *HST* and *Chandra* compared the flux densities in the X-ray and UV (2500 Å) by way of the optical-X-ray spectral index $\alpha_{\rm ox}$ (Tananbaum et al., 1979) for a sample of 9 ULXs. They find a negative correlation between the optical-X-ray spectral index $\alpha_{\rm ox}$, and the monochromatic luminosity at 2500

Å, a trend which is also found for active galactic nuclei potentially hinting at an intrinsic similarity of these sources to ULXs.

Nebulae

ULXs have been preferentially found to exist in young, high star-forming regions and are associated with shock-ionised bubble nebulae, the size of which may serve as indicators of the evolutionary history and age of the system as well as the mechanical power associated with the ULX.

Pakull & Mirioni 2002 were among the first to study optical counterparts in ULXs. A key finding was the discovery of emission nebulae at the position of several ULXs. These nebulae often showed both low and high ionisation emission lines, meaning that the gas must therefore be either photoionized by X-ray or UV photons, or shock-ionized by outflows. Kaaret et al. 2004 carried out follow up observations of the He-II nebulae around Holmberg II X-1 discovered by Pakull & Mirioni 2002 and confirmed that the nebula was being photoionized by the X-rays of the ULX. Grisé et al. 2006 discovered a very large 280×130 pc nebula in the source IC 342 X-1, a size much larger than normal supernova remnants, the authors state that the nebula is mainly shock ionized rather than photoionized and conclude that the source could be inflated by relativistic wind/jets similar to the W50 nebula surrounding SS 433 (Huang et al., 1983).

Urquhart et al. 2018 found nebulae in M51 surrounding two sources. Following analysis of the optical spectra, the authors argue that the gas in the source M51 ULX-1 was shock-ionized, consistent with jet emission. In contrast, the nebula found in M51 ULX-2 is likely a H-II region not physically related to the ULX but simply a chance alignment, these conclusions are strengthened by the detection of a radio counterpart in the first source but not the second.

Avdan et al. 2019 discovered nebulae associated with 5 ULXs in NGC 4490 and NGC 4485. Vinokurov et al. 2020 discovered one of the brightest optical ULX counterparts in the highly variable UGC 6456 ULX and also find a positive correlation between the optical and X-ray fluxes which the authors interpret as re-processing of the X-rays in the outer parts of the optically thick wind coming from the supercritical accretion disc. Lara-López et al. 2021 analysed three ULXs in NGC925, and showed that the nebula associated with NGC 925 ULX-1 had a low-metallicity, consistent with HMXB formation scenarios while the region in NGC 925 ULX-3 had a much higher metallicity which was interpreted as being consistent with the progenitor being a highly accreting neutron star within an evolved stellar population region. Nebulae in were also found in NCG4861 and NGC4449 by Ozdogan Ela et al. 2021.

2.7 Other Phenomena that reach ULX luminosities

In studying a specific class of object one can often be biased in attempting to explain all the observed phenomena under a known framework, that is to say, that all observed ULXs must be accreting binary systems with stellar mass BHs or NSs

as their accretors.

There are in fact several other processes that could be responsible for sources above 10^{39} erg s^{-1}. Tidal disruption events (TDEs) occur when a companion star that is within the tidal disruption radius of a compact object becomes disrupted resulting in a large amount of X-ray emission that may peak around $L \sim 10^{42-45}$ erg s^{-1}, however, there is also the possibility of lower luminosity TDEs occurring at around ULX luminosities. These events are relatively rare, and their study is somewhat of a new field, many more are being discovered, for example, 13 TDEs within a redshift of $z < 0.6$ were selected among X-ray transient events in the first two *eRASS* scans (Sazonov et al., 2021).

Supernovae are another transient phenomena that may reach ULX luminosities (for examples see Komossa & Bade 1999; Komossa & Greiner 1999; Grupe et al. 1999; Greiner et al. 2000; Komossa et al. 2004), among the most extreme cases known is that of SN 2018cow peaking at around 10^{43} erg s^{-1} (Rivera Sandoval et al., 2018).

AGN are another potential ULX impostor, especially in the case where they are unusually dim (AGN lie around $L \sim 10^{40-44}$ erg s^{-1}), AGN are the reason ULXs are clearly defined as being 'off-nuclear'. However, it is also possible that the reverse may also be true, there is no reason why a ULX could not exist near the centre of a galaxy, a clear example is M33 X-8, so by excluding central sources from surveys it is possible one may miss a number of ULXs, although these would probably be identified as not being AGN via other means. Distant background AGN are also often confused with being ULXs.

We have previously alluded to IMBHs one of the prime candidates for a potential IMBH is the hyper-luminous X-ray source (HLX) ESO 243-49 HLX-1 located at a distance of $\sim$ 100 Mpc (Wiersema et al., 2010) with a luminosity of $L \sim 10^{41}$ erg s^{-1} (Farrell et al., 2009) it has been argued that this source may be powered by a black hole with a mass of $\sim 9 \times 10^3 - \sim 9 \times 10^4$ $M_\odot$ (Webb et al., 2012).

Some other sources that have been touted as IMBHs include M82 X-1 because of its X-ray properties similar to the thermal state in BHBs (see Feng & Kaaret 2010; Pasham et al. 2014), however, see Brightman et al. 2020a for explanations against this theory. Another source that has been suggested as hosting an IMBH is NGC 2276–3c (Mezcua et al., 2015, 2018) the source displays an extended radio jet on pc scales possibly consistent with an IMBH of mass $\sim 10^{3.5} - 10^6$ M$_\odot$.

Predictions involving mergers of two neutrons stars have invoked luminosities as high as $\sim 10^{44}$ erg s^{-1} but are expected to quickly fade by a factor of ~ 3 within around ~ 2 days (Li & Paczyński, 1998).

We may also infer ULXs due to some 'trickery', these forms of deception may come from overestimated distances or summed contributions of several sources.

Chapter 3

The impact of precession on the observed population of ULXs

Abstract

The discovery of neutron stars powering several ULXs raises important questions about the nature of the underlying population. In this chapter I build on previous work studying simulated populations by incorporating a model where the emission originates from a precessing, geometrically beamed wind-cone, created by a super-critical inflow. I obtain estimates – independent of the prescription for the precession period of the wind – for the relative number of ULXs that are potentially visible (persistent or transient) for a range of underlying factors such as the relative abundance of black holes or neutron stars within the population, maximum precessional angle, and LMXB duty cycle. I make initial comparisons to existing data using a catalogue compiled from *XMM-Newton*. Finally, based on estimates for the precession period, I determine how the *eROSITA* all-sky survey (*eRASS*) will be able to constrain the underlying demographic.

3.1 Introduction

Since 2014, approximately a dozen out of the ~ 500 known ULXs (see section 2) have been found to harbour NSs (see section 2.4), this has brought into question what the underlying demographic of the ULX population may resemble. It is now accepted that *most* ULXs contain stellar mass BHs or NSs accreting at super Eddington (or 'super-critical') rates.

In the case of super-critical accretion, the accretion rate in Eddington units, $\dot{m}_0 = \dot{m}/\dot{m}_{\rm Edd} > 1$, with the accretion flow first reaching the local Eddington limit around the spherization radius at $r_{\rm sph} \approx \dot{m}_0 r_{\rm in}$, where $r_{\rm in}$ is the inner radius of the disc, presumed to be the ISCO. In the case of a magnetised neutron star, as long as $r_{\rm sph}$ is larger than the magnetospheric radius, then the Eddington limit is expected to be reached locally in the disc of both NS and BH ULXs (conversely, for very strong dipole fields, the flow will change accordingly - see Mushtukov et al. 2017, 2018a,b). At $r_{\rm sph}$, the radiation pressure inflates the disc towards scale heights of order unity (Poutanen et al., 2007). In order to stay locally below

the Eddington limit, mass must be lost in the form of an outflow, which forms an optically thick wind-cone (see Poutanen et al. 2007) which can collimate the radiation from within. This 'geometrical beaming' of the radiation naturally leads to deviations from isotropy and a higher inferred luminosity (King et al., 2001).

Under the assumption that geometrical beaming acts to some extent across the entire ULX population (i.e. ignoring the presence of very strong magnetic fields - see King & Lasota 2019 but also Mushtukov et al. 2021), the proportion of neutron stars and black holes within the ULX population has been analytically estimated by Middleton & King (2017), while estimates leveraging binary population synthesis have also recently been explored (Wiktorowicz et al., 2017, 2019). Both studies predict that, whilst NS systems almost certainly dominate the entire *intrinsic* population of ULXs, *observationally* the populations of NS and BH ULXs may be comparable (particularly for host regions with low metallicity), although this may be in conflict with spectral similarities between the brightest ULXs (typically $>$ a few $\times$ 10^{39} erg s^{-1}) and those systems confirmed to harbour neutron stars (Pinto et al., 2017a; Walton et al., 2018).

The light curves of several ULXs show modulations on month timescales (see section 2.5). These modulations may be explained by the forced rotation of the accretion curtain in the case of a very high dipole field NS (see Mushtukov et al. 2017) or, alternatively, a precessing accretion disc. The precession of an accretion disc may be driven by a variety of external torques, including tidal effects, radiation pressure driven instabilities, Lense-Thirring precession, magnetic warping and free-free precession (Pringle, 1996; Maloney & Begelman, 1997; Maloney et al., 1998; Fragile et al., 2007; Lei et al., 2013). Lense-Thirring (solid-body) precession of the large scale-height disc and wind has recently been proposed as the driving mechanism for the modulations (Middleton et al. 2018, 2019b sec: 1.3.4) and is somewhat compelling as it requires a misaligned spin and binary axis, which is theorised to be the same requirement for the detection of pulsations (King & Lasota, 2020).

Under the assumption that ULXs are geometrically beamed sources with a precessing disc/wind (regardless of the mechanism), then it follows that the true population of ULXs is composed of (i) sources where one always views at low inclinations to the wind-cone such that they are persistently *above* the 1×10^{39} erg s^{-1} limit, (ii) sources where one always views at high inclinations to the wind-cone such that they are persistently *below* the 1×10^{39} erg s^{-1} limit (e.g. SS433, Fabrika 2004; Middleton et al. 2021), and (iii) sources which precess, such that the effective observer inclination transitions between (i) and (ii) (Middleton et al., 2015b). In this chapter, I investigate the effect of geometrical beaming combined with precession on the observed population of ULXs.

The recent launch of the *eROSITA* mission (Cappelluti et al., 2011; Predehl et al., 2021) and the start of its all sky survey (*eRASS*) will enable the long-term X-ray variability of sources across the entire sky to be probed. As I will demonstrate, the rate of discovery of ULXs in *eRASS* monitoring may help in answering broad questions relating to the abundance of BH and NSs in the ULX population.

3.2 Simulation Methods

3.2.1 Population Synthesis

The STARTRACK population synthesis code was originally designed for the study of mergers in double compact object systems, and while it has still been used for studying these phenomena by explaining the first gravitational wave detection of a NS-NS merger (Belczynski et al., 2018), its scope has widened significantly since its creation.

STARTRACK places special emphasis on the evolution of the three main classes of compact objects (BH, NS & WD) but also allows the evolution of normal stars from a point on the zero-age main sequence and trajectories to be followed on the Hertzsprung–Russell diagram (HRD) based on analytic formulas set out in Hurley et al. (2000) until compact remnant formation. A total of 18 different stellar types are denoted in STARTRACK and are listed in table 3.1

K_i	Stellar Type	Acronym
0	Main Sequence	(MS)
1	Main Sequence	(MS)
2	Hertzsprung gap	(HG)
3	Red giant branch	(RG)
4	Core helium burning	(CHeB)
5	Early asymptotic giant branch	(EAGB)
6	Thermally pulsating asymptotic giant branch	(TPAGB)
7	Helium main sequence	(HeMS)
8	Helium HG	(HeHG)
9	Helium giant branch	(HeGB)
10	Helium white dwarf	(He WD)
11	Carbon /oxygen white dwarf	(CO WD)
12	Oxygen /neon white dwarf	(ONe WD)
13	Neutron star	(NS)
14	Black hole	(BH)
15	Massless remnant (after SN Ia explosion)	(MR Sn1a)
16	Hydrogen white dwarf	(H WD)
17	Hybrid white dwarf	(Hyb WD)

Table 3.1: The stellar types defined in STARTRACK.

Once the compact object is formed, STARTRACK is also capable of modelling the changes in orbital separation, a, and eccentricity e and spin a_*, by considering the effects of tidal interactions, as well as on angular momentum losses associated with magnetic braking, gravitational radiation, and stellar wind mass losses. The output from the population synthesis code comes as an irregularly sampled time series output that tracks the evolution of various quantities that are summarised in table 3.2.

Following the work of Wiktorowicz et al. (2017, 2019), I obtained a sample of simulated binary systems using the population synthesis code StarTrack (Belczynski et al., 2008, 2020). The code simulates the evolution of binaries while

Parameter	Description
t	Time (Myr)
dt	Time delta (Myr)
M_a	Mass of primary ($M_\odot$)
M_b	Mass of companion ($M_\odot$)
K_a	Stellar type of primary (see Tab 3.1)
K_b	Stellar type of companion (see Tab 3.1)
a	Semi-major axis ($R_\odot$)
e	Eccentricity ($R_\odot$)
R_a	Radius of primary ($R_\odot$)
R_b	Radius of companion ($R_\odot$)
L_a	Luminosity of primary ($L_\odot$)
L_b	Luminosity of companion ($L_\odot$)
$\dot{a}_a$	Spin of primary
$\dot{a}_b$	Spin of secondary
mt	Is mass transfer active (boolean)
$mttype$	Timescale of mass transfer (nuclear or thermal)
$Lxmt$	Luminosity of accretion disc during RLOF (erg s^{-1})
Lx	Luminosity coming from wind accretion (erg s^{-1})
$\dot{M}_a$	Mass loss from primary during RLOF ($M_\odot$ Myr^{-1})
$\dot{M}_b$	Mass loss from companion during RLOF ($M_\odot$ Myr^{-1})
$dMwind_a$	Mass loss from primary during via wind ($M_\odot$ Myr^{-1})
$dMwind_b$	Mass loss from companion via wind ($M_\odot$ Myr^{-1})
Z	Metallicity of progenitor gas ($Z_\odot$)
id	System identifier
$evroute$	Record of the evolutionary route

Table 3.2: Quantities available directly from STARTRACK, units are given in brackets.

accounting for all processes that can be important for the formation and evolution of ULXs such as the common envelope phase, Roche Lobe overflow (RLOF) and tidal interactions. In addition, population synthesis invokes multiple formation channels in a variety of stellar environments (metallicity, star formation history, age, etc.), and thereby provides synthetic data for comparison to observations. The code outputs comprehensive information about system parameters, which I use to calculate additional quantities required for my analysis which are shown in table 3.3.

3.2.2 Luminosity and Beaming Factor

I proceeded to select only those binary systems undergoing mass transfer from the simulated sample; this provided 104,883 unique binary systems. For each of these systems, their Eddington luminosity at each time interval was calculated using $L_{\rm Edd} = 1.3 \times 10^{38} m$ erg s^{-1} (i.e. assuming a Hydrogen composition), where m is the compact object mass in solar units. The Eddington mass transfer rate was calculated from $\dot{m}_{\rm Edd} = L_{\rm Edd}/\eta c^2$ where I use $\eta \approx 0.08$ for both NS and

Parameter	Equation	Description
$L_{\rm Edd}$	$1.3 \times 10^{39} M_a$	Eddington luminosity
$\dot{m}_{\rm Edd}$	$L_{\rm Edd}/(\eta c^2)$	Eddington accretion rate
$\dot{m}_a$	$\dot{M}_a/\dot{m}_{\rm Edd}$	Acc. rate of primary in Edd. units
$\dot{m}_b$	$\dot{M}_b/\dot{m}_{\rm Edd}$	Acc. rate of secondary in Edd. units
$L_{\rm iso}$	Eq 3.1	Isotropic luminosity
$L_{\rm x}$	Eq 3.3	Beamed luminoisty
b	Eq 3.2	Beaming factor
θ	$2\cos^{-1}(1-{\rm b})$	Wind cone opening angle
ζ	$\tan[\pi/2 - \cos^{-1}(1-{\rm b})]$	Wind opening parameter
R_g	$GM_aM_\odot/c^2$	Gravitational radius
a_*	0.01 for NS 0.998 for BH	CO spin
r_s	$(2GM_aM_\odot/c^2)/R_g$	Swartzchild radius
$r_{\rm isco}$	6 R_g for NS 1.25 R_g for BH	ISCO radius
$r_{\rm sph}$	$r_{\rm isco}\dot{m}_0$	Spherization radius
$r_{\rm out}$	$6 \times 3\epsilon/(\beta\zeta\dot{m}_0)^{3/2}$	Outer photospheric radius
$P_{\rm wind}$	Eq 1.21	Wind precession period
$P_{\rm orb}$	$2\pi\sqrt{(aR_\odot)^3/GM_\odot(M_b+M_a)}$	Orbital period
$P_{\rm sup}$	$22.1P_{\rm orb}$	Super-orbital period
$P_{\rm sup,err}$	$(0.1/22.1)P_{\rm sup}$	Super-orbital period 1σ error
$T_{\rm eff,b}$	$(L_bL_\odot/(4\pi(R_bR_\odot)^2\sigma)^{1/4}$	Effective temp of the secondary

Table 3.3: Secondary calculated quantities from STARTRACK outputs.

BH systems. Following Shakura & Sunyaev (1973) and Poutanen et al. (2007), I obtain the intrinsic isotropic luminosity of the source without beaming $L_{\rm iso}$ (and ignoring energy lost in driving a wind, or advected in the case of BHs):

$$L_{\rm iso} \approx \begin{cases} L_{\rm Edd}[1+\ln(\dot{m}_0)] & \text{if } \dot{m}_0 \geq 1 \\ L_{\rm Edd}\dot{m}_0 & \text{otherwise} \end{cases} \tag{3.1}$$

Following Wiktorowicz et al. (2017), I defined the beaming factor, b:

$$b = \begin{cases} 1 & \text{if } \dot{m}_0 < 8.5 \\ 73/\dot{m}_0^2 & \text{if } 8.5 \leq \dot{m}_0 < 150 \\ 3.2 \times 10^{-3} & \text{if } \dot{m}_0 \geq 150 \end{cases} \tag{3.2}$$

which is related to the solid angle of the wind-cone subtending a half-apex angle $\theta/2$ by $b = 1 - \cos(\theta/2)$. A beaming factor of $b = 1$ corresponds to no beaming and a half opening angle $\theta/2$ of 90°, while the smallest, limiting value of 3.2×10^{-3} corresponds to a half opening angle of $\sim$ 4.6° (see Lasota et al. 2016). Under the assumption of an isotropic volume distribution of sources, the beaming factor b is equal to the probability of observation, i.e. the probability that the beam enters the line-of-sight, which I account for in my calculations. The $b \propto 1/\dot{m}_0^2$ relation was derived by King (2009) as an extension to the treatment of black-body emission from the accretion disc around a black hole (King & Puchnarewicz, 2002), and supports the observation that several bright ULXs appear to show an anti-correlation between their peak luminosity and characteristic soft X-ray temperature (Feng & Kaaret, 2007; Kajava & Poutanen, 2009).

With values calculated for $L_{\rm iso}$ and b, I then obtained the *maximum* beamed luminosity $L_{\rm x}$ that would be observed for a given simulated system (noting the aforementioned caveats) by dividing the intrinsic luminosity by its beaming factor:

$$L_{\rm x} \approx \frac{L_{\rm iso}}{b} \tag{3.3}$$

In the above prescription, I have assumed the beamed luminosity corresponds to the observed luminosity; this is an over-simplification (see section 3.4), as the true effect of beaming on the spectrum (and therefore total X-ray luminosity) requires consideration of the radial dependence of beaming (which can be substantially different for regions around the spherization radius compared to the inner-most regions and advection. I also note that the above formula assumes that the flow is 'classically' super-critical and therefore that the magnetic field of a neutron star in a given ULX is typically weak enough such that the magneto-spheric radius is far smaller than the spherization radius (see Mushtukov et al. 2017 for a discussion of the nature of the flow when this condition is not met) and explicitly ignores emission from the accretion column.

3.2.3 Duty Cycle

Early observations of XRBs showed that some systems displayed outbursts (flares) whereby their X-ray luminosities would increase by factors of $\sim 2-20$. These outbursts were often recurrent on intervals of days to hundreds of days. Aql X-1 was among the first sources to display these X-ray outbursts using data obtained from the Vela 5B satellite between 1969-1976 (Priedhorsky & Terrell, 1984). Astronomers were quick to notice the similarity of such outbursts to those displayed in the optical by U Geminorum an accreting binary system observed to be transient as early as 1855 (Turner, 1906), this source is similar in nature to XRBs but with a white dwarf as the CO, these binary stars are commonly known as cataclysmic variables or dwarf novae and are thought to display many of the same phenomena as seen in LMXBs.

The disc instability model (DIM; Lasota 2001), modified for irradiation, explains the outbursts of low-mass X-ray binaries (LMXBs) as being mediated by the well-known thermal-viscous instability of an α disc (Shakura & Sunyaev 1973, see also Hameury & Lasota 2020 for a recent extension to higher accretion rates). The duty cycle of the resulting outbursts, d, is defined as the fraction of total time spent in outburst. Observationally, the value for d is not particularly well constrained; extreme cases include that of GRS 1915+105 with an outburst duration exceeding 20 years and a predicted recurrence time of $\sim 10^4$ years, giving it an X-ray duty cycle of $\sim 0.1\%$ ($d \sim 0.001$) (Deegan et al., 2009). The Galactic LMXB, GX 339-4 on the other hand has outbursts with a recurrence time of ~ 450 days; based on eight outbursts provided in Rubin et al. (1998), I estimate the duty cycle to be roughly $\sim 30\%$ ($d \sim 0.3$), whilst *Chandra* observations of two ULXs in NGC 5128 place an upper limit on their duty cycles of $d \sim 0.2$ (Burke et al., 2013), a table of duty cycle estimates in LMXBs may also be found in table 8 of Tetarenko et al. 2016.

In order to accommodate the observational impact of duty cycles within my

parent population, I defined a sub-sample of systems undergoing nuclear timescale mass transfer that are not wind fed, and had donor stars with an effective temperature of $T_{\rm eff} < 7000K$ (to be below the instability threshold, see Lasota 2001) and donor star masses below $5M_{\odot}$. For simplicity, I make the assumption that the outer regions of the disc have the same temperature as the companion star calculated via $T_{\rm eff} = (L_2/4\pi R_2^2\sigma)^{1/4}$, where σ is the Stefan-Boltzmann constant, and L_2, and R_2 are the luminosity and radius of the companion star respectively. For these systems likely to undergo outbursts mediated by the DIM, I selected a single value for d such that a system with, e.g. $d = 0.2$, could potentially reach ULX luminosities for 20% of its total lifetime. At gas temperatures exceeding 7000 K, I assume that the disc is constantly transporting angular momentum and does not display recurrent outbursts i.e $d = 1.0$. With relevance to these latter sources, I note that I have not included the propeller effect (see section 2.4.1) which may act to lower the duty cycle for wind-fed or persistently accreting neutron star systems. I have also not accounted for the duty cycles of Be-X-ray binaries, which undergo recurrent outbursts as a result of the neutron star's highly elliptical orbit and passage through the decretion disc (e.g. Reig 2011).

3.2.4 Obtaining a representative population of ULXs

The impact of precession on the observed population of ULXs depends on the underlying population demographic, and thus I adopt the following method for creating representative sample populations. Figure 3.1 illustrates my method for generating samples of ULXs from the initial populations created via StarTrack. The simulated results are grouped into three metallicities: $Z = 1\%Z_{\odot}$, $10\%Z_{\odot}$, $Z_{\odot}$ (where solar metallicity, $Z_{\odot} = 0.02$) and I perform simulations for each group separately as well as the combination of all three. As previously stated in section 3.2.2, I filtered to only include systems undergoing active mass transfer. Next, I filtered out the 16,135 binary systems that were undergoing mass transfer from a white dwarf or did not exceed $L_x = 1 \times 10^{39}$ erg s^{-1} at any point during their lifetime. I note that Steele et al. (2014) argue that a globular cluster ULX in NGC4472 (Maccarone et al., 2007) displays findings consistent with a white dwarf donor star (the primary being a black hole) and so it may be possible for such sources to exist, however as their evolution is dominated by dynamic processes in the cluster, the inclusion of such ULXs requires specific prescriptions beyond the scope of this work. The filtering left me with 88,748 BH/NS systems that were undergoing either nuclear or thermal timescale mass transfer and which serves as my parent ULX population. From here I split my sample into two groups depending on whether the compact object is a NS or BH. This allowed me to later specify a desired black hole percentage $\%_{\rm BH}$ within the population.

There are important differences in how long a given system may appear as a ULX, as the duration of thermal timescale mass transfer is orders of magnitude shorter than Roche lobe overflow on the nuclear timescale of the secondary (see sec 1.2.2) (with repeat outbursts mediated by the DIM). Therefore, should one sample *uniformly* over all the systems in my parent population, one would tend to over-represent short-lived ULXs. To correct for this, I apply a sampling prescription whereby the probability of selecting a given ULX is set by its lifetime as a ULX,

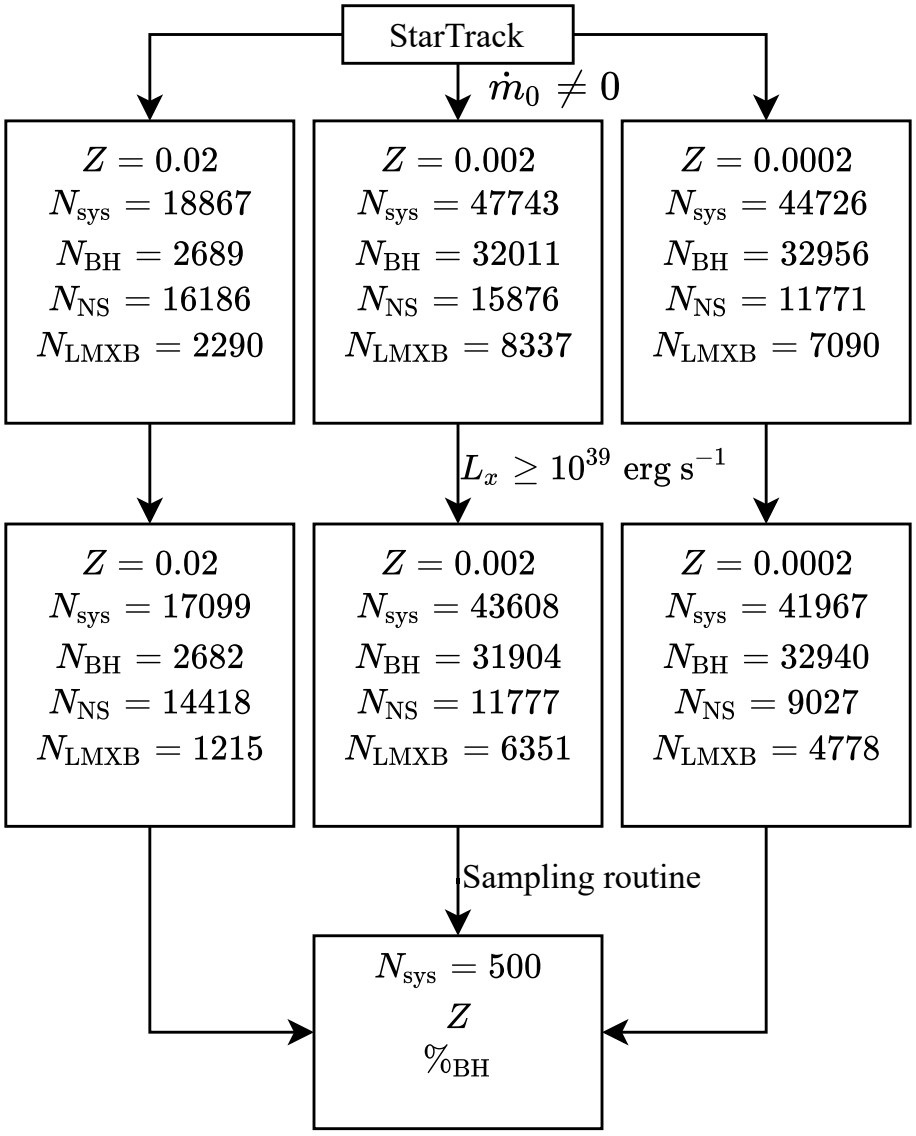

Figure 3.1: Flowchart showing the filtering process to obtain a representative sample population of ULXs. See section 3.2.4 for more detail.

divided by the summed lifetime of all the other systems in the parent population $P_{\rm sample} = t_{\rm ULX,n} / \sum_{n=0}^{N_{\rm ulx}} t_{\rm ULX,n}$. This sampling procedure explicitly assumes that there exists a constant star formation rate across cosmic time.

In the following simulations, I have chosen to re-sample the total population to produce smaller, volume-limited populations of $N_{\rm sys} = 500$ systems (for each metallicity); this is a little larger than the currently *observed* number of ULXs by *XMM-Newton* (Earnshaw et al., 2019) although through repeat re-sampling (via Monte-Carlo procedure), the results can be scaled to any desired population size.

3.2.5 Simulating ULX light curves

In order to investigate the impact of precession on the observed population of ULXs, I require a method for creating long term light curves for my synthesised

population. `ULXLC` is a numerical model developed by Dauser et al. (2017), to describe the luminosity emerging from within an optically thick ($\tau > 1$) conical outflow. A schematic of the `ULXLC` model is shown in figure 2.1, while some example light curves are shown in figure 3.3.

The conical outflow has a height of $h_{\rm cone} = 1000\ R_g$; inside the cone, located at a height $h_{\rm emit} = 10\ R_g$ exists a razor-thin disc from which the monochromatic photons are emitted isotropically in both directions. The path taken by the photons are traced with each electron scattering of the cone calculated via the Klein-Nishina formula which provides the differential cross-section and both the likelihood and angular distribution of photons scattered from a single free electron. The resultant flux boosts are pre-calculated via Monte-Carlo method. The maximum height in the cone and thus outflowing wind (at a height of $1000R_g$), was shown to be a parameter that was largely degenerate with the changes in the flux normalization and did not have a large effect on the overall emissivity profile.

The ULXLC model has 6 parameters which are summarised in table 3.2.5: the period P allows for stretching or squeezing of the lightcurve in the time axis, with a phase offset ϕ that may take values between 0 and 1. The observer inclination angle i is bound between $0 - 90°$ (and is defined such that $i = 0°$ is orientated looking down the cone). The precessional angle Δi may take values between 0 (no precession) and 45°, it corresponds to the angle of the axis about which the cone is made to precess. The last variable $\beta_{\rm wind}$ corresponds to the velocity of the outflow, which may be deduced from red (or blue) shifted atomic lines seen in the X-ray spectra (see section 2.3.1). I hereafter fix $\beta_{\rm wind} = 0.3c$ which is broadly consistent with the winds detected in ULXs and SS433: Middleton et al. 2014; Walton et al. 2016a; Pinto et al. 2016, 2017a; Kosec et al. 2018a,b; Middleton et al. 2021).

Parameter	Symbol
P	Light curve period
ϕ	Light curve phase
$\theta/2$	Half opening angle (°)
i	System inclination (°)
Δi	Precessional angle (°)
$\beta_{\rm wind}$	Velocity of the outflow (c)

Table 3.4: Main parameters for the ULXLC model.

Some finer details of the model implementation are that the emissivity profiles are pre-calculated and saved in a table for fast evaluation of the model. Values were calculated on a grid where $\beta_{\rm wind}$ was evaluated at 0.0, 0.2, 0.4, 0.6, 0.9 (in units of c) the inclination i is evaluated between 0 to 90° with 200 data points, and the values for the opening angle $\theta/2$ are gridded between 2 and 45° with 33 data points. Values for the emissivity that are evaluated between grid points are estimated via linear interpolation.

In the interest of computational efficiency, I made modifications to the `ULXLC` model written in `C` so that the model could run outside `XSPEC`. I also modified the model so that it could be run multiple times without having to re-load the precalculated grid for each run. Modifications were also made so that I could access the working memory of the model in `python` using the `ctypes` module,

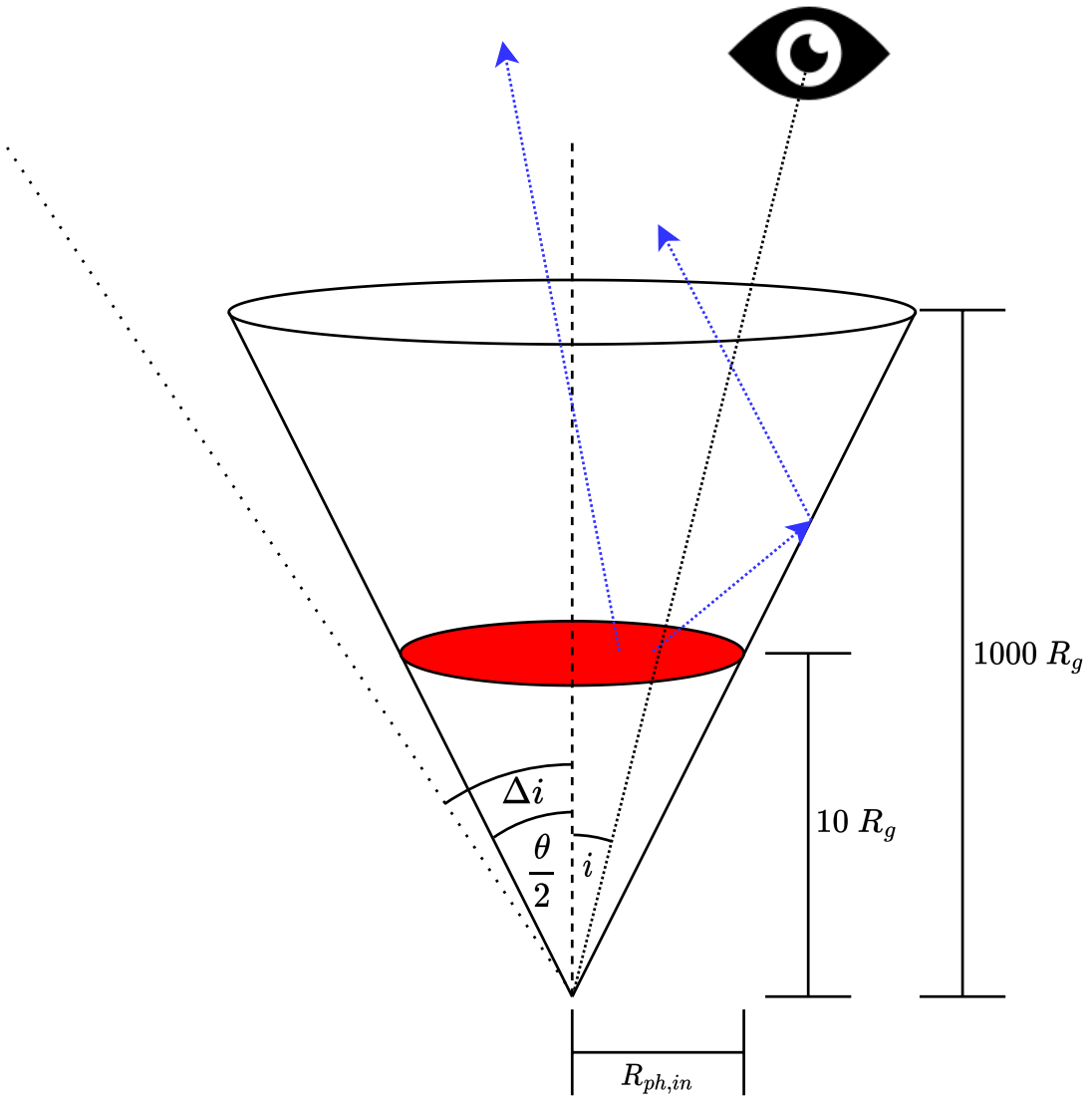

Figure 3.2: Geometry of the ULXLC model (not to scale). Some example photon paths are shown in blue. This diagram has a precessional angle that is greater than the opening angle ($\Delta i > \theta/2$)

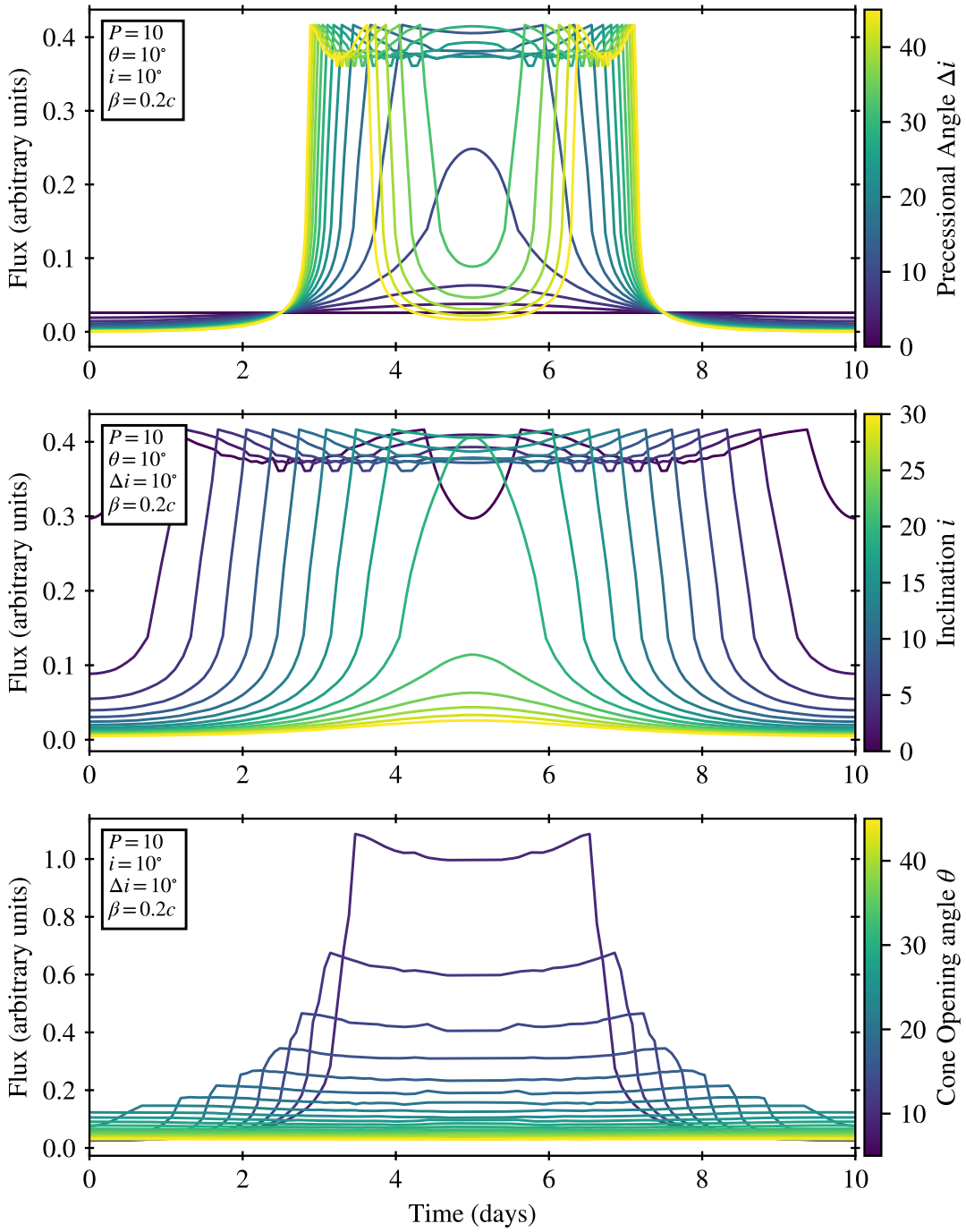

Figure 3.3: A variety of lightcurves from ULXLC showing the effect of changing 3 parameters. Top: changing the precessional angle Δi. Middle: Changing the inclination i. Bottom: Changing the opening angle θ. The system parameters are shown in the upper left of each plot

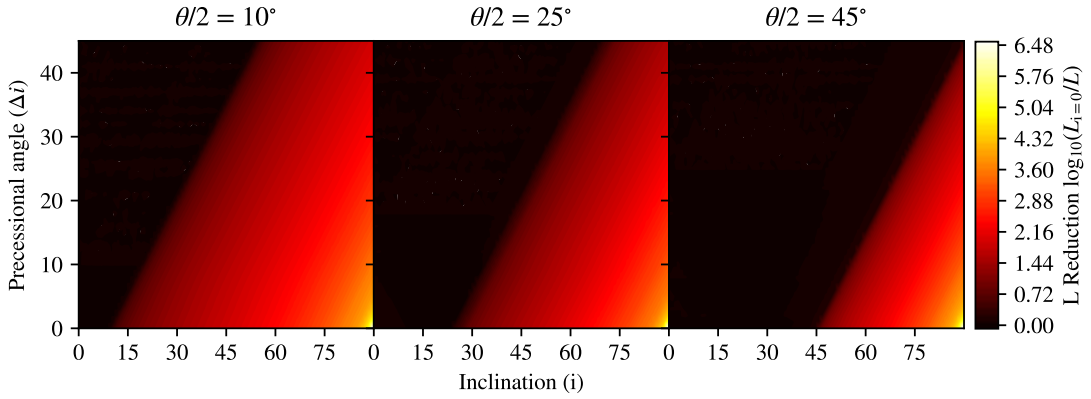

Figure 3.4: Logarithm of the luminosity reduction compared to zero inclination $i = 0°$ for a variety of ULXLC system parameters. The black region on the left corresponds to regions inside the cone and no reduction is observed, while as one moves out of the cone, the observed luminosity drops rapidly, sources that precess in the region of the boundary of black to red are those that are likely to be defined as transient ULXs.

which allowed for efficient communication between the population sampling code (sec 3.2.4) and `ULXLC`.

`ULXLC` does not assume any physical mechanism for *driving* the precession and so can be used without any additional *a-priori* assumptions. In order to use `ULXLC`, I require input model parameters; θ can be derived from the assumed relationship between accretion rate, beaming and opening angle (section 3.2.2), whilst $\cos i$ is uniformly distributed between zero and one, which ensures the random distribution of ULX orientations in space. Δi is an unknown, although if I assume SS433 to be a reasonable indicator, values of 20° are not implausible (Fabian & Rees, 1979; Milgrom, 1979; Margon et al., 1979). Using `ULXLC`, I simulated light curves for each ULX system, which took the form of a single precession cycle and a time series of 5000 data points.

The light curves from `ULXLC` required normalising to produce physical luminosity units. For any given combination of system parameters (i.e. my simulated population of ULXs), I simulated a light curve at zero inclination and set the maximum luminosity to be equal to the beamed luminosity given in equation 3.3. This allowed me to calculate a scaling constant which I used to renormalise any light curve at arbitrary inclination and obtain a luminosity in physical units, the reduction in luminosity for a variety of model parameters is shown in figure 3.4.

The light curves produced by `ULXLC` are periodic, even though in reality precession may be quasi-periodic if dependent on accretion rate (e.g. Middleton et al. 2019b). Although the period is not utilised until I consider the regular observations taken by *eROSITA* (section 3.3.3), at the point of creating the light curves, I also scale the period using formulae for Lense-Thirring precession (Middleton et al., 2019b) and an empirical-only relationship (Townsend & Charles, 2020) (see equations 3.4 & 3.7).

Lense-Thirring Precession

Lense-Thirring precession is a relativistic correction to the precession of a gyroscope near a large rotating mass (see sec:1.3.4). In ULXs it is speculated that the same effect may lead to precession of the large scale-height disc and wind cone (Middleton et al. 2018, 2019b).

Following Middleton et al. (2019b), I calculated the precession period of the wind-cone via equation 3.4:

$$P_{\rm wind} = \frac{GM\pi}{3c^3 a_*} r_{\rm out}^3 \left[\frac{1 - \left(\frac{r_{\rm in}}{r_{\rm out}}\right)^3}{\ln\left(\frac{r_{\rm out}}{r_{\rm in}}\right)} \right] \tag{3.4}$$

I make the simplifying assumption that $r_{\rm in} = r_{\rm isco}$ in units of the gravitational radius (GM/c^2), i.e. ignoring the role of magnetic fields (although see Vasilopoulos et al. 2019 and Middleton et al. 2019b for a discussion). I assume that neutron stars are low spin ($a_* = 0.01,\ r_{\rm isco} = 6\ R_g$) as indicated by observations of pulsar ULXs (PULXs) to-date, with spin periods of 1-10s of seconds (King & Lasota, 2020), and that black holes may have very high spins ($a_* = 0.998,\ r_{\rm isco} = 1.25\ R_g$) as a consequence of the high accretion rates, the ability to advect matter and angular momentum, and the lack of a propeller mechanism to limit the spin-up. In the above, $r_{\rm out}$ is the outer photospheric radius of the wind (the point at which radiation can free-stream) for which I assume (Poutanen et al., 2007):

$$r_{\rm out} \approx \frac{3\epsilon_{\rm wind}}{\beta\zeta} \dot{m_0}^{3/2} r_{\rm isco} \tag{3.5}$$

where – for the purposes of determining this radius – I have assumed $r_{\rm isco} = 6R_g$ for both NS and BHs (and an accretion efficiency of 0.08). Note that the discrepancy between assuming a high BH spin for the precession period and a larger ISCO radius here does not have a substantial effect on the location of the photosphere for large accretion rates (see Middleton et al. 2019b for details). In the above, β is the ratio of asymptotic wind velocity relative to the Keplerian velocity at $r_{\rm sph}$, and, for simplicity, I set this to 1.4. $\epsilon_{\rm wind} = L_{\rm wind}/L_{\rm tot}$ is the fraction of dissipated energy used to launch the wind, which I set to $\epsilon_{\rm wind} = 0.25$ (Jiang et al. 2014, see also Pinto et al. 2016 for a higher inferred value from observation). Finally, ζ is the cotangent of the opening angle of the wind cone which I assume is equal to:

$$\zeta = \tan\left[\frac{\pi}{2} - \mathrm{acos}\,(1-b)\right] \tag{3.6}$$

I assume a lower-limit of $\zeta = 2$ based on radiative magnetohydrodynamic simulations at moderate super-Eddington rates (Sądowski et al. 2014, and noting that in reality, ζ – and therefore b – likely increases in a more complicated fashion with $\dot{m}_0$: Jiang et al. 2019).

Empirical Precession

In addition to the above physical precession mechanism, I also utilise the result of Townsend & Charles (2020), where the mechanism for precession is unknown but the super-orbital ($\rm P_{sup}$) and orbital periods ($\rm P_{orb}$) are inferred to be related by:

$$P_{\rm sup} = 22.9 \pm 0.1 P_{\rm orb} \tag{3.7}$$

where $P_{\rm orb}$ is given by:

$$P_{\rm orb} = 2\pi \sqrt{\frac{a^3}{G(M_{\rm c} + M)}} \tag{3.8}$$

where $M_{\rm c}$ is the mass of the companion star and a is the semi-major axis of the binary system.

3.2.6 Effects of precession on the observed population of ULXs

In order to explore the impact of various key parameters on observations of ULXs, I re-sample the parent population 10,000 times, each time producing a smaller sample of 500 ULXs. For each ULX in my smaller sample, I provided the following parameters to ULXLC: $\theta/2$, i, Δi, $L_{\rm x}$, P, ϕ, $\beta_{\rm wind} = 0.3$. Δi and ϕ are sampled from uniform distributions with the following ranges: $0^\circ \leq \Delta i \leq \Delta i_{\rm max}$, $0 \leq \phi \leq 1$. $\cos i$ is uniformly distributed between zero and one. $\theta/2$, L_x and P are calculated quantities of the particular system. I explore the impact of $\Delta i_{\rm max} = 45^\circ$ and 20°, as we do not have strong constraints on the precessional angle (other than for SS433). I then proceeded to classify each light curve in my sample, created using ULXLC, into one of three categories:

- *Alive*: Persistently above 1×10^{39} erg s^{-1}
- *Transient*: Systems that crossed 1×10^{39} erg s^{-1}
- *Hidden*: Persistently below 1×10^{39} erg s^{-1}

I note that this act of classifying sources is independent of the precession period, with systems merely being defined based on the above definitions. The numbers of systems in each classification were recorded and saved such that the total number of systems ($N_{\rm sys} = 500$) = the number alive ($N_{\rm A}$) + the number of transients ($N_{\rm T}$) + the number of hidden systems ($N_{\rm Hid}$). Light curves that were classified as *transient* were subjected to further analysis (see section 3.2.8), whilst ULX systems with half opening angles of $\theta/2 > 45^\circ$ (set by the accretion rate – see equation 3.2) were considered to be sources that do not display precession (see Dauser et al. 2017) and thus were classified as being alive without the need to simulate light curves.

3.2.7 Simulations of the X-ray Luminosity Function

X-ray luminosity functions (XLFs) – both in their differential and cumulative forms – have been commonly extracted from survey data in order to study population demographics (see sec 2.2.1 and Fabbiano 1989; Grimm et al. 2003; Wang et al. 2016). XLFs can provide insights into the star-formation history (Fragos et al., 2013a,b) and impose constraints on theoretical models of binary evolution. It is

important to consider how the combination of precession and geometrical beaming can together affect the overall shape of observed XLFs. To this end I explored how a synthetic XLF would appear under six different scenarios that could describe a given source's luminosity:

- $L_{\rm iso}$: the isotropic luminosity obtained in the absence of beaming (eq. 3.1)
- $L_{\rm x}$: the above including geometrical beaming (eq. 3.3)
- $L_{\rm x,b}$: the above including the probability of observation set by the beaming factor (i.e. assuming obscuration by the wind)
- $L_{\rm x,b*d}$: the above including the additional effect of the LMXB duty cycle on the observation probability
- $L_{\rm x,prec}$: the luminosity obtained via the generation and uniform sampling of light curves produced by `ULXLC` (sec. 3.2.5)
- $L_{\rm prec,vis}$: the above including the additional effect of the LMXB duty cycle.

As described in section 3.2.2, I re-sampled $N_{\rm sys} = 500$ binaries from across all metallicites from my **full** parent population weighted by their lifetimes in the active mass transfer phase (top row in Figure 3.1), while specifying a black hole percentage of $\%_{\rm BH} = 0,\ 50\%$ & 100% within the population of $N_{\rm sys} = 500$ binaries. For the construction of these XLFs, I separate the BHs, NSs, and LMXBs, as well as those defined as alive or transient; this is useful for illustrating the relative contributions of each component to the XLF.

LMXB sources were set to have a duty cycle of $d = 0.2$ so that there was a 20% chance of them being observed at their luminosity given by $L_{\rm x}$, and an 80% chance of them not being observed at all (i.e. $L_{\rm x} = 0$). Thermal timescale or wind-fed systems in the population were set to have a duty cycle of $d = 1.0$. For each system (with $\theta/2 < 45°$) a light curve was then generated using ULXLC assuming a precessional angle uniformly sampled between 0 and $\Delta i_{\rm max} = 45°$; I then randomly sampled the system's light curve to obtain its new luminosity. Re-sampling the parent population (as described in section 3.2.4), then allows me to obtain 1σ errors on each luminosity bin for any given XLF.

3.2.8 Simulating *eRASS*'s view of the ULX population

The *eROSITA* X-ray telescope was launched in July 2019 and has already begun its all-sky survey, *eRASS*, which takes snapshots of the entire sky in the $0.2 - 10$ keV band, repeating every six months for a period of four years (Merloni et al., 2012). Using the generated light curves for my artificial population of ULXs, I can obtain predictions for what *eROSITA* might observe given an underlying population demographic, and explore how my constraints might improve over the course of the *eRASS* four-year survey.

Whilst the previous sections had no requirement to use the periods given by equations 3.4 & 3.7, given *eRASS's* regular observations it is important to factor in the deterministic nature of such a periodic (or, in reality quasi-periodic – Middleton et al. 2019b) modulation of the luminosity.

I note that my simulations make the assumption that all the systems in my parent population have an equal probability of observation regardless of their spatial distribution, luminosity or spectra. In reality, there will be a natural bias towards detecting the brighter sources, which is further compounded by the anisotropic sensitivity of *eRASS* (with greater effective exposure occurring near the ecliptic poles and deeper coverage between 0.2 - 2.3 keV, Predehl et al. 2021). To obtain a more realistic picture requires the distribution of simulated binaries amongst galaxies out to a few 10s of Mpc, some estimate for the true number per galaxy type (and per unit star formation), their spectra and the convolution of the exposure time and detector response. Whilst this is beyond the scope of this work, I discuss the impact of resulting bias in section 3.4.

eRASS Sampling Routine

The light curves that were created in section 3.2.6, were scaled to have a period of both $P_{\rm wind}$ and $P_{\rm sup}$ and their luminosity was then sampled in intervals of six months to match the observing cadence of *eRASS*. At each *eRASS* cycle (c), I keep track of the following:

- Sources above 1×10^{39} erg s^{-1}, $N_{\rm ulx}(c)$
- Sources below 1×10^{39} erg s^{-1}, $\neg N_{\rm ulx}(c)$
- Newly detected ULXs, $N_{\rm new}(c)$
- Previously detected ULXs that fell below the ULX threshold, $N_{\rm dip}(c)$
- The change in the number of ULXs $\Delta N_{\rm ulx}(c) = N_{\rm new}(c) - N_{\rm dip}(c)$
- The number of transient sources, $N_{\rm T}(c) = N_{\rm new}(c) + N_{\rm dip}(c)$ (for $c > 1$)
- The number of alive sources, $N_{\rm A}(c)$

The above quantities are naturally *eRASS* cycle-specific and the cumulative equivalents for these quantities may be obtained by summing over all *eRASS* cycles, e.g. I define the cumulative number of observed sources by $N_{\rm obs}(c) = \sum_{c=1}^{8} N_{\rm new}(c)$. I also note that the quantity $N_{\rm A}(c)$ includes the $N_{\rm A}$ systems classified as *alive*, with opening angles $\theta/2 > 45°$, and for which light curves were not simulated (see section section 3.2.6).

Over the first 6 months of *eRASS* (cycle 1), I make the assumption that the survey will not detect any transient sources due to precession, as the exposure time is very short relative to the typical precession timescale. At the conclusion of cycle 1 I therefore have a starting value for the total number of observed ULXs which will subsequently increase as the survey continues.

I performed 10,000 sets of Monte Carlo simulations for a given combination of input parameters which covered Z (0.02, 0.002, 0.0002 and the combination of all three), $\%_{\rm BH}$ ($0 \rightarrow 100$ % in steps of 25%), $\Delta i_{\rm max}$ (20° and 45°), P ($P_{\rm wind}$ and $P_{\rm sup}$) and d (0.2 and 1.0). At each *eRASS* cycle, I recorded quantities which may be compared to actual *eRASS* measurements, such as the number of sources detected in a given *eRASS* cycle $N_{\rm ulx}(c)$. The repeat simulations allowed the construction

of distributions from which I extracted the key statistics related to the various quantities in each cycle as a function of my physical parameters (notably $\%_{\rm BH}$).

An example set of results from a single Monte-Carlo iteration is shown in Table 3.5.

c	$N_{\rm new}(c)$	$N_{\rm dip}(c)$	$\Delta N_{\rm ulx}(c)$	$N_{\rm T}(c)$	$\sum_{c=1}^{8} N_{\rm A}(c)$	$N_{\rm obs}(c)$
1	303	0	+303	0	303	303
2	24	12	+12	36	291	327
3	8	4	+4	12	287	335
4	3	0	+3	3	287	338
5	2	2	0	4	285	340
6	1	0	+1	1	285	341
7	1	2	-1	3	283	342
8	2	0	+2	2	283	344

Table 3.5: An example of a single *eRASS* Monte-Carlo iteration showing a subset of observed quantities, created from an underlying population of $N_{\rm sys} = 500$ ULXs with $\%_{\rm BH} = 50$, $\Delta i_{max} = 20°$, $Z = 0.02$ and $d = 1.0$. The numbers illustrate the evolution of the observed population as seen by *eRASS* over its 8 cycles.

3.3 Results

3.3.1 The Impact of Precession on the XLF

Following the method detailed in section 3.2.7, Figure 3.5 shows several of my synthetic cumulative XLFs, created using the method described in section 3.2.4. I now use the total lifetime of the source during active mass transfer as opposed to the lifetime of the source during only the ULX phase, so that the sampling probability is given by $P_{\rm sample} = t_{\rm mt,n} / \sum_{n=0}^{N} t_{\rm mt,n}$, where $t_{\rm mt,n}$ is the amount of time spent undergoing active mass transfer for the nth source, and N is the number of sources in the population.

Panel **A** shows an XLF assuming $\%_{\rm BH} = 50\%$ and isotropic emission in the absence of any geometrical beaming, with no neutron stars exceeding the 1×10^{39} erg s^{-1} luminosity threshold (as the beaming only begins at a NS luminosity around 6×10^{38} erg s^{-1}), and a few BHs reaching up to $\sim 10^{40}$ erg s^{-1}.

Panel **B** (also for $\%_{\rm BH} = 50\%$) shows the same XLF as in Panel **A** after incorporating beaming but does not account for the observation probability (i.e. it assumes every detected source is observed directly down the wind cone). Between 10^{38} and $\sim 10^{41}$ erg s^{-1}, NSs appears to dominate, while at the highest luminosities, $> 10^{41}$ erg s^{-1}, BH accretors dominate.

Panel **C** includes the observation probability provided by the beaming factor b, and the LMXB duty cycle d; the brightest sources above $\sim 10^{40}$ erg s^{-1} are suppressed and are no longer visible.

Panel **D** (also for $\%_{\rm BH} = 50\%$) includes the combined effects of geometrical beaming, precession (via ULXLC) and a LMXB duty cycle of $d = 0.2$; both NS and BH systems are observed in similar numbers across the full range of luminosities, with none detected above $\sim 10^{41}$ erg s^{-1}.

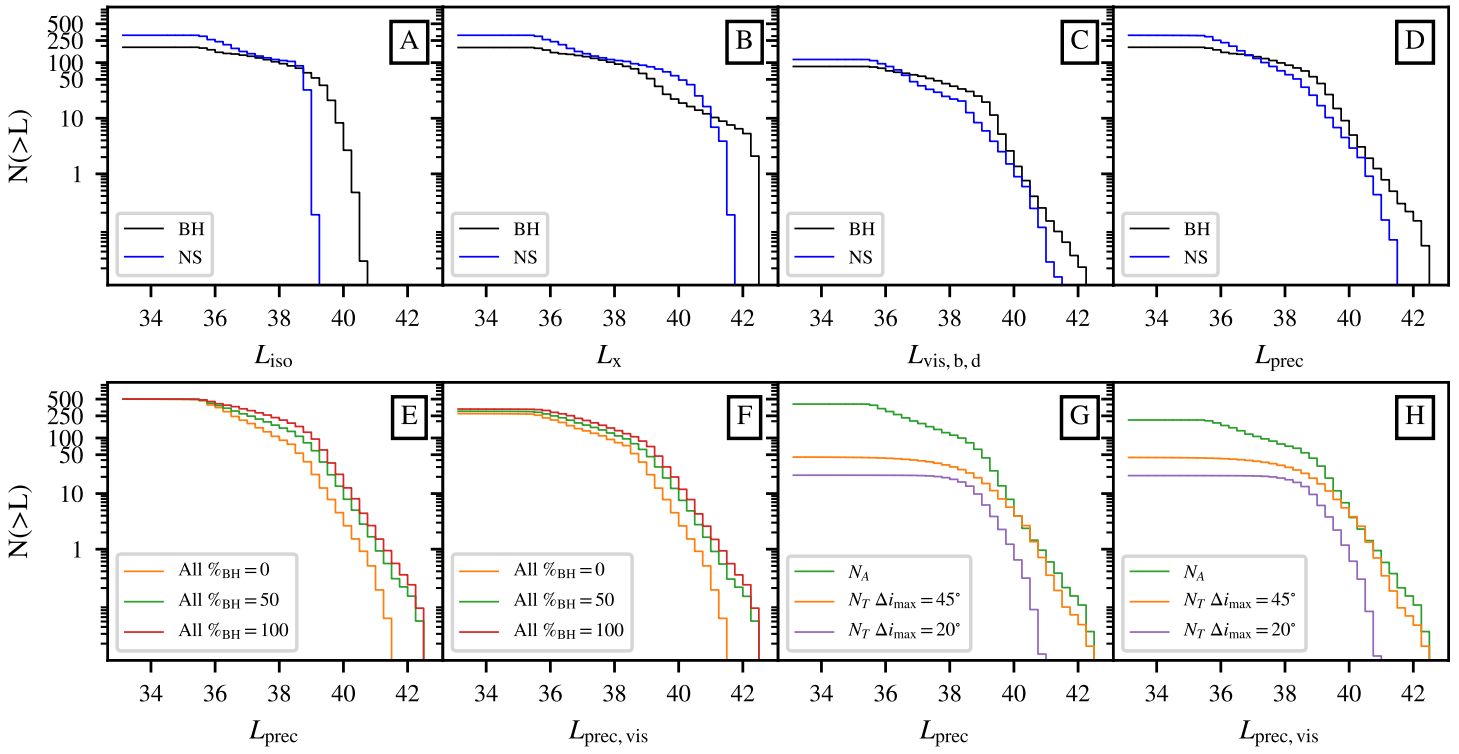

Figure 3.5: Cumulative XLFs shown for a variety of luminosity prescriptions. **A:** the XLF for BHs and NSs when assumed to emit isotropically (L_{iso}). **B:** the same for beamed emission (L_x). **C:** The same but factoring in the observation probability from beaming and LMXB duty cycle (but without precession: $L_{vis,b,d}$). **D:** the XLF after incorporating the probability obtained from precession L_{prec}. (see section 3.3.1). **E:** L_{prec} for different $\%_{BH}$. **F:** The XLF incorporating precession and the addition of a LMXB duty cycle ($L_{prec,vis}$). **G:** The XLF incorporating precession split into the classifications described in section 3.2.6. **H:** The XLF incorporating precession and duty cycle split into the classifications described in section 3.2.6. ($L_{prec,vis}$). The first four and last two panels assume $\%_{BH} = 50$, while the estimates for the impact of precession assume a maximum precessional angle of $\Delta i_{max} = 45°$ unless otherwise stated. Where I have included its effect, the LMXB duty cycle was set to $d = 0.2$. The XLF obtained via sampling from the ULX catalogue of Earnshaw et al. (2019) is shown in cyan. The method for the creation of this plot is detailed in section 3.2.7.

Panels **E** and **F** are created following the same process as panel **D** and show the XLF with and without the addition of the LMXB duty cycle respectively. Here I have combined the NS and BH populations into a single observed population and varied $\%_{\rm BH}$. I observe that the general shape of the XLF is not strongly affected by the underlying $\%_{\rm BH}$, however, for a higher proportion of BHs in the underlying population, there are a larger number of detected systems across all luminosities (with systems still being detected at a few $\times 10^{41}$ erg s^{-1}).

Panels **G** and **H** show the same as panels **E** and **F** except I have now split the XLF into the classifications of alive and transient, with results shown for different maximum precessional angles as described in section 3.2.6.

Modelling the XLF

The differential forms of observed XLFs (dN/dL) are often fitted with power-laws, or variants such as broken or exponential cutoff power-laws (see Grimm et al. 2003; Swartz et al. 2011; Mineo et al. 2012; Wang et al. 2016; Wolter et al. 2018; Kovlakas et al. 2020). In Figure 3.6 I plot a subset of the differential forms of my synthetic XLFs versus the best fit models from Wang et al. (2016) who used *Chandra* observations of 343 galaxies (totalling 4970 sources, 218 of which are ULXs) to create differential XLFs. Whilst there appears to be agreement at higher luminosities ($L > 10^{39}$), at lower luminosities my XLFs appear to flatten off which is inconsistent with the models based on observation; this is likely due to the excluded systems from my sampling which emit at lower luminosities (e.g. white dwarf accretors). In order to make a fair, quantitative comparison to reported slopes in the literature, I therefore model only the high luminosity tail ($> 10^{39}$ erg s^{-1}) of the differential form of my synthetic XLFs.

My differential luminosity functions obtained via $L_{\rm prec}$ and $L_{\rm prec,vis}$ are fitted using a power-law of the form $dN/dL = AL^{-\alpha}$ via a method of maximum likelihood (for limitations on this method see Clauset et al. 2007) where the errors on each bin are the standard deviation (rather than standard error which are considerably less representative in this case). Table 3.6 reports the corresponding best fit parameters and their 1σ errors.

As can be seen from Table 3.6, I observe a slight flattening of the XLF slope with increasing $\%_{\rm BH}$ with slightly steeper slopes found for $\Delta i_{\rm max} = 20°$ when compared to $\Delta i_{\rm max} = 45°$. The effect of the duty cycle is to lower the maximum height reached by the XLF (i.e. the total number of sources, see bottom row in Figure 3.5) which flattens the slope, especially when the population is BH dominated and thus extends to higher luminosities.

The existing literature contains a great deal of variation in the normalisation when fitting functional forms to XLFs. However, the slopes of my synthetic differential XLFs (α) are found to be somewhat flatter than those found in Grimm et al. (2003) (created from HMXBs in five different galaxies), with an observed slope of $\alpha = 1.61 \pm 0.12$, in (Swartz et al., 2011) (using observations of 127 nearby galaxies) with an observed slope of $\alpha = 1.4 \pm 0.2$ above 10^{39}erg s^{-1}, and in Wang et al. (2016) who applied a broken power-law (with a break at $L_b = 2.5 \times 10^{38}$ erg s^{-1}), finding the slope above the break to be $\alpha_2 = 1.1 \pm 0.02$. I discuss the impact of observational bias as the likely reason for this difference in the section 3.4.

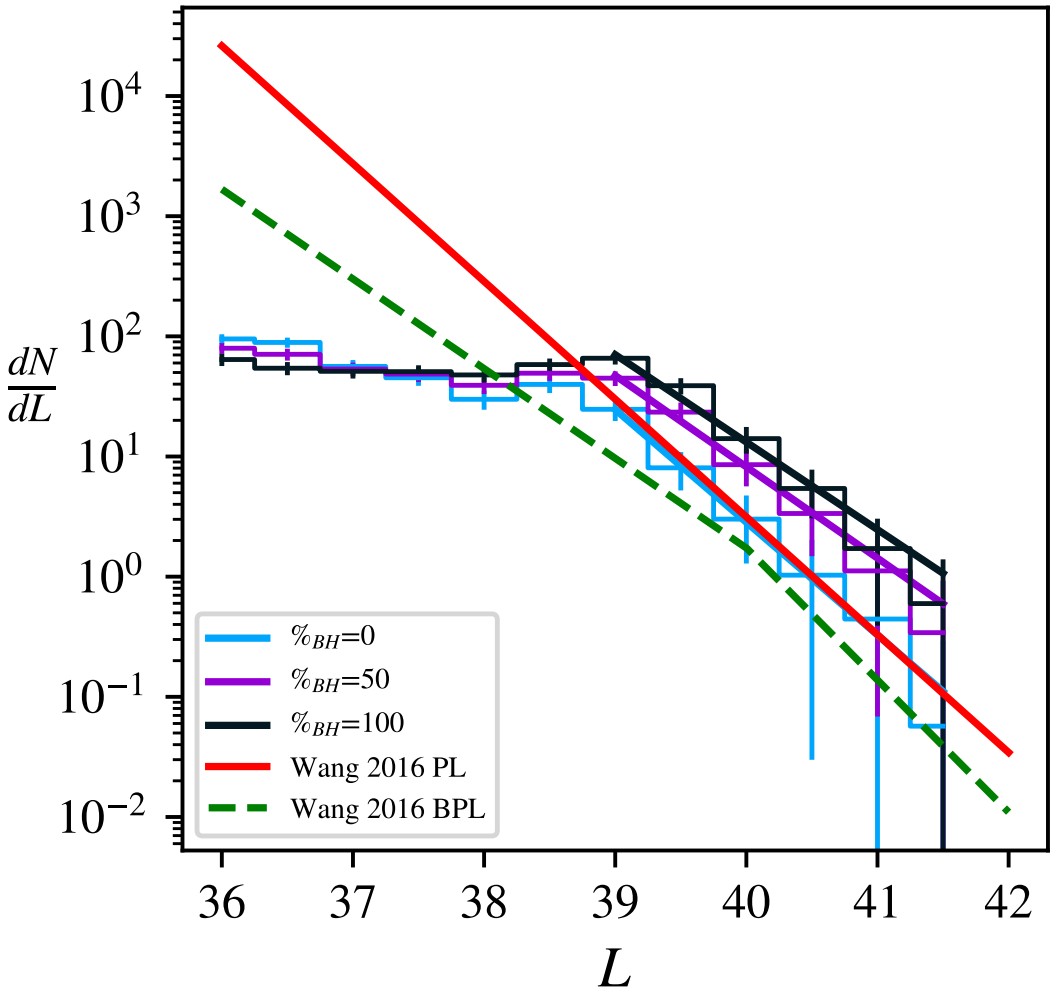

Figure 3.6: Several realisations of my synthetic, differential XLFs (showing $L_{\rm prec}$), for different black hole percentages: $\%_{\rm BH} = 0$ (cyan), 50 (magneta) and 100 (black) and a maximum precessional angle of $\Delta i_{\rm max} = 45°$. Two best fit models from Wang et al. (2016) are overlaid for comparison, unbroken power-law (red) and broken-power-law (green dashed).

L	$\Delta i_{\max}$	$\%_{\mathrm{BH}}$	A	α
L_{prec}	45	0	24.60 ± 0.77	0.94 ± 0.03
L_{prec}	45	25	36.18 ± 1.71	0.81 ± 0.03
L_{prec}	45	50	47.16 ± 3.00	0.76 ± 0.04
L_{prec}	45	75	59.23 ± 4.56	0.74 ± 0.05
L_{prec}	45	100	70.40 ± 6.13	0.73 ± 0.06
L_{prec}	20	0	23.95 ± 0.45	1.06 ± 0.02
L_{prec}	20	25	35.61 ± 1.79	0.88 ± 0.04
L_{prec}	20	50	47.36 ± 3.38	0.83 ± 0.05
L_{prec}	20	75	59.86 ± 5.53	0.79 ± 0.06
L_{prec}	20	100	71.20 ± 7.33	0.78 ± 0.07
$L_{\mathrm{prec,vis}}$	45	0	24.24 ± 0.76	0.93 ± 0.03
$L_{\mathrm{prec,vis}}$	45	25	29.28 ± 1.42	0.77 ± 0.03
$L_{\mathrm{prec,vis}}$	45	50	34.06 ± 2.34	0.70 ± 0.04
$L_{\mathrm{prec,vis}}$	45	75	39.61 ± 3.43	0.66 ± 0.05
$L_{\mathrm{prec,vis}}$	45	100	44.44 ± 4.64	0.64 ± 0.06
$L_{\mathrm{prec,vis}}$	20	0	23.60 ± 0.44	1.06 ± 0.02
$L_{\mathrm{prec,vis}}$	20	25	28.63 ± 1.26	0.84 ± 0.03
$L_{\mathrm{prec,vis}}$	20	50	34.19 ± 2.58	0.77 ± 0.05
$L_{\mathrm{prec,vis}}$	20	75	39.98 ± 3.95	0.72 ± 0.06
$L_{\mathrm{prec,vis}}$	20	100	44.96 ± 5.39	0.69 ± 0.07

Table 3.6: Best fit parameters and 1σ errors from modelling my synthetic, differential XLFs above 10^{39} erg/s using a power law of the form $AL^{-\alpha}$.

3.3.2 Dependence of Light Curve Classifications on Model Parameters

Following from my simulations and the placing of sources into the three categories described in section 3.2.6, I now describe how the underlying nature of the population might affect the observations of ULXs.

Figure 3.7 shows the distributions for the number of the three light curve classifications, as well as the percentage of transient to total observable $N_{\mathrm{T}}/(N_{\mathrm{A}} + N_{\mathrm{T}})$ systems. The results are presented as a corner plot (Foreman-Mackey, 2016) over a subset grid of simulation parameters (see section 3.2.6). The two distinct regions of parameter space in Figure 3.7 denoted by dotted and solid contours arise from the two different maximum precessional angles, $\Delta i_{\max}$ 20° (dotted) & 45° (solid). There is considerable overlap in the number of alive and hidden systems from populations drawn when using a maximum precessional angle of 20° when compared to 45°. However, the error contours describing the number of transient sources, N_{T}, overlap less, with smaller maximum precessional angles (up to 20°) resulting in fewer transient sources by around a factor two when compared to the larger maximum precessional angle (up to 45°). The darker regions in Figure 3.7 correspond to populations drawn with higher fractional abundances of BHs, while blue-er regions correspond to populations with a higher abundance of NSs. I observe that the number of hidden and transient sources, N_{Hid} and N_{T}, are negatively correlated with increasing black hole percentage, while the number of

alive systems increases with increasing $\%_{\rm BH}$, this trend is observed across all the simulated metallicities, maximum precessional angles and simulated duty cycles. The latter observation follows naturally from the expectation that NS ULXs are beamed (under my assumptions which do not factor in the emission from the column nor the effects of strong dipole fields) and, combined with precession, are more likely to be observed as *transient* or *hidden*. I note that, in the absence of a LMXB duty cycle (i.e. $d = 1.0$), the correlation between the number of transient sources and black hole percentage is markedly less pronounced, this is due to my prescription for LMXB systems (section 3.2.3) resulting in a higher number of black hole systems displaying outburst duty cycles when compared to NS systems.

In terms of the most extreme scenarios, from Figure 3.7 I can see that for a population composed entirely of neutron stars, around $\sim 40-50\%$ of the observable sources are defined as being transient for $\Delta i_{\rm max} = 20°$, or $\sim 60-75\%$ for $\Delta i_{\rm max} = 45°$. Conversely, for an underlying population composed entirely of black holes, the proportion of sources being defined as transient is $\sim 10-25\%$ for $\Delta i_{\rm max} = 20°$ or $\sim 30-45\%$ for $\Delta i_{\rm max} = 45°$.

The effect of changing the parent population's metallicity, Z, which is shown for a fixed set of model parameters in Figure 3.8, does have an impact on the absolute numbers of each classification, however, the general trends previously described hold true for all metallicities and their combination.

3.3.3 Comparison to observations

From Figure 3.7 I deduce that the black hole percentage in the underlying population, and maximum precessional angle, substantially affects the percentage of transient to observed sources. This implies that, with constraints on the maximum precessional angle and suitable coverage (both in terms of sky area observed and cadence), it may be possible to constrain the ratio of BHs to NSs in the underlying population simply by determining the ratio of transient to alive systems (under the assumption that the variability is driven by precession and the beaming is highly sensitive to accretion rate – see section 3.4).

In the following sections, I discuss initial constraints from *XMM-Newton* and then discuss implications for *eROSITA* and *eRASS*.

Constraints from *XMM-Newton*

To obtain some initial observational constraints on the number of alive and transient ULXs, I used the catalogue of 1314 X-ray sources compiled by Earnshaw et al. (2019), created from the 3XMM-DR4 data release of the *XMM-Newton* Serendipitous Source Catalogue (Rosen et al., 2016). The catalogue identifies 384 candidate ULXs, 81 of which were observed more than once. Each entry within the catalogue includes a full band ($0.2-12$ keV) apparent (absorbed) luminosity and associated 1σ errors. From the 81 ULXs with multiple observations, I sampled the luminosity (i.e. using their associated errors) 100,000 times, and separated these systems into *alive* or *transient* based on my previous definitions, and calculated associated 1σ error intervals on the respective distributions. I find that $81 \pm 12\%$ of the systems may be classified as *alive*, while $19 \pm 3.8\%$ may be classified as *transient*; by

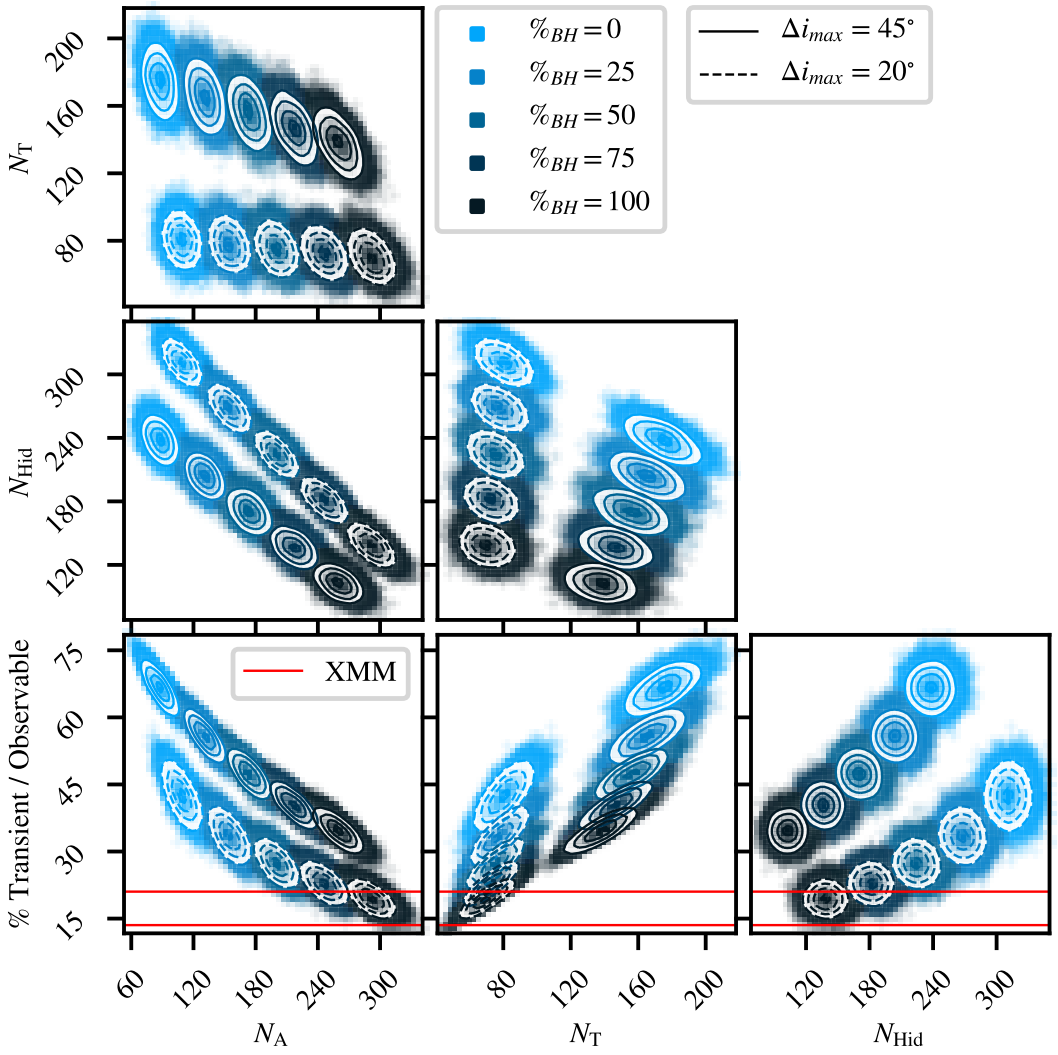

Figure 3.7: 2D 1σ error contours for the distributions of the number of alive, transient and hidden systems (N_A, N_T, N_{Hid}), as well as the percentage of transient to observed systems, ($N_T/(N_A + N_T)$) and how these vary with the black hole percentage ($\%_{BH}$) of the underlying population. This particular simulation used the following fixed parameters: $N_{sys} = 500$, $Z = 0.02$, $\Delta i_{max} = 20°$ (dashed contours) 45° (solid contours) and $d = 0.2$. $\%_{BH}$ was varied between 0, 25, 50, 75 & 100%, where a higher abundance of BH systems is shown on the figure as darker colours and blue-er colours correspond to higher abundances of NS systems. The red lines denote the 1σ confidence bounds for the percentage of transient systems to observable systems obtained from the most recent *XMM-Newton* ULX catalogue (Earnshaw et al., 2019)

comparison to my simulated results, I can thereby obtain a crude estimate of the underlying, intrinsic properties of the observed population. The region denoted by the red lines on Figure 3.7 indicates the 1σ interval for the percentage of transient to observed sources obtained from Earnshaw et al. (2019) and implies abundances of BHs of around 75-100% (assuming $\Delta i_{\rm max} = 45°$ or $10-100\%$ (for $\Delta i_{\rm max} \leq 20°$), see Figure 3.7). As the ULXs in the Earnshaw et al. (2019) catalogue have only been observed 2-3 times, there is an observational bias towards alive systems and I underestimate the true number of transients. The inferred percentage of transient to observed systems is therefore only a lower limit and, as more transients are located, the upper limit on $\%_{\rm BH}$ will steadily push to smaller values.

I also note that the luminosities obtained via sampling the observed population of Earnshaw et al. (2019) are subject to interstellar absorption, whilst the luminosities obtained from my simulations do not account for this effect. As such, my results are most valid for observations made out of the Galactic plane and of other galaxies viewed at low inclinations.

Having established in section 3.3.2 that the relative abundance of *alive*, *hidden* and *transient* sources may serve to provide diagnostic information on the quantities describing the underlying population, I now explore the broad implications for constraining the underlying nature of the observed ULX population using *eROSITA*.

Following the method described in section 3.2.8, I subject the transient light curves to regular sampling, matching the cadence of *eRASS*, and investigate whether any of my measured quantities, such as the relative number of transient to observed sources, are affected by my input parameters, (e.g. the black hole percentage, maximum precessional angle or period prescription). Figure 3.9 shows three directly observable quantities and their evolution over the course of *eRASS*: the cumulative number of alive and transient ULXs, and the proportion of transient to total observed ULXs, for five different black hole percentages (with 1σ bounds on the quantities via 10,000 MC iterations). The model parameters used to make Figure 3.9 are $Z = 0.02$, $d = 0.2$, $\Delta i_{\rm max} = 45°$ (left-hand column) & $20°$ (right-hand column), and here I use the Lense-Thirring precession period (eqn 3.4).

Observational predictions for *eRASS*

From the first row of Figure 3.9, I observe the absolute number of *alive* sources detected by *eRASS* appears to be sensitive to the underlying black hole percentage, with the number being positively correlated with the proportion of BHs in the underlying populations. I also observe that the number of transient sources (middle row) detected by *eRASS* is not sensitive to the black hole percentage, i.e. for a given set of parameters (Z, $\Delta i_{\rm max}$, d & P), the inferred 1σ regions overlap. Instead, I find that the number of transient sources *is* sensitive to the maximum precessional angle, with $\Delta i_{\rm max} = 20°$ providing around half the number of transients when compared to $\Delta i_{\rm max} = 45°$. This may mean that if I have a well-informed prior on the maximum precessional angle, one may, by considering the relative percentage of transient to observed sources, obtain some indication of the black hole percentage in the underlying population.

In Figure 3.10 I also show three quantities not directly observable by *eRASS*

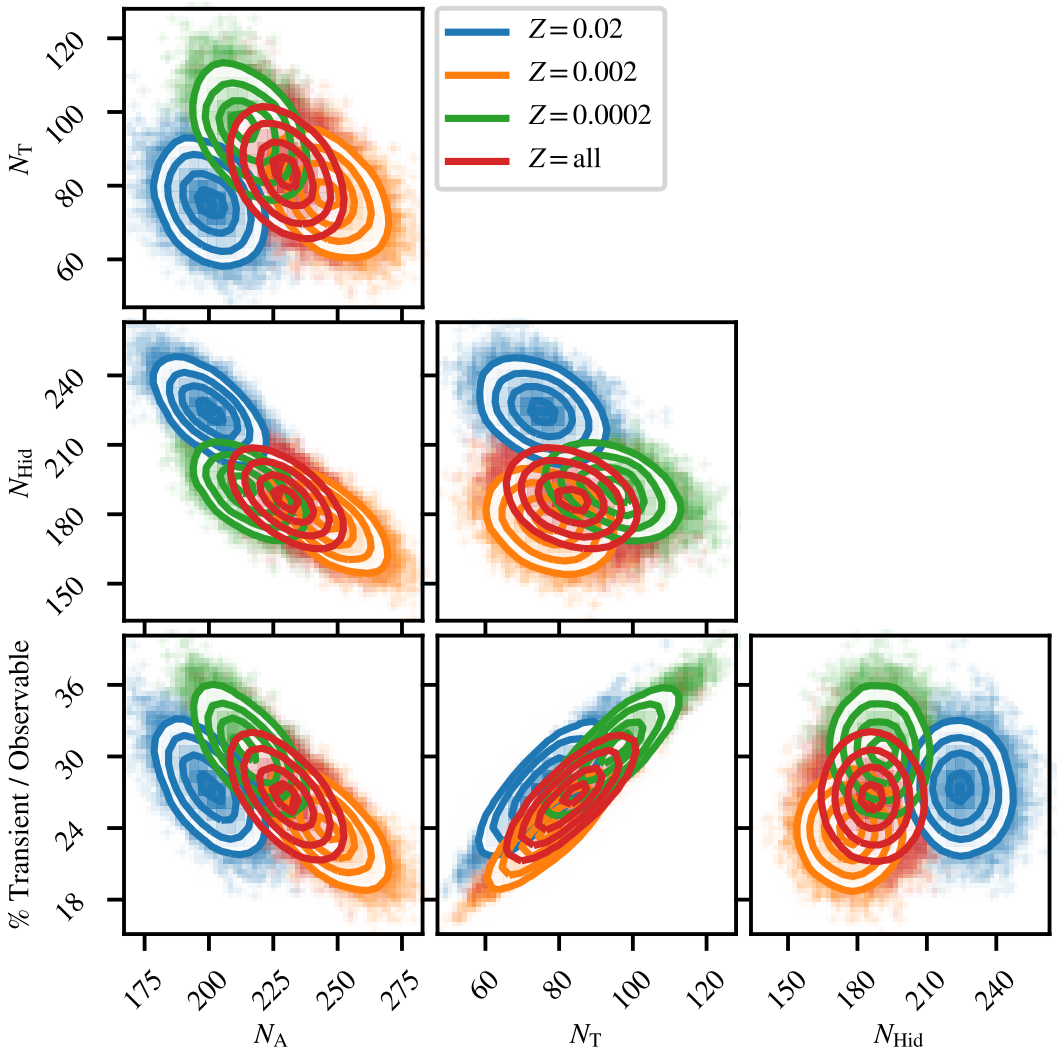

Figure 3.8: 2D 1σ error contours for the distributions of light curve classifications for different parent population metallicities, $Z = 0.02$ (blue), $Z = 0.002$ (orange), $Z = 0.0002$ (green) and the combination of all three (red) for fixed parameters: $\Delta i_{\max} = 20°$, $d = 0.2$, $\%_{BH} = 50$.

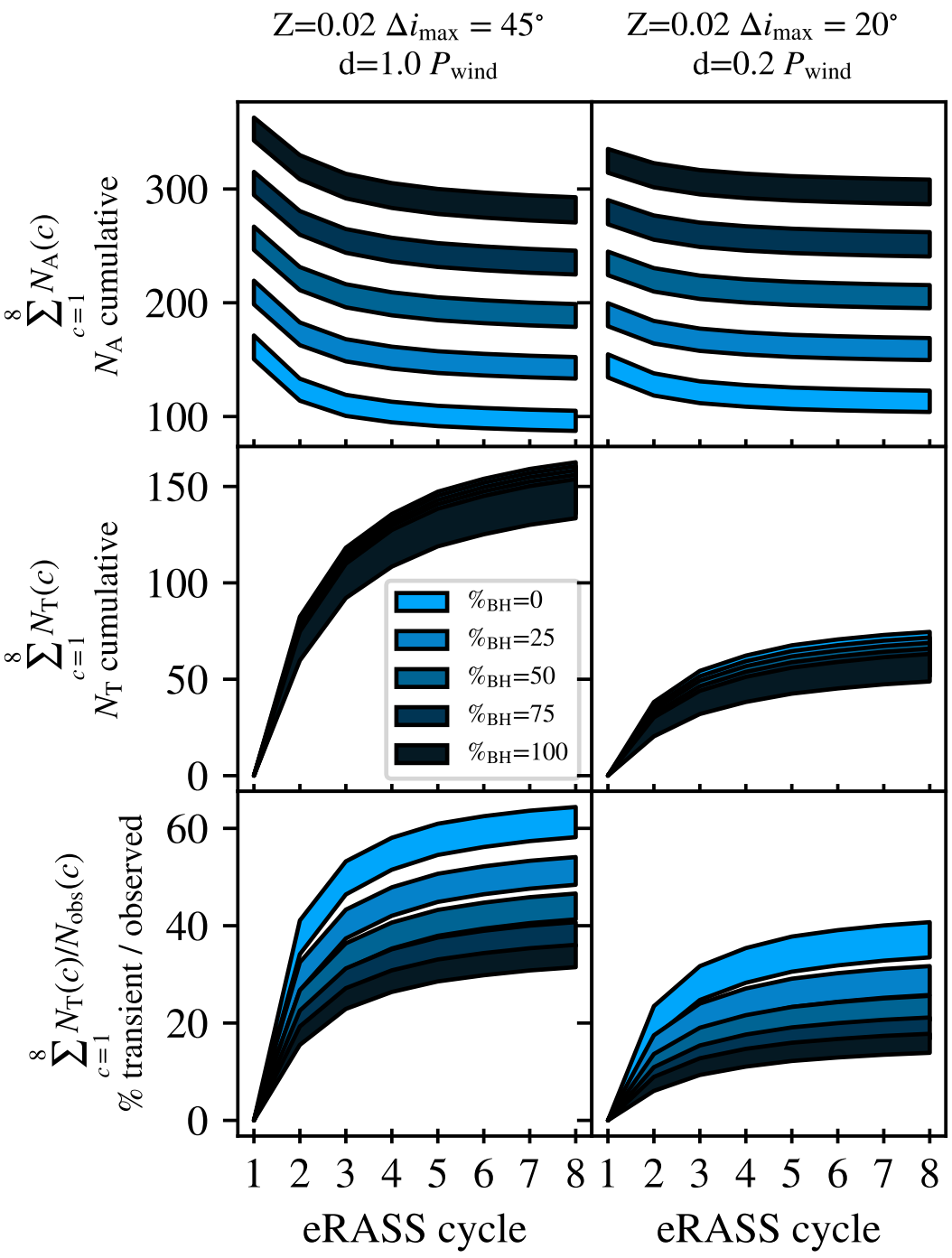

Figure 3.9: The evolution over *eRASS* cycles of three quantities that may be directly observed: the number of alive (top row), transient (middle) and proportion of transient to observed sources (bottom). Each column shows a different set of model parameters, while the different colours correspond to the underlying black hole percentage, with darker colours corresponding to a higher abundance of BHs. The width of the lines indicate the 1σ error regions of the quantities being explored.

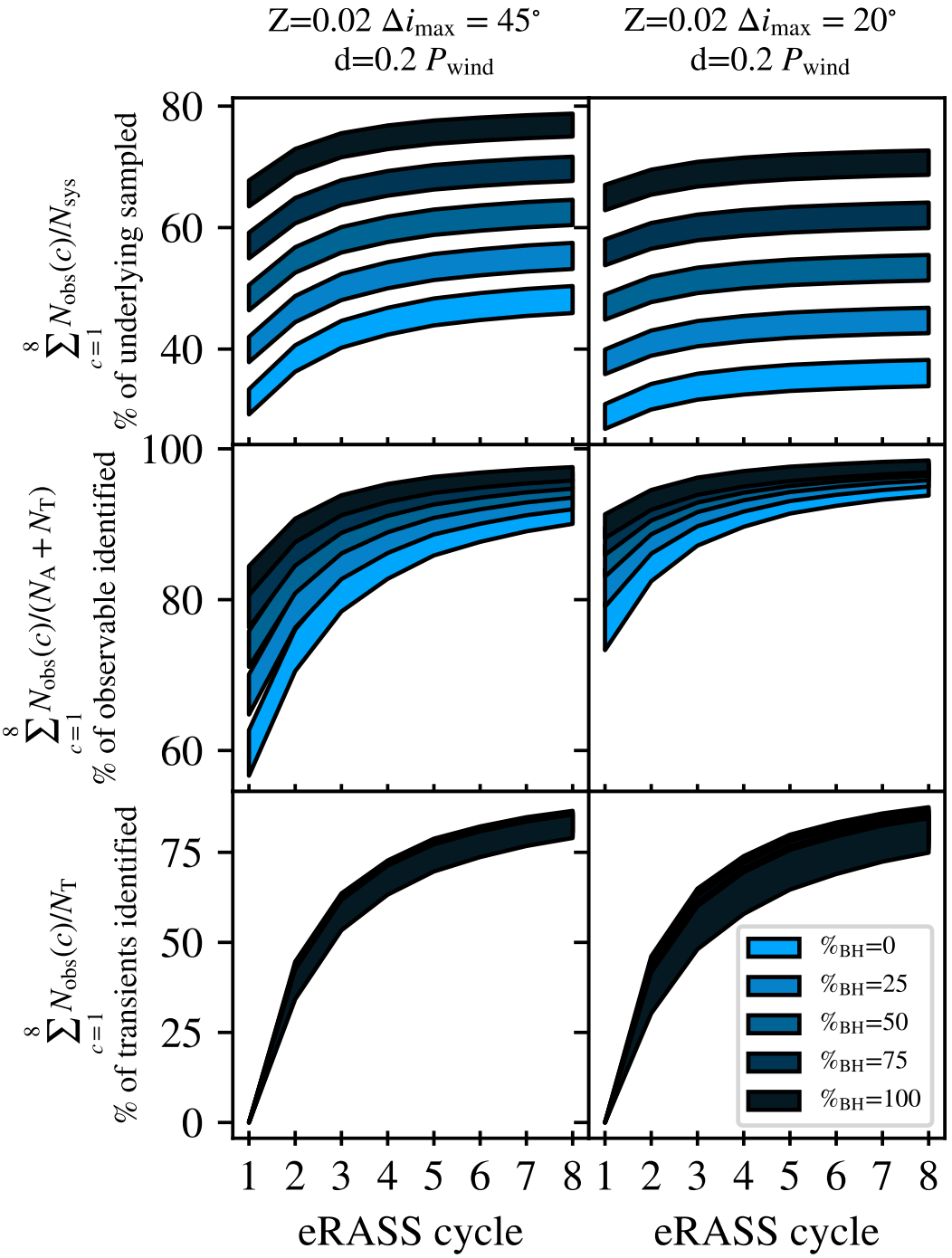

Figure 3.10: The evolution over *eRASS* cycles of the percentage of the underlying sources sampled (top), the percentage of the potentially observable sources sampled (middle) and the percentage of transient sources sampled (bottom). The width of the lines indicate the 1σ error regions of the quantities being explored.

but useful for gaining insight into the performance of the survey:

- $\sum_{c=1}^{8} N_{\rm obs}(c)/N_{\rm sys}$ provides the percentage of the full ULX population sampled by a given *eRASS* cycle
- $\sum_{c=1}^{8} N_{\rm obs}(c)/(N_{\rm A} + N_{\rm T})$ which quantifies the percentage of the *potentially observable* population which has been observed
- $\sum_{c=1}^{8} N_{\rm obs}(c)/N_{\rm T}$ which quantifies the percentage of the transient population only which was sampled

I will now briefly summarise the effect of each of my model parameters on the observed population as seen by *eRASS*.

- **Effect of metallicity**:

  Lower metallicity environments are commonly associated with a higher abundance of BH systems, as lower metallicity stars experience less mass loss than their higher metallicity counterparts and are therefore more likely to end up as BHs (Heger et al., 2003). However, as I am manually specifying the relative abundance of BHs in my simulations, the effect of Z does not strongly correlate with many of the observable quantities.

- **Effect of underlying demographic**:

  Figure 3.9 shows the effect of changing the percentage of black holes within the sample, for a given set of model parameters over *eRASS* cycles. I observe that there is a sizeable increase in the number of alive systems for higher abundances of black holes. There is also an essentially constant number of transient sources across all black hole percentages. The combination of these last two effects means that the percentage of transient to observed sources also shows a dependence on the black hole percentage. For the set of simulation parameters shown in Figure 3.9, and for a maximum precessional angle of 45°, it can be seen that, for a population composed entirely of black holes, around $\sim$ 30% of observed sources may be identified as transient by cycle eight, whilst up to $\sim$ 60% would be observed as transient for a population composed entirely of neutron stars. For a maximum precessional angle of 20°, these values are instead around $\sim$ 20% and $\sim$ 40% respectively.

  From Figure 3.10 I also note that the underlying (both full and potentially observable) ULX populations are better sampled for higher black hole percentages in the underlying population.

- **Effect of maximum precessional angle**:

  While the Galactic ULX SS433 is well known to have a precessional half-angle of $\sim$ 20° (Fabian & Rees, 1979), the light curve of NGC 5907 X-1 was described using `ULXLC` with a precessional half-angle of only $\Delta i = 7.30^{+0.13}_{-0.15}$ (Dauser et al., 2017). With only two observational constraints (the one for NGC 5907 X-1 naturally being model-dependent), the precessional angle, Δi, remains one of the least constrained free parameters in my analysis. As such, I have throughout this work assumed a flat prior, however, the physics

of the underlying precession mechanism (e.g. in the case of Lense-Thirring precession, the misalignment angle between the CO spin axis and binary axis) could plausibly result in precessional angles which tend towards the smaller range of values.

From Figure 3.9, a maximum precessional angle of $\Delta i_{\rm max} = 45°$ roughly halves the absolute number of transients detected in each *eRASS* cycle, while also halving the percentage of transients to total observed systems when compared to a maximum precessional angle of $\Delta i_{\rm max} = 20°$. As seen in Figure 3.10, a larger precessional angle results in a higher number of the potentially observable (alive or dead) sources being identified but interestingly results in a lower proportion of the entire underlying population being sampled.

- **Effect of the precession prescription**:

  Remarkably, both the empirical relation of Townsend & Charles (2020) (eq 3.7) and the prediction from the Lense-Thirring model (eq 3.4) produce similar results (see Figure A.1). This is intriguing as it implies that, regardless of the mechanism, if the disc and wind are precessing then we can infer the properties of the underlying sample. Of course, should the mechanism be substantially different (e.g. precession of the curtain Mushtukov et al. 2017), then this assertion may be invalid.

- **Effect of the LMXB duty cycle**:

  I find that a lower duty cycle for the LMXB ULX population serves to reduce the absolute number of transients detected in each cycle. However, when I consider the relative proportion of transients to the total number of observed sources, I find the impact of changing the duty cycle to be negligible.

3.4 Discussion

The relative proportion of black holes to neutron stars within the observed ULX population still remains an important unanswered question; of the current sample of roughly 500 ULXs, around ten are confirmed to have NS accretors, and there are strong indications that certain objects may harbour black holes (e.g. Cseh et al. 2014), but for the vast majority of the population, the nature of the accretor remains unknown. Wiktorowicz et al. (2019) approached this issue by analysing how anisotropic emission of radiation (geometrical beaming) affects the observed sample of ULXs, finding that, in regions of constant star formation, the expected number of NS ULXs is higher than the total number of BH ULXs, however due to the effect of beaming, they concluded that the total *observed* population was potentially comparable (cf. Middleton & King 2017). My work has built on this by exploring the additional effect of precession of the wind cone.

My simulations have allowed me to construct synthetic XLFs (Figure 3.5) and explore the changes resulting from varying the underlying population demographic. Fitting to only the high luminosity end ($L \geq 1 \times 10^{39}$ erg s^{-1}) appears to indicate a range of slopes which are somewhat steeper than observation (Table 3.6 and

Figure 3.6) at least where the percentage of black holes in the underlying population are non-zero. It may be that the proportion of black holes is indeed low (as one would expect many more neutron stars than black holes in the intrinsic, underlying population: Wiktorowicz et al. 2019), however there are also several effects which may contribute to differences between simulation and observation. It is important to note that the XLFs I have created from simulation represent a time-averaged and idealised view of a large population of ULXs, whilst XLFs constructed from single (or from a small number of) observations instead suffer from a bias towards detecting bright, persistent ULXs rather than transient ULXs (and will also depend on the star formation history of the target galaxy which I have not accounted for Fragos et al. 2013a,b). I also note that – unlike the observational XLFs – my simulated luminosities do not assume any absorption; whilst accounting for this effect is complicated (it for instance depends on the unknown spectral shape and local column of a given ULX at a given point in its precessional cycle, e.g. Middleton et al. 2015b), this is unlikely to have a major effect as long as the line-of-sight column is low. Finally, I have assumed a form for the beaming which does not take into account the full complexity of the system, e.g. radial collimation profile, re-processing and outwards advection, all as functions of accretion rate. These complicating effects could potentially bring the highest sources down to lower luminosities, making the XLF steeper.

One of the key results to emerge from my analysis is the indication that a measure of the relative number of *transient* to *observed* ULXs can constrain the nature of the intrinsic population. Such a result is naturally important as it would allow for a more concrete understanding of the accreting binary population and related fields (i.e. studies relying on binary population synthesis, e.g. Fragos et al. 2013b). However, it is important to consider the limitations of my approach. I have made the explicit assumption that either Lense-Thirring torques ($P_{\rm wind}$) or a different unspecified process ($P_{\rm sup}$: Townsend & Charles 2020) are the dominant form of variability on the timescales I am investigating. Whilst Lense-Thirring torques are certainly unavoidable where the compact object is misaligned (expected in light of the time required to align the binary – see King & Nixon 2018), there are other torques which can dilute or dominate over this effect. These are discussed at length in Middleton et al. (2018) but perhaps most notably I might expect radiation pressure driven warps and precession (Pringle, 1996), or neutron star dipole precession (see Mushtukov et al. 2017) to occur where the field is very strong (in the case of the former, the outer disc can be essentially unshielded for high dipole field NSs, unless the accretion rate is extreme). I also note that free-body precession may occur as a result of neutron star oblateness and misalignment of the rotation axis with the axis of symmetry of the star (see sec 1.3.4). This latter effect has been explored as an alternative origin for the month timescale modulation seen in ULXs (Vasilopoulos et al., 2020).

In addition – and unlike my consideration of the impact of a LMXB duty cycle – I have not included the effect of propeller states which occur when neutron stars are close to spin equilibrium. In such cases, increasing the neutron star spin by a small amount leads to a period of relative quiescence where emission from the accretion column and accretion curtain is switched off due to the centrifugal barrier. If the accretion rate is high or dipole field strength low enough, then

we would still expect radiation to emerge from the disc between $r_{\rm sph}$ and the magnetospheric radius, $r_{\rm M}$, which could be substantial (the luminosity then going as $\ln(r_{\rm sph}/r_{\rm M})$. However, where the dipole field strength is high or accretion rate low, entering a propeller state could effectively switch off most of the emission, potentially dropping the source below the empirical ULX threshold.

Throughout this work I have made the assumption that NSs have a low spin of $a_* = 0.01$ while black holes have a maximal spin of $a_* = 0.998$. The former is based on the observation of ∼1 s periods in ULX pulsars to-date (see King & Lasota 2020 and references in introduction). Naturally, we cannot rule out higher spins for NS systems (as an example, the fastest known spin frequency of a NS at 716Hz Hessels et al. 2006 would correspond to a maximal spin of $a_* = 0.2 - 0.3$ Miller & Miller 2015, which would reduce the Lense-Thirring precession timescale accordingly, but the lack of evidence for such spins in ULXs presently limits one's ability to explore this. Black hole ULXs may also not be maximally spinning (implying a slower precession period if Lense-Thirring), however, once again I have limited information at this time.

It is interesting to note that around half of the known PULXs appear to be transient ULXs, with luminosities spanning over a factor of 100 (Song et al., 2020). A propeller state has already been reported in one NS ULX to-date (Fürst et al. 2016, although the spin evolution implies the drop in flux is instead driven by obscuration/precession: Fürst et al. 2021). Earnshaw et al. (2018) have searched for propeller state ULXs within the entire *XMM-Newton* 3XMM-DR4 serendipitous source catalogue, identifying five ULXs that demonstrated long term variability over an order of magnitude in brightness, while one source (M51 ULX-4) demonstrates an apparent bi-modal flux distribution that may be consistent with a source undergoing propeller (although this may also be due to sampling a precessional light curve (e.g. Dauser et al. 2017). They also note that there are potentially up to ∼ 200 sources in the *XMM-Newton* catalogue which may simply lack a sufficient number of observations using *XMM-Newton* to reveal their transient nature. Subsequent simulations by the same authors suggest that *eROSITA* may be able to identify 96% of sources that are undergoing the propeller effect by cycle 8 of *eRASS* (for a duty cycle of 0.5). This means that if NS ULXs undergoing the propeller effect are present in a large number within the population, the true number of transient sources in this chapter could be largely underestimated.

In *practice* this means that, without an indication of whether a given source's variability is driven by precession or propeller, the regular observations taken within *eRASS* may lead one to somewhat overestimate the underlying number of transients driven by precession (although this relies on the sample being large and not many sources precessing on very long timescales). As a result, we would tend to over-estimate the abundance of neutron stars in the underlying population. However, if we are able to isolate sources that display precession (e.g. via fitting of long term light-curves or ruling out the propeller effect), then, given a large enough sample, we would then obtain a *lower* limit on the number of transient (via precession) to observed sources and a lower limit on the abundance of neutron stars in the underlying population.

Finally, I have assumed that NSs in my simulations may only reach ULX luminosities via geometrical beaming, while it is possible that a drop in the electron

scattering cross-section due to a high strength dipole magnetic field, as well as the structure of the accretion column itself could also boost the luminosity (e.g. Basko & Sunyaev 1976; Mushtukov et al. 2017).

3.5 Conclusions

Starting from a synthetic population of binary systems, and using a simple geometrical model for a precessing cone of emission, I have investigated the effect precession and beaming might together play on the observed population of ULXs. I have investigated the effect precession has on the XLF and the relative numbers of *alive* (persistently $\geq 1{\times}10^{39}$ erg s^{-1}), *transient* (varying across $1{\times}10^{39}$ erg s^{-1}) and *hidden* (persistently $< 1{\times}10^{39}$ erg s^{-1}) sources, and, by factoring in the observational cadence of *eRASS*, I have made predictions for how well the underlying population may be constrained over the course of four years of monitoring.

In this chapter I propose a novel method for constraining the underlying demographic within the population of ULXs, as the percentage of ULXs observed to be transient or observed is sensitive to parameters such as maximum precessional angle, and crucially to the relative fraction of BHs and NSs in the underlying population (whilst not sensitive to the duty cycle of LMXB ULXs). This follows from the fact that – under the assumptions of geometrical beaming – populations containing a higher percentage of BHs are observationally associated with higher percentages of systems persistently above 10^{39} erg s^{-1} and with lower percentages of transient systems, when compared to populations dominated by NSs.

Determining the underlying ULX demographic presently relies on detecting unambiguous indicators for the presence of a neutron star such as pulsations or a CRSF. However, it has been proposed that many NS ULXs with high accretion rates may not exhibit pulsations King et al. (2017), that large pulse fractions may be absent in the presence of strong beaming (Mushtukov et al., 2021), and CRSFs may not fall within the accessible X-ray energy range or may be diluted (see Mushtukov et al. 2017). An independent and simple method to constrain the nature of the underlying population in ULXs such as the one I have explored here is therefore of value (and joins others such as observing the evolution of quasi-periodic oscillations, see Middleton et al. 2019b).

In an initial application of my approach, I have used the Earnshaw et al. (2019) catalogue of ULX and ULX candidates (accepting that this catalogue is incomplete relative to a true flux-limited survey). Finding that $\sim 80\%$ of the catalogue ULXs are always visible, while $\sim 20\%$ are transient; this implies a black hole percentage in the underlying population in the region of $10 - 100\%$ (for $\Delta i_{\rm max} \leq 20^{\circ}$) or $75 - 100\%$ (for $\Delta i_{\rm max} \leq 45^{\circ}$). However, the number of transients (which we expect to be mostly neutron star ULXs) is likely to be highly underestimated in such low cadence, pointed observing. The introduction of *eROSITA* and its all sky survey, *eRASS*, will revolutionise the view of the transient X-ray sky and is optimally placed to better constrain the underlying demographic of ULXs via this approach. Simulating using two different prescriptions for the precession period: Lense-Thirring (Middleton et al. 2019b) and empirical (Townsend & Charles 2020), I predict a variety of observational possibilities for the evolution of the relative

numbers of transient to persistent ULXs over the course of *eRASS*, for a variety of population characteristics. I conclude that neither prescription for precession significantly alters the observed view of the ULX population.

I have invoked several simplifications in this work. The model for precession (`ULXLC`) currently does not account for the energy dependence of the emission; we are developing models which account for the radial dependence of beaming and which will improve on the accuracy of my simulations. We also presently have limited constraints on the precession angle of the wind cone in ULXs which can have a significant impact on my predictions; this can be estimated through direct modelling (Dauser et al., 2017) and, in future, will be developed and applied more widely to improve my constraints. Finally, I have not included the effects of magnetic fields in the neutron star systems in the population; this can have the effect of changing the X-ray spectrum and beaming but, perhaps more importantly, can lead to periods of relative quiescence via the propeller effect (Fürst et al., 2016; Earnshaw et al., 2018) as well as dipole precession on ∼month timescales when the field is very strong (Lipunov & Shakura, 1980).

Data Availability

The data obtained from StarTrack underlying this article are freely accessible at the following URLs:
https://universeathome.pl/universe/pub/z02_data1.dat
https://universeathome.pl/universe/pub/z002_data1.dat
https://universeathome.pl/universe/pub/z0002_data1.dat

The source code for this project may be found at:
https://github.com/nx1/ulx_pop

Chapter 4

Long-Term X-Ray/UV Variability in ULXs

Abstract

The transient nature of the *Swift* observatory's observing schedule has meant that many observations have been made of ultraluminous X-ray sources (ULX) over the last $\sim$ 20 years. For the vast majority of these observations, simultaneous data has been obtained using both the X-ray telescope (XRT) the ultraviolet and optical telescope (UVOT). The combination of both X-rays and UV/Optical data provides a unique opportunity to study joint variability in ULXs across these energy bands.

By cross-matching several ULX catalogues against the *Swift* master catalogue I obtained a sample of roughly forty ULXs with numerous recurrent observations, I also include a handful of sub-ULX sources as a form of comparison.

I investigate the spatial UV/Optical emission by stacking UVOT exposures and divide our sample into ULXs with point-like emission, ULXs associated with extended emission and sources with low emission.

By extracting light curves long-term light curves in the X-ray and UV/Optical bands, we search for first-order correlations, we find a small subset of our sources show weakly correlated joint variability, while many sources appear to display non-linear relations between the bands.

We conclude that more complicated analysis or higher quality data may be required to accurately constrain the nature of the joint X-ray and UV/Optical emission in these sources.

4.1 Introduction

As established in earlier chapters, it appears inescapable that the accretion flow in ULXs is super-critical, either in the flow or onto the CO itself. A corollary of such accretion flows is that, providing the wind is optically thick, there should be some degree of collimation and the assumption of isotropic emission breaks down (King et al., 2001). The resulting spectrum (and timing properties) of a given ULX then depends on both the accretion rate and inclination of the source (see section 2.3).

Should the accretion rate be high, one would naturally expect high inclination

ULXs to not be bright in the X-rays, but instead peak at lower frequencies (Poutanen et al., 2007). With emission from the photosphere being $\sim$ Eddington, these may be prime candidates for detection by next-generation deep surveys. A prime example of such an edge-on ULX is the Galactic source SS433 ($i = 79°$), which despite having an X-ray luminosity of only $\sim 10^{36}$ erg s^{-1} appears to share many of the same characteristics of ULXs (and is inferred to have considerably brighter, face-on X-ray luminosities (Cherepashchuk, 2002; Fabrika, 2004; Khabibullin & Sazonov, 2016; Liu et al., 2015; Middleton et al., 2021) and emit at $\sim 10^{40}$ erg s^{-1} in the UV (Dolan et al., 1997).

Whilst the intrinsic emission from high inclination ULXs may peak at low frequencies, in the optical/UV band, there will also be emission from the secondary star which can be amplified if effectively irradiated, as well as emission from the outer disc (again, if effectively irradiated). Whilst there has been a great deal of study of ULXs in the optical (see section 2.6), specifically to elucidate the nature of the companion star (Heida et al., 2014), there has been limited exploration of the UV emission. However, it has been observed that in one ULX NGC 6946 ULX3, the UV emission appears extremely bright ($> 10^{39}$ erg/s: Kaaret et al. 2010) and in the case of the PULX, NGC 7793 P13, a super-orbital period is seen, with the UV out of phase with the X-ray super-orbital period (Fürst et al., 2016, 2021). Although not well explored, the correlation between X-ray and low frequency emission could provide invaluable insights into the origin of the emission and the geometry and nature of the accretion flow. In this chapter, I explore the general shapes of the X-ray/UV correlations we might expect for various plausible scenarios and search for these within the *Swift* light curves of several prominent ULXs.

4.2 Predictions

Changes in the X-ray emission in ULXs may be driven by either changes in mass accretion rate or changes in inclination. The former may be a result of mass loss at large radii (Middleton et al., 2022), whilst the latter may be a result of disc warping due to irradiation (Pringle 1996; Pasham & Strohmayer 2013) or precession of the super-critical disc and wind (Middleton et al. 2018, 2019b). Below, I consider the likely ramifications on the observable X-ray/UV properties of ULXs of various origins of the low frequency emission. To simplify this picture, I make the explicit assumption that the ULXs considered all have dipole fields weak enough (or accretion rates high enough) that the classical super-critical picture of disc accretion (Poutanen et al., 2007) holds.

4.2.1 Emission from the outer wind photosphere

Following the standard super-critical model of Poutanen et al. 2007, I assume that the wind photosphere extends out to some radius $r_{\rm out}$ and reprocesses the flux from below the wind where the disc starts to become locally super-critical, and some fraction of the radiation produced interior to $r_{\rm out}$, with an emergent luminosity greater than or equal to the Eddington luminosity.

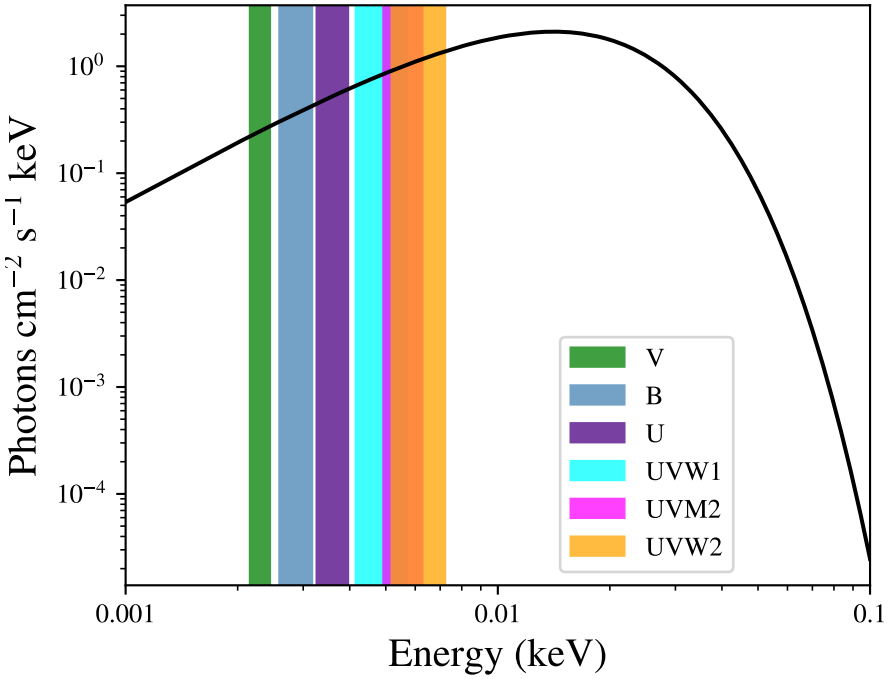

Figure 4.1: Black body spectrum (`bbody` in `xspec`) set at $T = 0.005$ keV plotted in the energy range 0.001 to 0.1 keV in log-space. Coloured are the effective widths of the UVOT bands (see section 1.4) used for the flux calculation shown in figure 4.2.

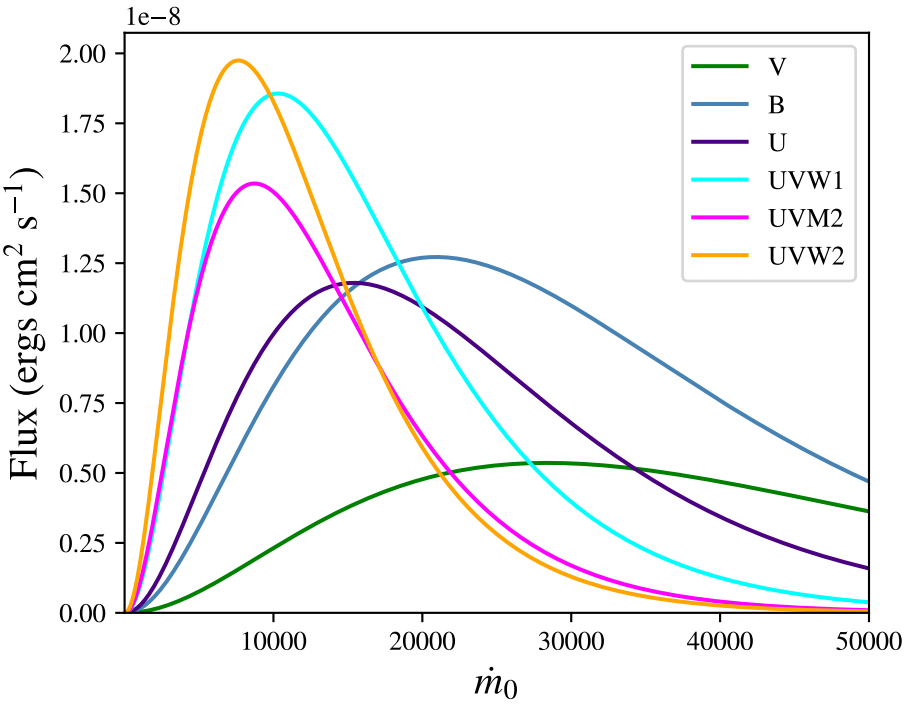

Figure 4.2: Flux in each of the UVOT bands as a function of the mass accretion rate $\dot{m}_0$. The peak flux is reached at $\dot{m}_0 \sim 7000$ for the highest energy band UVW2, much higher than is expected for ULXs, this means our UV view of high inclination ULXs, where the observed emission is from the wind photosphere, exists entirely within the rising region of UV emission on the left of the plot. The plot was made using the `xspec` model `bbody` with a normalized luminosity and a temperature set to $T_{\rm ph}$ (eq 4.1), $m = 1.4\ M_\odot$, $\beta = \zeta = 1$, $f_{\rm col} = 1.7$ and $\epsilon_{\rm w} = 0.95$.

A full understanding of the shape and intensity of the emergent SED requires full GRMHD simulations and extensive post-processing, which is not yet available (although see the work by Narayan et al. 2017 and Dai et al. 2018a). In the absence of numerical studies, I can make some simple qualitative predictions for what must occur. For a fixed inclination, increasing the mass accretion rate pushes $r_{\rm out}$ to a larger radius due to increased mass loading of the wind and the larger radial location of $r_{\rm sph}$ (Poutanen et al., 2007). Should the opening angle of the wind be connected to the accretion rate at large radii (as it would seem to be cf Jiang et al. 2014, 2019), then an increase in mass accretion rate will increasingly collimate the X-ray emission from within. What follows depends on the orientation of the observer. Should one be able to see into the wind cone, then the X-ray luminosity at all energies will increase, and the characteristic temperature associated with the spherization radius, $T_{\rm sph}$ will decrease. The expansion of the wind photosphere to larger radius will lead to a reduction in its temperature according to the formula of Poutanen et al. 2007 (eq 4.1):

$$T_{\rm sph} \approx 0.8 f_{\rm col} \left(\frac{\zeta\beta}{\epsilon_{\rm w}}\right)^{1/2} m^{-1/4} \dot{m}_0{}^{-3/4} \text{ keV} \tag{4.1}$$

where $f_{\rm col}$ is a colour temperature correction factor, ζ, β and $\epsilon_{\rm w}$ are constants relating to the wind cone opening angle, outflow velocity and energy content, m is the accretor mass in $M_\odot$ and $\dot{m}$ is the Eddington-scaled accretion rate.

By assuming the photosphere radiates as a blackbody at the characteristic temperature $T_{\rm sph}$ and that $\zeta\beta/\epsilon_{\rm w} \approx 1$ and $f_{\rm col} \approx 2$ and accretor masses of $10M_\odot$ and $1.4M_\odot$, the UV emission in the highest energy band (UVW2) (taking the form of a blackbody, peaking around 3 kT) will increase in brightness until accretion rates in excess of ≈5000 × Eddington are reached for a 10 $M_\odot$ black hole and ≈ 7000 × Eddington $M_\odot$ for a 1.4 $M_\odot$ neutron star (see figure 4.2). Such rates are safely above those inferred for known ULXs. Below this limit and for this orientation, one would expect a positive correlation between X-rays and UV. It is conceivable that one could be oriented such that the closing of the wind cone, inhibits our ability to see the collimated emission. In this case, one would expect a change in the ratio between hard and soft X-ray emission (the soft being more visible) accompanying a drop in $T_{\rm sph}$. This would result in an anti-correlation between $T_{\rm sph}$ and the UV brightness and a more complex correlation with spectral hardness.

For a fixed accretion rate, a change in the inclination of the disc/wind, driven by precession (e.g. Middleton et al. 2018, 2019b) would result in changes to the X-ray spectral colours similarly to as if the cone was closing (see Middleton et al. 2015b). In short, the X-ray emission should diminish, and the low frequency emission should become brighter, leading to an anti-correlation between the X-ray and UV emission (assuming the accretion rate is high enough for the wind photosphere to emit as such low energies.)

4.2.2 Irradiated outer disc

It has been suggested that the outer disc could be irradiated by X-ray emission from the inner regions after scattering by the wind (Sutton et al., 2013). As long as this irradiating SED has sufficient intensity above 2 keV, down-scattering of these photons can produce a UV-shoulder (Gierliński et al., 2008). Exploring irradiation requires radiative transfer calculations with RMHD simulations to follow the photons from the inner regions to the outer disc. However, such calculations have yet to be performed, and so I instead base my reasoning on a simplified picture (see figure 4.3).

Should the accretor be a black hole or low dipole field neutron star ($\leq 10^9 G$), then the spectrum from the inner regions is insensitive to accretion rate (Poutanen et al., 2007) due to mass loss at larger radii. If the ULX contains a high dipole field-strength neutron star (up to $\sim 10^{13}$G), the emergent spectrum above 2 keV is predicted to be dominated by emission from the accretion column with photons scattering to escape the magnetosphere (Mushtukov et al., 2017). Assuming the magnetospheric radius lies within $r_{\rm sph}$, then the accretion rate through the curtain is likely insensitive to the accretion rate at larger radii (see e.g. Chashkina et al. 2019; King & Lasota 2020). Assuming the intrinsic spectrum from the accretion column above 2 keV does not change, I need only consider the changes in the scattering medium between the outer disc and inner regions. As the accretion rate at large radius increases, the wind cone closes and the optical depth of the wind

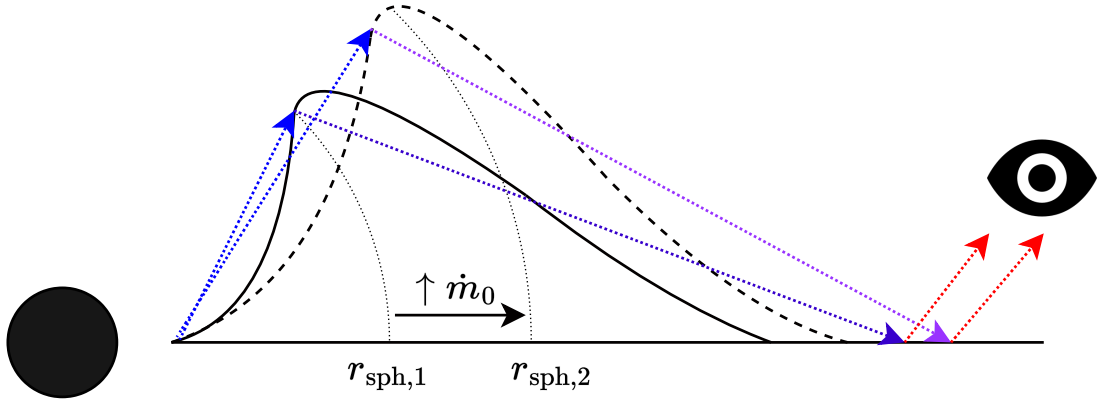

Figure 4.3: Schematic for the geometry of irradiated outer disc, an increase in the mass accretion rate results in the spherization radius moving outwards and decreasing in temperature. High energy photons arising from the inner parts of the accretion absorption and scattered by the large scale-height wind cone.

increases (see figure 4.3). There are more scatterings within the wind cone, which reduces the energy of those photons created in the inner regions; any escaping photons are therefore likely to be at lower energy and less likely to thermalise in the outer disc (Gierliński et al., 2008). The converse is true for a drop in accretion rate.

For a fixed observer inclination to the ULX but a varying accretion rate, the presence, or lack of, a correlation between the X-rays and UV depends once again on whether one can observe into the wind cone. Should one be able to view the innermost regions directly, then an increase in accretion rate will lead to an increase in X-ray flux (and decrease in T_{sph}) and a drop in UV flux, as fewer hard X-rays impinge on the outer disc. Should one view at higher inclinations then, as with the case above, one would expect a more complex change in spectral hardness (as described in Middleton et al. 2015b). For a fixed accretion rate, a change in inclination of the inner disc and wind will not change the UV emission (even if the wind were to tilt away from us, it would still irradiate the far side of the disc) and the UV and X-rays will be uncorrelated.

4.2.3 Irradiated companion star

A third option, distinct from the above, and proposed to explain the anti-phase optical super-orbital period seen in NGC 7793 P13 (Fürst et al., 2021), is that the X-ray cone sweeps over the companion star and hard X-rays thermalise in the outer layers leading to enhanced low frequency emission (Motch et al., 2014).

To explore this scenario, I simulate a ULX as a cone of X-ray emission irradiating a star at different orbital phases and different orientations relative to each other and the observer, an example of this is shown in figure 4.4 while the model code may be found in the link in the data availability statement at the end of this chapter. It is worth noting that in order for the wind cone to irradiate the star there would likely have to be a significant tilt to the normal axis of the wind

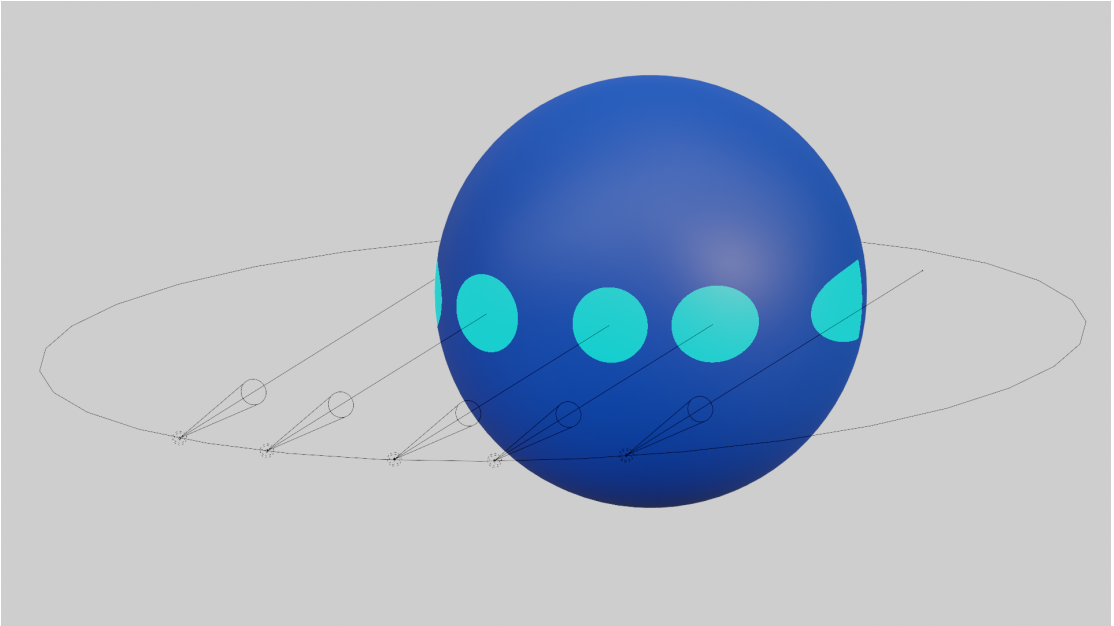

Figure 4.4: Schematic of irradiation of the secondary star as a tight cone of X-ray emission travelling on an elliptical orbit.

compared with respect to the normal of the axis of the orbit, otherwise only half opening angles of the cone that satisfy $\theta/2 > 90 - \arctan(R_\star/a)$ would be able to irradiate the star where $R_\star$ is the star radius and a the semi major axis. As we are only interested in the overall shape and presence of a correlation between the low frequency emission (from the stellar surface) and high frequency emission (from the ULX), I do not explore the microphysics of the thermalisation and ignore the role of limb darkening. Figure 4.5 shows how the observed irradiated area of the star can change as the cone of emission sweeps across the star's surface and reaches the edge.

We predict that in the absence of precession, the X-rays originating from a fixed orientation wind cone orbiting around a companion star would likely produce the same amount of observed X-rays for its entire orbit unless it was eclipsed by the companion. The 2D projected irradiated area on the star naturally depends strongly upon the observer's inclination, however, if we place the observer to be in the same inclination as the wind cone (i.e. in behind the middle cone and looking towards the star in fig 4.4) then the area that is responsible for reprocessing the X-ray emission into Optical/UV emission would increase in size as the cone first begins to intersect with the star (right to left in fig 4.5) then once the cone the fully intersects with the star the projected area will stay roughly the same for the entire transit until it reaches the other side of the star where it would once again begin to shrink. There is the possibility that if there is an extremely eccentric orbit, the increasing distance between the cone and the star could mean a larger circular area could be illuminated over the course of the orbit, this would mean that the UV/Optical emission would be constantly increasing or decreasing during the entire orbit, rather than for a circular orbit where a near-maximum would be

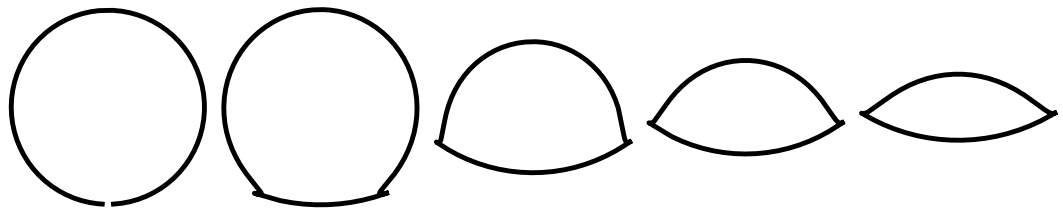

Figure 4.5: Projected irradiated area at $i = 0$ (in the frame of the cone) of a cone and a sphere. The area initially appears circular as the entire cone intersects with the star, however as the cone reaches the edge of the sphere, the projected irradiated area begins to decrease. The sphere in this example has a radius of $r = 2$ and is located at a distance of $z = 10$ above the cone the which has a full opening angle of $\theta = 15°$ and the transit is simulated for 5 values from $x = 0$ to $x = 2.5$.

reached and the circular area stays roughly the same for the transit. Once again, I stress that these predictions are heavily dependent on the observer's inclination.

4.3 Observations and Data Reduction

4.3.1 Sample Selection

To explore whether observations match any of the theoretical expectations summarised in Table 1, I begin by creating the sample. I crossmatch several ULX catalogues, (Earnshaw et al., 2019; Kovlakas et al., 2020; Bernadich et al., 2022; Walton et al., 2022) with the *Swift* Master Catalogue (`SWIFTMASTR`), accessible via HEASARC. For comparison for high signal-to-noise sources local to us, I also include three extensively studied Galactic sources, Swift J0243.6+6124 SS433 and V404 Cygni. Swift J0243.6+6124 is known to contain a magnetised neutron star and appear as a ULX (van den Eijnden et al., 2020), SS433 is widely considered to be an edge-on ULX (Fabrika 2004; Middleton et al. 2021) and V404 Cygni is a LMXB which reached around or just in excess of its Eddington luminosity during its 2015 outburst (Motta et al. 2017).

I locate all observations where the source lies within the nominal (23.6') XRT field-of-view. Due to the differences between the XRT and UVOT field-of-view, there is a mismatch between the number of observations in both bands. I place a requirement of 20 observations for a source to appear in my sample. For each source in my sample, I manually cross-matched all remaining sources with SIMBAD to obtain distances and positions. The final sample used for my analysis is shown in Table 4.3.

4.3.2 XRT Data Reduction

XRT data was extracted using the standard *Swift*/XRT processing pipeline (Evans et al., 2009), using the SIMBAD coordinates of the source, and the 'simple' centroid

Source Name	RA "h:m:s"	DEC "d:m:s"	λ	POS REF	D Mpc	D method	D ref
V404 Cygni	20 24 03.8254	+33 52 01.962	O	Gaia Collaboration (2018)	0.0023	parallax	Miller-Jones et al. (2009)
Swift J0243.6+6124	02 43 40.4252	+61 26 03.757	O	Gaia Collaboration (2020)	0.0055	parallax	Gaia Collaboration (2020)
SS433	19 11 49.5647	+04 58 57.827	O	Gaia Collaboration (2020)	0.0055		Blundell & Bowler (2004)
SMC X-3	00 52 05.6251	-72 26 04.228	O	Gaia Collaboration (2020)	0.0600	cepheid	Karachentsev et al. (2017)
IC10 X-1	00 20 29.09	+59 16 51.9	X	Bauer & Brandt (2004)	0.7943	redshift	Lianou et al. (2019)
M31 ULX-1	00 42 53.15	+41 14 22.9	X	Kaur et al. (2012)	0.8200	T-RDB	Karachentsev et al. (2017)
M33 ULX-1	01 33 50.8965	+30 39 36.630	O	Gaia Collaboration (2020)	0.9300	T-RDB	Karachentsev et al. (2017)
NGC300 ULX-1	00 55 04.86	-37 41 43.7	O	Barbon et al. (2008)	2.0230	redshift	Lianou et al. (2019)
NGC55 ULX	00 15 28.89	-39 13 18.8	X	Lin et al. (2012)	2.1100	T-RDB	Karachentsev et al. (2017)
IC342 ULX-1	03 45 55.612	+68 04 55.29	O	Feng & Kaaret (2008)	3.4356	redshift	Lianou et al. (2019)
IC342 ULX-2	03 46 15.61	+68 11 12.8	X	Heida et al. (2014)	3.4356	redshift	Lianou et al. (2019)
NGC4945 XMM-1	13 05 32.89	-49 27 34.1	X	Swartz et al. (2004)	3.4674	redshift	Lianou et al. (2019)
Holmberg II X-1	08 19 28.99	+70 42 19.4	X	Heida et al. (2014)	3.4674	redshift	Lianou et al. (2019)
M81 ULX-1	09 55 32.95	+69 00 33.6	X	Heida et al. (2014)	3.5975	redshift	Lianou et al. (2019)
M81 X-6	09 55 32.95	+69 00 33.6	X	Heida et al. (2014)	3.5975	redshift	Lianou et al. (2019)
M82 X-2	09 55 51.040	+69 40 45.49	X	Kaaret et al. (2006)	3.6141	redshift	Lianou et al. (2019)
NGC253 X-2	00 47 32.97	-25 17 50.2	X	Liu & Bregman (2005)	3.6983	redshift	Lianou et al. (2019)
NGC253 X-9	00 47 22.59	-25 20 50.9	X	Heida et al. (2014)	3.6983	redshift	Lianou et al. (2019)
NGC247 ULX-1	00 47 04.00	-20 47 45.7	X	Liu & Bregman (2005)	3.7200	T-RDB	Karachentsev et al. (2017)
NGC7793 P13	23 57 50.90	-32 37 26.6	X	Pannuti et al. (2011)	3.7325	redshift	Lianou et al. (2019)
Holmberg IX X-1	09 57 53.290	+69 03 48.20	O	Abazajian et al. (2009)	3.8500	T-RDB	Karachentsev et al. (2017)
NGC1313 X-1	03 18 20.00	-66 29 10.9	X	Heida et al. (2014)	4.2500		Tully et al. (2016)
NGC1313 X-2	03 18 22.00	-66 36 04.3	X	Liu & Bregman (2005)	4.2500		Tully et al. (2016)
NGC5204 ULX-1	13 29 38.62	+58 25 05.6	X	Heida et al. (2014)	4.5900	T-RDB	Karachentsev et al. (2017)
UGC6456 ULX	11 28 03.000	+78 59 53.41	O	Vinokurov et al. (2020)	4.6300	T-RDB	Karachentsev et al. (2017)
NGC4395 ULX-1	12 26 01.53	+33 31 30.6	X	Heida et al. (2014)	4.7600		Tully et al. (2016)
M83 ULX-1	13 37 05.13	-29 52 07.1	X	Long et al. (2014)	4.8978	redshift	Lianou et al. (2019)
M83 ULX-2	13 37 20.12	-29 53 47.7	X	Liu & Bregman (2005)	4.8978	redshift	Lianou et al. (2019)
NGC5408 ULX-1	14 03 19.63	-41 22 58.7	X	Heida et al. (2014)	5.3211	redshift	Lianou et al. (2019)
NGC6946 ULX-1	20 35 00.11	+60 09 08.5	X	Lin et al. (2012)	6.7298	redshift	Lianou et al. (2019)
NGC6946 ULX-3	20 35 00.74	+60 11 30.6	X	Swartz et al. (2004)	6.7298	redshift	Lianou et al. (2019)
M101 ULX-1	14 03 32.38	+54 21 03.0	X	Heida et al. (2014)	7.1121	redshift	Lianou et al. (2019)
NGC4559 ULX-1	12 35 51.71	+27 56 04.1	X	Heida et al. (2014)	7.1450	redshift	Lianou et al. (2019)
M51 ULX-7	13 30 01.01	+47 13 43.9	X	Heida et al. (2014)	7.6000	redshift	Cappellari et al. (2011)
NGC5585 ULX	14 19 39.39	+56 41 37.8	X	Heida et al. (2014)	7.8300		Tully et al. (2016)
NGC925 ULX-1	02 27 27.53	+33 34 42.9	X	Heida et al. (2014)	9.2045	redshift	Lianou et al. (2019)
NGC925 ULX-2	02 27 21.52	+33 35 00.8	X	Heida et al. (2014)	9.2045	redshift	Lianou et al. (2019)
NGC7090 ULX-3	21 36 31.94	-54 33 57.2	X	Lin et al. (2012)	9.5060	redshift	Lianou et al. (2019)
NGC5907 ULX	15 15 58.60	+56 18 10.0	X	Swartz et al. (2011)	17.2187	redshift	Lianou et al. (2019)
NGC1365 X-1	03 33 34.60	-36 09 35.0	X	Liu & Bregman (2005)	17.2982	redshift	Lianou et al. (2019)
NGC1365 X-2	03 33 41.85	-36 07 31.4	X/O	Strateva & Komossa (2009)	17.2982	redshift	Lianou et al. (2019)
NGC1042 ULX-1	02 40 25.62	-08 24 28.9	X	Lin et al. (2012)	19.2000		Oey et al. (2007)
ESO 243-49 HLX-1	01 10 28.30	-46 04 22.3	X	Webb et al. (2010)	115.3500		Tully et al. (2016)

Table 4.1: Position of Sources investigated in this chapter, sorted by host galaxy distance

method with a positional error of 1 arcsecond. I extract light curves in three bands, `full` ($0.3-10.0$keV), `soft` ($0.3-1.5$keV) and `hard` ($1.5-10.0$keV), with one bin per observation.

I set the minimum significance, defined as the counts in the source region divided by the square root of the counts in the background ($C_{src}/\sqrt{C_{bkg}}$), to the default value of 3, values that are not detected to this threshold are provided as upper limits, this is only for the `full` band observation data points.

The pipeline additionally calculates the hardness ratio defined as the ratio of soft and hard count rates $HR = C_{hard}/C_{soft}$, 1 sigma errors are provided for each of these measurements. I also extract summed spectra by combining all the observations for each source using the *Swift* XRT pipeline. The pipeline also includes `GOOD` and `BAD` values, which refers to whether or not the pipeline was able to obtain a centroid in a given snapshot, meaning that `BAD` values are potentially unreliable.

4.3.3 UVOT Data Reduction

UVOT data were processed locally using `HEASARC v6.29` and the latest CALDB for UVOT (November 8, 2021). I stacked all UVOT and XRT observations, combining them into a single image and manually inspected to identify any clear counterparts (see A.3). An example of one of the finding plots is shown in fig 4.6.

For each source, a circular extraction region with a radius of 5" was created centred on the *Swift* XRT position, while background regions were manually positioned in a contaminant-free location with a size of 15" as recommended by the UVOT data analysis manual[1]. The distances between the centres of the UVOT and XRT (SIMBAD) source regions as well as the position of the UVOT background regions are given in Table 4.3.3.

Level 2 UVOT images were processed locally using first the `uvotimsum` to combine all snapshot extensions, then I used `uvotsource` with a signal-to-noise threshold of 3 to obtain photometric magnitudes of my desired sources in a given observation. I then determined whether the source was detected using the `NSIGMA` column provided as output from `uvotsource`. All observations of a given source were then combined to produce a long term light-curve in all of the observed bands: U (3465 Å), B (4392 Å), V (5469 Å), UVW1 (2600 Å), UVM2 (2246 Å), UVW2 (1928 Å).

4.4 Analysis and Results

4.4.1 UV Counterparts

From the plots shown in A.3, unique UV counterparts are found with emission regions comparable to *Swift's* PSF in the sources:

- V404 Cygi
- SS 433
- M33 ULX-1
- Swift J0243.6+6124
- SMC X-3
- NGC300 ULX-1

[1] https://swift.gsfc.nasa.gov/analysis/UVOT_swguide_v2_2.pdf

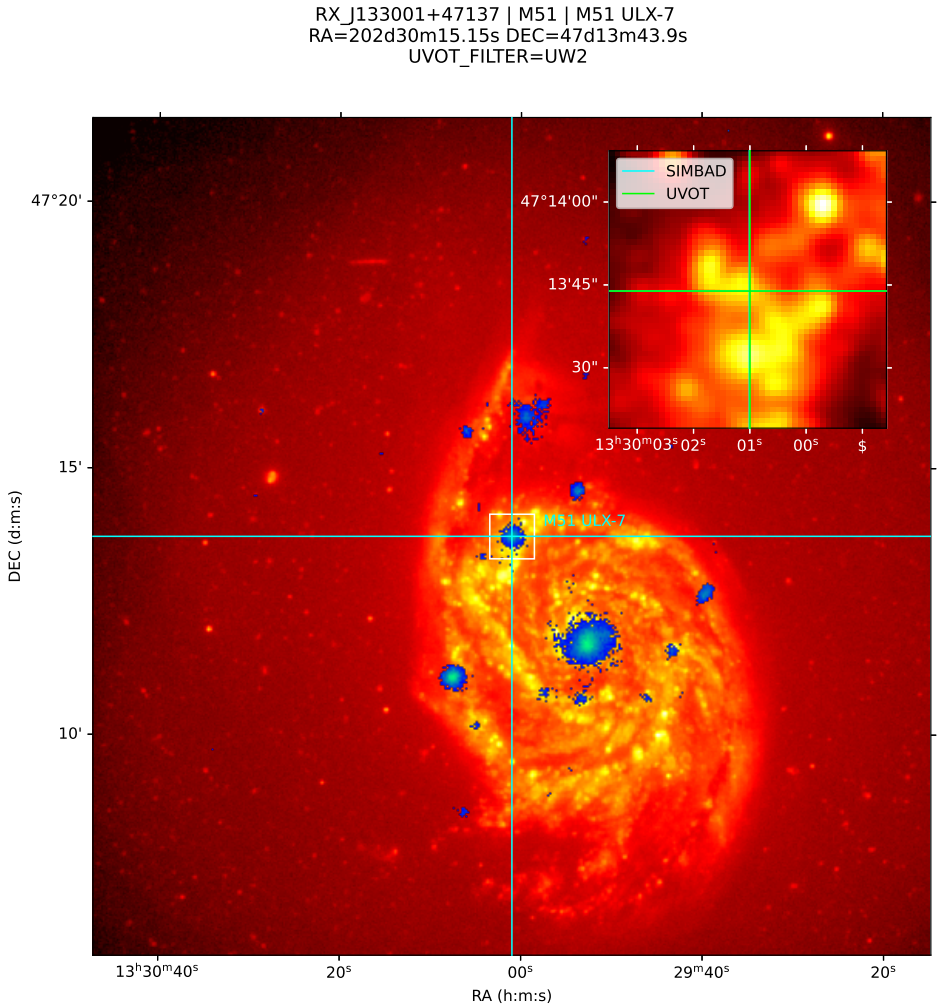

Figure 4.6: Finding plot for used M51 ULX-7 showing the stacked XRT image (blue) overlaid over the stacked UW2 image, the zoomed inset shows 50x50 pixel cutout with coordinates centred on the SIMBAD position.

Source Name	RA_{src}	DEC_{src}	r_{src} (")	Sep (")	RA_{bkg}	DEC_{bkg}	r_{bkg} (")
NGC247 ULX-1	11d45m55.4505s	-20d47m43.502s	5.000"	4.79757	11d43m12.006s	-20d45m46.68s	15.000"
M83 ULX-2	204d19m57.4095s	-29d53m48.465s	5.000"	3.9125	204d22m20.829s	-29d53m05.725s	15.000"
M82 X-2	148d57m34.6635s	69d40m46.014s	5.000"	3.83284	148d50m36.1125s	69d42m18.103s	15.000"
NGC4395 ULX-1	186d30m19.869s	33d31m31.001s	5.000"	2.60813	186d31m45.6855s	33d33m35.304s	15.000"
NGC5408 ULX-1	210d49m51.2505s	-41d22m58.475s	5.000"	2.44234	210d49m12.7815s	-41d21m21.149s	15.000"
NGC1365 X-1	53d25m27.75s	-36d07m31.4s	5.000"	2.39611	53d27m02.5575s	-36d11m12.87s	15.000"
NGC55 ULX	3d52m11.076s	-39d13m18.328s	5.000"	1.82646	3d42m45.894s	-39d15m56.003s	15.000"
NGC5204 ULX-1	202d24m35.901s	58d25m05.727s	5.000"	1.77807	202d18m52.11s	58d23m51.654s	15.000"
NGC925 ULX-2	36d50m02.7s	33d34m12.84s	5.000"	1.57024	36d51m20.862s	33d31m44.123s	15.000"
IC10 X-1	5d07m13.38s	59d16m51.728s	5.000"	1.55695	5d03m18.5235s	59d16m19.1s	15.000"
M31 ULX-1	10d43m18.264s	41d14m21.636s	5.000"	1.46483	10d42m57.597s	41d13m32.606s	15.000"
UGC6456 ULX	172d00m39.588s	78d59m54.407s	5.000"	1.43393	172d06m08.5155s	78d59m23.951s	15.000"
NGC1042 ULX-1	40d06m24.21s	-8d24m30.312s	5.000"	1.41033	40d08m48.231s	-8d26m19.825s	15.000"
M83 ULX-1	204d19m57.4095s	-29d53m48.465s	5.000"	1.32774	204d22m20.829s	-29d53m05.725s	15.000"
NGC6946 ULX-3	308d45m08.511s	60d11m30.857s	5.000"	1.32418	308d45m44.844s	60d12m43.789s	15.000"
NGC7090 ULX-3	324d05m41.1s	-54d32m33.8s	5.000"	1.30031	324d08m48.1785s	-54d35m19.085s	15.000"
NGC7793 P13	359d27m44.847s	-32d37m26.6s	5.000"	1.12591	359d27m02.3805s	-32d38m32.35s	15.000"
NGC4559 ULX-1	188d57m56.3235s	27d56m05.04s	5.000"	1.112	188d56m50.0115s	27d55m24.809s	15.000"
NGC925 ULX-1	36d50m02.7s	33d34m12.84s	5.000"	1.04992	36d51m20.862s	33d31m44.123s	15.000"
IC342 ULX-1	56d33m55.995s	68d11m12.956s	5.000"	1.01851	56d23m02.418s	68d03m57.414s	15.000"
SS433	287d57m24.4995s	4d58m57.844s	5.000"	1.00253	287d58m15.771s	4d58m11.821s	15.000"
ESO 243-49 HLX-1	17d37m03.129s	-46d04m21.989s	5.000"	1.00009	17d35m22.1505s	-46d05m38.793s	15.000"
NGC253 X-2	11d50m38.6085s	-25d20m51.039s	5.000"	0.817525	11d55m47.1855s	-25d19m46.772s	15.000"
NGC4945 XMM-1	196d23m14.181s	-49d27m33.623s	5.000"	0.699559	196d23m21.0345s	-49d29m15.285s	15.000"
IC342 ULX-2	56d33m55.995s	68d11m12.956s	5.000"	0.680777	56d23m02.418s	68d03m57.414s	15.000"
Swift J0243.6+6124	40d55m05.949s	61d26m04.367s	5.293"	0.659281	40d58m48.2775s	61d25m42.49s	15.000"
M33 ULX-1	23d27m43.107s	30d39m36.118s	5.000"	0.606133	23d31m36.5565s	30d32m34.497s	15.000"
M81 X-6	148d53m12.6255s	69d00m33.518s	5.000"	0.582129	148d53m12.6255s	69d00m33.518s	5.000"
NGC6946 ULX-1	308d45m08.511s	60d11m30.857s	5.000"	0.519501	308d45m44.844s	60d12m43.789s	15.000"
NGC1313 X-2	49d35m30.3705s	-66d36m03.832s	5.000"	0.502178	49d43m51.912s	-66d30m49.671s	15.000"
Holmberg II X-1	124d52m14.4795s	70d42m18.949s	5.000"	0.447656	124d38m32.2575s	70d42m00.598s	15.000"
NGC5907 ULX	228d59m38.4915s	56d18m09.743s	5.000"	0.38497	229d02m53.2485s	56d19m10.824s	15.000"
NGC1313 X-1	49d35m30.3705s	-66d36m03.832s	5.000"	0.356626	49d43m51.912s	-66d30m49.671s	15.000"
Holmberg IX X-1	149d28m18.603s	69d03m48.328s	5.000"	0.301148	149d32m44.61s	69d01m59.287s	15.000"
NGC253 X-9	11d50m38.6085s	-25d20m51.039s	5.000"	0.271102	11d55m47.1855s	-25d19m46.772s	15.000"
NGC300 ULX-1	13d46m12.75s	-37d41m43.5s	5.000"	0.231668	13d43m43.8225s	-37d33m54.238s	15.000"
M51 ULX-7	202d30m14.9565s	47d13m43.893s	5.000"	0.131046	202d34m23.7105s	47d13m23.018s	15.000"
V404Cyg	306d00m57.381s	33d52m01.962s	5.000"	0.0303212	306d00m02.1885s	33d53m08.251s	15.000"
SMC X-3	13d01m24.381s	-72d26m04.231s	5.000"	0.0166157	12d17m24.1335s	-72d23m41.825s	15.000"
NGC1365 X-2	53d25m27.75s	-36d07m31.4s	5.000"	0.0127784	53d27m02.5575s	-36d11m12.87s	15.000"
NGC5585 ULX	214d54m50.85s	56d41m37.8s	5.000"	0.00669034	214d54m22.119s	56d40m52.512s	15.000"
M101 ULX-1	210d53m05.7s	54d21m03s	5.000"	0.00495058	210d55m17.8635s	54d20m51.082s	15.000"

Table 4.2: Source and Background regions used for UVOT photometry. The Sep column provides the offset between the SIMBAD coordinates in table 4.3 and the source region used for extraction, the table is sorted by this column.

Source Name	U	B	V	UVM2	UVW1	UVW2	WHITE
V404Cyg	79 (52)	22 (22)	23 (24)	16 (3)	63 (8)	7 (0)	3 (3)
Swift J0243.6+6124	27 (27)	31 (31)	31 (36)	38 (38)	13 (13)	19 (19)	1 (1)
SS433	5 (5)	7 (7)	1 (1)	4 (0)	7 (7)	4 (4)	0
SMC X-3	12 (8)	3 (1)	2 (2)	11 (10)	6 (5)	2 (2)	0
IC10 X-1	119 (117)	0	0	5 (0)	3 (3)	3 (3)	0
M31 ULX-1	36 (31)	3 (2)	3 (2)	84 (28)	373 (354)	76 (65)	0
M33 ULX-1	4 (4)	0	0	3 (2)	5 (5)	2 (2)	0
NGC300 ULX-1	18 (18)	48 (48)	43 (49)	21 (21)	28 (28)	32 (32)	0
NGC55 ULX	20 (20)	3 (3)	3 (3)	29 (28)	36 (36)	15 (15)	0
IC342 ULX-1	11 (9)	1 (1)	1 (1)	12 (1)	10 (8)	13 (5)	0
IC342 ULX-2	9 (3)	1 (0)	1 (0)	12 (0)	10 (3)	13 (0)	0
Holmberg II X-1	98 (98)	3 (3)	3 (3)	31 (31)	52 (52)	46 (46)	0
NGC4945 XMM-1	3 (3)	3 (3)	3 (3)	39 (38)	22 (21)	36 (34)	0
M81 X-6	43 (36)	86 (84)	85 (77)	52 (40)	132 (127)	314 (300)	0
M82 X-2	81 (81)	41 (41)	41 (41)	108 (108)	100 (100)	98 (98)	0
NGC253 X-2	6 (4)	7 (7)	7 (7)	1 (1)	2 (2)	1 (1)	0
NGC253 X-9	6 (4)	7 (7)	7 (7)	1 (1)	2 (2)	1 (1)	0
NGC247 ULX-1	21 (20)	1 (1)	1 (1)	69 (69)	53 (53)	25 (25)	0
NGC7793 P13	258 (258)	2 (2)	2 (0)	25 (25)	14 (14)	12 (12)	0
Holmberg IX X-1	43 (41)	24 (14)	0	53 (51)	132 (129)	174 (172)	0
NGC1313 X-1	280 (278)	5 (5)	0	92 (92)	49 (49)	58 (58)	0
NGC1313 X-2	280 (264)	5 (3)	0	93 (91)	49 (49)	58 (57)	0
NGC5204 ULX-1	35 (35)	0	0	21 (21)	3 (3)	6 (6)	0
UGC6456 ULX	6 (6)	5 (5)	1 (2)	13 (13)	6 (6)	4 (4)	0
NGC4395 ULX-1	12 (12)	138 (129)	1 (1)	42 (42)	13 (13)	45 (45)	0
M83 ULX-2	31 (31)	6 (6)	6 (6)	20 (20)	10 (10)	8 (8)	0
M83 ULX-1	31 (31)	6 (6)	6 (6)	20 (20)	10 (10)	8 (8)	0
NGC5408 ULX-1	0	0	0	147 (147)	0	0	0
NGC6946 ULX-1	1 (1)	88 (87)	92 (91)	13 (7)	1 (1)	1 (0)	0
NGC6946 ULX-3	1 (1)	88 (83)	92 (79)	13 (5)	1 (1)	1 (0)	0
M101 ULX-1	1 (1)	57 (57)	55 (55)	23 (13)	5 (4)	8 (6)	0
M51 ULX-7	56 (56)	66 (66)	1 (1)	58 (58)	33 (33)	47 (47)	0
NGC5585 ULX	0	0	0	16 (15)	0	0	0
NGC4559 ULX-1	15 (15)	7 (7)	7 (9)	12 (12)	46 (46)	10 (10)	1 (1)
NGC925 ULX-1	16 (16)	0	0	29 (29)	27 (27)	26 (26)	0
NGC925 ULX-2	16 (16)	0	0	29 (29)	27 (27)	26 (26)	0
NGC7090 ULX-3	10 (10)	2 (2)	2 (2)	10 (10)	8 (8)	4 (4)	0
NGC5907 ULX	147 (147)	0	0	161 (160)	98 (97)	104 (104)	0
NGC1365 X-2	9 (9)	62 (62)	60 (64)	51 (51)	4 (4)	12 (12)	1 (1)
NGC1365 X-1	9 (8)	62 (61)	60 (57)	51 (50)	4 (3)	12 (12)	1 (1)
NGC1042 ULX-1	8 (6)	5 (2)	5 (2)	2 (1)	4 (2)	4 (3)	0
ESO 243-49 HLX-1	0	0	0	0	0	0	0

Table 4.3: Number of observations in each UVOT filter with the number of observations with `NSIGMA` > 3 in brackets.

Source Name	U	B	V	UVM2	UVW1	UVW2	WHITE
V404Cyg	11.03 ± 32.36	32.36 ± 54.06	31.13 ± 52.40	0.06 ± 0.14	0.04 ± 0.18	0.01 ± 0.01	11.44 ± 3.00
Swift J0243.6+6124	78.89 ± 6.88	112.67 ± 7.43	88.14 ± 4.86	1.94 ± 0.17	12.90 ± 0.69	4.19 ± 0.49	310.10 ± 0.00
SS433	1.92 ± 0.67	14.36 ± 2.54	14.65 ± 0.00	-0.00 ± 0.00	0.25 ± 0.08	0.08 ± 0.01	0
SMC X-3	48.59 ± 34.44	7.75 ± 10.96	6.96 ± 6.96	27.60 ± 8.86	31.10 ± 17.58	44.31 ± 1.02	0
IC10 X-1	0.36 ± 0.06	0	0	0.01 ± 0.00	0.09 ± 0.01	0.02 ± 0.00	0
M31 ULX-1	1.86 ± 0.90	2.76 ± 1.97	2.87 ± 2.04	0.03 ± 0.02	0.32 ± 0.08	0.10 ± 0.09	0
M33 ULX-1	36.62 ± 10.01	0	0	4.25 ± 3.01	13.01 ± 0.26	10.84 ± 0.19	0
NGC300 ULX-1	2.33 ± 0.52	5.75 ± 2.91	2.84 ± 1.37	0.27 ± 0.04	0.63 ± 0.13	0.42 ± 0.07	0
NGC55 ULX	2.11 ± 0.43	3.00 ± 0.71	2.00 ± 0.53	0.29 ± 0.08	0.60 ± 0.07	0.49 ± 0.05	0
IC342 ULX-1	0.36 ± 0.30	0.87 ± 0.00	0.63 ± 0.00	0.01 ± 0.02	0.10 ± 0.06	0.02 ± 0.02	0
IC342 ULX-2	-0.10 ± 0.87	0.22 ± 0.00	0.01 ± 0.00	-0.01 ± 0.03	0.01 ± 0.08	-0.02 ± 0.04	0
Holmberg II X-1	4.62 ± 0.25	3.66 ± 0.20	1.01 ± 0.10	2.01 ± 0.19	3.04 ± 0.38	3.74 ± 0.48	0
NGC4945 XMM-1	1.93 ± 0.10	4.57 ± 0.10	3.49 ± 0.16	0.11 ± 0.03	0.34 ± 0.16	0.16 ± 0.08	0
M81 X-6	0.86 ± 0.41	1.82 ± 0.57	1.11 ± 0.35	0.12 ± 0.07	0.34 ± 0.09	0.26 ± 0.06	0
M82 X-2	11.67 ± 0.31	28.89 ± 1.47	27.75 ± 1.34	0.35 ± 0.03	2.02 ± 0.08	0.78 ± 0.04	0
NGC253 X-2	4.23 ± 3.01	22.69 ± 0.65	19.62 ± 1.07	0.10 ± 0.00	0.98 ± 0.08	0.32 ± 0.00	0
NGC253 X-9	1.92 ± 1.36	6.36 ± 0.16	4.00 ± 0.36	0.30 ± 0.00	0.75 ± 0.05	0.49 ± 0.00	0
NGC247 ULX-1	2.17 ± 0.11	2.69 ± 0.00	1.16 ± 0.00	0.67 ± 0.06	1.00 ± 0.06	0.95 ± 0.09	0
NGC7793 P13	1.31 ± 0.09	2.09 ± 0.19	-0.01 ± 0.07	0.26 ± 0.03	0.49 ± 0.06	0.41 ± 0.07	0
Holmberg IX X-1	0.56 ± 0.38	2.45 ± 2.76	0	0.08 ± 0.03	0.21 ± 0.11	0.17 ± 0.05	0
NGC1313 X-1	5.05 ± 0.65	8.51 ± 0.38	0	1.06 ± 0.05	1.97 ± 0.08	1.68 ± 0.13	0
NGC1313 X-2	0.38 ± 0.46	0.40 ± 0.08	0	0.12 ± 0.02	0.21 ± 0.03	0.21 ± 0.03	0
NGC5204 ULX-1	5.69 ± 0.12	0	0	1.67 ± 0.09	2.56 ± 0.04	2.61 ± 0.07	0
UGC6456 ULX	1.94 ± 0.11	1.75 ± 0.14	0.87 ± 0.00	0.80 ± 0.07	1.07 ± 0.05	1.28 ± 0.02	0
NGC4395 ULX-1	1.13 ± 0.06	1.28 ± 0.23	0.57 ± 0.00	0.38 ± 0.03	0.61 ± 0.04	0.66 ± 0.05	0
M83 ULX-2	5.01 ± 0.93	13.32 ± 2.03	9.00 ± 1.26	0.31 ± 0.06	1.06 ± 0.25	0.55 ± 0.17	0
M83 ULX-1	3.85 ± 0.66	9.87 ± 1.06	6.95 ± 0.69	0.23 ± 0.07	0.83 ± 0.18	0.41 ± 0.13	0
NGC5408 ULX-1	0	0	0	2.08 ± 0.16	0	0	0
NGC6946 ULX-1	1.44 ± 0.00	3.35 ± 0.46	2.31 ± 0.25	0.08 ± 0.02	0.33 ± 0.00	0.20 ± 0.00	0
NGC6946 ULX-3	0.85 ± 0.00	1.21 ± 0.35	0.68 ± 0.26	0.05 ± 0.04	0.23 ± 0.00	0.15 ± 0.00	0
M101 ULX-1	1.78 ± 0.00	2.49 ± 0.29	1.23 ± 0.18	0.23 ± 0.17	0.55 ± 0.33	0.59 ± 0.18	0
M51 ULX-7	11.47 ± 0.52	13.63 ± 0.70	6.58 ± 0.00	3.44 ± 0.25	5.65 ± 0.41	5.07 ± 0.45	0
NGC5585 ULX	0	0	0	0.12 ± 0.02	0	0	0
NGC4559 ULX-1	2.21 ± 0.07	1.90 ± 0.07	0.59 ± 0.15	0.97 ± 0.12	1.36 ± 0.08	1.49 ± 0.12	1.65 ± 0.00
NGC925 ULX-1	1.20 ± 0.05	0	0	0.33 ± 0.05	0.52 ± 0.05	0.51 ± 0.05	0
NGC925 ULX-2	2.20 ± 0.11	0	0	0.37 ± 0.03	0.71 ± 0.03	0.57 ± 0.04	0
NGC7090 ULX-3	2.49 ± 0.12	5.43 ± 0.08	3.09 ± 0.19	0.29 ± 0.02	0.71 ± 0.05	0.48 ± 0.03	0
NGC5907 ULX	1.41 ± 0.06	0	0	0.09 ± 0.01	0.28 ± 0.08	0.16 ± 0.02	0
NGC1365 X-2	9.77 ± 0.66	11.55 ± 0.73	4.88 ± 0.45	2.53 ± 0.17	4.32 ± 0.42	4.22 ± 0.24	57.10 ± 0.00
NGC1365 X-1	1.06 ± 0.16	2.81 ± 0.37	1.51 ± 0.26	0.13 ± 0.02	0.28 ± 0.06	0.24 ± 0.02	16.92 ± 0.00
NGC1042 ULX-1	0.30 ± 0.13	1.51 ± 2.05	0.82 ± 1.11	0.05 ± 0.05	0.08 ± 0.08	0.10 ± 0.06	0
ESO 243-49 HLX-1	0	0	0	0	0	0	0

Table 4.4: Mean count rate and 1 sigma errors in each UVOT filter.

Source Name	N_{obs}	N_{UL}	N_{BAD}	N_{GOOD}	full	soft	hard	HR
V404Cyg	190	21	36	154	94.29 ± 755.62	26.73 ± 181.03	89.78 ± 660.56	5.17 ± 9.01
Swift J0243.6+6124	127	6	23	104	394.58 ± 847.88	66.34 ± 150.92	329.55 ± 700.15	8.68 ± 6.00
SS433	33	2	3	30	2.03 ± 1.12	0.36 ± 0.15	1.67 ± 0.99	4.33 ± 1.29
SMC X-3	413	217	259	154	5.47 ± 9.97	2.02 ± 3.83	3.46 ± 6.21	2.74 ± 1.41
IC10 X-1	145	7	29	116	0.05 ± 0.02	0.02 ± 0.01	0.03 ± 0.01	1.76 ± 0.72
M31 ULX-1	610	567	581	29	0.18 ± 0.30	0.01 ± 0.00	-0.00 ± 0.00	-0.14 ± 0.33
M33 ULX-1	27	0	0	27	0.53 ± 0.08	0.26 ± 0.06	0.27 ± 0.03	1.09 ± 0.11
NGC300 ULX-1	164	77	0	164	0.04 ± 0.14	0.01 ± 0.02	0.02 ± 0.09	0.65 ± 2.33
NGC55 ULX	186	2	8	178	0.07 ± 0.03	0.05 ± 0.02	0.02 ± 0.01	0.41 ± 0.17
IC342 ULX-1	52	0	4	48	0.11 ± 0.06	0.02 ± 0.01	0.09 ± 0.05	3.67 ± 0.97
IC342 ULX-2	51	0	5	46	0.06 ± 0.03	0.00 ± 0.00	0.05 ± 0.03	8.28 ± 39.39
Holmberg II X-1	231	7	4	227	0.16 ± 0.08	0.10 ± 0.05	0.06 ± 0.03	0.54 ± 0.24
NGC4945 XMM-1	145	7	29	116	0.05 ± 0.02	0.02 ± 0.01	0.03 ± 0.01	1.76 ± 0.72
M81 X-6	706	28	57	649	0.06 ± 0.10	0.02 ± 0.01	0.03 ± 0.02	1.57 ± 1.05
M82 X-2	429	9	0	429	1.91 ± 0.41	1.20 ± 0.25	0.71 ± 0.21	0.60 ± 0.16
NGC253 X-2	17	0	3	14	0.15 ± 0.04	0.07 ± 0.02	0.08 ± 0.03	1.02 ± 0.24
NGC253 X-9	15	1	5	10	0.02 ± 0.01	0.01 ± 0.01	0.01 ± 0.01	0.80 ± 0.62
NGC247 ULX-1	182	7	65	117	0.02 ± 0.01	0.02 ± 0.01	0.00 ± 0.00	0.08 ± 0.09
NGC7793 P13	363	85	129	234	0.07 ± 0.03	0.03 ± 0.01	0.04 ± 0.02	1.66 ± 0.61
Holmberg IX X-1	702	5	9	693	0.28 ± 0.13	0.12 ± 0.05	0.16 ± 0.08	1.35 ± 0.30
NGC1313 X-1	510	2	7	503	0.11 ± 0.06	0.05 ± 0.03	0.06 ± 0.04	1.08 ± 0.30
NGC1313 X-2	510	5	53	457	0.06 ± 0.03	0.03 ± 0.01	0.04 ± 0.02	1.37 ± 0.62
NGC5204 ULX-1	79	1	3	76	0.06 ± 0.02	0.04 ± 0.01	0.02 ± 0.01	0.60 ± 0.20
UGC6456 ULX	35	12	23	12	0.03 ± 0.02	0.02 ± 0.01	0.02 ± 0.01	1.58 ± 1.80
NGC4395 ULX-1	261	23	118	143	0.03 ± 0.01	0.02 ± 0.01	0.00 ± 0.00	0.15 ± 0.13
M83 ULX-2	98	6	29	69	0.02 ± 0.01	0.01 ± 0.01	0.01 ± 0.01	0.68 ± 0.31
M83 ULX-1	99	4	59	40	0.04 ± 0.03	0.03 ± 0.02	0.01 ± 0.01	0.56 ± 0.50
NGC5408 ULX-1	499	4	20	479	0.08 ± 0.02	0.06 ± 0.02	0.02 ± 0.01	0.29 ± 0.11
NGC6946 ULX-1	119	45	117	2	0.02 ± 0.00	0.01 ± 0.00	0.01 ± 0.00	0.57 ± 0.12
NGC6946 ULX-3	119	1	5	114	0.04 ± 0.02	0.03 ± 0.01	0.02 ± 0.01	0.61 ± 0.24
M101 ULX-1	117	1	8	109	0.04 ± 0.02	0.03 ± 0.01	0.02 ± 0.01	0.60 ± 0.28
M51 ULX-7	318	116	143	175	0.02 ± 0.01	0.01 ± 0.00	0.01 ± 0.01	0.72 ± 2.02
NGC5585 ULX	16	3	14	2	0.02 ± 0.00	0.01 ± 0.00	0.01 ± 0.00	2.14 ± 1.30
NGC4559 ULX-1	117	1	8	109	0.04 ± 0.02	0.03 ± 0.01	0.02 ± 0.01	0.60 ± 0.28
NGC925 ULX-1	98	0	7	91	0.05 ± 0.03	0.02 ± 0.01	0.03 ± 0.02	1.53 ± 0.50
NGC925 ULX-2	98	7	59	39	0.02 ± 0.00	0.01 ± 0.00	0.01 ± 0.00	1.35 ± 0.69
NGC7090 ULX-3	34	15	34	0	nan ± nan	nan ± nan	nan ± nan	nan ± nan
NGC5907 ULX	578	221	501	77	0.03 ± 0.06	0.01 ± 0.06	0.02 ± 0.01	2.99 ± 6.04
NGC1365 X-2	139	48	139	0	nan ± nan	nan ± nan	nan ± nan	nan ± nan
NGC1365 X-1	139	48	139	0	nan ± nan	nan ± nan	nan ± nan	nan ± nan
NGC1042 ULX-1	21	1	13	8	0.03 ± 0.01	0.02 ± 0.01	0.02 ± 0.00	1.11 ± 0.58
ESO 243-49 HLX-1	626	416	546	80	0.03 ± 0.01	0.03 ± 0.01	0.00 ± 0.00	0.08 ± 0.08

Table 4.5: XRT Number of observations, upper limits GOOD and BAD. full, soft, hard band count rates as well as hardness ratio values with 1 sigma errors calculated over the GOOD subset are shown

- NGC7793 P13 (dim)
- NGC6946 ULX-3
- NGC5585 ULX (dim)
- NGC1365 X-2

Many of my sources appear in or near regions of extended UV emission these sources are:

- NGC4945 XMM-1
- Holmberg II X-1
- M81 X-6
- M82 X-2
- NGC253 X-2
- Holmberg IX X-1
- NGC1313 X-2
- NGC5204 ULX-1
- UGC6456 ULX
- NGC6946 ULX-1
- NGC4395 ULX-1
- NGC4559 ULX-1
- M51 ULX-7
- NGC925 ULX-1
- NGC925 ULX-2

Sources that do not display strong UV emission in the images, either extended or point-like are:

- IC10 X-1
- M31 ULX-1
- IC342 ULX-1
- IC342 ULX-2
- NGC253 X-9
- NGC247 ULX-1
- NGC1313 X-1
- M83 ULX-1
- M83 ULX-2
- NGC5408 ULX-1
- M101 ULX-1
- NGC1365 X-1
- NGC1042 ULX-1
- ESO 243-49 HLX-1

Three sources in my sample appear in edge-on galaxies and the UV observations are heavily confused for these systems:

- NGC55 ULX
- NGC7090 ULX-3
- NGC5907 ULX

One particular source of interest is NGC1365 X-2 as it is the most distant source ($d \sim 17$ Mpc) to show point-like UV emission in my sample. This source has only been studied in two publications (see Soria et al. 2009; Strateva & Komossa 2009), and is known to be highly variable in the X-rays, spending most of its time below the XRT detection threshold. To examine the nature of the source I used a James Webb Space Telescope (JWST) (Gardner et al., 2006) observation of the great barred spiral galaxy using the Mid-Infrared Instrument (MIRI) camera which can be seen in figure 4.7. Although the JWST observation is in the mid-infrared, a region of hot gas $\sim$ 200 pc across is visible. It is possible that point-like UV emission observed by *Swift* is likely just a poorly resolved region of this extended hot gas cloud and or a summation of the emission from the star forming region. The geometry of the emission region does seem to be centred on X-ray coordinates and so could possibly be associated with the source itself, however, more detailed studies would be required to confirm this.

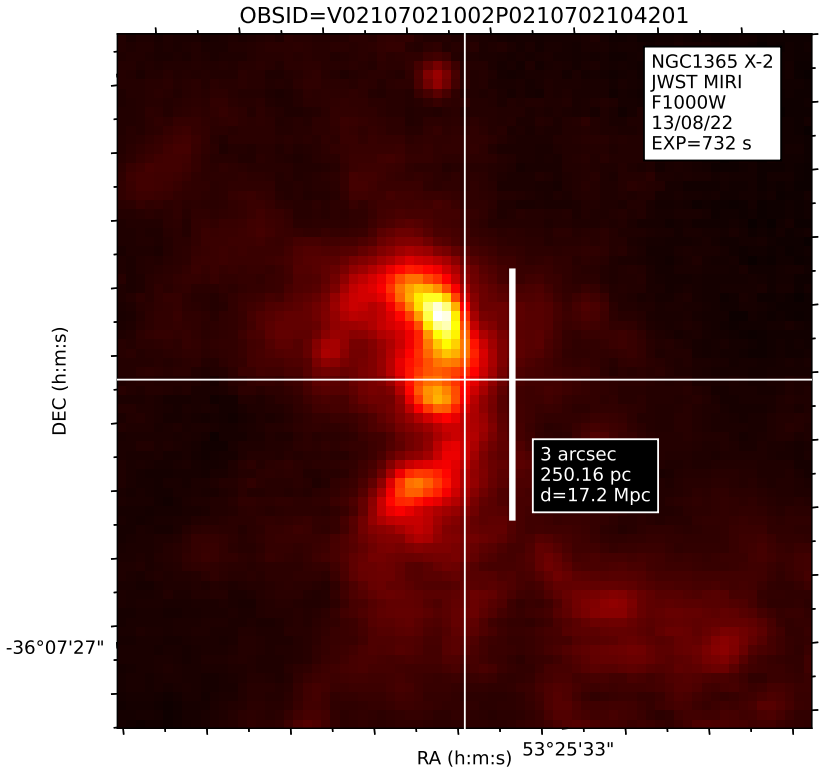

Figure 4.7: JWST MIRI observation 21002P0210702104201 in the F10000W filter (10 Å) of the region surrounding NGC1365 X-2 showing an extended region of gas roughly centred on the X-ray position of the ULX. The vertical white bar shows a scale of 3".

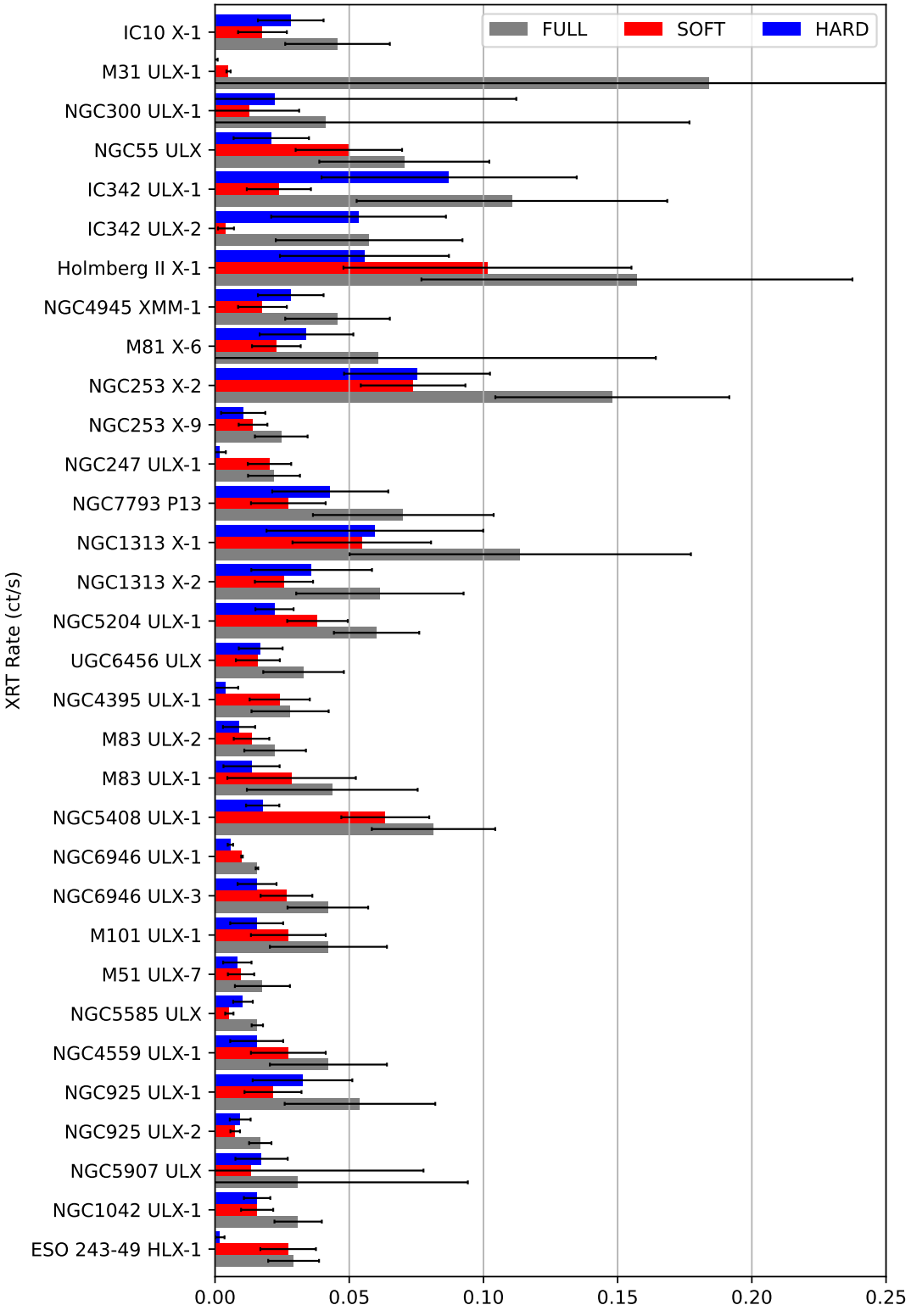

Figure 4.8: Mean XRT count for `GOOD` observations rates for sources with rates < 0.25 ct/s. Error bars correspond to 1 sigma calculated over all observations. For the full list see table 4.3.3.

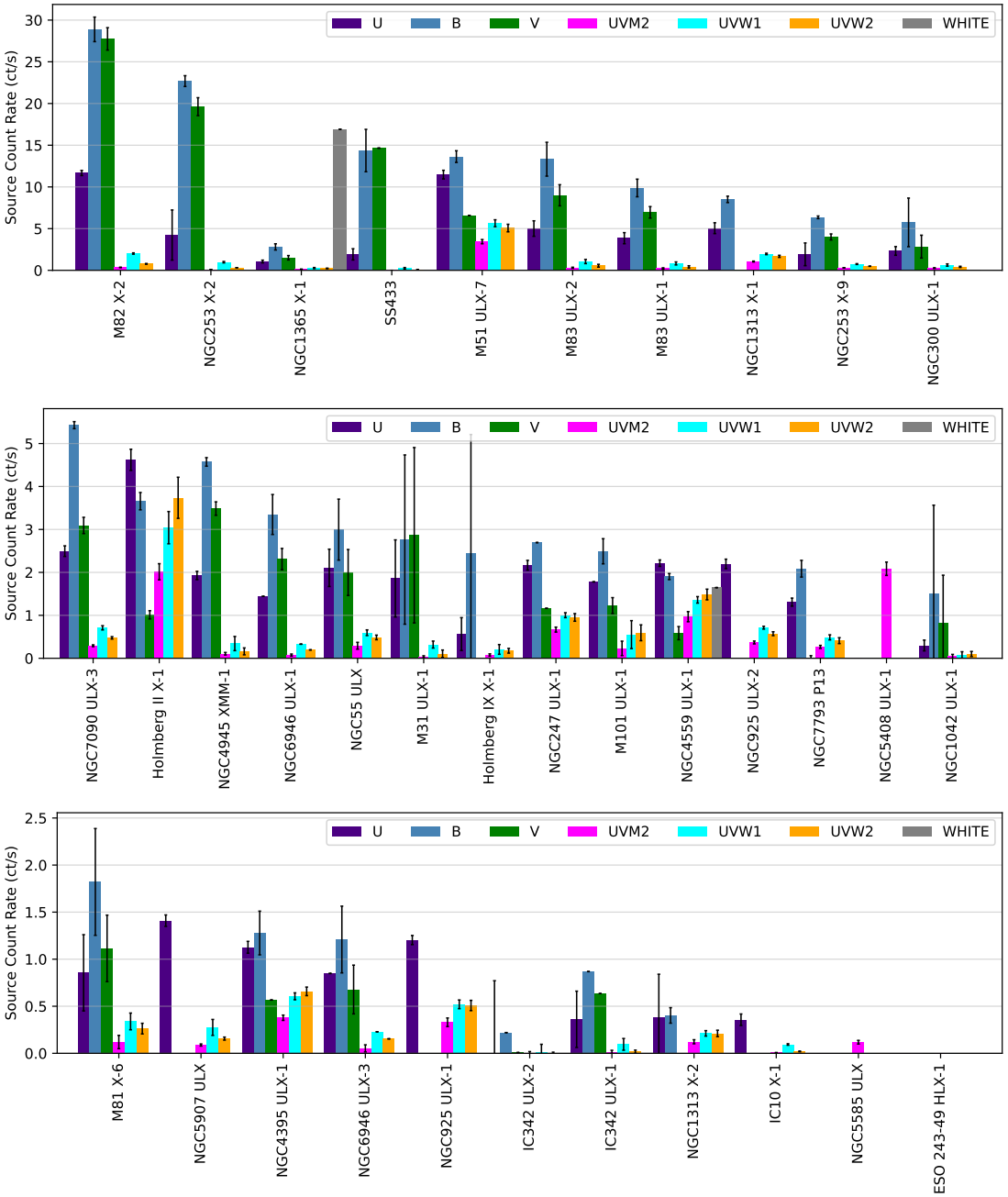

Figure 4.9: Mean UVOT count rates for some sources in the sample. Error bars correspond to 1 sigma calculated over all observations. For the full list see table 4.3.3.

4.4.2 Testing for linear X-ray/UV correlations

To test for linear correlations between the X-ray and UVOT light curves I employ the following method: for each observation data point, I sampled the 1 sigma errors in both the XRT and UVOT bands assuming Gaussian distributions, if the observation contained an upper limit, the data point was sampled assuming a uniform distribution between 0 and the upper limit. This sampling provides a realization of the light curve with the same time sampling as the original.

I then performed a least-squares fit with a straight line of the form $y = mx + c$ to the resultant sampled data points, as well as calculated the Pearson correlation coefficient r given by equation 4.2.

$$r = \frac{\sum_{i=1}^{n}(x_i - \bar{x})(y_i - \bar{y})}{\sqrt{\sum_{i=1}^{n}(x_i - \bar{x})^2}\sqrt{\sum_{i=1}^{n}(y_i - \bar{y})^2}} \tag{4.2}$$

where x_i and y_i are the ith values in the sample, while $\bar{x}$ and $\bar{y}$ the means over all the n data points.

This process was then repeated 10,000 times to obtain posterior distributions for the three fitted parameters, r, m and c, from which the mean and standard deviation were calculated.

To assess how well constrained the distribution on the fit parameters are, I calculate the inverse coefficient of variation (ICV) (eq 4.3) by dividing the mean of the fit parameters ($\overline{\text{par}}$) by its standard deviation (σ_{par}). The absolute value of $\overline{\text{par}}$ may be interpreted as a significance value, with higher values corresponding to more strongly peaked distributions.

$$\hat{\gamma}_{\text{par}} = \overline{\text{par}}/\sigma_{\text{par}} \tag{4.3}$$

Where $\overline{\text{par}}$ is the mean of one of the fit parameters (m, c or r), and σ_{par} is the standard deviation of the parameter. A higher value of $\hat{\gamma}$ implies that the distribution has less scatter.

Simulations were carried out for the over the grid of the four X-ray bands (`full`, `soft`, `hard`, `HR`), and the six UVOT filters. Simulations were additionally carried out including and excluding `BAD` and upper limit data points (for the XRT `full` band), a filter was imposed for values $\pm 5\sigma$ on both the UVOT and XRT count rate prior to simulating.

The above grid means that a single source may have a total of $1 \times 6 \times 2 \times 2 = 24$ possible simulation combinations for the `full` XRT band and $3 \times 6 \times 2 = 36$ for the remaining XRT bands (`hard`, `soft` and `HR`). These amount to a maximum total of 60 correlations to consider per source, assuming that the source has been visited in all UVOT bands and its XRT light curves contain both `BAD` and upper limit data points. In practice, since this is not the case and the total number of simulations on each source is almost always lower than 60.

Figure 4.10 shows the mean value of the slope m and the ICV of the Pearson correlation coefficient ($\hat{\gamma}_r$) over all of our simulations. Sources appear multiple times on the plot due to the aforementioned grid over the different XRT and UVOT light curves. The distance from the centre in this parameter space may provide an indication that a correlation may exist, the upper right would correspond to

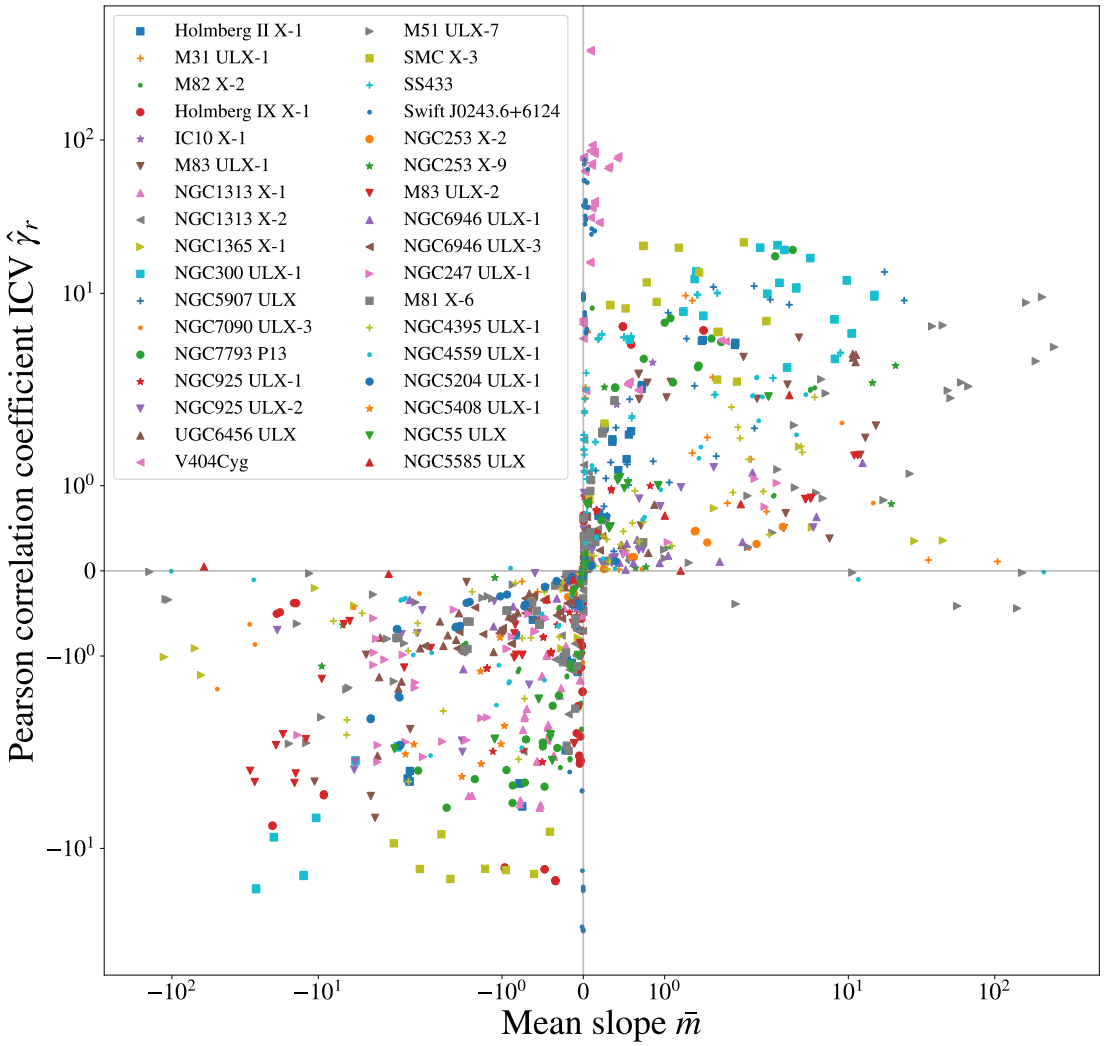

Figure 4.10: Mean slope $\bar{m}$ (x) vs the inverse coefficient of variation of the Pearson correlation coefficient $\hat{\gamma}_r$ for all simulations, the axis are plotting in log units.

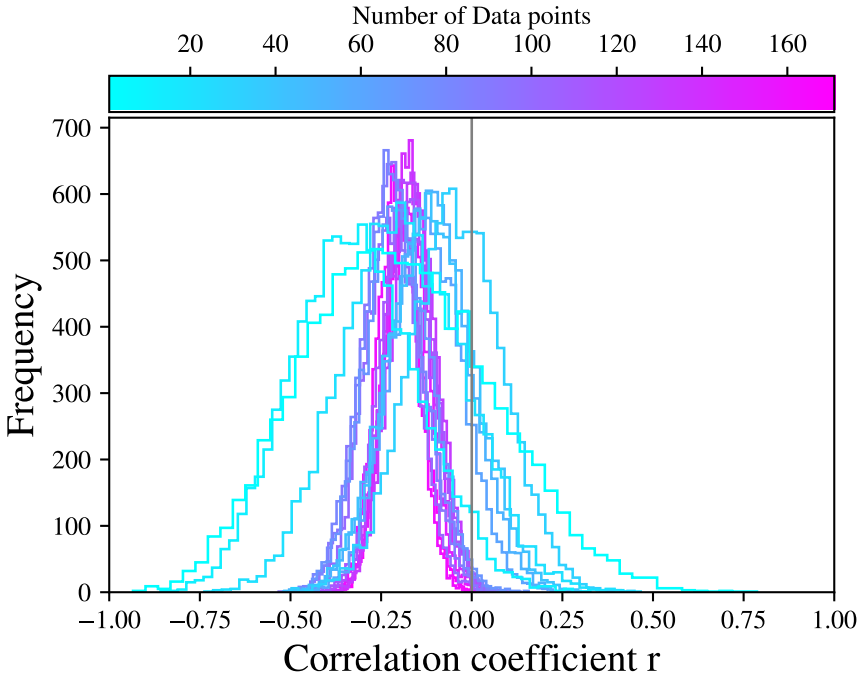

Figure 4.11: Shows the effect on the distribution of r by removing 10 data points at a time from the joined (`full`-U) light curve of NGC7793 P13. We can see that the distribution becomes less constrained as the number of data points falls.

positive correlations, the lower left to negative, however as I will demonstrate figure 4.10 is not sufficient to determine this.

A more informative visualisation may be obtained by plotting the actual values obtained from the 10,000 simulations in the parameter space. Doing so for Holmberg IX, we obtain figure 4.12, (note here we have simply plotted r on the y-axis and not $\hat{\gamma}_r$) The plot shows four panels, each corresponding to one of the four X-ray bands, with the "include bad" and "include UL" parameters listed at the top of each plot. Plotted are the values obtained from the 10,000 simulation fits in the UVOT bands, the numbers next to the filter names follow the form to $N_{\rm obs}(N_{\rm bad},N_{\rm UL})$ which are the number of observations, bad and upper limit data points in the fit data. One consideration when obtaining constraints via our approach of re-sampling the light curves is that the number of observations (i.e. $N_{\rm obs}$ in the light curve can significantly affect how strongly constrained a given correlation is, this can be visualised in figure 4.11 which shows the effect on the distribution of the correlation coefficient r as datapoints are removed.

From figure 4.12 it may be seen that the U band and UVW1 bands are distributed entirely in one quadrant, indicating that all of the performed fits ended up providing either a positive or a negative correlation, this is in contrast with UVM2 and UVW1 where the distributions cross the centre point meaning that some realisations provided both positive and negative correlations.

Figure 4.13 shows the light curves and fit results for Holmberg IX X-1 in the `full` band UVW1 filter, i.e. the blue cyan distribution in upper left panel of figure 4.12. By eye, it may be seen that the X-ray appears high when the UV is

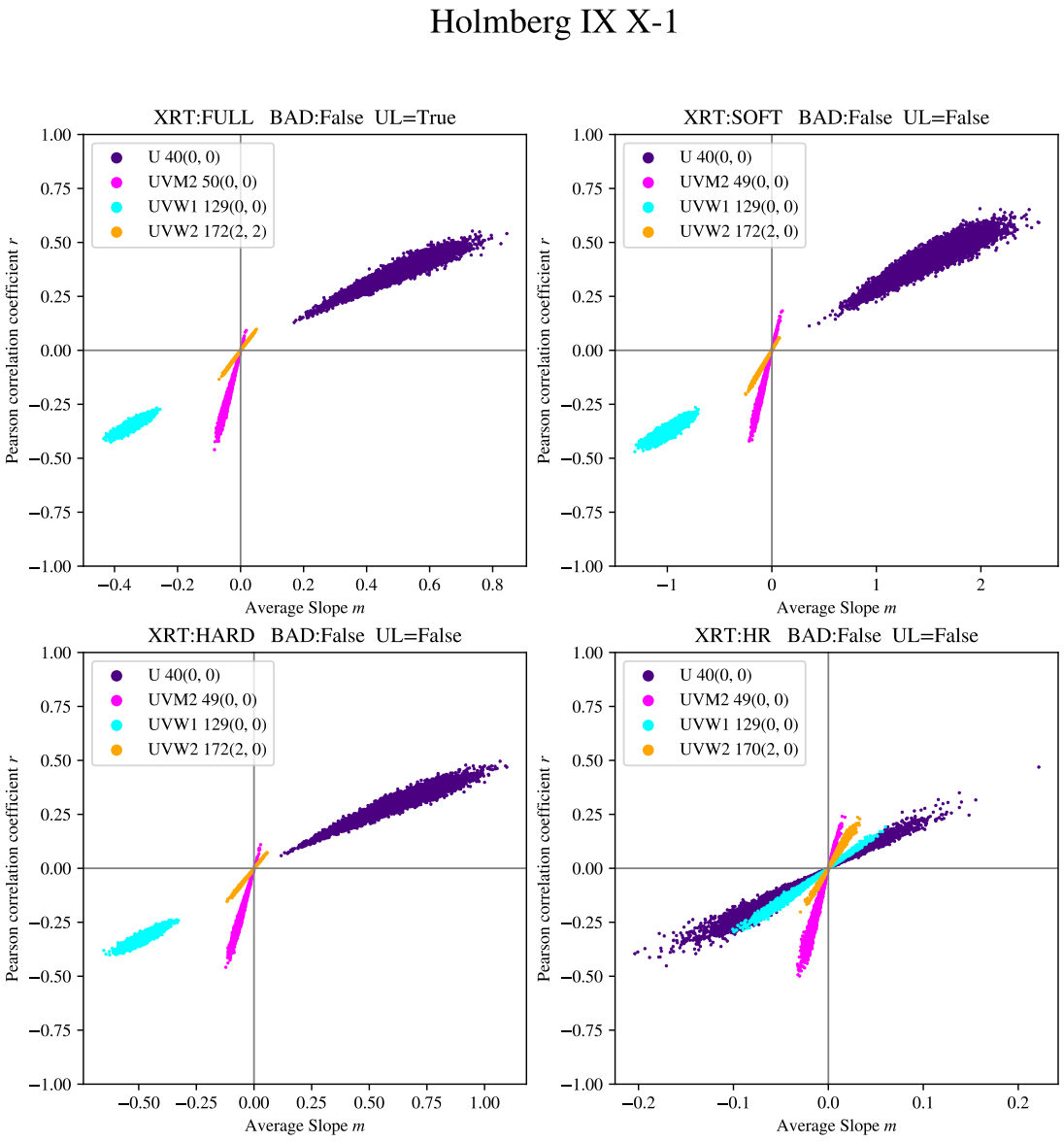

Figure 4.12: Distribution of fit parameters m and r for Holmberg IX X-1 obtained from 10,000 light curve samples. Each panel corresponds to a different X-ray band shown at the top of each figure, the correlation against the UVOT filters are colour coded and shown in the legend of each plot. The numbers next to the UVOT filters correspond to $N_{\rm obs}(N_{\rm bad},N_{\rm UL})$.

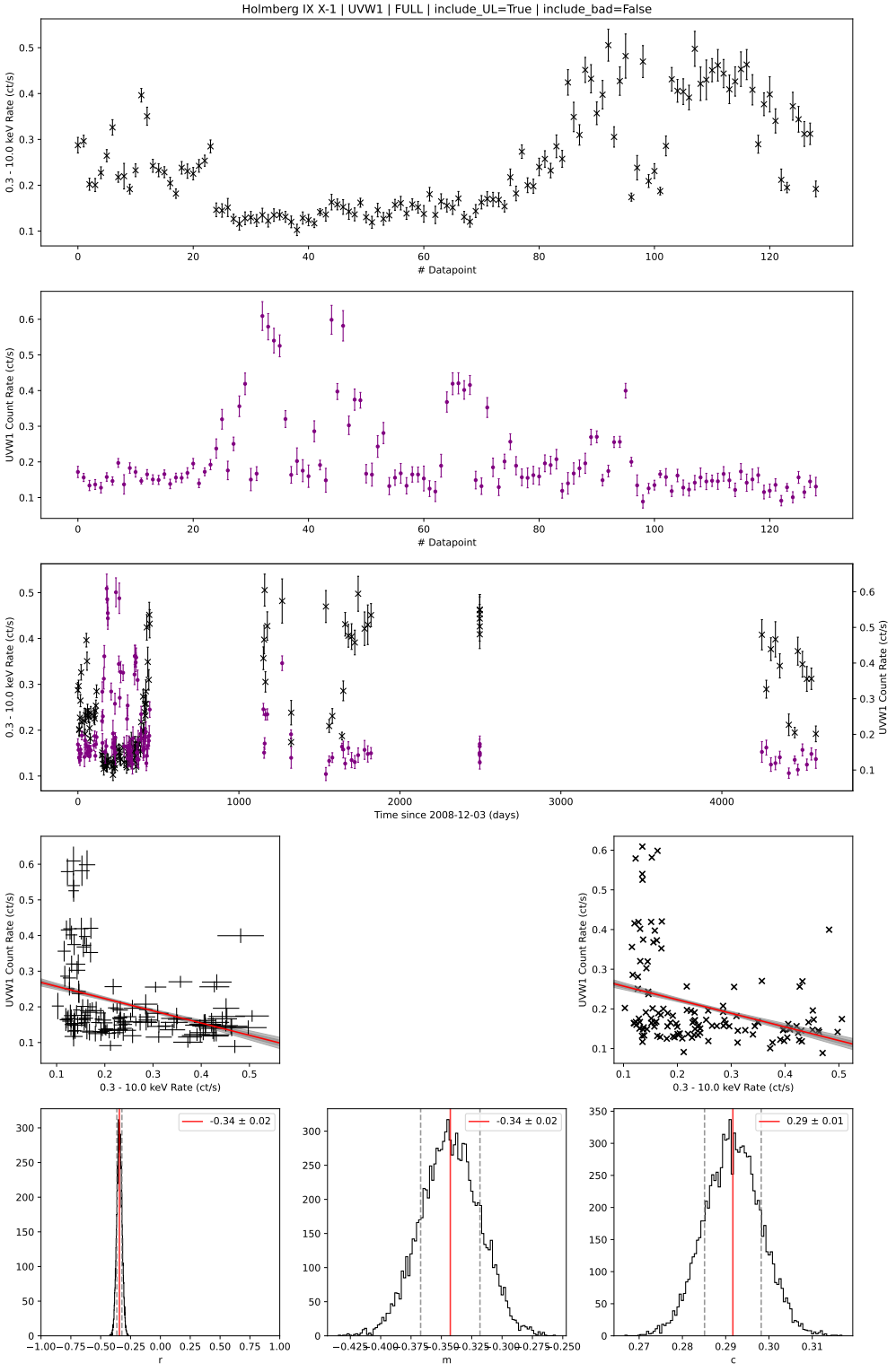

Figure 4.13: Row 1 & 2: The `full` band XRT and UVW1 light curve for Holmberg IX X-1 (plotted sequentially) with simultaneous observations. Row 3: The same light curves plotted in the time domain. Row 4: The data points, with and without errors, plotted in X, Y with the best fit in red and 1 and 2σ contours shades in grey. Row 5: The distribution of the fit parameters r, m and c.

low and vice-versa, which gives rise to the observed negative correlation. However when looking at the actual fit to the data, we see that the points are not really distributed around a straight line but rather follow an 'L' shape, despite this, our results would suggest that a negative correlation is consistently reproduced for this data. For many of our simulations, we find similar results, which demonstrates that our assumption of linear correlations between the two fluxes is likely an over-simplification and that more complicated analysis may be required.

4.5 Discussion & Conclusions

Although ULXs are defined empirically by their X-ray luminosity, they are well-known broad band emitters of radiation. Indeed, bright optical/UV emission (in excess of 10^{39} erg s^{-1}) is observed to originate in both Galactic super-critical accretors (SS 433: Dolan et al. 1997) and well studied ULXs (NGC6946 ULX-3: Kaaret et al. 2010) with a mixture of potential origins. In this chapter, we have made clear predictions about how the UV and X-ray emission might correlate (or anti-correlate) depending on the dominant mechanism for the low frequency radiation: the irradiated donor star, irradiated outer disc or wind photosphere.

Based on simple arguments, we predict a lack of any correlation between the UV and X-ray emission where the star is irradiated by radiation emerging from a wind-cone (i.e. unless very large inclinations are realised, the X-ray emission is independent of the UV emission in the absence of precession). In the case of disc irradiation or precession of the super-critical disc/wind, the exact nature of the correlation depends mostly on the observer inclination and any changes in accretion rate at large radius. Certainly for a fixed inclination (again, in the absence of precession), a negative correlation would be expected for disc irradiation as the X-ray emission (assumed here to originate within the wind-cone) increases with increasing $\dot{m}$, but the optical depth to the outer regions also increases. A negative correlation must also result in the case of precession, but can deviate and even become positive when changes in $\dot{m}$ are also invoked. In the absence of precession, the emission in both bands is a sensitive function of inclination (see Middleton et al. 2015a).

NASA's *Swift* satellite offers an unrivalled opportunity to explore the long timescale changes in both the X-ray and UV bands through simultaneous observing with the XRT and UVOT instruments. For a sample of ~ 40 ULXs (where the data quality permits), we have extracted the UV and X-ray light curves and correlated the two, placing constraints on the Pearson correlation value via simulations. Figures 4.14, 4.15 and 4.16, show the systems where correlations, significant at the $\geq 2\sigma$ (95%) level in the `hard` band have been found. In total, 21 ULXs out of our sample of ~ 40 are found to show a correlation in at least a single UVOT band. It is apparent from figures 4.14, 4.15 and 4.16 that both negative and positive linear correlations appear to be present for our sample.

in Figure 4.17 and 4.18, we show the correlation strength ($\hat{\gamma}_r$) versus the mean r value for those sources where a correlation is found in three or more UVOT bands. It is clear that for certain objects, a positive correlation is found with increasing strength, e.g. V404 Cygni, NGC 300 ULX-1, NGC 7793 P13 which

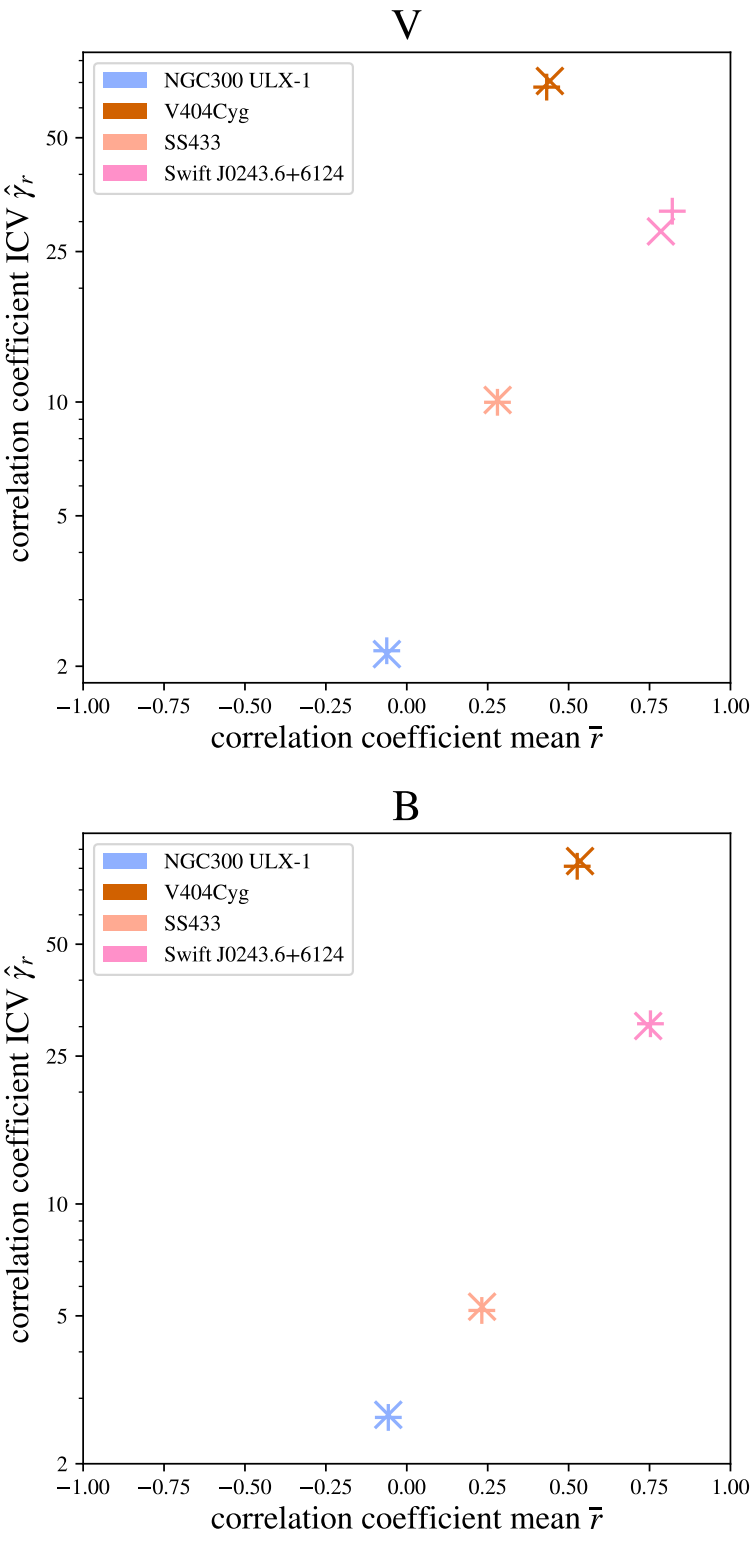

Figure 4.14: Mean correlation coefficient $\bar{r}$ vs the absolute value of $\hat{\gamma}_r$ for the `hard` X-ray band simulations in the V and B bands. Only sources with $\hat{\gamma}_r \geq 2$ are shown. Data points indicated with '×' include bad values, while datapoints with + markers do not.

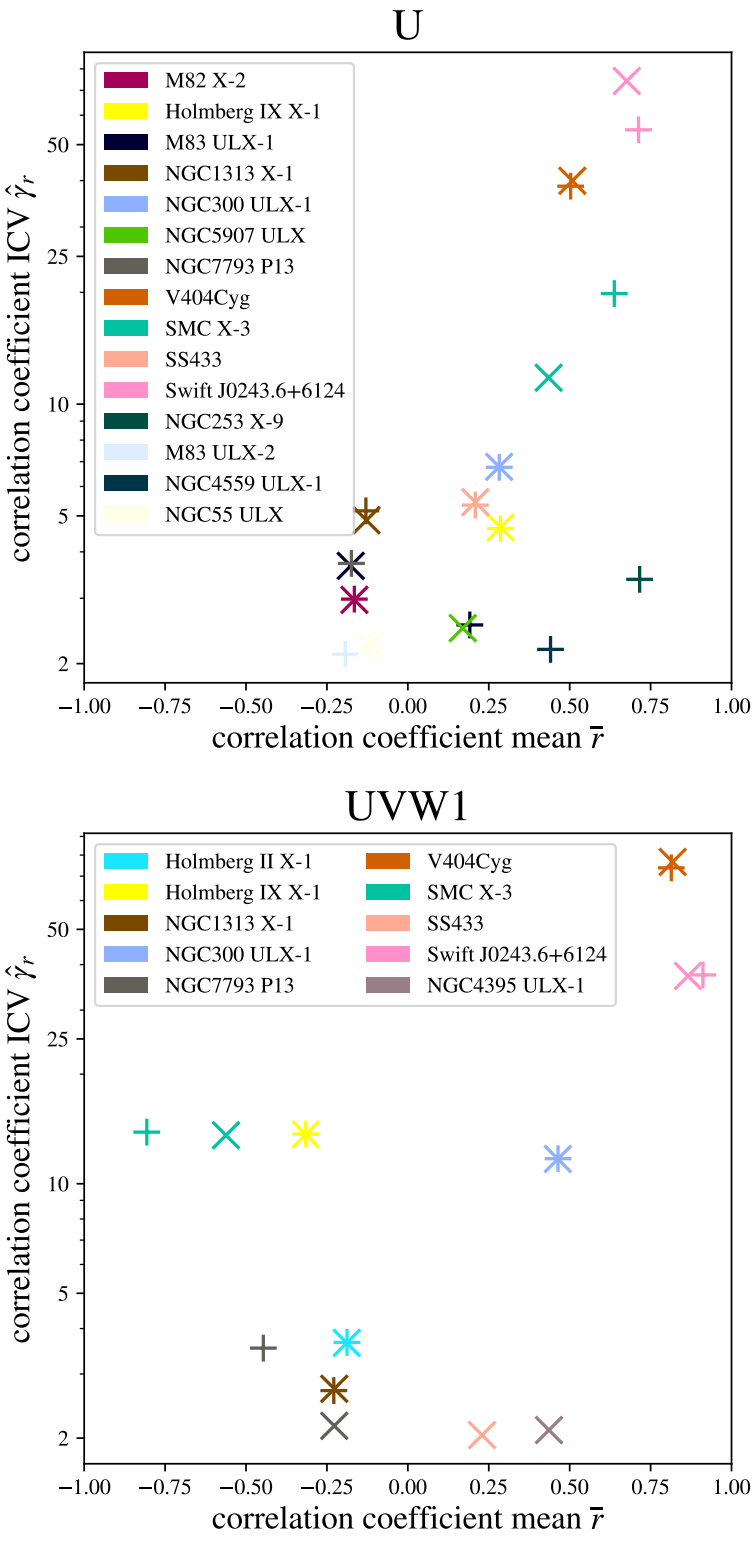

Figure 4.15: Mean correlation coefficient $\overline{r}$ vs the absolute value of $\hat{\gamma}_r$ for the `hard` X-ray band simulations in the U and UVW1 bands. Only sources with $\hat{\gamma}_r \geq 2$ are shown. Data points that with '$\times$' include bad values, while datapoints with $+$ markers do not.

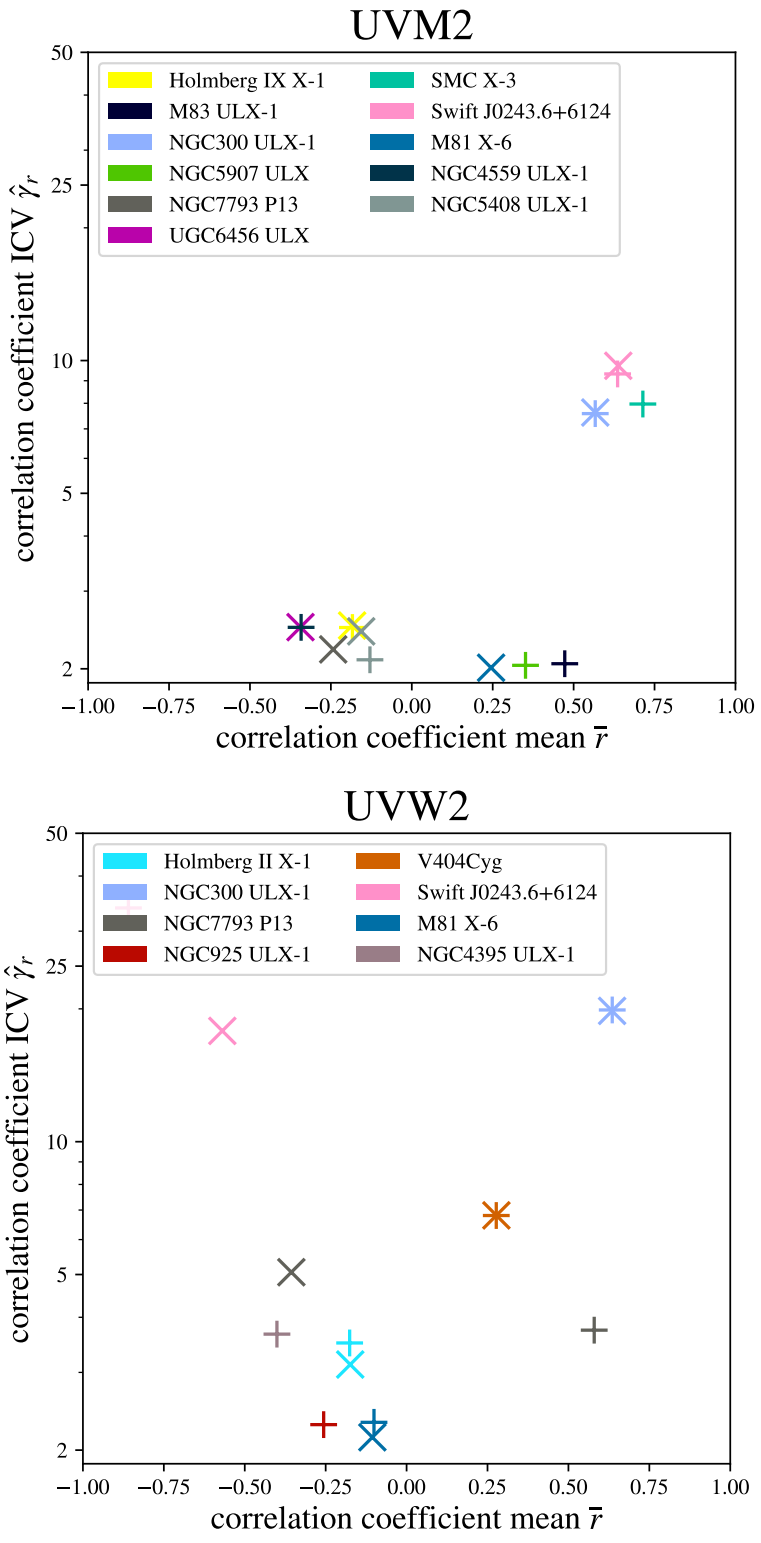

Figure 4.16: Mean correlation coefficient $\bar{r}$ vs the absolute value of $\hat{\gamma}_r$ for the `hard` X-ray band simulations in the UVM2 and UVW2 bands. Only sources with $\hat{\gamma}_r \geq 2$ are shown. Data points indicated with '$\times$' include bad values, while datapoints with $+$ markers do not.

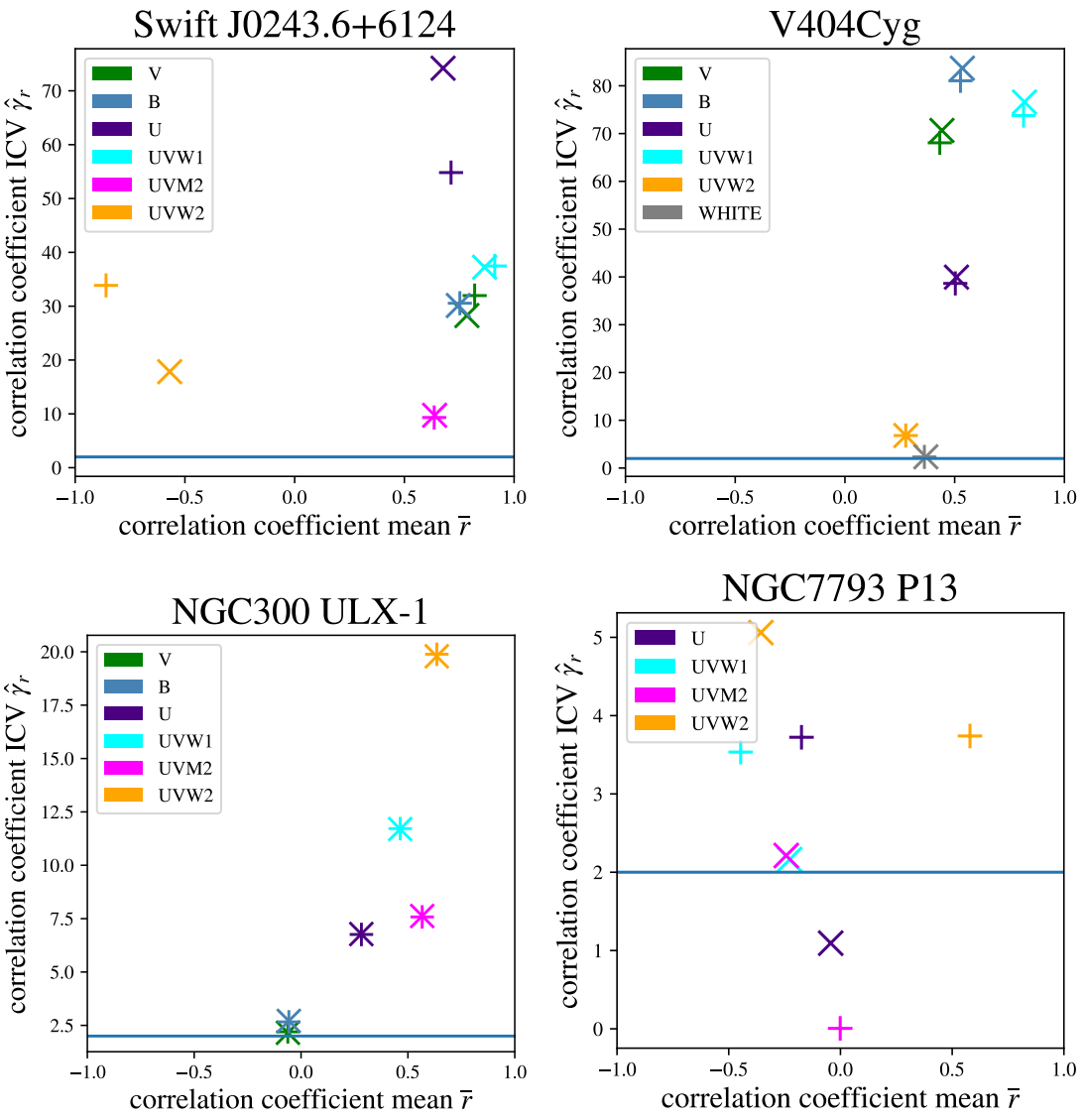

Figure 4.17: Correlation significance plots for individual sources that showed correlations greater than 2 $\hat{gamma}_r$ (horizontal line) between the `hard` X-ray band and three or more UVOT bands. Data points marked with a $\times$ correspond to simulations containing `bad` data points while datapoints marked with $+$ use only `good` data points.

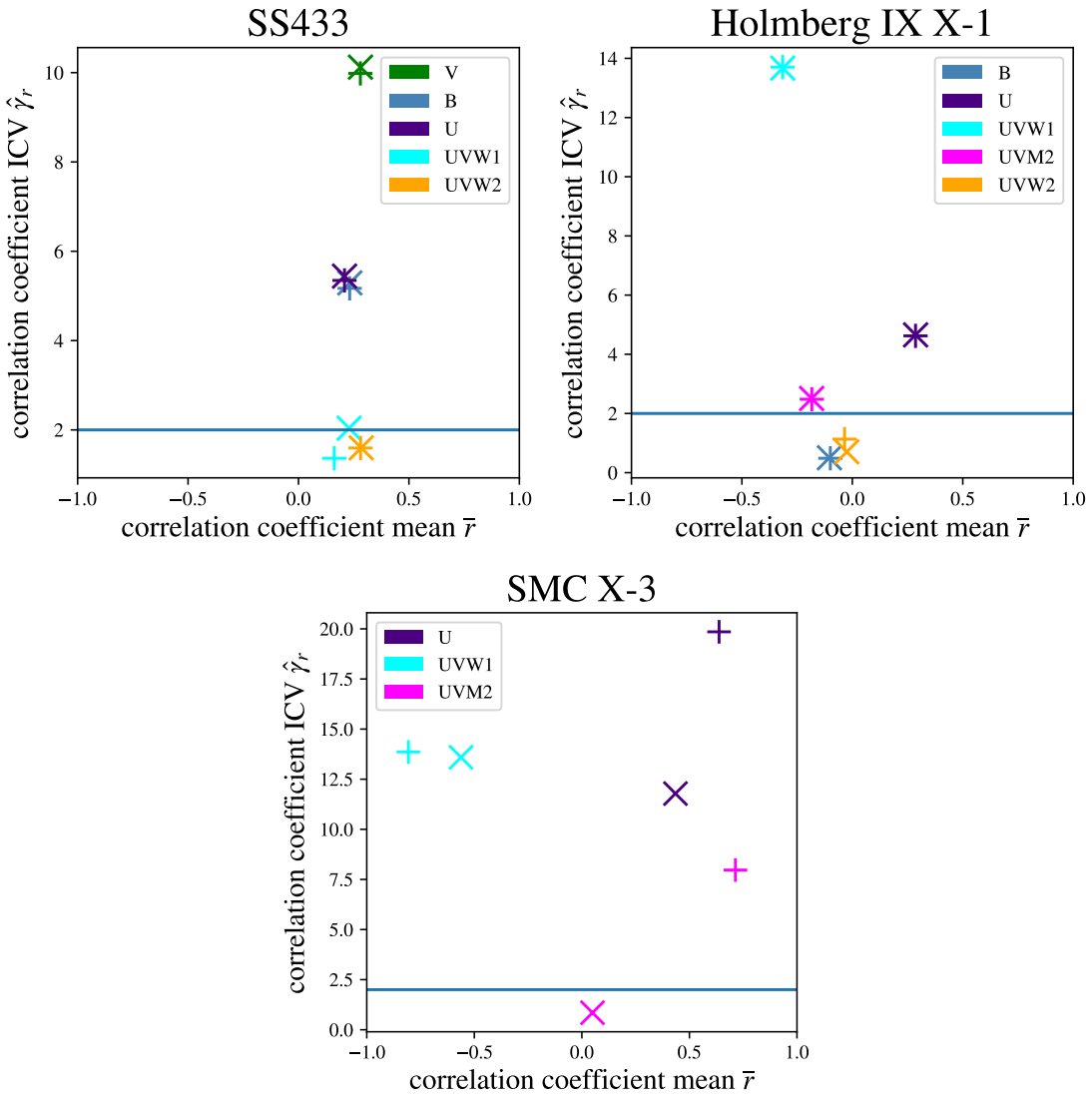

Figure 4.18: Correlation significance plots for individual sources that showed correlations greater than 2 $\hat{gamma}_r$ (horizontal line) between the `hard` X-ray band and three or more UVOT bands. Data points marked with a $\times$ correspond to simulations containing `bad` data points while datapoints marked with $+$ use only `good` data points.

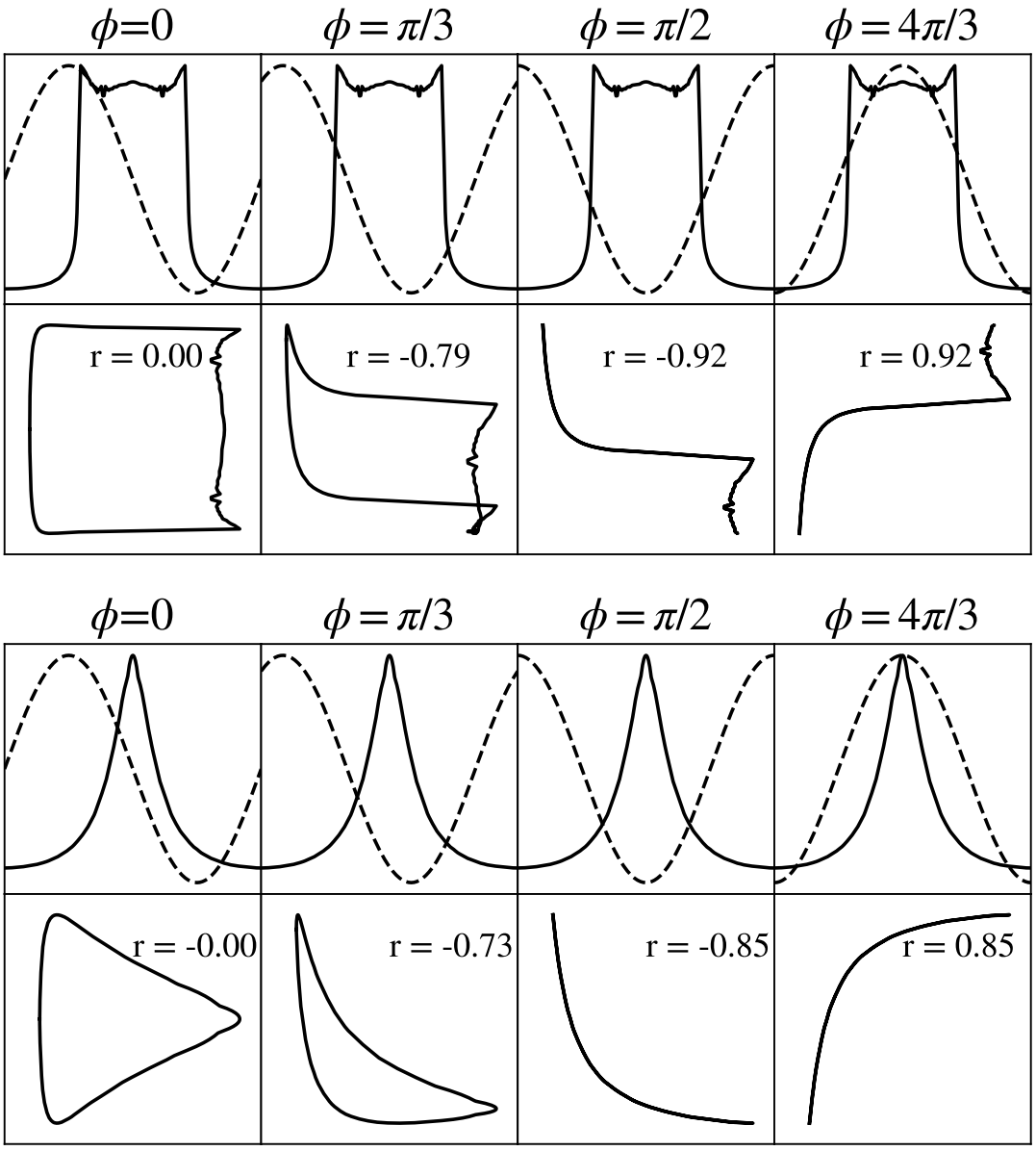

Figure 4.19: Possible correlation shapes obtained from the profiles in the top row as well as their respective r values, two different light curves shapes from `ULXLC` are shown in solid, one 'double peaked' obtained using $\theta = 10°$, $\Delta i = 20°$ and $i = 15°$, and a 'sigmoid' profile obtained from using $\theta = 5°$, $\Delta i = 9°$ and $i = 15°$.

likely points towards the emission being from a single component (such that it increases in lock-step across bands) or that our line-of-sight is such that we always view into the wind-cone. However, this is demonstrably not the case for SS433, which is viewed at large inclinations ($i \sim 73°$ Cherepashchuk et al. 2021)

There are clearly several objects where the correlation between bands is negative. This can result from precession at fixed accretion rate, a changing accretion rate without precession but at viewer inclinations **not** into the wind-cone, or from irradiation of the outer disc for viewer inclinations into the wind-cone. Notably, this appears to be the case for Holmberg IX X-1 and NGC 300 (see bottom left figure 4.10) which have been associated with precession induced changes by past authors (Weng & Feng, 2018; Vasilopoulos et al., 2019). It is also apparent that in some cases the nature of the correlation changes for a single source between bands (e.g. Holmberg IX X-1). This likely indicates that each band is affected to a differing degree by one of the different processes mentioned above.

In our analysis, we have assumed the simplest case of a linear correlation. However, numerous sources show clear patterns of behaviour where an 'L' shape is mapped out, while some others show non-linear shapes. As a result, a simple linear correlation test (Pearson) is less sensitive to detecting such behaviour. Intriguingly, an 'L' shape naturally results from precession of the wind-cone; using `ULXLC` (Dauser et al. 2017, see also section 3.2.5) we create two curves; the first is a 'double peaked' profile (created using the parameters $\theta = 10°$, $\Delta i = 20°$ and $i = 15°$, such that the cone of emission moves completely out of the line-of-sight). The second curve uses $\theta = 5°$, $\Delta i = 9°$ and $i = 15°$ which is a quasi-sigmoid profile. These X-ray curves are plotted in the first and third row of figure 4.19. We assume that the UV/Optical curve profile is sinusoidal, motivated by the assumed quasi-spherical geometry of the outer photosphere of the wind, and plot the subsequent profile of the correlation that would result for different phases of the sinusoid. We can see that the resultant shapes follow a square in the case of $\phi = 0$ (which results in a Pearson correlation coefficient of $r = 0$) which gets compressed along the y-axis as a result of changing phase, reducing to an 'L' shape for the case of perfect anti-phase as the upwards and downwards segment overlap exactly. For the sigmoid profile, an almost triangular shape results for $\phi = 0$ and an exponential decay-type profile at the point of the anti-phase. This preliminary result may suggest that more complicated models may be required to accurately constrain the joint variability between the two bands, and that systems which show such 'L' shaped correlations as in Holmberg IX X-1 (see figure 4.13) may be our clearest examples of precession.

Moving beyond simple modelling will require the post-processing of magneto-hydrodynamic (MHD) simulations to obtain the broad-band flux distribution as a function of inclination; this has started to be explored in the case of a SMBH by Dai et al. 2018b but has not yet been investigated for ULXs.

Data Availability

The source code, as well as processed light curves for this project may be found at:

https://github.com/nx1/anticorr_data/

Chapter 5

Concluding Remarks

In this concluding chapter, I shall briefly summarise the original contribution to the subject presented in this work, while commenting on the relative strengths and weaknesses of the scientific research. I will also provide some recommendations for future research, as well as some of my thoughts on upcoming developments that will likely revolutionise the field of X-ray astronomy in the next several decades.

5.1 The Impact of precession on observed ULXs

In chapter three I combined a synthetic population of X-ray binaries obtained from Wiktorowicz et al. 2019, with the predicted effects of beaming, to estimate the effect on the X-ray luminosity function. Using the geometric precession model of Dauser et al. 2017, I took this even further and obtained estimates for the observational bias on the number of potentially visible ULXs and investigated the role of the the *eROSITA* all sky survey, *eRASS*. Additionally, I investigated the effect of beaming and precession on the X-ray luminosity function.

The key results of this work include a novel method of probing some underlying properties of the ULX population based on the observed number of transient and persistent sources. By using the ULX catalogue by Earnshaw et al. 2018 we obtained a preliminary estimate of $81\pm12\%$ of ULXs being persistent and $19\pm3.8\%$ of ULXs being transient. Based on our modelling, these figures would lead us to infer a population of ULXs dominated by BHs. However, I stress that, due to the low number of repeated observations in the catalogue for many of the ULXs, the number of transient sources obtained through this method is an under-estimate.

As I have shown, the percentage of observed transient ULXs may increase greatly with the introduction of *eRASS*. I have predicted for an underlying ULX population predominantly composed of NSs (in-line with the estimates from literature e.g. Wiktorowicz et al. 2017; King & Lasota 2020) it may be possible that by cycle 8 of *eRASS* around $\sim 30-40\%$ of the *underlying* ULX population will be sampled by *eRASS*, while up to $\sim 90\%$ of the potentially observable sources will be sampled. I also predict that by cycle 8, around 75% of the transient ULXs will be correctly identified as being transient by *eRASS* independent of the underlying black hole percentage.

For the first time, I have characterised the effect of beaming, precession and observation probability on the X-ray luminosity function (XLF). I have shown how

there can be a significant change in the shape of the XLF at luminosities above $\sim 10^{39}$ erg s^{-1} when considering each of these effects. There will be wider implications if there is an observational bias present in observed XLFs, e.g. inferences derived from XLFs such as star-formation history and theoretical constraints on binary evolution will be affected (Mineo et al., 2012; Misra et al., 2022).

There are clear possible extensions to this work including increasing the complexity of modelling the *eRASS* survey, by distributing the sources spatially, accounting for the effect of interstellar absorption and considering the survey exposure maps. By incorporating the above, the number of predicted sources may be more reliably compared to actual results from survey data. The inclusion of the energy-dependence of the beaming and precession (lacking in my present work) would also provide deeper insights and predictions for *eRASS* and similar surveys.

The many forms of variability known to exist in ULXs that are not caused by precession may also impact the number of transient sources we observe. In my work, I have investigated how a duty cycle applied to LMXB systems could impact our results, however a possible extension to this could include a more complex implementation of the disc instability model (Lasota, 2001; Hameury & Lasota, 2020), which, when used in conjunction with the precessional model for ULXLC will allow us to obtain light curves that model both precession and outbursts simultaneously.

Additionally, I have not included the effect of magnetic fields in the NS ULXs. In NSs, these fields may be dipolar or multi-polar (e.g. Israel et al. 2017a; Middleton et al. 2019a; Kong et al. 2022) and will vary over time due to suppression (see Igoshev et al. 2021). The complexity of modelling magnetic fields in neutron stars is far beyond the scope of this thesis, but one of the main sources of variability I have not considered is the propeller effect (Basko & Sunyaev, 1976) which would increase the number of transient ULXs detected in our sample (see Earnshaw et al. 2018).

Finally, one of the key uncertainties in this work is the lack of constraints on parameters for the precession model entering into ULXLC (the wind cone opening angle and precessional angle); these may be estimated by direct lightcurve fitting (Dauser et al. 2017) and which might also reveal quasi periods that may be missed by traditional searches for strict periods. On the same note, whilst the most common method for detecting periodicities is through the Lomb-Scargle (LS) periodogram (Lomb, 1976; Scargle, 1981) – which works by performing a least-squares sinusoidal fit to the data – there are other methods such as the weighted wavelet Z-transform (WWZ) (Foster, 1996) (which was used by An et al. 2016 to identify what appears to be a secondary orbital period of 189 days in NGC5408 X-1). A somewhat recent development that may prove useful in this regard is the von Mises periodogram (Baluev, 2013), which allows for the detection of non-sinusoidal periodicities in time series. Such an analysis could be revealing, as many of the modulations observed from precessing sources do not appear sinusoidal (Dauser et al., 2017).

5.2 Long-Term UV/X-ray variability of ULXs

In chapter four, I performed the first search for correlations between the UV-optical and X-ray emission in approximately 40 ULXs. I found that for the majority of sources, there does not appear to be a strong level of linearly correlated variability between the two bands. Some ULXs in the sample, notably Swift J0243.6+6124, SMC X-3, NGC300 ULX-1, Holmberg IX X-1 and NGC7793 P13 may in fact show signs of weakly linearly correlated (or anti-correlated) variability and could be prime candidates for further study.

The fact that many of the ULXs in the sample do not appear to show linear correlations between the X-ray and UV/optical bands should not discount them from further study in these wavelengths. As I have noted, it is possible that linear correlations may not be expected in the case of precession of the wind, as the correlation of the Lorentzian-like light-curve in the X-rays (Dauser et al., 2017), and the more sinusoidal shape expected in the UV/optical may result in a non-linear relation between the two bands. More detailed time-resolved modelling, whereby physical models describing the energy-dependent emission over time are fitted to the light curves may be required to uncover the nature of the emission in many of the sources I have studied. This work will be enhanced considerably in future through the exploitation of MHD simulations which capture the energy-dependent flux emerging from the photosphere of the wind (Dai et al., 2018b). One key piece of data that I have omitted from the analysis is the spectral component of the emission, this is because high-quality spectra at the observation level require long exposures, which are often absent in *Swift* observations, if these spectra could be obtained it could be possible to fit spectral-timing models that may provide a unique view of the accretion flow in ULXs. An example of such a spectral-timing model was presented in Middleton et al. 2015a, whereby two primary sources of variability are considered, the first is the effect of changing the line-of-sight on the clumpy/inhomogeneous outflows created by the ULX wind, and the second is due to inwardly propagating variations in mass accretion rate or surface density through the accretion disc (Lyubarskii, 1997; Ingram & Done, 2012). The combination of these effects, combined with precession, allow for predictions of how the spectral energy distribution and short timescale variability of ULXs can vary over time, which may then be compared to observations of ULXs. There is significant work that can be done in exploring the complex nature of such a model; extensions include the application of these models to the broad-band spectra using *NuSTAR* or in future using high quality-spectra over multiple epochs which may be obtained by next generation missions such as *Athena*.

5.3 Placing my work into context

Despite the monumental amount of progress that has been made in understanding ULXs over the last couple of decades (see King et al. 2023 for a recent review), numerous questions and issues still remain. A key issue is undoubtedly the relative number of neutron stars to black holes in the observed population. Some authors (Koliopanos et al., 2017; King & Lasota, 2020) have taken the view that "almost all" ULXs may contain neutron star accretors, an argument derived from the claim

that most HMXB systems are NS systems. This idea is in agreement with population synthesis models Wiktorowicz et al. 2017 which suggest that NS systems outnumber BHs in the **intrinsic** population. However, the effect of beaming and precession change our ability to observe the population, as I have demonstrated.

Many questions still remain with regard to the modelling of ULX spectra, such as the suppressed spectral variability above $\sim 10 - 15$keV (Walton et al., 2020) and the relationship between the soft excess luminosity and temperature (Kajava & Poutanen, 2009) which is still not fully understood and may be degenerate with choice of spectral model. To learn more about the spectral emission, especially at soft energies, requires us to extend to lower energies, i.e. the UV. As I have shown, the X-ray and UV emission may be correlated or anti-correlated, providing unique clues to the geometry of the system.

5.4 Looking Forward

The future of X-ray astronomy and ULXs looks bright; the recently launched *eROSITA* satellite will no doubt discover many new ULXs and also provide long baselines to more thoroughly test our understanding and obtain a more complete census of the observable population. In the next 10-20 years, ESA's flagship *Athena* mission will revolutionise our view of the X-ray sky, providing easy access to ULX winds and placing tight constraints on the geometry of these super-critical sources (Pinto et al., 2020).

Future theoretical modelling of the radial dependence of beaming, and the physics of Lense-Thirring precession at super-critical rates is expected to provide unique tests for ULXs, and non-linear models for the coupled X-ray and UV emission will likely be required to explain the results in chapter 4. Whilst an exhaustive timing analysis has yet to be performed on many of the optical/UV light curves in my sample, I leave this in the capable hands of Andrés Gúrpide who has recently developed a novel implementation of the Lomb-Scargle method.

Approximately ~ 1.2 million unique X-ray sources are known (Webb et al., 2020; Evans et al., 2020b,a), and this number will only increase in future. Eventually, it will be the case that so many ULXs have been discovered that detailed human analysis on all of them will be prohibitive. Large-scale analysis, involving artificial intelligence and/or machine learning will be required to analyse the extremely large datasets and high dimensionality of the incident data. As I have learned from my time within the DISCNet CDT, these tools will always continue to work with the astronomer, and not for the astronomer. Far beyond this, it is anyone's guess as to what strange and wonderful things are still out there waiting to be found.

5.5 Summary of Other Research Contributions

I have collaborated in two other peer reviewed publications over the course of my PhD, A brief overview of my contribution for these papers is provided here.

The filtered population of ULXs obtained from `StarTrack` detailed in in 3.2.1 of this thesis has additionally been used to study thermally driven winds in ULXs

in Middleton et al. (2022). The population was used to try and identify regions of parameter space occupied by thermally unstable ULXs that could experience significant mass loss via a wind. It was found that almost all NS and BH ULXs with accretion rates of $\dot{m}_0 < 100$ could display thermal instabilities in the atmosphere of the outer disc due to reprocessing of radiation, thereby resulting in the production of thermally driven outflows.

I also contributed to a study predicting the self-lensing population in optical surveys Wiktorowicz et al. (2021). In binaries containing a NS/BH and normal star, self-lensing events are predicted to appear as optical flares as the compact object gravitationally lenses visible light coming from the companion. These flares may be periodic in nature if they are the result of the orbital motion of the binary. Detecting these self-lensing events serves as an important tool for detecting binaries that are in a quiescent state and otherwise extremely challenging to observe.

The paper predicted the number of self-lensing events that might be expected in three large optical surveys: the Transiting Exoplanet Survey Satellite (TESS; Ricker et al. 2014), the Zwicky Transient Facility (ZTF; Masci et al. 2019) and the The Vera C. Rubin Observatory LSST (Ivezić et al. 2019). Each of these instruments has specific magnitude limits depending on the filter used, thus the bolometric magnitudes obtained via population synthesis must be converted to visible magnitude values via a bolometric correction. Calculation of the bolometric correction varies depending on the specific stellar parameters, and many stellar spectral libraries have been developed for the modelling of different types of stellar classification. YBC is a stellar bolometric corrections database (Chen et al., 2019) that was created from the combination of several stellar libraries and thus is robust to a wide range of different stellar types. My specific contribution to the paper was writing a code that uses YBC to calculate bolometric corrections for stars obtained from `StarTrack` for the specific instrument and filter combination. The study predicted that potentially $\sim 100 - 10,000$s of self-lensing events could be detected, which can shed light on difficult to study stages of binary evolution which will provide new constraints on evolutionary models.

Acknowledgements

The work in this thesis would not have been possible without the help of my supervisor Dr. Matthew Middleton, I thank him for giving me the opportunity to pursue this PhD and his continued support even during illness, lockdown, and the birth of his first child.

I thank my peers at Southampton Dominic Ashton, James Leftley, Adam Hill, Maddie Ward, Matthew Greyling, Peter Boorman, David Price, Andrés Gúrpide, Jakub Orwat-Kapola, Alessio D'addabbo and the countless number I could not fit on this page...

I thank my collaborators on my first paper, notably Grzegorz Wiktorowicz, who provided me with the synthetic sample of binaries used in my first paper.

Thank you to my family and especially my grandparents for their love (and food) while allowing me to finish writing up at their place in Bertrimont, Normandy.

Finally, I thank you, the reader, for reading this thesis :)
STFC studentship project reference: 2115300.

Bibliography

Abazajian K. N., et al., 2009, ApJS, 182, 543

Abbott R., et al., 2020a, Phys. Rev. Lett., 125, 101102

Abbott R., et al., 2020b, ApJ, 902, L21

Abell G. O., Margon B., 1979, Nature, 279, 701

Abolmasov P., Karpov S., Kotani T., 2009, PASJ, 61, 213

Abramowicz M. A., Czerny B., Lasota J. P., Szuszkiewicz E., 1988, ApJ, 332, 646

Abt H. A., Levy S. G., 1976, ApJS, 30, 273

Allak S., Akyuz A., Sonbas E., Dhuga K. S., 2022, MNRAS, 515, 3632

An T., Lu X.-L., Wang J.-Y., 2016, A&A, 585, A89

Avdan S., et al., 2019, ApJ, 875, 68

Baade W., Zwicky F., 1934, Proceedings of the National Academy of Science, 20, 259

Bachetti M., et al., 2014, Nature, 514, 202

Balbus S. A., Hawley J. F., 1991, ApJ, 376, 214

Balbus S. A., Hawley J. F., 1998, Reviews of Modern Physics, 70, 1

Baluev R. V., 2013, MNRAS, 431, 1167

Barbon R., Buondi V., Cappellaro E., Turatto M., 2008, VizieR Online Data Catalog,

Barra F., et al., 2022, arXiv e-prints, p. arXiv:2207.12870

Barthelmy S. D., et al., 2005, Space Sci. Rev., 120, 143

Basko M. M., Sunyaev R. A., 1976, MNRAS, 175, 395

Bauer F. E., Brandt W. N., 2004, ApJ, 601, L67

Begelman M. C., Volonteri M., Rees M. J., 2006, MNRAS, 370, 289

Belczynski K., Kalogera V., Rasio F. A., Taam R. E., Zezas A., Bulik T., Maccarone T. J., Ivanova N., 2008, ApJS, 174, 223

Belczynski K., et al., 2018, A&A, 615, A91

Belczynski K., et al., 2020, A&A, 636, A104

Bernadich M. C., Schwope A. D., Kovlakas K., Zezas A., Traulsen I., 2022, A&A, 659, A188

Blundell K. M., Bowler M. G., 2004, ApJ, 616, L159

Brightman M., et al., 2018, Nature Astronomy, 2, 312

Brightman M., Walton D. J., Xu Y., Earnshaw H. P., Harrison F. A., Stern D., Barret D., 2020a, ApJ, 889, 71

Brightman M., et al., 2020b, ApJ, 895, 127

Brorby M., Kaaret P., Prestwich A., 2014, MNRAS, 441, 2346

Burke M. J., et al., 2013, ApJ, 775, 21

Burrows D. N., et al., 2005, Space Sci. Rev., 120, 165

Canuto V., Lodenquai J., Ruderman M., 1971, Phys. Rev. D, 3, 2303

Cappellari M., et al., 2011, MNRAS, 413, 813

Cappelluti N., et al., 2011, Memorie della Societa Astronomica Italiana Supplementi, 17, 159

Carpano S., Haberl F., Maitra C., Vasilopoulos G., 2018, MNRAS, 476, L45

Chandra A. D., Roy J., Agrawal P. C., Choudhury M., 2020, MNRAS, 495, 2664

Chashkina A., Lipunova G., Abolmasov P., Poutanen J., 2019, A&A, 626, A18

Chen Y., et al., 2019, A&A, 632, A105

Cherepashchuk A., 2002, Space Sci. Rev., 102, 23

Cherepashchuk A. M., Belinski A. A., Dodin A. V., Postnov K. A., 2021, MNRAS, 507, L19

Clauset A., Rohilla Shalizi C., Newman M. E. J., 2007, arXiv e-prints, p. arXiv:0706.1062

Colbert E. J. M., Mushotzky R. F., 1999, ApJ, 519, 89

Cseh D., et al., 2014, MNRAS, 439, L1

Dai L., McKinney J. C., Roth N., Ramirez-Ruiz E., Miller M. C., 2018a, ApJ, 859, L20

Dai L., McKinney J. C., Roth N., Ramirez-Ruiz E., Miller M. C., 2018b, ApJ, 859, L20

Dall'Osso S., Perna R., Papitto A., Bozzo E., Stella L., 2016, MNRAS, 457, 3076

Dauser T., Middleton M., Wilms J., 2017, MNRAS, 466, 2236

Davis S. W., Narayan R., Zhu Y., Barret D., Farrell S. A., Godet O., Servillat M., Webb N. A., 2011, ApJ, 734, 111

Deegan P., Combet C., Wynn G. A., 2009, MNRAS, 400, 1337

Dolan J. F., et al., 1997, A&A, 327, 648

Done C., Gierliński M., Kubota A., 2007, A&A Rev., 15, 1

Doroshenko V., Tsygankov S., Santangelo A., 2018, A&A, 613, A19

Dubus G., Charles P. A., Long K. S., Hakala P. J., 1997, ApJ, 490, L47

Earnshaw H. P., Roberts T. P., Sathyaprakash R., 2018, MNRAS, 476, 4272

Earnshaw H. P., Roberts T. P., Middleton M. J., Walton D. J., Mateos S., 2019, MNRAS, 483, 5554

Earnshaw H. P., Brightman M., Harrison F. A., Heida M., Jaodand A., Middleton M. J., Roberts T. P., Walton D. J., 2022, ApJ, 934, 42

Eggleton P. P., 1983, ApJ, 268, 368

Einstein A., 1916, Annalen der Physik, 354, 769

Eksi K. Y., Andac I. C., Cikintoglu S., Gencali A. A., Gungor C., Oztekin F., 2015, MNRAS, 448, L40

Esin A. A., McClintock J. E., Narayan R., 1997, ApJ, 489, 865

Evans P. A., et al., 2009, MNRAS, 397, 1177

Evans I. N., et al., 2020a, in American Astronomical Society Meeting Abstracts #235. p. 154.05

Evans P. A., et al., 2020b, ApJS, 247, 54

Everitt C. W. F., et al., 2011, Phys. Rev. Lett., 106, 221101

Fabbiano G., 1989, ARA&A, 27, 87

Fabian A. C., Rees M. J., 1979, MNRAS, 187, 13P

Fabrika S., 2004, Astrophys. Space Phys. Res., 12, 1

Fabrika S., Ueda Y., Vinokurov A., Sholukhova O., Shidatsu M., 2015, Nature Physics, 11, 551

Farrell S. A., Webb N. A., Barret D., Godet O., Rodrigues J. M., 2009, Nature, 460, 73

Feng H., Kaaret P., 2007, ApJ, 660, L113

Feng H., Kaaret P., 2008, ApJ, 675, 1067

Feng H., Kaaret P., 2010, ApJ, 712, L169

Foreman-Mackey D., 2016, The Journal of Open Source Software, 1, 24

Foster G., 1996, AJ, 112, 1709

Fragile P. C., Blaes O. M., Anninos P., Salmonson J. D., 2007, ApJ, 668, 417

Fragos T., et al., 2013a, ApJ, 764, 41

Fragos T., Lehmer B. D., Naoz S., Zezas A., Basu-Zych A., 2013b, ApJ, 776, L31

Frank J., King A., Raine D. J., 2002, Accretion Power in Astrophysics: Third Edition

Fürst F., et al., 2016, ApJ, 831, L14

Fürst F., Walton D. J., Stern D., Bachetti M., Barret D., Brightman M., Harrison F. A., Rana V., 2017, ApJ, 834, 77

Fürst F., et al., 2021, A&A, 651, A75

Gaia Collaboration 2018, VizieR Online Data Catalog, p. I/345

Gaia Collaboration 2020, VizieR Online Data Catalog, p. I/350

Gardner J. P., et al., 2006, Space Sci. Rev., 123, 485

Gebhardt K., et al., 2001, AJ, 122, 2469

Gehrels N., et al., 2004, ApJ, 611, 1005

Geller A. M., Leigh N. W. C., Giersz M., Kremer K., Rasio F. A., 2019, ApJ, 872, 165

Ghosh T., Rana V., Bachetti M., 2022, arXiv e-prints, p. arXiv:2202.01432

Giacconi R., et al., 1979, ApJ, 230, 540

Gierliński M., Done C., 2004, MNRAS, 347, 885

Gierliński M., Done C., Page K., 2008, MNRAS, 388, 753

Gladstone J. C., Roberts T. P., Done C., 2009, MNRAS, 397, 1836

Gladstone J. C., Copperwheat C., Heinke C. O., Roberts T. P., Cartwright T. F., Levan A. J., Goad M. R., 2013, ApJS, 206, 14

Goad M. R., Roberts T. P., Knigge C., Lira P., 2002, MNRAS, 335, L67

Godet O., Barret D., Webb N. A., Farrell S. A., Gehrels N., 2009, ApJ, 705, L109

Gregory P. C., Loredo T. J., 1992, ApJ, 398, 146

Greiner J., Schwarz R., Zharikov S., Orio M., 2000, A&A, 362, L25

Grimm H. J., Gilfanov M., Sunyaev R., 2003, MNRAS, 339, 793

Grisé F., Pakull M., Motch C., 2006, in Wilson A., ed., ESA Special Publication Vol. 604, The X-ray Universe 2005. p. 451 (arXiv:astro-ph/0603769)

Grisé F., Kaaret P., Pakull M. W., Motch C., 2011, ApJ, 734, 23

Grisé F., Kaaret P., Corbel S., Feng H., Cseh D., Tao L., 2012, ApJ, 745, 123

Grupe D., Thomas H. C., Leighly K. M., 1999, A&A, 350, L31

Hameury J. M., Lasota J. P., 2020, A&A, 643, A171

Heger A., Fryer C. L., Woosley S. E., Langer N., Hartmann D. H., 2003, ApJ, 591, 288

Heida M., et al., 2014, MNRAS, 442, 1054

Heida M., et al., 2015, MNRAS, 453, 3510

Heida M., Jonker P. G., Torres M. A. P., Roberts T. P., Walton D. J., Moon D. S., Stern D., Harrison F. A., 2016, MNRAS, 459, 771

Heida M., Harrison F. A., Brightman M., Fürst F., Stern D., Walton D. J., 2019, ApJ, 871, 231

Helfand D. J., 1984, PASP, 96, 913

Hessels J. W. T., Ransom S. M., Stairs I. H., Freire P. C. C., Kaspi V. M., Camilo F., 2006, Science, 311, 1901

Hewish A., Bell S. J., Pilkington J. D. H., Scott P. F., Collins R. A., 1968, Nature, 217, 709

Hobbs G., Manchester R., Teoh A., Hobbs M., 2004, 218, 139

Huang Y. L., Dame T. M., Thaddeus P., 1983, ApJ, 272, 609

Humphrey P. J., Fabbiano G., Elvis M., Church M. J., Bałucińska-Church M., 2003, MNRAS, 344, 134

Hurley J. R., Pols O. R., Tout C. A., 2000, MNRAS, 315, 543

Ichimaru S., 1977, ApJ, 214, 840

Igoshev A. P., Popov S. B., Hollerbach R., 2021, Universe, 7, 351

Illarionov A. F., Sunyaev R. A., 1975, A&A, 39, 185

Ingram A., Done C., 2012, MNRAS, 419, 2369

Israel G. L., et al., 2017a, Science, 355, 817

Israel G. L., et al., 2017b, MNRAS, 466, L48

Ivezić Ž., et al., 2019, ApJ, 873, 111

Jaroszynski M., Abramowicz M. A., Paczynski B., 1980, Acta Astron., 30, 1

Jeans J. H., 1919, MNRAS, 79, 408

Jenke P., Wilson-Hodge C. A., 2017, The Astronomer's Telegram, 10812, 1

Jiang Y.-F., Stone J. M., Davis S. W., 2014, ApJ, 796, 106

Jiang Y.-F., Stone J. M., Davis S. W., 2019, ApJ, 880, 67

Jones D. I., Andersson N., 2001, MNRAS, 324, 811

Jonker P. G., et al., 2012, ApJ, 758, 28

Kaaret P., Ward M. J., Zezas A., 2004, MNRAS, 351, L83

Kaaret P., Simet M. G., Lang C. C., 2006, ApJ, 646, 174

Kaaret P., Feng H., Wong D. S., Tao L., 2010, ApJ, 714, L167

Kaaret P., Feng H., Roberts T. P., 2017, ARA&A, 55, 303

Kajava J. J. E., Poutanen J., 2009, MNRAS, 398, 1450

Karachentsev I. D., Kaisina E. I., Kashibadze Nasonova O. G., 2017, AJ, 153, 6

Kaur A., et al., 2012, A&A, 538, A49

Khabibullin I., Sazonov S., 2016, MNRAS, 457, 3963

Khan N., Middleton M. J., Wiktorowicz G., Dauser T., Roberts T. P., Wilms J., 2022, MNRAS, 509, 2493

King A. R., 2009, MNRAS, 393, L41

King A., Lasota J.-P., 2019, MNRAS, 485, 3588

King A., Lasota J.-P., 2020, MNRAS, 494, 3611

King A., Nixon C., 2018, ApJ, 857, L7

King A. R., Puchnarewicz E. M., 2002, MNRAS, 336, 445

King A. R., Ritter H., 1999, MNRAS, 309, 253

King A. R., Davies M. B., Ward M. J., Fabbiano G., Elvis M., 2001, ApJ, 552, L109

King A. R., Pringle J. E., Livio M., 2007, MNRAS, 376, 1740

King A., Lasota J.-P., Kluźniak W., 2017, MNRAS, 468, L59

King A., Lasota J.-P., Middleton M., 2023, New A Rev., 96, 101672

Kippenhahn R., Weigert A., 1967, ZAp, 65, 251

Koliopanos F., Vasilopoulos G., Godet O., Bachetti M., Webb N. A., Barret D., 2017, A&A, 608, A47

Koliopanos F., Vasilopoulos G., Buchner J., Maitra C., Haberl F., 2019, A&A, 621, A118

Komossa S., Bade N., 1999, A&A, 343, 775

Komossa S., Greiner J., 1999, A&A, 349, L45

Komossa S., Halpern J., Schartel N., Hasinger G., Santos-Lleo M., Predehl P., 2004, ApJ, 603, L17

Kong A. K. H., Hu C.-P., Lin L. C.-C., Li K. L., Jin R., Liu C. Y., Yen D. C.-C., 2016, MNRAS, 461, 4395

Kong L.-D., et al., 2022, ApJ, 933, L3

Körding E., Falcke H., Markoff S., 2002, A&A, 382, L13

Kosec P., Pinto C., Fabian A. C., Walton D. J., 2018a, MNRAS, 473, 5680

Kosec P., Pinto C., Walton D. J., Fabian A. C., Bachetti M., Brightman M., Fürst F., Grefenstette B. W., 2018b, MNRAS, 479, 3978

Kosec P., et al., 2021, MNRAS, 508, 3569

Kovlakas K., Zezas A., Andrews J. J., Basu-Zych A., Fragos T., Hornschemeier A., Lehmer B., Ptak A., 2020, MNRAS, 498, 4790

Kriss G. A., Canizares C. R., 1982, ApJ, 261, 51

Kroupa P., Weidner C., 2003, ApJ, 598, 1076

Kuntz K. D., Gruendl R. A., Chu Y.-H., Chen C. H. R., Still M., Mukai K., Mushotzky R. F., 2005, ApJ, 620, L31

Lai D., 1999, ApJ, 524, 1030

Lara-López M. A., et al., 2021, ApJ, 906, 42

Lasota J.-P., 2001, New A Rev., 45, 449

Lasota J. P., Vieira R. S. S., Sadowski A., Narayan R., Abramowicz M. A., 2016, A&A, 587, A13

Lei W.-H., Zhang B., Gao H., 2013, ApJ, 762, 98

Lense J., Thirring H., 1918, Physikalische Zeitschrift, 19, 156

Li L.-X., Paczyński B., 1998, ApJ, 507, L59

Lianou S., Barmby P., Mosenkov A. A., Lehnert M., Karczewski O., 2019, A&A, 631, A38

Licquia T. C., Newman J. A., 2015, ApJ, 806, 96

Lin D., Webb N. A., Barret D., 2012, ApJ, 756, 27

Lipunov V. M., Shakura N. I., 1980, Soviet Astronomy Letters, 6, 14

Lipunova G. V., 1999, Astronomy Letters, 25, 508

Liu J.-F., Bregman J. N., 2005, ApJS, 157, 59

Liu J., Di Stefano R., 2008, ApJ, 674, L73

Liu Q. Z., Mirabel I. F., 2005, A&A, 429, 1125

Liu J.-F., Bregman J. N., Seitzer P., 2002, ApJ, 580, L31

Liu J.-F., Bregman J. N., Seitzer P., 2004, ApJ, 602, 249

Liu J.-F., Bregman J., Miller J., Kaaret P., 2007, ApJ, 661, 165

Liu J., Bregman J. N., McClintock J. E., 2009, ApJ, 690, L39

Liu J.-F., Bregman J. N., Bai Y., Justham S., Crowther P., 2013, Nature, 503, 500

Liu J.-F., et al., 2015, Nature, 528, 108

Lomb N. R., 1976, Ap&SS, 39, 447

Long K. S., Dodorico S., Charles P. A., Dopita M. A., 1981, ApJ, 246, L61

Long K. S., Kuntz K. D., Blair W. P., Godfrey L., Plucinsky P. P., Soria R., Stockdale C., Winkler P. F., 2014, ApJS, 212, 21

López K. M., Heida M., Jonker P. G., Torres M. A. P., Roberts T. P., Walton D. J., Moon D. S., Harrison F. A., 2017, MNRAS, 469, 671

Luangtip W., Roberts T. P., Done C., 2016, MNRAS, 460, 4417

Lyubarskii Y. E., 1997, MNRAS, 292, 679

Maccarone T. J., Kundu A., Zepf S. E., Rhode K. L., 2007, Nature, 445, 183

Maeder A., 1992, A&A, 264, 105

Malmquist K. G., 1922, Meddelanden fran Lunds Astronomiska Observatorium Serie I, 100, 1

Malmquist K. G., 1925, Meddelanden fran Lunds Astronomiska Observatorium Serie I, 106, 1

Maloney P. R., Begelman M. C., 1997, ApJ, 491, L43

Maloney P. R., Begelman M. C., Pringle J. E., 1996, ApJ, 472, 582

Maloney P. R., Begelman M. C., Nowak M. A., 1998, ApJ, 504, 77

Mapelli M., Ripamonti E., Zampieri L., Colpi M., Bressan A., 2010, MNRAS, 408, 234

Margon B., Grandi S. A., Downes R., 1979, in Bulletin of the American Astronomical Society. p. 786

Markert T. H., Rallis A. D., 1983, ApJ, 275, 571

Masci F. J., et al., 2019, PASP, 131, 018003

McGowan K. E., Charles P. A., 2003, MNRAS, 339, 748

Merloni A., et al., 2012, arXiv e-prints, p. arXiv:1209.3114

Mezcua M., Roberts T. P., Lobanov A. P., Sutton A. D., 2015, MNRAS, 448, 1893

Mezcua M., Kim M., Ho L. C., Lonsdale C. J., 2018, MNRAS, 480, L74

Michell J., 1784, Philosophical Transactions of the Royal Society of London Series I, 74, 35

Middleton M. J., King A., 2017, MNRAS, 470, L69

Middleton M. J., Walton D. J., Roberts T. P., Heil L., 2014, MNRAS, 438, L51

Middleton M. J., Heil L., Pintore F., Walton D. J., Roberts T. P., 2015a, MNRAS, 447, 3243

Middleton M. J., Walton D. J., Fabian A., Roberts T. P., Heil L., Pinto C., Anderson G., Sutton A., 2015b, MNRAS, 454, 3134

Middleton M. J., et al., 2018, MNRAS, 475, 154

Middleton M. J., Brightman M., Pintore F., Bachetti M., Fabian A. C., Fürst F., Walton D. J., 2019a, MNRAS, 486, 2

Middleton M. J., Fragile P. C., Ingram A., Roberts T. P., 2019b, MNRAS, 489, 282

Middleton M. J., et al., 2021, MNRAS, 506, 1045

Middleton M. J., Higginbottom N., Knigge C., Khan N., Wiktorowicz G., 2022, MNRAS, 509, 1119

Milgrom M., 1979, A&A, 78, L9

Miller M. C., Miller J. M., 2015, Phys. Rep., 548, 1

Miller-Jones J. C. A., Jonker P. G., Dhawan V., Brisken W., Rupen M. P., Nelemans G., Gallo E., 2009, ApJ, 706, L230

Miller J. M., Fabian A. C., Miller M. C., 2004, ApJ, 607, 931

Milosavljević M., Merritt D., 2001, ApJ, 563, 34

Mineo S., Gilfanov M., Sunyaev R., 2012, MNRAS, 419, 2095

Misra D., et al., 2022, arXiv e-prints, p. arXiv:2209.05505

Mizuno T., Ohnishi T., Kubota A., Makishima K., Tashiro M., 1999, PASJ, 51, 663

Motch C., Pakull M. W., Grisé F., Soria R., 2011, Astronomische Nachrichten, 332, 367

Motch C., Pakull M. W., Soria R., Grisé F., Pietrzyński G., 2014, Nature, 514, 198

Motta S. E., et al., 2017, MNRAS, 471, 1797

Mushtukov A. A., Suleimanov V. F., Tsygankov S. S., Poutanen J., 2015, MNRAS, 454, 2539

Mushtukov A. A., Suleimanov V. F., Tsygankov S. S., Ingram A., 2017, MNRAS, 467, 1202

Mushtukov A. A., Verhagen P. A., Tsygankov S. S., van der Klis M., Lutovinov A. A., Larchenkova T. I., 2018a, MNRAS, 474, 5425

Mushtukov A. A., Tsygankov S. S., Suleimanov V. F., Poutanen J., 2018b, MNRAS, 476, 2867

Mushtukov A. A., Portegies Zwart S., Tsygankov S. S., Nagirner D. I., Poutanen J., 2021, MNRAS, 501, 2424

Narayan R., Yi I., 1994, ApJ, 428, L13

Narayan R., SaÌ§dowski A., Soria R., 2017, MNRAS, 469, 2997

O'Connell R. W., 1983, ApJ, 267, 80

Oey M. S., et al., 2007, ApJ, 661, 801

Ozdogan Ela M., et al., 2021, MNRAS, 505, 771

Pakull M. W., Mirioni L., 2002, arXiv e-prints, pp astro–ph/0202488

Pallavicini R., Golub L., Rosner R., Vaiana G. S., Ayres T., Linsky J. L., 1981, ApJ, 248, 279

Pannuti T. G., Schlegel E. M., Filipović M. D., Payne J. L., Petre R., Harrus I. M., Staggs W. D., Lacey C. K., 2011, AJ, 142, 20

Pasham D. R., Strohmayer T. E., 2013, ApJ, 774, L16

Pasham D. R., Strohmayer T. E., Mushotzky R. F., 2014, Nature, 513, 74

Pinto C., Middleton M. J., Fabian A. C., 2016, Nature, 533, 64

Pinto C., Fabian A., Middleton M., Walton D., 2017a, Astronomische Nachrichten, 338, 234

Pinto C., et al., 2017b, MNRAS, 468, 2865

Pinto C., et al., 2020, MNRAS, 492, 4646

Poutanen J., Krolik J. H., Ryde F., 1997, MNRAS, 292, L21

Poutanen J., Lipunova G., Fabrika S., Butkevich A. G., Abolmasov P., 2007, MNRAS, 377, 1187

Predehl P., et al., 2021, A&A, 647, A1

Prestwich A. H., Tsantaki M., Zezas A., Jackson F., Roberts T. P., Foltz R., Linden T., Kalogera V., 2013, ApJ, 769, 92

Priedhorsky W. C., Terrell J., 1984, ApJ, 280, 661

Pringle J. E., 1992, MNRAS, 258, 811

Pringle J. E., 1996, MNRAS, 281, 357

Ptak A., Colbert E., van der Marel R. P., Roye E., Heckman T., Towne B., 2006, ApJS, 166, 154

Quast M., Langer N., Tauris T. M., 2019, A&A, 628, A19

Quintin E., Webb N. A., Gúrpide A., Bachetti M., Fürst F., 2021, MNRAS, 503, 5485

Reig P., 2011, Ap&SS, 332, 1

Reynolds C. S., 2021, ARA&A, 59

Ricker G. R., et al., 2014, in Oschmann Jacobus M. J., Clampin M., Fazio G. G., MacEwen H. A., eds, Society of Photo-Optical Instrumentation Engineers (SPIE) Conference Series Vol. 9143, Space Telescopes and Instrumentation 2014: Optical, Infrared, and Millimeter Wave. p. 914320 (arXiv:1406.0151), doi:10.1117/12.2063489

Rivera Sandoval L. E., Maccarone T. J., Corsi A., Brown P. J., Pooley D., Wheeler J. C., 2018, MNRAS, 480, L146

Roberts W. J., 1974, ApJ, 187, 575

Roberts T. P., 2007, Ap&SS, 311, 203

Roberts T. P., Warwick R. S., 2000, MNRAS, 315, 98

Roberts T. P., Goad M. R., Ward M. J., Warwick R. S., O'Brien P. T., Lira P., Hands A. D. P., 2001, MNRAS, 325, L7

Roberts T. P., Levan A. J., Goad M. R., 2008, MNRAS, 387, 73

Rodríguez Castillo G. A., et al., 2020, ApJ, 895, 60

Roming P. W. A., et al., 2005, Space Sci. Rev., 120, 95

Rosen S. R., et al., 2016, A&A, 590, A1

Rubin B. C., Harmon B. A., Paciesas W. S., Robinson C. R., Zhang S. N., Fishman G. J., 1998, ApJ, 492, L67

Sadowski A., 2011, arXiv e-prints, p. arXiv:1108.0396

Sana H., et al., 2012, Science, 337, 444

Sathyaprakash R., et al., 2019, MNRAS, 488, L35

Sazonov S. Y., Sunyaev R. A., Lund N., 1997, Astronomy Letters, 23, 286

Sazonov S., et al., 2021, MNRAS, 508, 3820

Scargle J. D., 1981, ApJS, 45, 1

Schlegel E. M., 2017, in AAS/High Energy Astrophysics Division #16. p. 110.07

Schnittman J., 2021, in APS April Meeting Abstracts. p. H03.001

Schreier E., Giacconi R., Gursky H., Kellogg E., Tananbaum H., 1972, ApJ, 178, L71

Schreier E. J., Feigelson E., Delvaille J., Giacconi R., Grindlay J., Schwartz D. A., Fabian A. C., 1979, ApJ, 234, L39

Schreier E. J., Gorenstein P., Feigelson E. D., 1982, ApJ, 261, 42

Schwarzschild K., 1916, Abh. Konigl. Preuss. Akad. Wissenschaften Jahre 1906,92, Berlin,1907, 1916, 189

Scott Barrows R., Comerford J. M., Stern D., Heida M., 2022, ApJ, 932, 27

Servillat M., Farrell S. A., Lin D., Godet O., Barret D., Webb N. A., 2011, ApJ, 743, 6

Shakura N. I., Sunyaev R. A., 1973, A&A, 500, 33

Shen R. F., Barniol Duran R., Nakar E., Piran T., 2015, MNRAS, 447, L60

Sądowski A., Narayan R., McKinney J. C., Tchekhovskoy A., 2014, MNRAS, 439, 503

Sonbas E., Dhuga K. S., Göğüş E., 2019, ApJ, 873, L12

Song X., Walton D. J., Lansbury G. B., Evans P. A., Fabian A. C., Earnshaw H., Roberts T. P., 2020, MNRAS, 491, 1260

Soria R., Cropper M., Pakull M., Mushotzky R., Wu K., 2005, MNRAS, 356, 12

Soria R., Risaliti G., Elvis M., Fabbiano G., Bianchi S., Kuncic Z., 2009, ApJ, 695, 1614

Soria R., Long K. S., Blair W. P., Godfrey L., Kuntz K. D., Lenc E., Stockdale C., Winkler P. F., 2014, Science, 343, 1330

Sridhar N., Metzger B. D., Beniamini P., Margalit B., Renzo M., Sironi L., Kovlakas K., 2021, ApJ, 917, 13

Steele M. M., Zepf S. E., Maccarone T. J., Kundu A., Rhode K. L., Salzer J. J., 2014, ApJ, 785, 147

Stella L., Vietri M., 1998, ApJ, 492, L59

Stella L., White N. E., Rosner R., 1986, ApJ, 308, 669

Stobbart A. M., Roberts T. P., Wilms J., 2006, MNRAS, 368, 397

Strateva I. V., Komossa S., 2009, ApJ, 692, 443

Strohmayer T. E., 2009, ApJ, 706, L210

Sutton A. D., Roberts T. P., Middleton M. J., 2013, MNRAS, 435, 1758

Swartz D. A., Ghosh K. K., Tennant A. F., Wu K., 2004, ApJS, 154, 519

Swartz D. A., Soria R., Tennant A. F., Yukita M., 2011, ApJ, 741, 49

Tananbaum H., Gursky H., Kellogg E., Giacconi R., Jones C., 1972, ApJ, 177, L5

Tananbaum H., et al., 1979, ApJ, 234, L9

Tao L., Feng H., Grisé F., Kaaret P., 2011, ApJ, 737, 81

Tetarenko B. E., Sivakoff G. R., Heinke C. O., Gladstone J. C., 2016, ApJS, 222, 15

Tong H., 2015, Research in Astronomy and Astrophysics, 15, 517

Townsend L. J., Charles P. A., 2020, MNRAS, 495, 139

Trudolyubov S. P., 2008, MNRAS, 387, L36

Trudolyubov S. P., Priedhorsky W. C., Córdova F. A., 2007, ApJ, 663, 487

Tsygankov S. S., Mushtukov A. A., Suleimanov V. F., Poutanen J., 2016, MNRAS, 457, 1101

Tsygankov S. S., Doroshenko V., Lutovinov A. A., Mushtukov A. A., Poutanen J., 2017, A&A, 605, A39

Tully R. B., Courtois H. M., Sorce J. G., 2016, AJ, 152, 50

Turner H. H., 1906, MNRAS, 67, 119

Tzanavaris P., Hornschemeier A. E., Gallagher S. C., Lenkić L., Desjardins T. D., Walker L. M., Johnson K. E., Mulchaey J. S., 2016, ApJ, 817, 95

Urquhart R., Soria R., Johnston H. M., Pakull M. W., Motch C., Schwope A., Miller-Jones J. C. A., Anderson G. E., 2018, MNRAS, 475, 3561

Vasilopoulos G., Petropoulou M., Koliopanos F., Ray P. S., Bailyn C. B., Haberl F., Gendreau K., 2019, MNRAS, 488, 5225

Vasilopoulos G., Lander S. K., Koliopanos F., Bailyn C. D., 2020, MNRAS, 491, 4949

Vasilopoulos G., Koliopanos F., Haberl F., Treiber H., Brightman M., Earnshaw H. P., Gúrpide A., 2021, ApJ, 909, 50

Vinokurov A., Fabrika S., Atapin K., 2018, ApJ, 854, 176

Vinokurov A., Atapin K., Solovyeva Y., 2020, ApJ, 893, L28

Voges W., et al., 1999, A&A, 349, 389

Walton D. J., et al., 2016a, ApJ, 826, L26

Walton D. J., et al., 2016b, ApJ, 827, L13

Walton D. J., et al., 2018, ApJ, 857, L3

Walton D. J., et al., 2020, MNRAS, 494, 6012

Walton D. J., Mackenzie A. D. A., Gully H., Patel N. R., Roberts T. P., Earnshaw H. P., Mateos S., 2022, MNRAS, 509, 1587

Wang S., Liu J., Bai Y., Guo J., 2015, ApJ, 812, L34

Wang S., Qiu Y., Liu J., Bregman J. N., 2016, ApJ, 829, 20

Watarai K.-y., Fukue J., Takeuchi M., Mineshige S., 2000, PASJ, 52, 133

Webb N. A., Barret D., Godet O., Servillat M., Farrell S. A., Oates S. R., 2010, ApJ, 712, L107

Webb N., et al., 2012, Science, 337, 554

Webb N. A., et al., 2020, A&A, 641, A136

Weng S.-S., Feng H., 2018, ApJ, 853, 115

Wenger M., et al., 2000, A&AS, 143, 9

White N. E., Carpenter G. F., 1978, MNRAS, 183, 11P

Whitmire D. P., Matese J. J., 1980, MNRAS, 193, 707

Wiersema K., Farrell S. A., Webb N. A., Servillat M., Maccarone T. J., Barret D., Godet O., 2010, ApJ, 721, L102

Wiktorowicz G., Sobolewska M., Lasota J.-P., Belczynski K., 2017, ApJ, 846, 17

Wiktorowicz G., Lasota J.-P., Middleton M., Belczynski K., 2019, ApJ, 875, 53

Wiktorowicz G., Middleton M., Khan N., Ingram A., Gandhi P., Dickinson H., 2021, MNRAS, 507, 374

Wolter A., Fruscione A., Mapelli M., 2018, ApJ, 863, 43

Zdziarski A. A., Gierliński M., 2004, Progress of Theoretical Physics Supplement, 155, 99

Zezas A. L., Georgantopoulos I., Ward M. J., 1999, Astronomical and Astrophysical Transactions, 18, 425

van den Eijnden J., et al., 2019, MNRAS, 487, 4355

van den Eijnden J., et al., 2020, MNRAS, 496, 4127

van den Heuvel E. P. J., 1993, Space Sci. Rev., 66, 309

Appendix A

Appendix

A.1 Comparison of Period Prescriptions

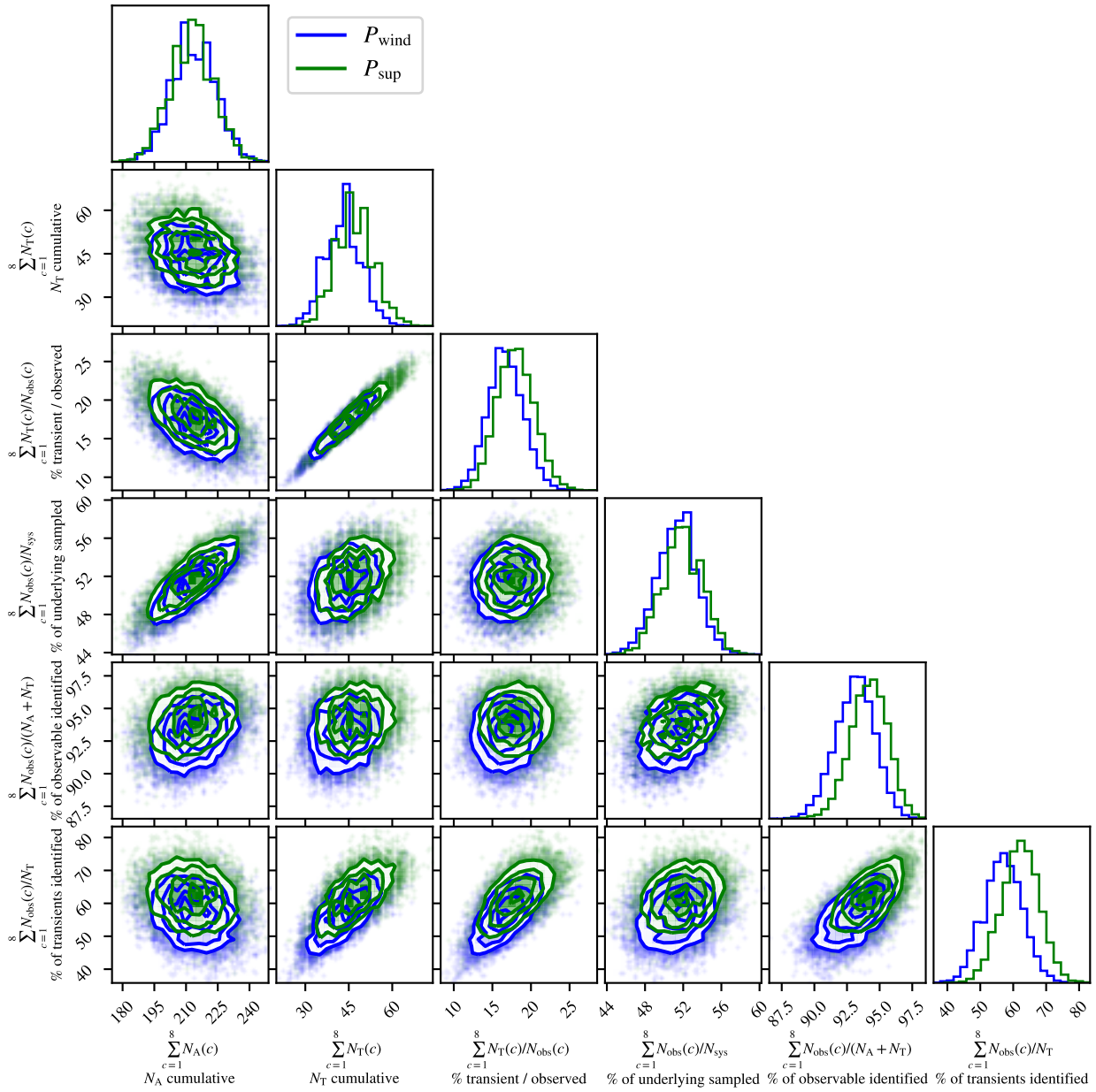

Figure A.1: Corner plot comparing two precession mechanisms for cycle 3 of *eRASS* showing the minimal impact of using P_{wind} over P_{sup}. Model parameters $Z = 0.02$, $\%_{\text{BH}} = 50$, Δi_{max} $d = 0.2$.

A.2 Luminosity / Soft-Excess Temperature Relation

Gierliński & Done 2004 analysed 10 black hole binaries with disk-dominated spectra with luminosities in the range 10^{36-37} erg s^{-1} and showed as sources increased in luminosity, the peak temperature of the soft excess would also increase, mathematically these two quantities were found to be related by $L \propto T^4$.

Feng & Kaaret 2007 used 12 *XMM-Newton* observations of the ULX NGC1313 X-2 and investigated two spectral models i) a MCD disc with a radial temperature profile of $kT \propto R^{3/4}$ and ii) a p-free model where the radial temperature profile was allowed to be a free parameter treated as $kT \propto R^p$. They find that, using the MCD model (the same as used in Gierliński & Done 2004) the $L \propto T^4$ relation did not hold, and instead the luminosity decreased as the soft-excess temperature increased, following a $L \propto T^{-3.1\pm0.5}$. This result was extended to a sample of 9 ULXs by Kajava & Poutanen 2009 and as can be seen in figure A.2 it was found that the objects cluster around the line:

$$L_{\rm soft} = \frac{7 \times 10^{40}}{T^4_{\rm 0.1keV}} \text{ erg s}^{-1} \tag{A.1}$$

where $T_{\rm 0.1keV}$ is the temperature in units of 0.1 keV.

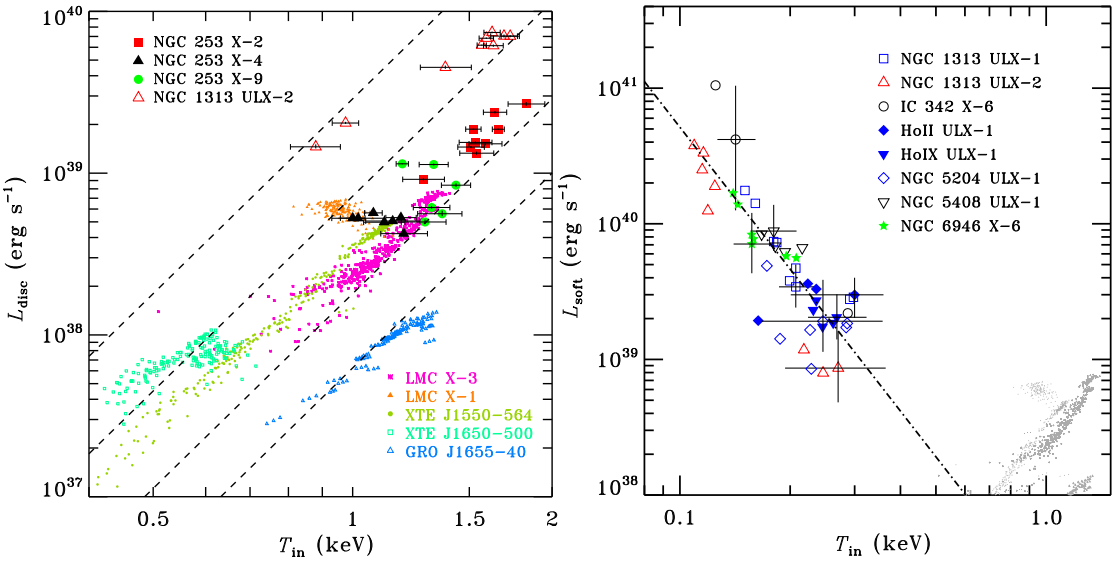

Figure A.2: Left: $L \propto T^4$ relationship found for sub-Eddington BHBs. Right: $L \propto T^{-4}$ relationship found for bright ULXs. From (Kajava & Poutanen, 2009)

King 2009 used this result combined with a previously obtain derivation from King & Puchnarewicz 2002 to show that a that a relation between the beaming factor and the mass accretion rate could exist as $b \sim 73/\dot{m}^2$.

Starting from the Stefan-Boltzmann law $F = \sigma T^4$, the luminosity and effective temperature of an optically thick region around a black hole may be given by:

$$L = \sigma T^4 4\pi R^2 \tag{A.2}$$

next, we define the radius in units of Schwarzschild radii $r = R/R_s$, where $R_s = 2GM/c^2$ we obtain:

$$L = \sigma T^4 4\pi \left(\frac{2GMr}{c^2}\right)^2 = \frac{16\pi G^2 M^2 r^2}{c^4}\sigma T^4 \tag{A.3}$$

We next define l as the luminosity in units of the Eddington luminosity such that $l = L/L_{Edd}$ where $L_{Edd} = 4\pi GMm_p c/\sigma_T$ (see section 1.3.1), by re-arranging and eliminating M from equation A.3 we obtain:

$$L = \frac{\pi m_p c^6}{\sigma T^4 \sigma_T^2}\frac{l^2}{r^2} \tag{A.4}$$

The L in the above equation is the isotropic luminosity under the assumption of spherical symmetry, however if there is anisotropic emission characterised by a beaming factor b (see section 3.2.1) then the observed luminosity by a distant observer is given by $L_{\rm obs} = L/b$. Inserting the beaming dependence and evaluating the constants numerically, we obtain:

$$L_{\rm obs} = \frac{2.3 \times 10^{44}}{T^4_{\rm 0.1keV}}\frac{l^2}{br^2} \text{ erg s}^{-1} \tag{A.5}$$

Where we have converted T to units of 0.1 keV $T_{\rm 0.1keV}$ using $E = kT$ where k is the Boltzmann constant. Thus, we can see that the observed luminosity is proportional to $L_{\rm obs} \propto T^{-4}$, consistent with the observation made by Kajava & Poutanen 2009.

The next step is re-normalising the derived result with that of observation, to do this we set $L_{\rm soft} = L_{\rm obs}$ in equations A.1 and A.5 respectively resulting in

$$\frac{7 \times 10^{40}}{2.3 \times 10^{44}} \approx 3 \times 10^{-4} = \frac{l^2}{br^2} \tag{A.6}$$

We then substitute $r = R_{\rm sph}/R_{\rm s}$ where is spherization radius given by roughly $R_{\rm sph} \approx 27\dot{m}R_{\rm s}/4$ this gives:

$$3 \times 10^{-4} \times \left(\frac{27}{4}\dot{m}\right)^2 = \frac{l^2}{b} \tag{A.7}$$

Finally, re-arranging gives:

$$b \propto \frac{73}{\dot{m}^2} \tag{A.8}$$

A.3 Stacked UVOT Images

This section contains stacked UVOT images in the available filters in a 50x50 pixel region surrounding the SIMBAD coordinates. A 5 arcsec scale-bar is plotted in the bottom right of each plot and I have converted the scale to the equivalent size in parsecs for each source. Each row contains a single source, with each panel corresponding to increasing energy bands (left to right), and they are ordered in increasing distance as in table 4.3.

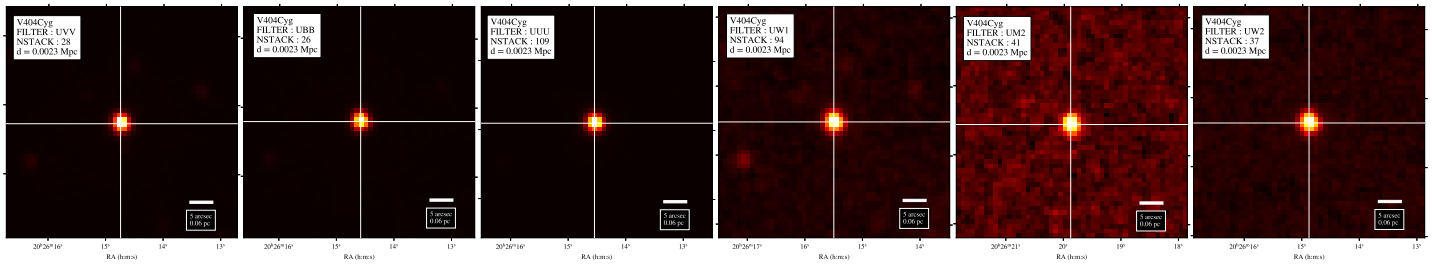
V404Cyg
FILTER : UVV
NSTACK : 28
d = 0.0023 Mpc
V404Cyg
FILTER : UBB
NSTACK : 26
d = 0.0023 Mpc
V404Cyg
FILTER : UUU
NSTACK : 109
d = 0.0023 Mpc
V404Cyg
FILTER : UW1
NSTACK : 94
d = 0.0023 Mpc
V404Cyg
FILTER : UM2
NSTACK : 41
d = 0.0023 Mpc
V404Cyg
FILTER : UW2
NSTACK : 37
d = 0.0023 Mpc

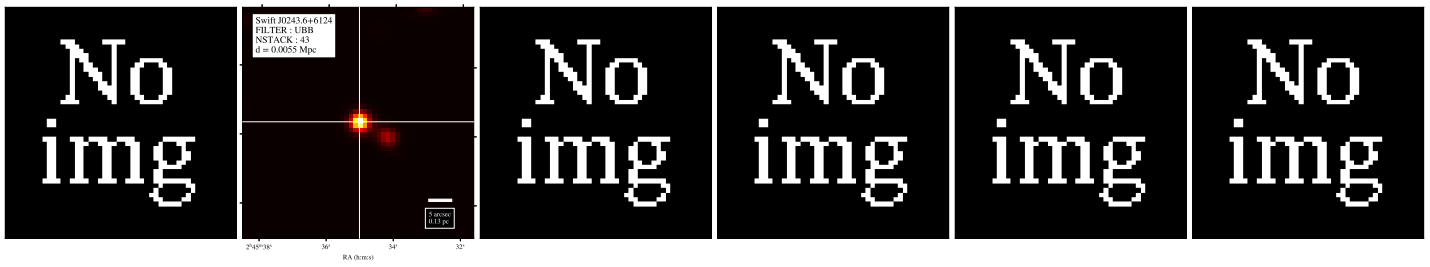
No img
Swift J0243.6+6124
FILTER : UBB
NSTACK : 43
d = 0.0055 Mpc
No img
No img
No img
No img

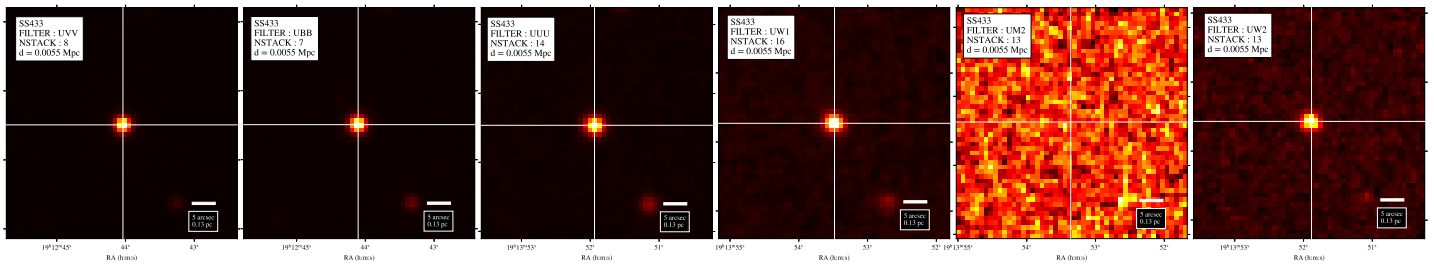
SS433
FILTER : UVV
NSTACK : 8
d = 0.0055 Mpc
SS433
FILTER : UBB
NSTACK : 7
d = 0.0055 Mpc
SS433
FILTER : UUU
NSTACK : 14
d = 0.0055 Mpc
SS433
FILTER : UW1
NSTACK : 16
d = 0.0055 Mpc
SS433
FILTER : UM2
NSTACK : 13
d = 0.0055 Mpc
SS433
FILTER : UW2
NSTACK : 13
d = 0.0055 Mpc

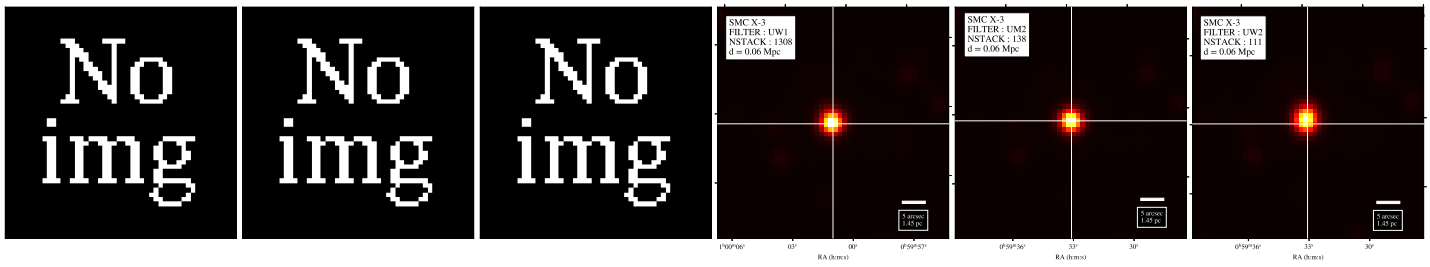
No img
No img
No img
SMC X-3
FILTER : UW1
NSTACK : 1308
d = 0.06 Mpc
SMC X-3
FILTER : UM2
NSTACK : 138
d = 0.06 Mpc
SMC X-3
FILTER : UW2
NSTACK : 111
d = 0.06 Mpc

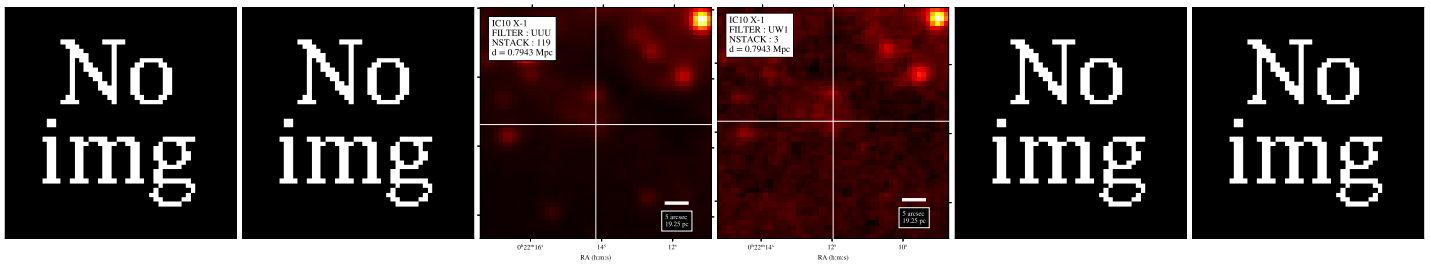
No img
No img
IC10 X-1
FILTER : UUU
NSTACK : 119
d = 0.7943 Mpc
IC10 X-1
FILTER : UW1
NSTACK : 3
d = 0.7943 Mpc
No img
No img

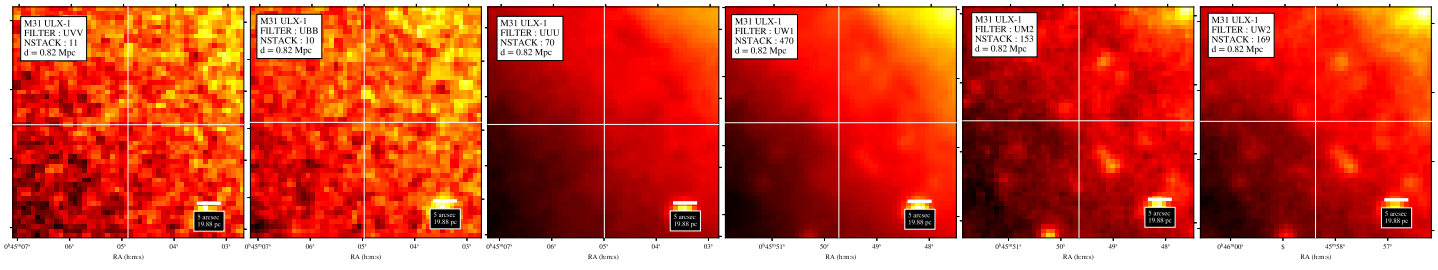
M31 ULX-1
FILTER : UVV
NSTACK : 11
d = 0.82 Mpc
M31 ULX-1
FILTER : UBB
NSTACK : 10
d = 0.82 Mpc
M31 ULX-1
FILTER : UUU
NSTACK : 70
d = 0.82 Mpc
M31 ULX-1
FILTER : UW1
NSTACK : 470
d = 0.82 Mpc
M31 ULX-1
FILTER : UM2
NSTACK : 153
d = 0.82 Mpc
M31 ULX-1
FILTER : UW2
NSTACK : 169
d = 0.82 Mpc

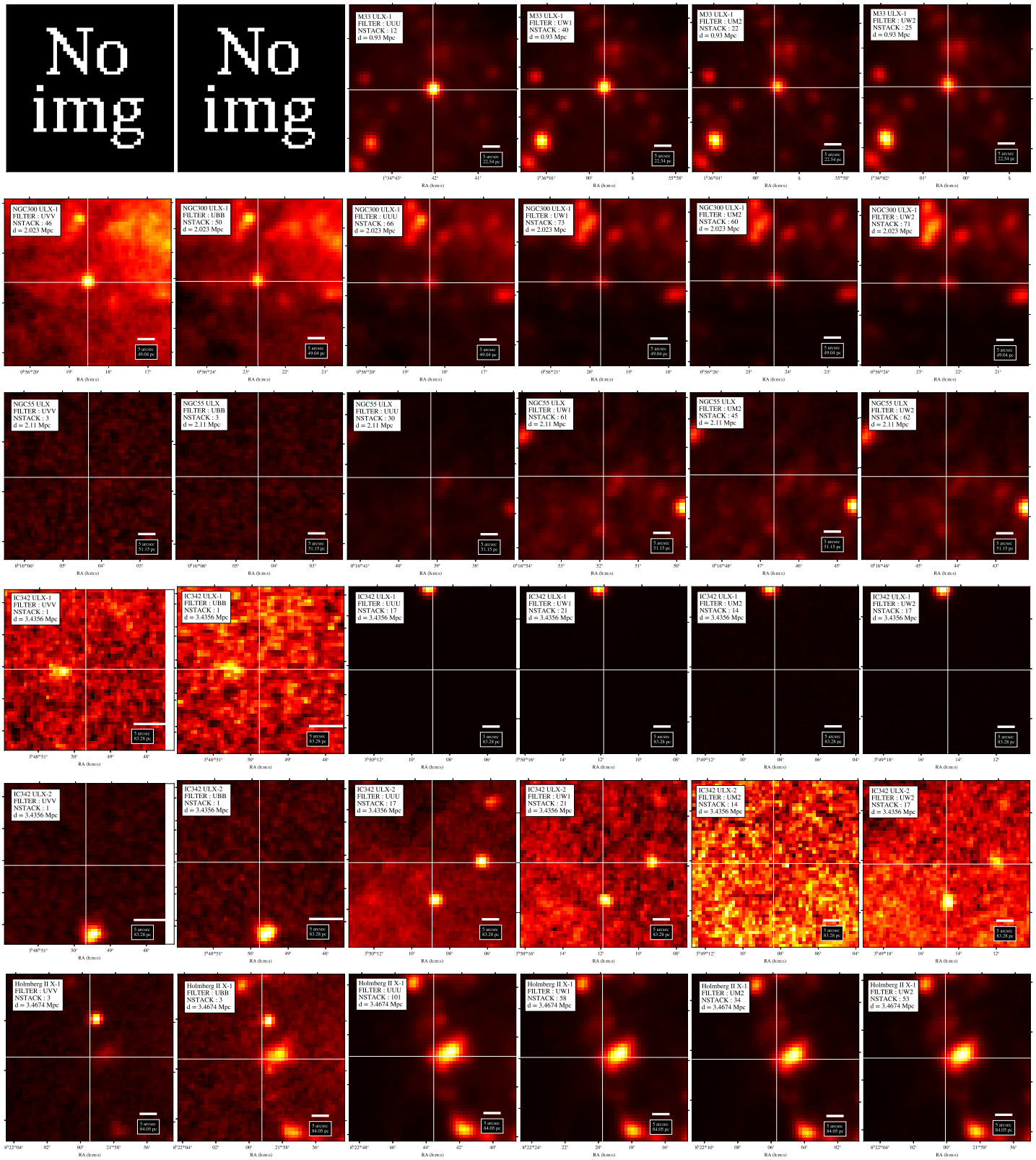
No img
No img
M33 ULX-1 FILTER : UUU NSTACK : 12 d = 0.93 Mpc
M33 ULX-1 FILTER : UW1 NSTACK : 40 d = 0.93 Mpc
M33 ULX-1 FILTER : UM2 NSTACK : 22 d = 0.93 Mpc
M33 ULX-1 FILTER : UW2 NSTACK : 25 d = 0.93 Mpc
NGC300 ULX-1 FILTER : UVV NSTACK : 46 d = 2.023 Mpc
NGC300 ULX-1 FILTER : UBB NSTACK : 50 d = 2.023 Mpc
NGC300 ULX-1 FILTER : UUU NSTACK : 66 d = 2.023 Mpc
NGC300 ULX-1 FILTER : UW1 NSTACK : 73 d = 2.023 Mpc
NGC300 ULX-1 FILTER : UM2 NSTACK : 60 d = 2.023 Mpc
NGC300 ULX-1 FILTER : UW2 NSTACK : 71 d = 2.023 Mpc
NGC55 ULX FILTER : UVV NSTACK : 3 d = 2.11 Mpc
NGC55 ULX FILTER : UBB NSTACK : 3 d = 2.11 Mpc
NGC55 ULX FILTER : UUU NSTACK : 30 d = 2.11 Mpc
NGC55 ULX FILTER : UW1 NSTACK : 61 d = 2.11 Mpc
NGC55 ULX FILTER : UM2 NSTACK : 45 d = 2.11 Mpc
NGC55 ULX FILTER : UW2 NSTACK : 62 d = 2.11 Mpc
IC342 ULX-1 FILTER : UVV NSTACK : 1 d = 3.4356 Mpc
IC342 ULX-1 FILTER : UBB NSTACK : 1 d = 3.4356 Mpc
IC342 ULX-1 FILTER : UUU NSTACK : 17 d = 3.4356 Mpc
IC342 ULX-1 FILTER : UW1 NSTACK : 21 d = 3.4356 Mpc
IC342 ULX-1 FILTER : UM2 NSTACK : 14 d = 3.4356 Mpc
IC342 ULX-1 FILTER : UW2 NSTACK : 17 d = 3.4356 Mpc
IC342 ULX-2 FILTER : UVV NSTACK : 1 d = 3.4356 Mpc
IC342 ULX-2 FILTER : UBB NSTACK : 1 d = 3.4356 Mpc
IC342 ULX-2 FILTER : UUU NSTACK : 17 d = 3.4356 Mpc
IC342 ULX-2 FILTER : UW1 NSTACK : 21 d = 3.4356 Mpc
IC342 ULX-2 FILTER : UM2 NSTACK : 14 d = 3.4356 Mpc
IC342 ULX-2 FILTER : UW2 NSTACK : 17 d = 3.4356 Mpc
Holmberg II X-1 FILTER : UVV NSTACK : 3 d = 3.4674 Mpc
Holmberg II X-1 FILTER : UBB NSTACK : 3 d = 3.4674 Mpc
Holmberg II X-1 FILTER : UUU NSTACK : 101 d = 3.4674 Mpc
Holmberg II X-1 FILTER : UW1 NSTACK : 58 d = 3.4674 Mpc
Holmberg II X-1 FILTER : UM2 NSTACK : 34 d = 3.4674 Mpc
Holmberg II X-1 FILTER : UW2 NSTACK : 53 d = 3.4674 Mpc

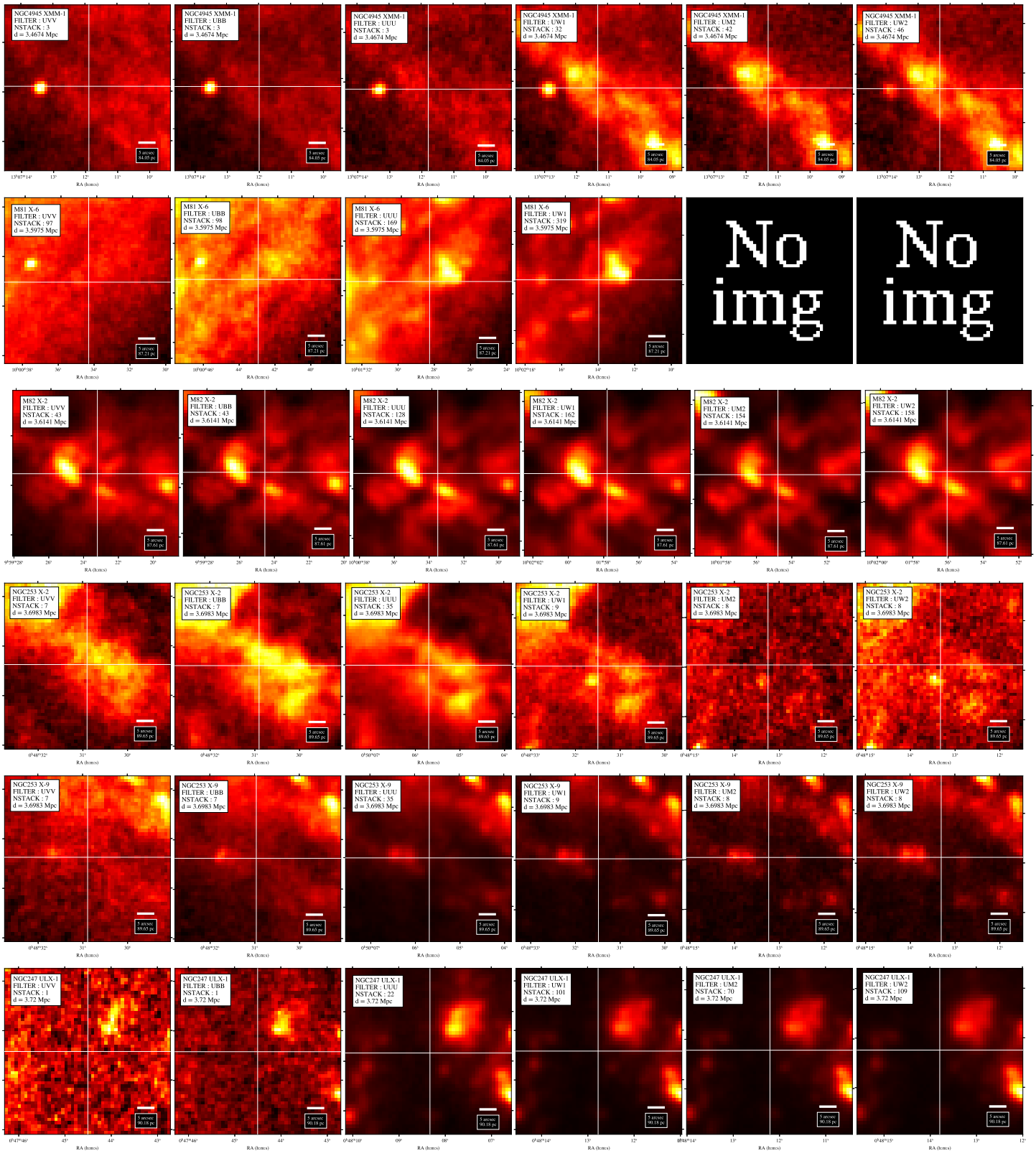
NGC4945 XMM-1
FILTER : UVV
NSTACK : 3
d = 3.4674 Mpc
NGC4945 XMM-1
FILTER : UBB
NSTACK : 3
d = 3.4674 Mpc
NGC4945 XMM-1
FILTER : UUU
NSTACK : 3
d = 3.4674 Mpc
NGC4945 XMM-1
FILTER : UW1
NSTACK : 32
d = 3.4674 Mpc
NGC4945 XMM-1
FILTER : UM2
NSTACK : 42
d = 3.4674 Mpc
NGC4945 XMM-1
FILTER : UW2
NSTACK : 46
d = 3.4674 Mpc
M81 X-6
FILTER : UVV
NSTACK : 97
d = 3.5975 Mpc
M81 X-6
FILTER : UBB
NSTACK : 98
d = 3.5975 Mpc
M81 X-6
FILTER : UUU
NSTACK : 169
d = 3.5975 Mpc
M81 X-6
FILTER : UW1
NSTACK : 319
d = 3.5975 Mpc
No
img
No
img
M82 X-2
FILTER : UVV
NSTACK : 43
d = 3.6141 Mpc
M82 X-2
FILTER : UBB
NSTACK : 43
d = 3.6141 Mpc
M82 X-2
FILTER : UUU
NSTACK : 128
d = 3.6141 Mpc
M82 X-2
FILTER : UW1
NSTACK : 162
d = 3.6141 Mpc
M82 X-2
FILTER : UM2
NSTACK : 154
d = 3.6141 Mpc
M82 X-2
FILTER : UW2
NSTACK : 158
d = 3.6141 Mpc
NGC253 X-2
FILTER : UVV
NSTACK : 7
d = 3.6983 Mpc
NGC253 X-2
FILTER : UBB
NSTACK : 7
d = 3.6983 Mpc
NGC253 X-2
FILTER : UUU
NSTACK : 35
d = 3.6983 Mpc
NGC253 X-2
FILTER : UW1
NSTACK : 9
d = 3.6983 Mpc
NGC253 X-2
FILTER : UM2
NSTACK : 8
d = 3.6983 Mpc
NGC253 X-2
FILTER : UW2
NSTACK : 8
d = 3.6983 Mpc
NGC253 X-9
FILTER : UVV
NSTACK : 7
d = 3.6983 Mpc
NGC253 X-9
FILTER : UBB
NSTACK : 7
d = 3.6983 Mpc
NGC253 X-9
FILTER : UUU
NSTACK : 35
d = 3.6983 Mpc
NGC253 X-9
FILTER : UW1
NSTACK : 9
d = 3.6983 Mpc
NGC253 X-9
FILTER : UM2
NSTACK : 8
d = 3.6983 Mpc
NGC253 X-9
FILTER : UW2
NSTACK : 8
d = 3.6983 Mpc
NGC247 ULX-1
FILTER : UVV
NSTACK : 1
d = 3.72 Mpc
NGC247 ULX-1
FILTER : UBB
NSTACK : 1
d = 3.72 Mpc
NGC247 ULX-1
FILTER : UUU
NSTACK : 22
d = 3.72 Mpc
NGC247 ULX-1
FILTER : UW1
NSTACK : 101
d = 3.72 Mpc
NGC247 ULX-1
FILTER : UM2
NSTACK : 70
d = 3.72 Mpc
NGC247 ULX-1
FILTER : UW2
NSTACK : 109
d = 3.72 Mpc

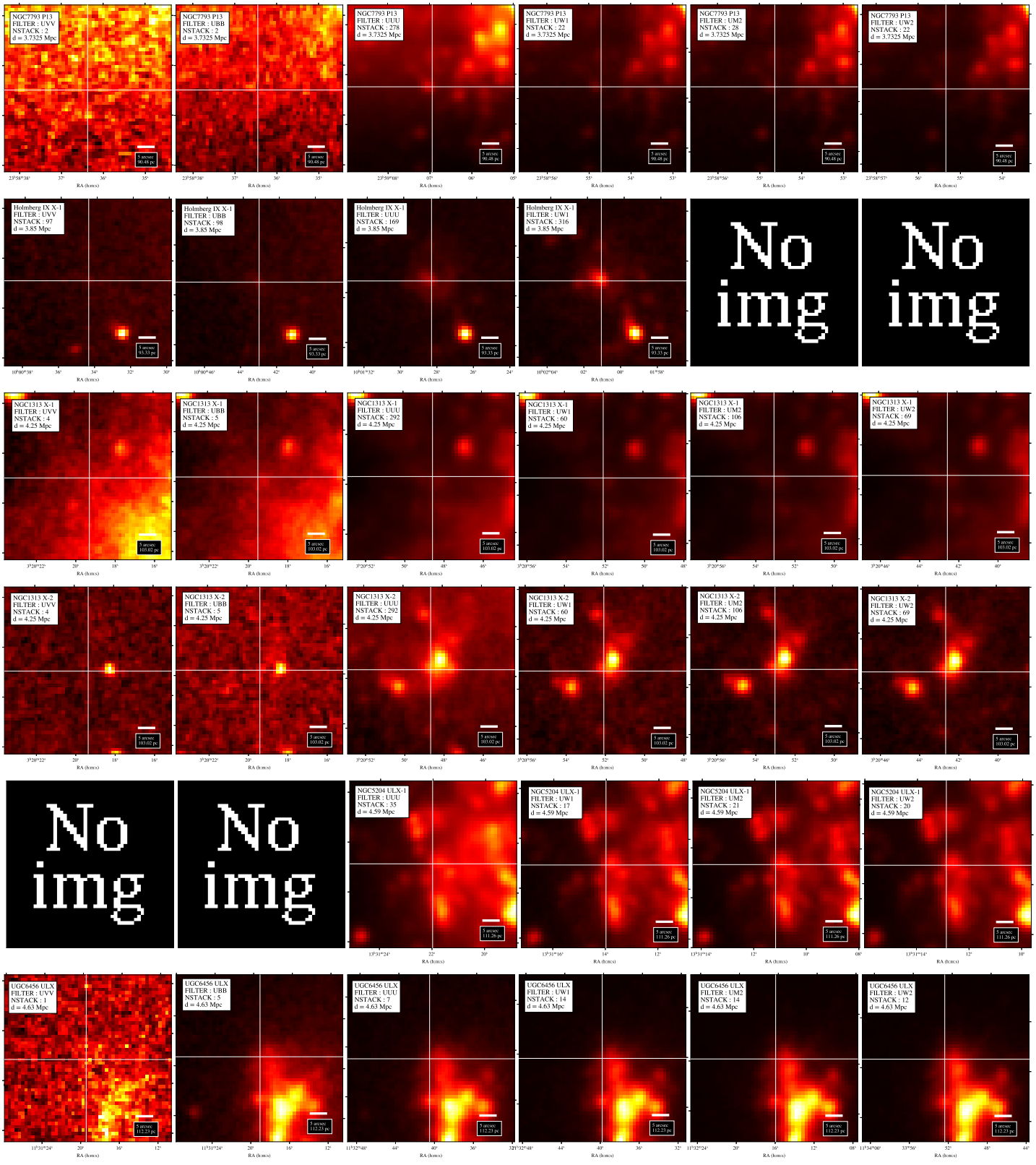
NGC7793 P13
FILTER : UVV
NSTACK : 2
d = 3.7325 Mpc
NGC7793 P13
FILTER : UBB
NSTACK : 2
d = 3.7325 Mpc
NGC7793 P13
FILTER : UUU
NSTACK : 278
d = 3.7325 Mpc
NGC7793 P13
FILTER : UW1
NSTACK : 22
d = 3.7325 Mpc
NGC7793 P13
FILTER : UM2
NSTACK : 28
d = 3.7325 Mpc
NGC7793 P13
FILTER : UW2
NSTACK : 22
d = 3.7325 Mpc
Holmberg IX X-1
FILTER : UVV
NSTACK : 97
d = 3.85 Mpc
Holmberg IX X-1
FILTER : UBB
NSTACK : 98
d = 3.85 Mpc
Holmberg IX X-1
FILTER : UUU
NSTACK : 169
d = 3.85 Mpc
Holmberg IX X-1
FILTER : UW1
NSTACK : 316
d = 3.85 Mpc
No img
No img
NGC1313 X-1
FILTER : UVV
NSTACK : 4
d = 4.25 Mpc
NGC1313 X-1
FILTER : UBB
NSTACK : 5
d = 4.25 Mpc
NGC1313 X-1
FILTER : UUU
NSTACK : 292
d = 4.25 Mpc
NGC1313 X-1
FILTER : UW1
NSTACK : 60
d = 4.25 Mpc
NGC1313 X-1
FILTER : UM2
NSTACK : 106
d = 4.25 Mpc
NGC1313 X-1
FILTER : UW2
NSTACK : 69
d = 4.25 Mpc
NGC1313 X-2
FILTER : UVV
NSTACK : 4
d = 4.25 Mpc
NGC1313 X-2
FILTER : UBB
NSTACK : 5
d = 4.25 Mpc
NGC1313 X-2
FILTER : UUU
NSTACK : 292
d = 4.25 Mpc
NGC1313 X-2
FILTER : UW1
NSTACK : 60
d = 4.25 Mpc
NGC1313 X-2
FILTER : UM2
NSTACK : 106
d = 4.25 Mpc
NGC1313 X-2
FILTER : UW2
NSTACK : 69
d = 4.25 Mpc
No img
No img
NGC5204 ULX-1
FILTER : UUU
NSTACK : 35
d = 4.59 Mpc
NGC5204 ULX-1
FILTER : UW1
NSTACK : 17
d = 4.59 Mpc
NGC5204 ULX-1
FILTER : UM2
NSTACK : 21
d = 4.59 Mpc
NGC5204 ULX-1
FILTER : UW2
NSTACK : 20
d = 4.59 Mpc
UGC6456 ULX
FILTER : UVV
NSTACK : 1
d = 4.63 Mpc
UGC6456 ULX
FILTER : UBB
NSTACK : 5
d = 4.63 Mpc
UGC6456 ULX
FILTER : UUU
NSTACK : 7
d = 4.63 Mpc
UGC6456 ULX
FILTER : UW1
NSTACK : 14
d = 4.63 Mpc
UGC6456 ULX
FILTER : UM2
NSTACK : 14
d = 4.63 Mpc
UGC6456 ULX
FILTER : UW2
NSTACK : 12
d = 4.63 Mpc

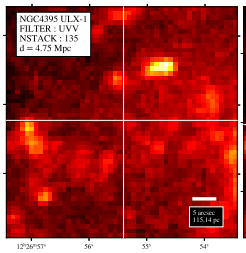

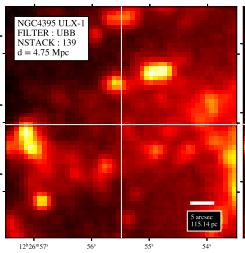

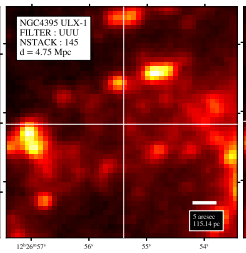

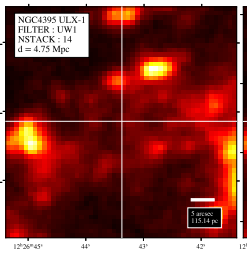

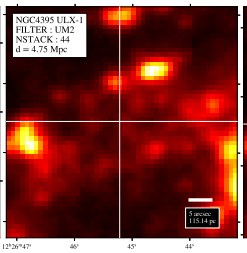

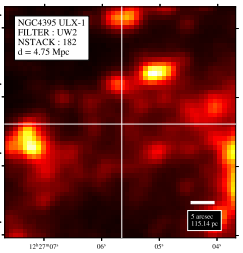

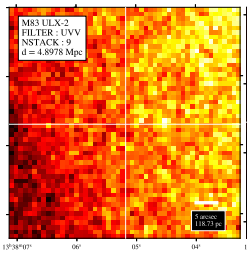

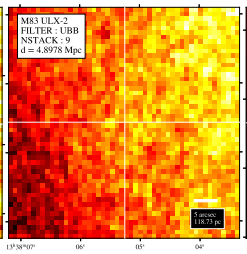

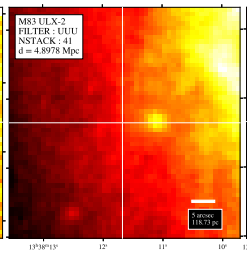

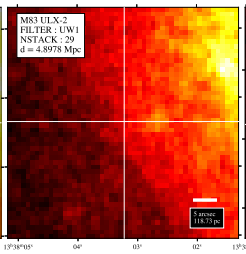

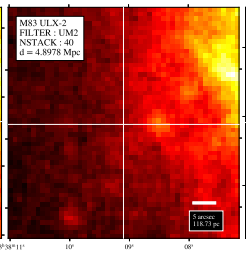

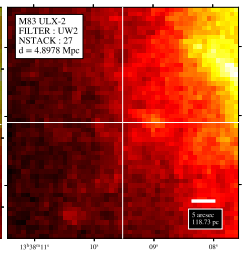

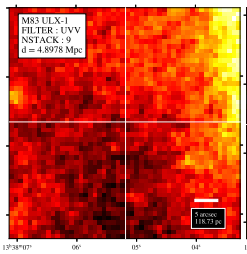

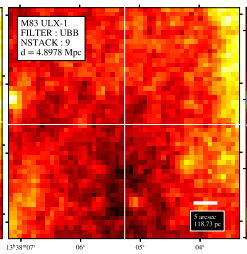

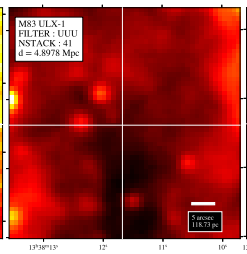

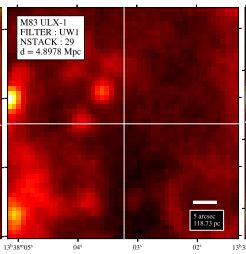

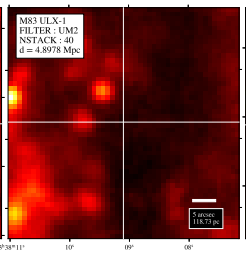

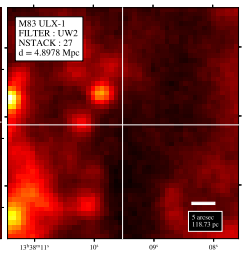

No img

No img

No img

No img

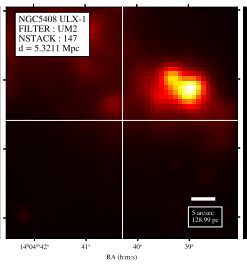

No img

No img

No img

No img

No img

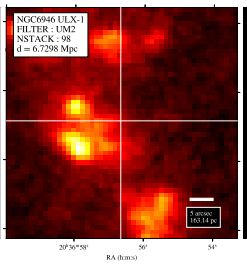

No img

No img

No img

No img

No img

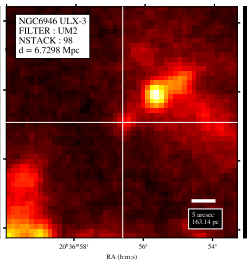

No img

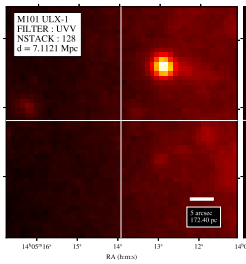

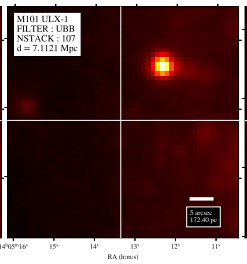

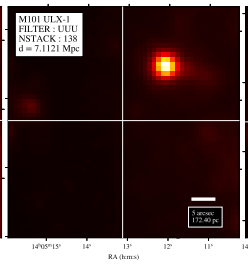

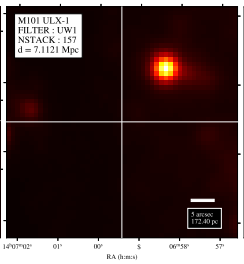

No img

No img

No img

No img

No img

No img

No img

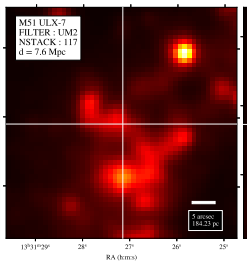

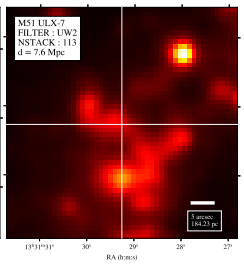

No img

No img

No img

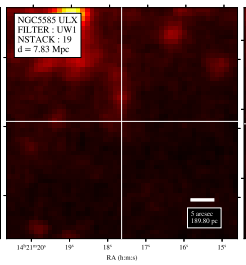

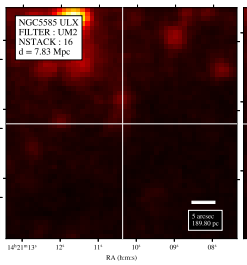

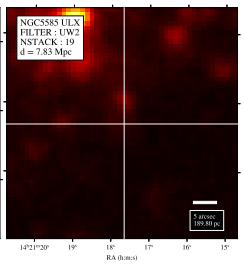

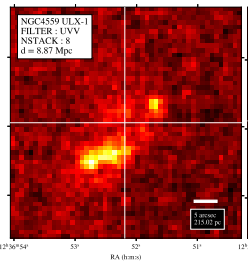

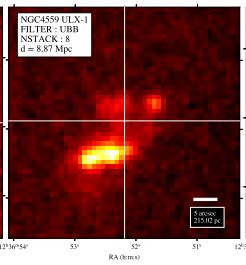

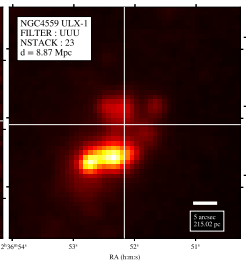

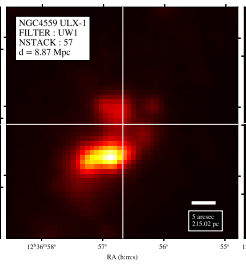

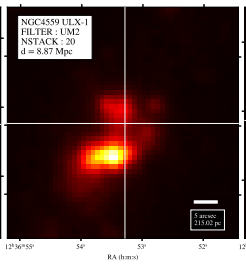

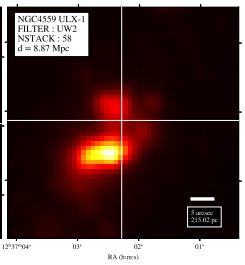

No img

No img

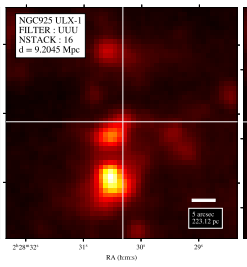

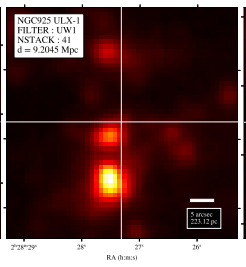

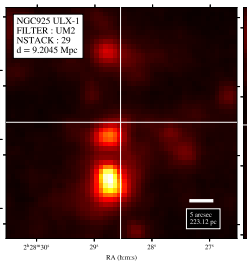

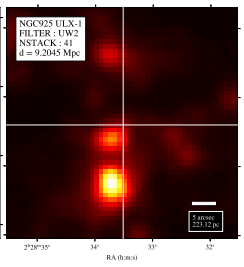

No img

No img

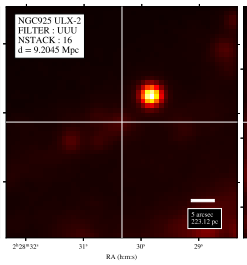

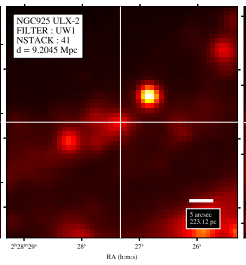

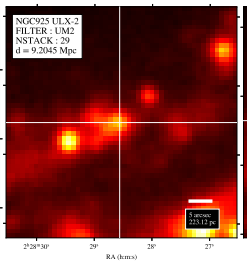

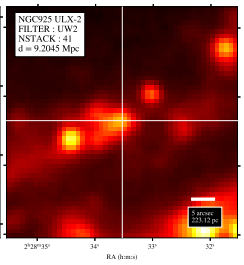

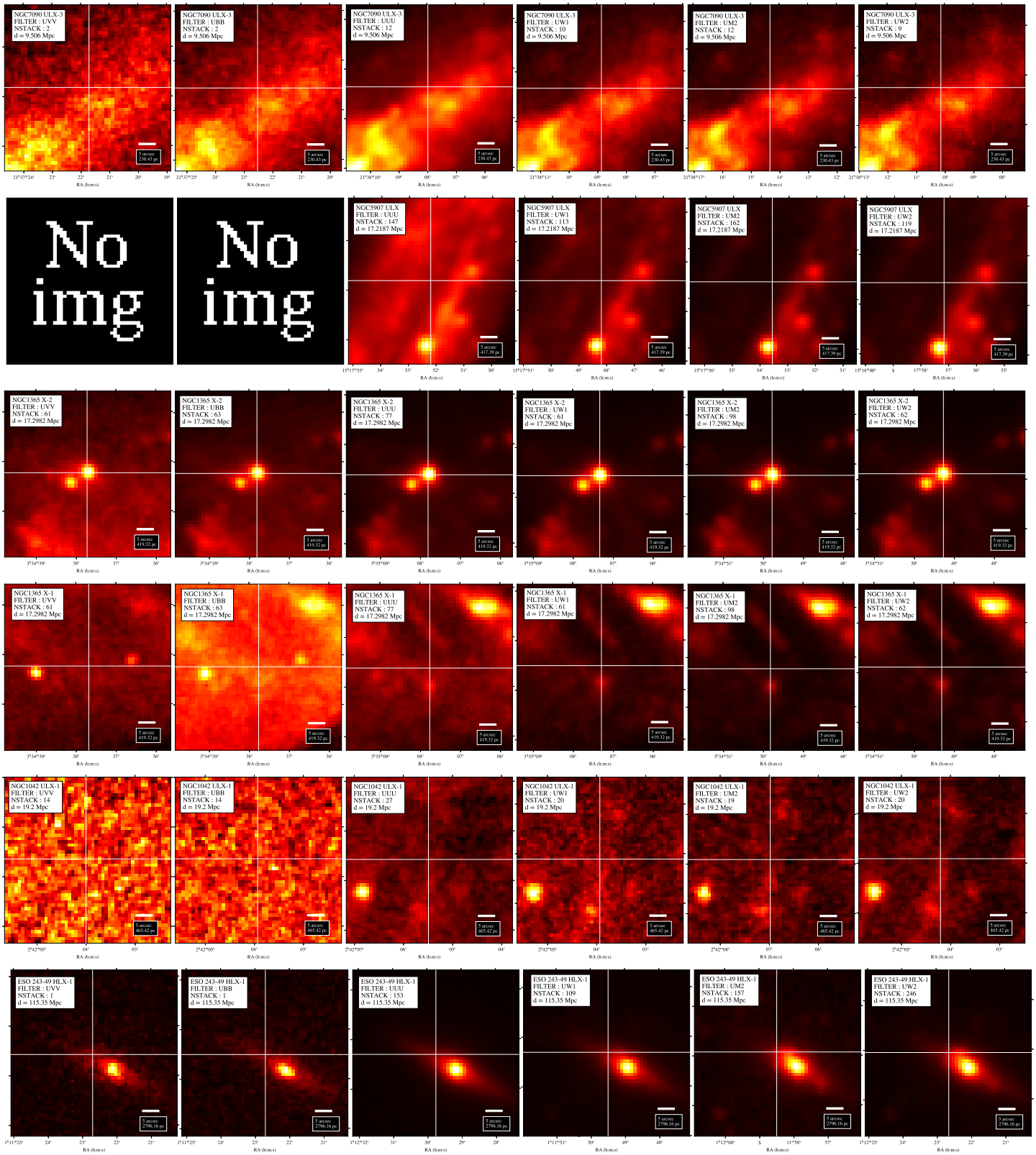
NGC7090 ULX-3
FILTER : UVV
NSTACK : 2
d = 9.506 Mpc
NGC7090 ULX-3
FILTER : UBB
NSTACK : 2
d = 9.506 Mpc
NGC7090 ULX-3
FILTER : UUU
NSTACK : 12
d = 9.506 Mpc
NGC7090 ULX-3
FILTER : UW1
NSTACK : 10
d = 9.506 Mpc
NGC7090 ULX-3
FILTER : UM2
NSTACK : 12
d = 9.506 Mpc
NGC7090 ULX-3
FILTER : UW2
NSTACK : 9
d = 9.506 Mpc
No img
No img
NGC5907 ULX
FILTER : UUU
NSTACK : 147
d = 17.2187 Mpc
NGC5907 ULX
FILTER : UW1
NSTACK : 113
d = 17.2187 Mpc
NGC5907 ULX
FILTER : UM2
NSTACK : 162
d = 17.2187 Mpc
NGC5907 ULX
FILTER : UW2
NSTACK : 119
d = 17.2187 Mpc
NGC1365 X-2
FILTER : UVV
NSTACK : 61
d = 17.2982 Mpc
NGC1365 X-2
FILTER : UBB
NSTACK : 63
d = 17.2982 Mpc
NGC1365 X-2
FILTER : UUU
NSTACK : 77
d = 17.2982 Mpc
NGC1365 X-2
FILTER : UW1
NSTACK : 61
d = 17.2982 Mpc
NGC1365 X-2
FILTER : UM2
NSTACK : 98
d = 17.2982 Mpc
NGC1365 X-2
FILTER : UW2
NSTACK : 62
d = 17.2982 Mpc
NGC1365 X-1
FILTER : UVV
NSTACK : 61
d = 17.2982 Mpc
NGC1365 X-1
FILTER : UBB
NSTACK : 63
d = 17.2982 Mpc
NGC1365 X-1
FILTER : UUU
NSTACK : 77
d = 17.2982 Mpc
NGC1365 X-1
FILTER : UW1
NSTACK : 61
d = 17.2982 Mpc
NGC1365 X-1
FILTER : UM2
NSTACK : 98
d = 17.2982 Mpc
NGC1365 X-1
FILTER : UW2
NSTACK : 62
d = 17.2982 Mpc
NGC1042 ULX-1
FILTER : UVV
NSTACK : 14
d = 19.2 Mpc
NGC1042 ULX-1
FILTER : UBB
NSTACK : 14
d = 19.2 Mpc
NGC1042 ULX-1
FILTER : UUU
NSTACK : 27
d = 19.2 Mpc
NGC1042 ULX-1
FILTER : UW1
NSTACK : 20
d = 19.2 Mpc
NGC1042 ULX-1
FILTER : UM2
NSTACK : 19
d = 19.2 Mpc
NGC1042 ULX-1
FILTER : UW2
NSTACK : 20
d = 19.2 Mpc
ESO 243-49 HLX-1
FILTER : UVV
NSTACK : 1
d = 115.35 Mpc
ESO 243-49 HLX-1
FILTER : UBB
NSTACK : 1
d = 115.35 Mpc
ESO 243-49 HLX-1
FILTER : UUU
NSTACK : 153
d = 115.35 Mpc
ESO 243-49 HLX-1
FILTER : UW1
NSTACK : 109
d = 115.35 Mpc
ESO 243-49 HLX-1
FILTER : UM2
NSTACK : 157
d = 115.35 Mpc
ESO 243-49 HLX-1
FILTER : UW2
NSTACK : 246
d = 115.35 Mpc

A.4 Joined light curves

Here a present the fully joined light UVOT light curves across all filters and all energy bands. The top row in each plot corresponds to the XRT rate in the `hard`, `soft` and `full` bands, while the bottom row corresponds to the UVOT rates in all filters.

Since it is often the case that the count rates in the UV filters (UVW1, UVM2, UVW2) are often much lower than the optical filters (U, V, B) I have separated the optical and UV bands on separate y-axis. The left axis gives the optical count rate, while the right axis gives the UV count rate.

The choice of plotting the data in this way is to aim to maximize the visibility of the relative changes in flux.

Sometimes the X-ray data points extend further than the UV, this is because the X-ray light curves were re-processed more recently compared to the UVOT ones and so there can be additional data for the X-ray. Similarly, sometimes there is no UVOT data for an X-ray observation, this is as the UVOT does not observe for all observations.

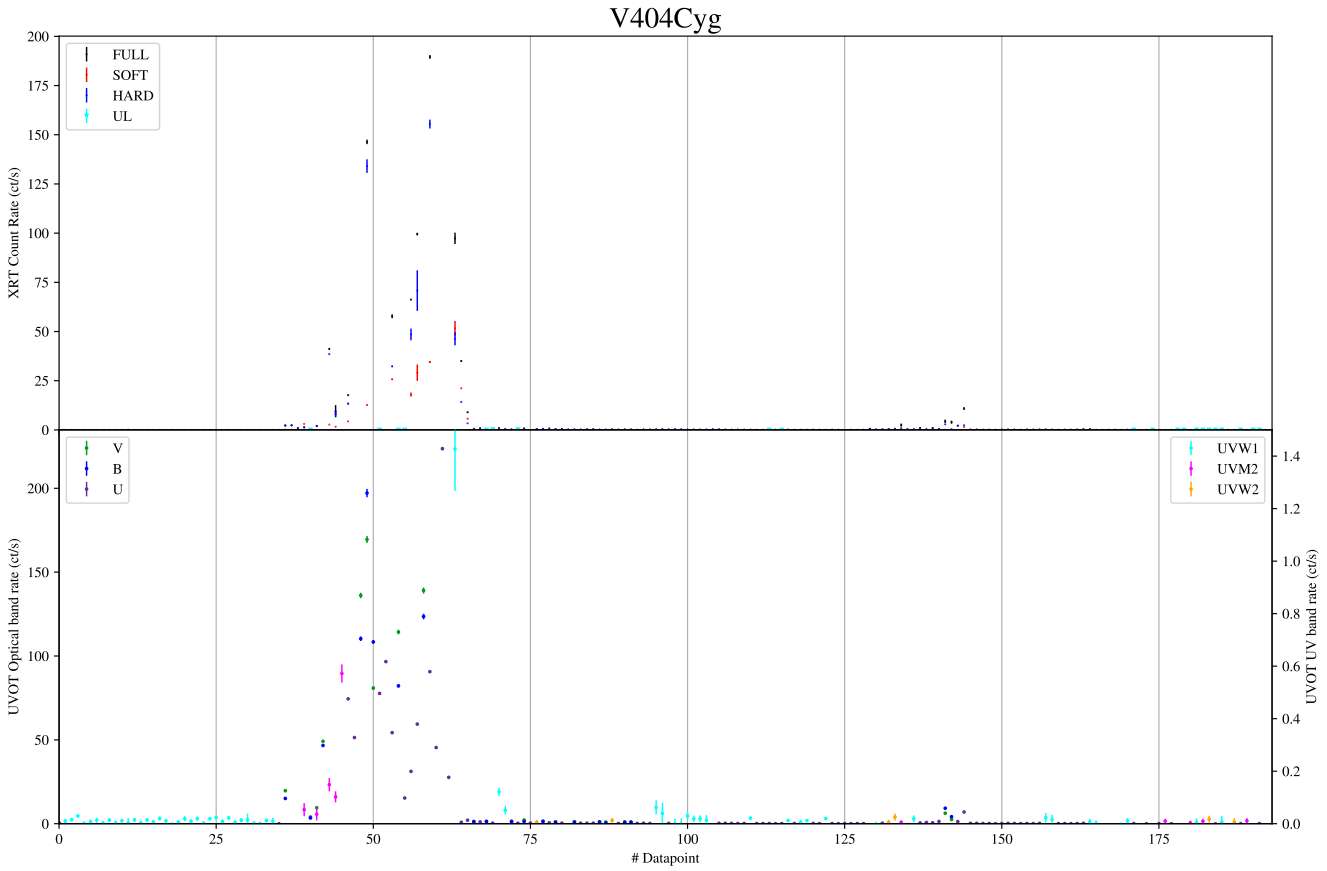
V404Cyg
FULL
SOFT
HARD
UL
XRT Count Rate (ct/s)
V
B
U
UVW1
UVM2
UVW2
UVOT Optical band rate (ct/s)
UVOT UV band rate (ct/s)
Datapoint

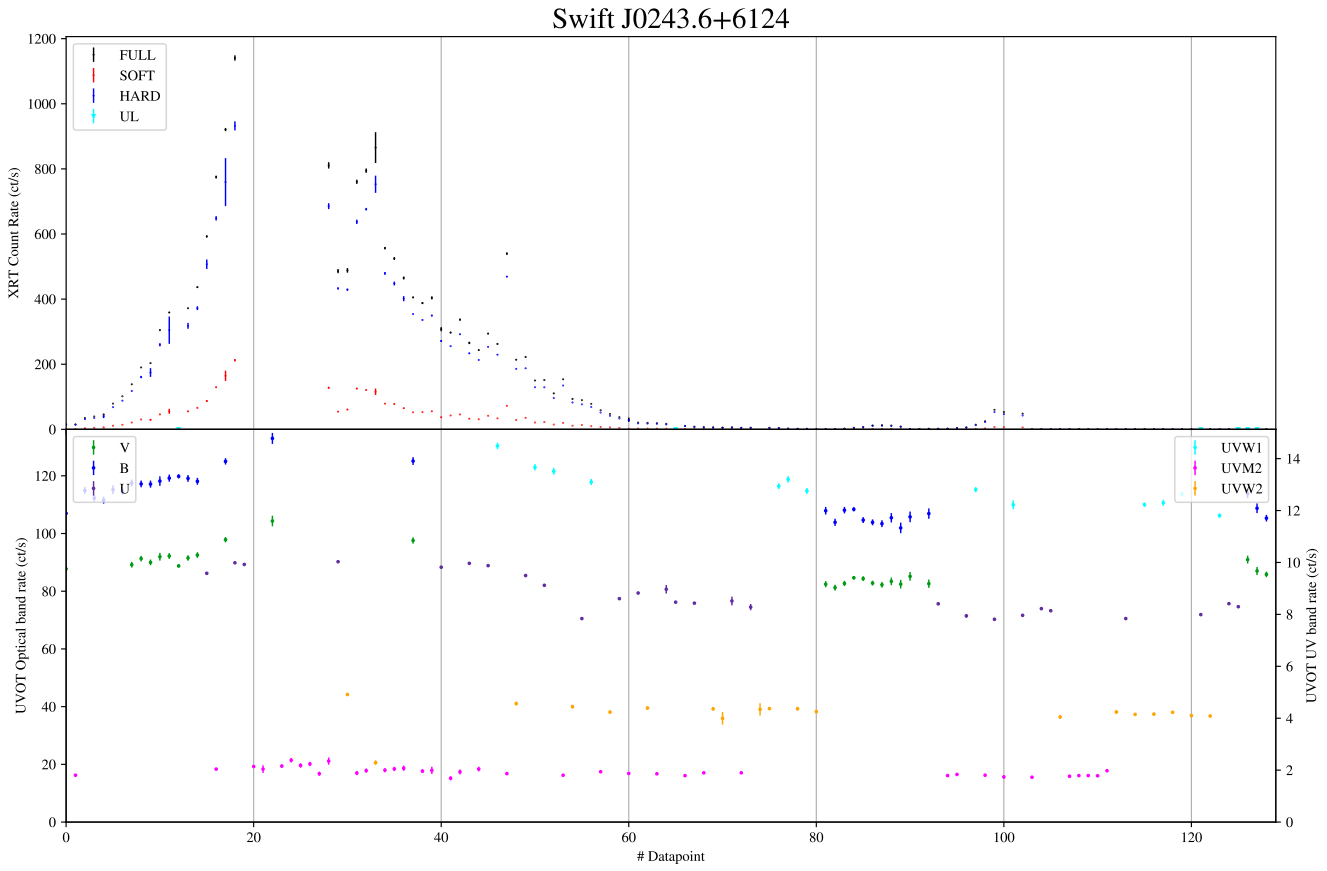
Swift J0243.6+6124
FULL
SOFT
HARD
UL
XRT Count Rate (ct/s)
V
B
U
UVW1
UVM2
UVW2
UVOT Optical band rate (ct/s)
UVOT UV band rate (ct/s)
Datapoint

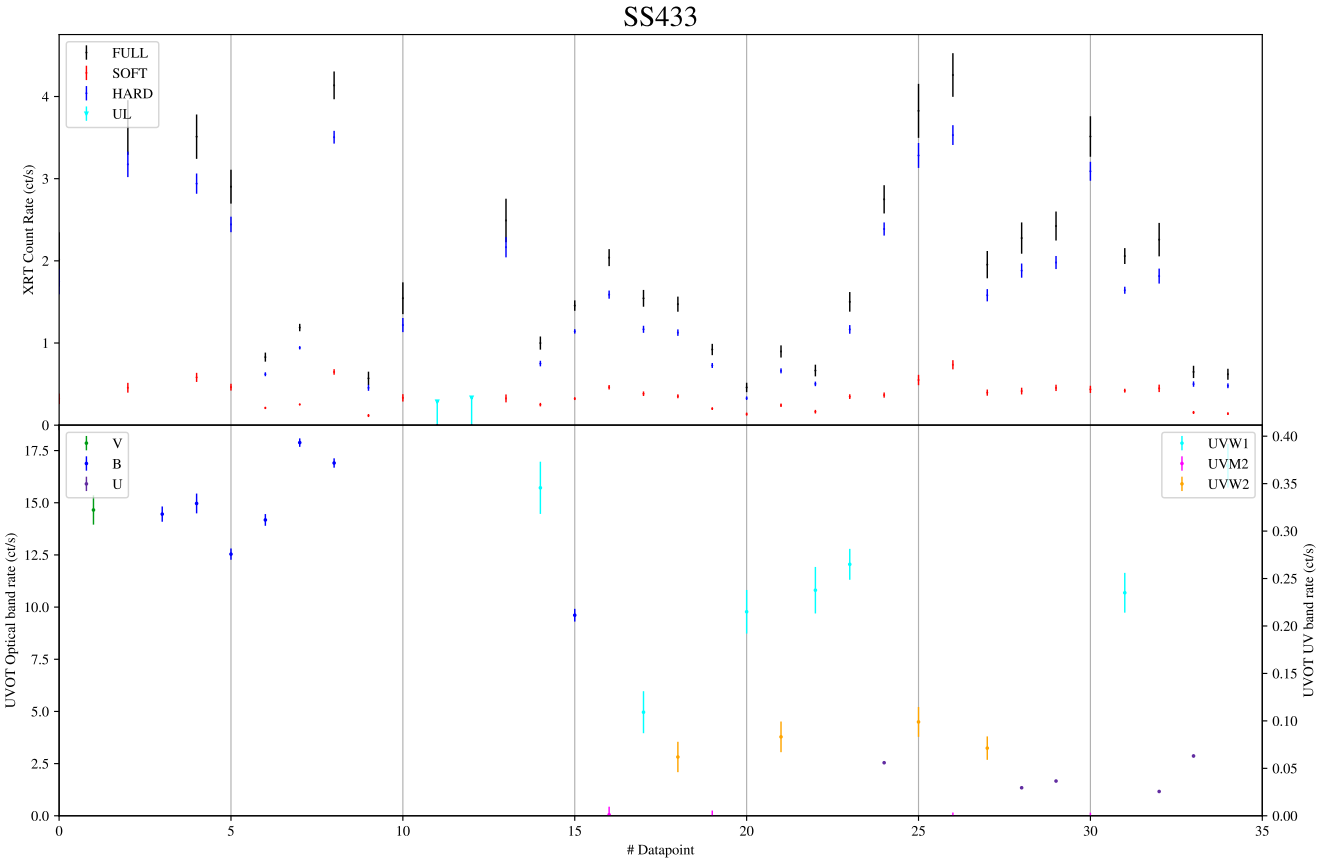
SS433
FULL
SOFT
HARD
UL
XRT Count Rate (ct/s)
V
B
U
UVW1
UVM2
UVW2
UVOT Optical band rate (ct/s)
UVOT UV band rate (ct/s)
Datapoint

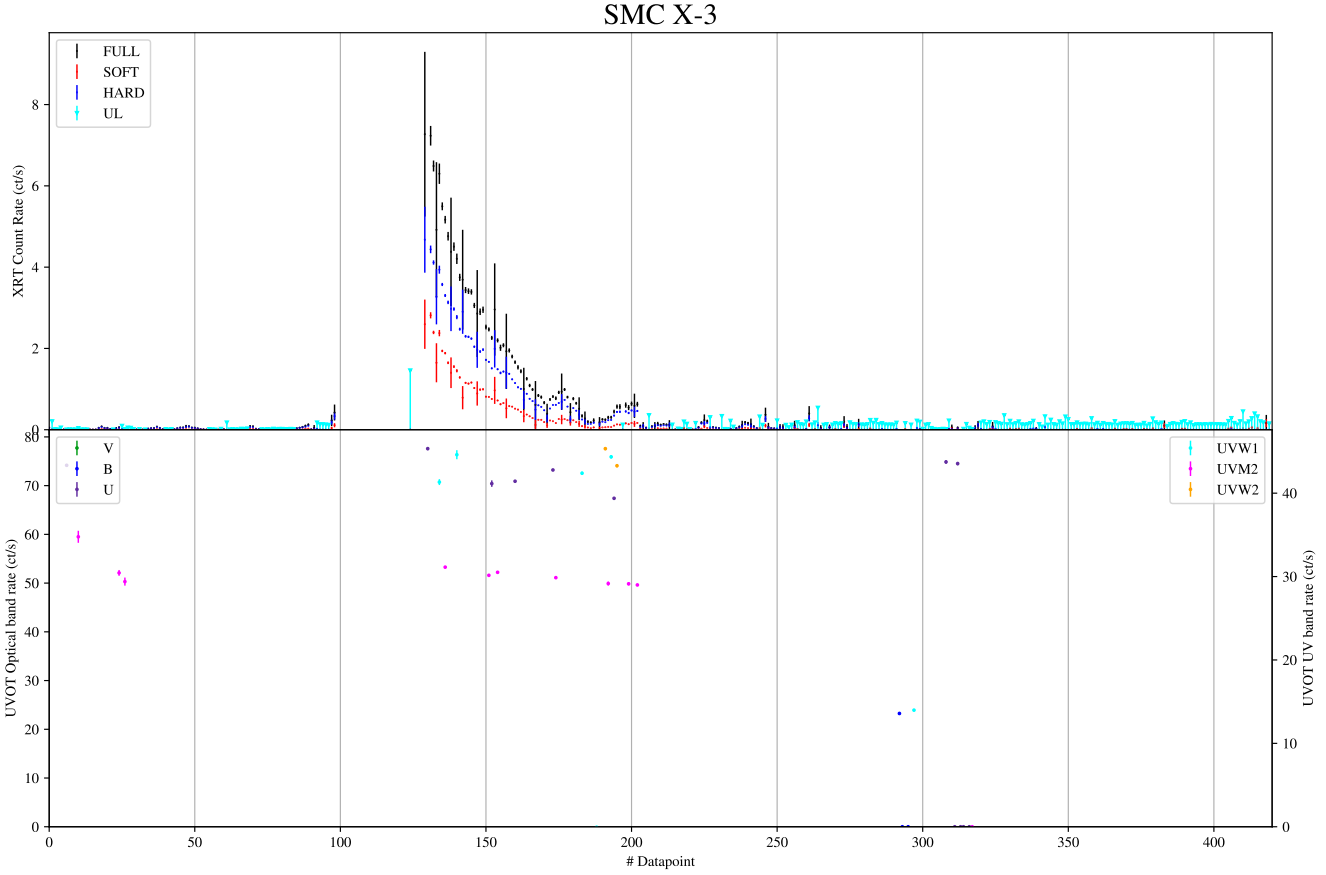
SMC X-3
FULL
SOFT
HARD
UL
XRT Count Rate (ct/s)
V
B
U
UVW1
UVM2
UVW2
UVOT Optical band rate (ct/s)
UVOT UV band rate (ct/s)
Datapoint

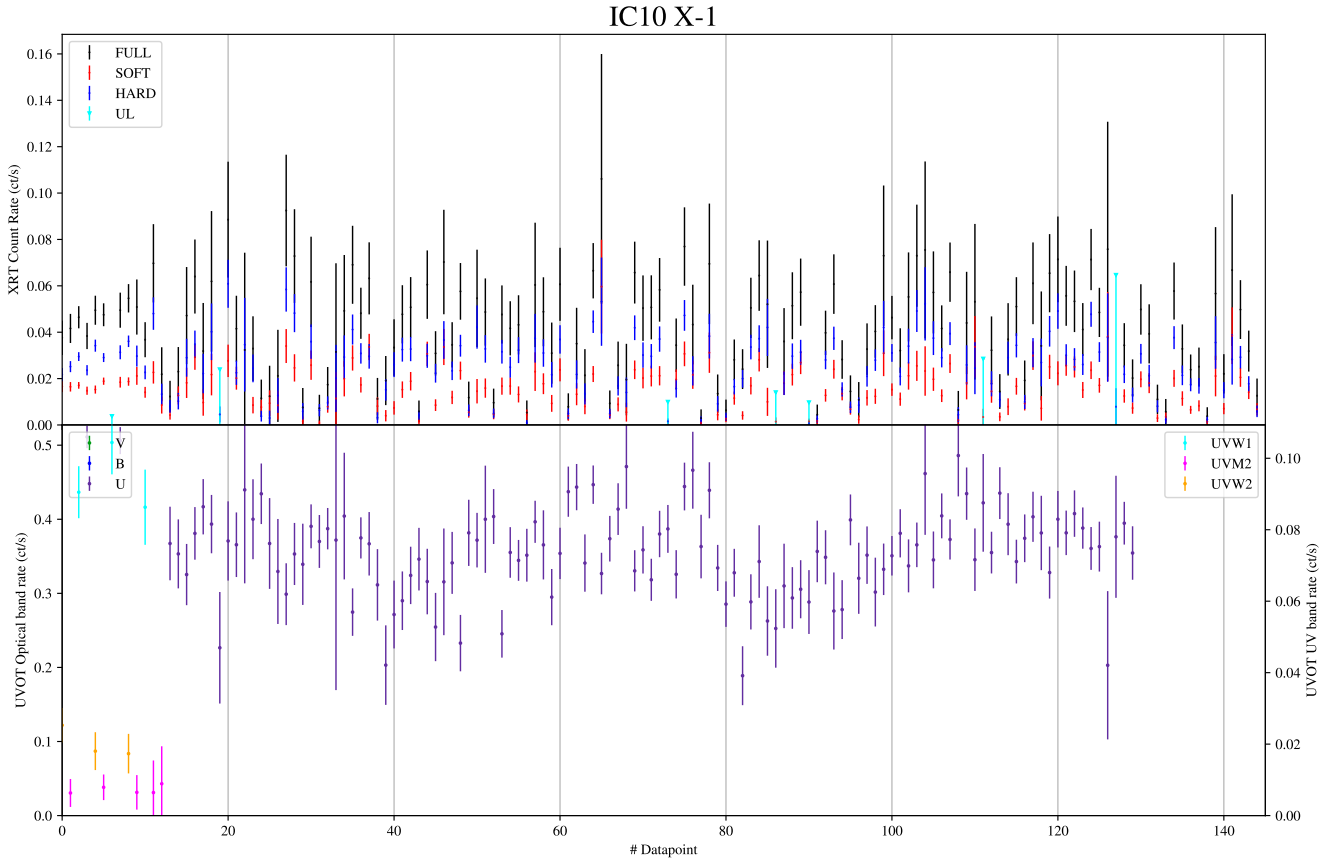
IC10 X-1
FULL
SOFT
HARD
UL
XRT Count Rate (ct/s)
V
B
U
UVW1
UVM2
UVW2
UVOT Optical band rate (ct/s)
UVOT UV band rate (ct/s)
Datapoint

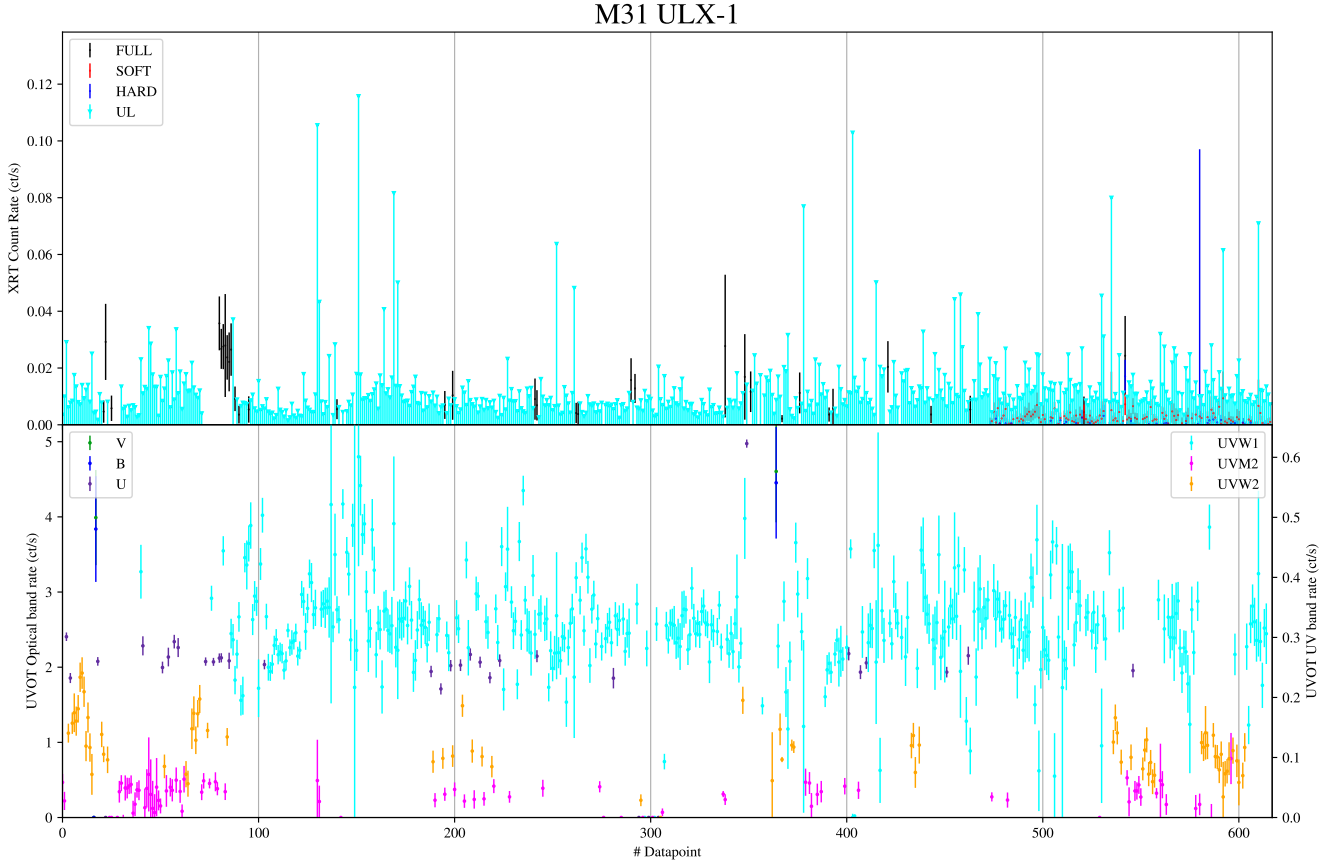
M31 ULX-1
FULL
SOFT
HARD
UL
XRT Count Rate (ct/s)
V
B
U
UVW1
UVM2
UVW2
UVOT Optical band rate (ct/s)
UVOT UV band rate (ct/s)
Datapoint

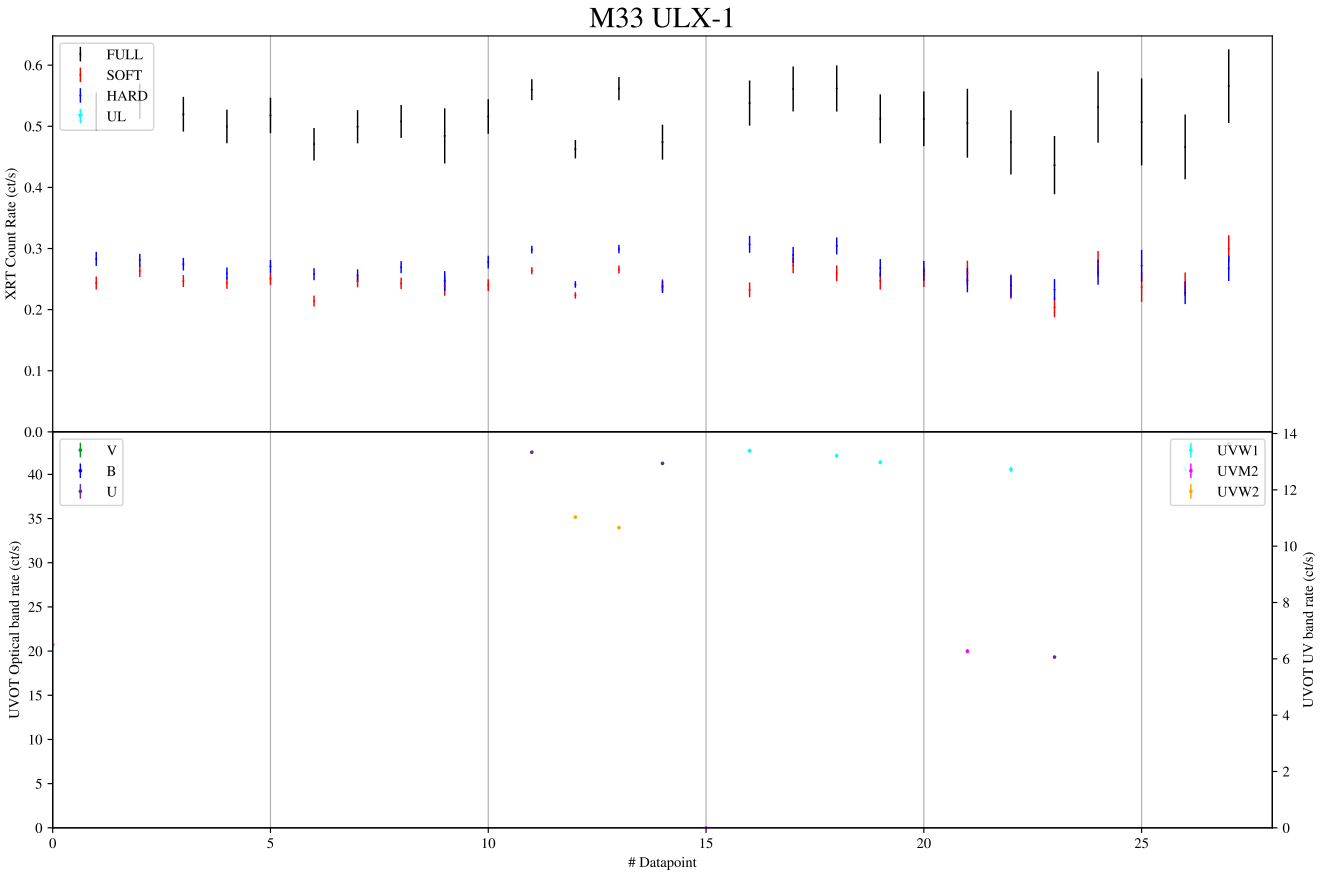
M33 ULX-1
FULL
SOFT
HARD
UL
XRT Count Rate (ct/s)
V
B
U
UVW1
UVM2
UVW2
UVOT Optical band rate (ct/s)
UVOT UV band rate (ct/s)
Datapoint

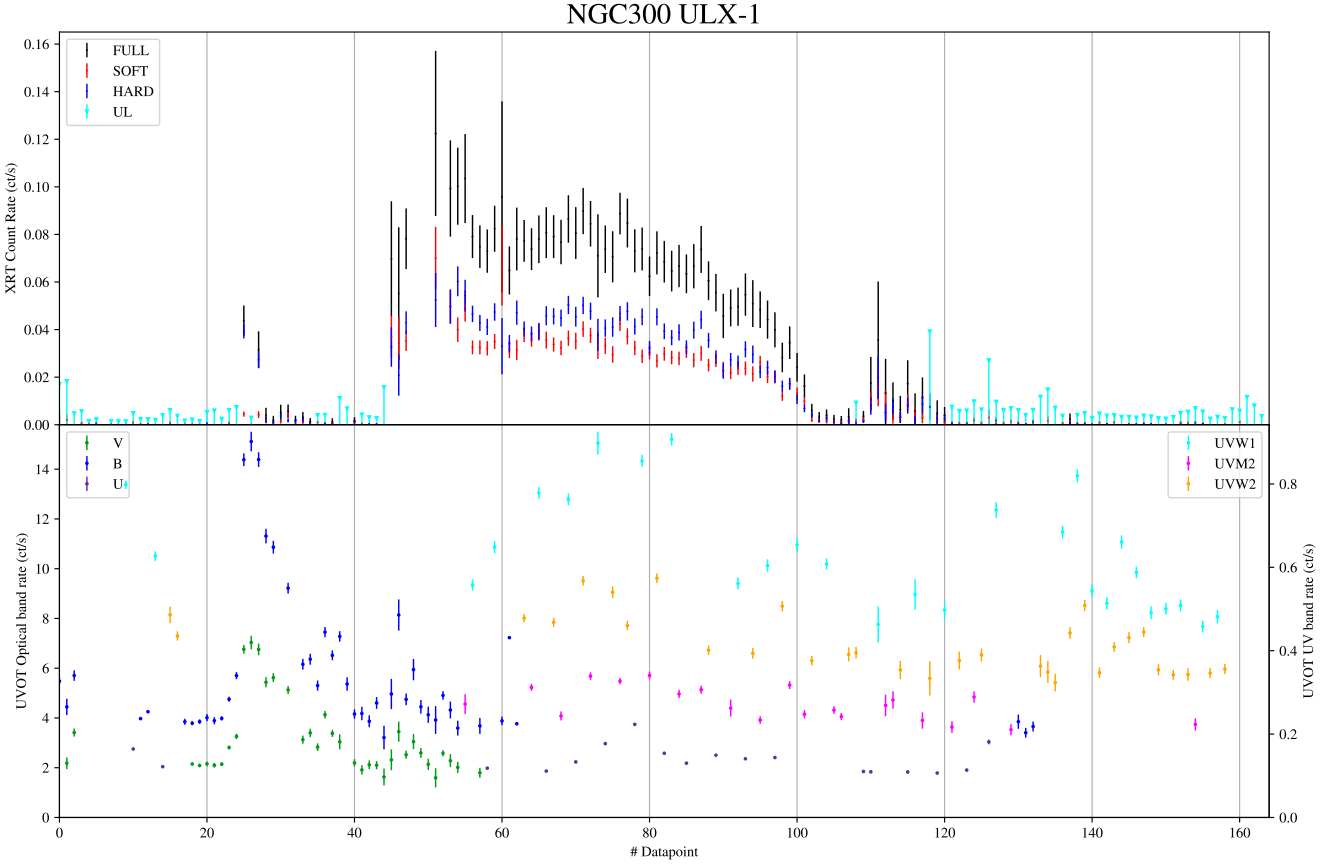
NGC300 ULX-1
FULL
SOFT
HARD
UL
XRT Count Rate (ct/s)
V
B
U
UVW1
UVM2
UVW2
UVOT Optical band rate (ct/s)
UVOT UV band rate (ct/s)
Datapoint

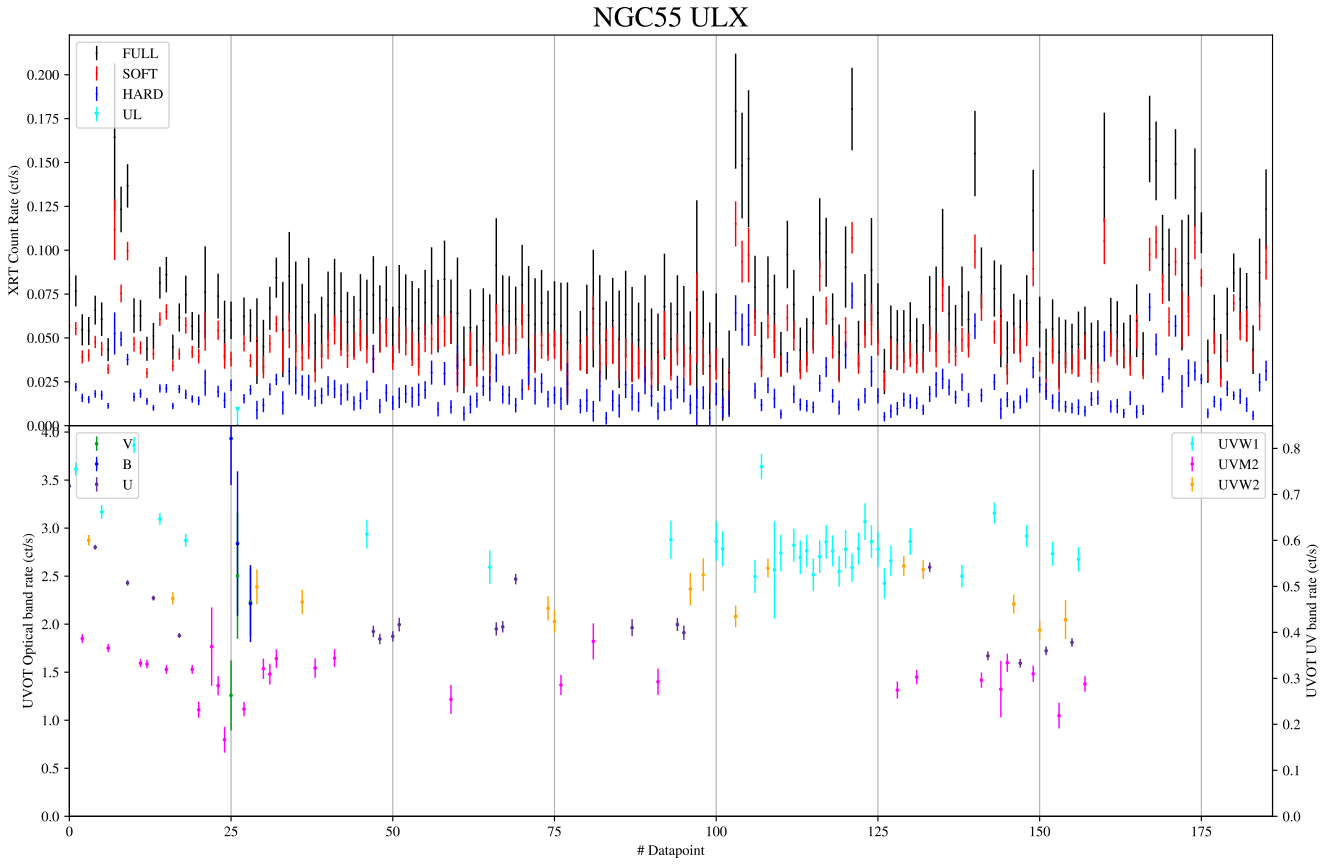
NGC55 ULX
FULL
SOFT
HARD
UL
XRT Count Rate (ct/s)
V
B
U
UVW1
UVM2
UVW2
UVOT Optical band rate (ct/s)
UVOT UV band rate (ct/s)
Datapoint

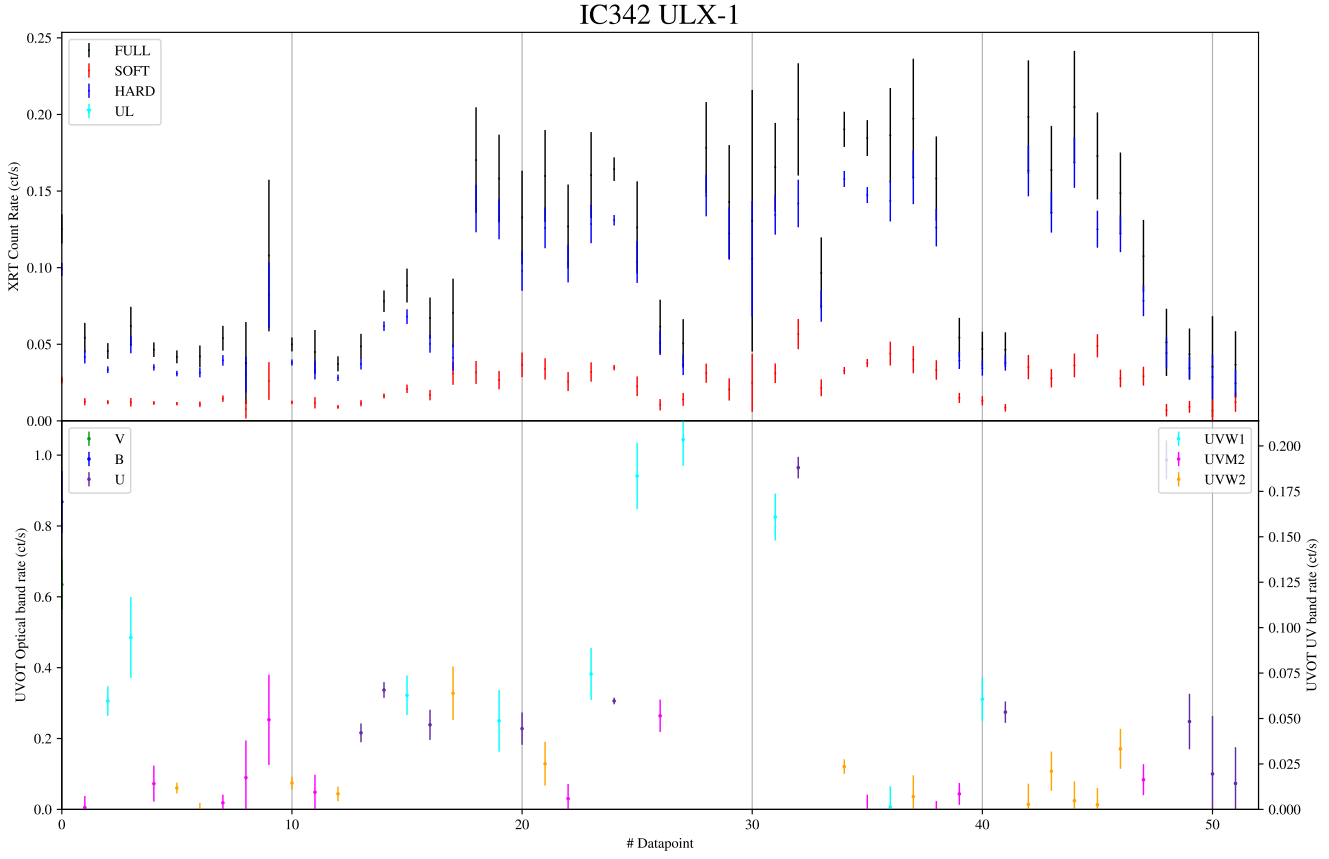
IC342 ULX-1
FULL
SOFT
HARD
UL
XRT Count Rate (ct/s)
V
B
U
UVW1
UVM2
UVW2
UVOT Optical band rate (ct/s)
UVOT UV band rate (ct/s)
Datapoint

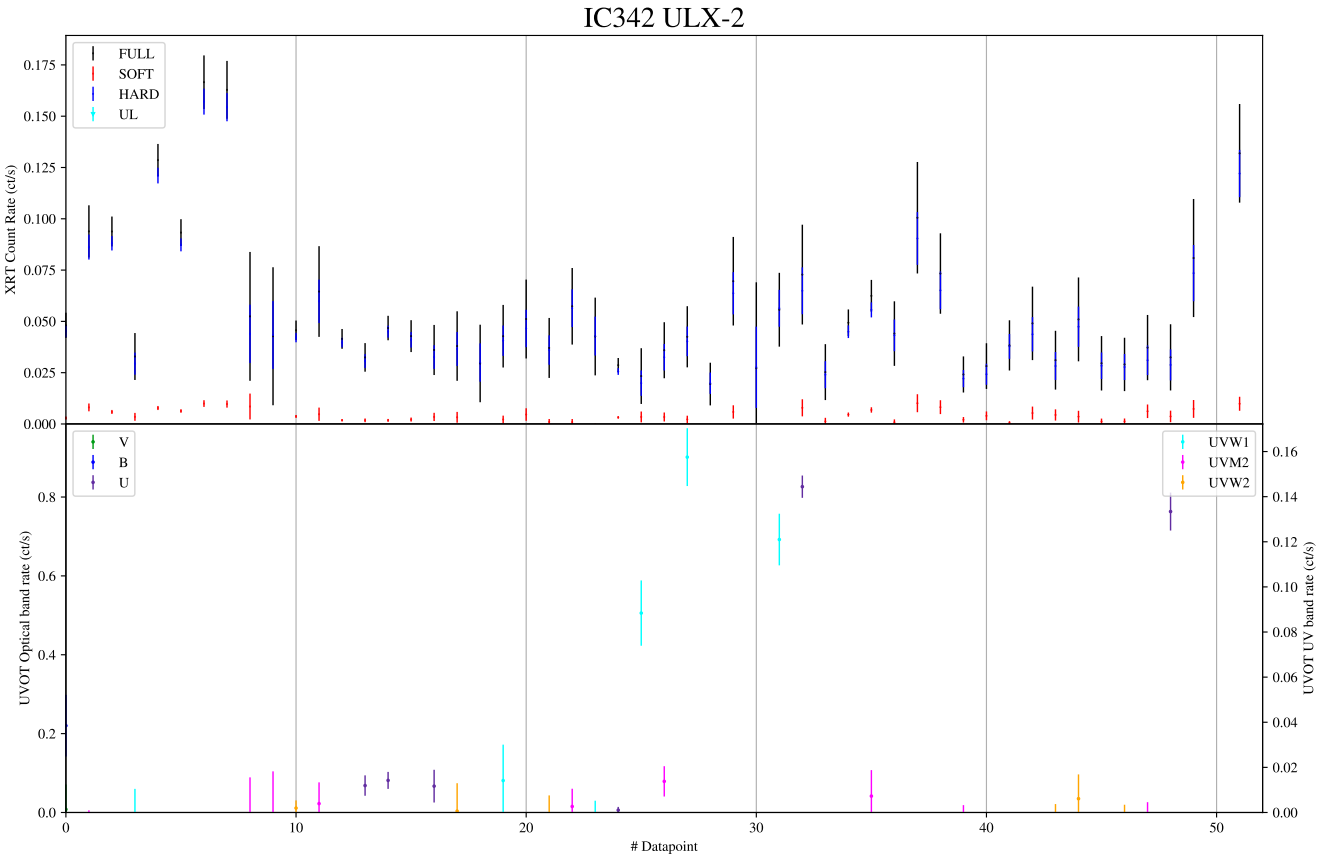
IC342 ULX-2
FULL
SOFT
HARD
UL
XRT Count Rate (ct/s)
V
B
U
UVW1
UVM2
UVW2
UVOT Optical band rate (ct/s)
UVOT UV band rate (ct/s)
Datapoint

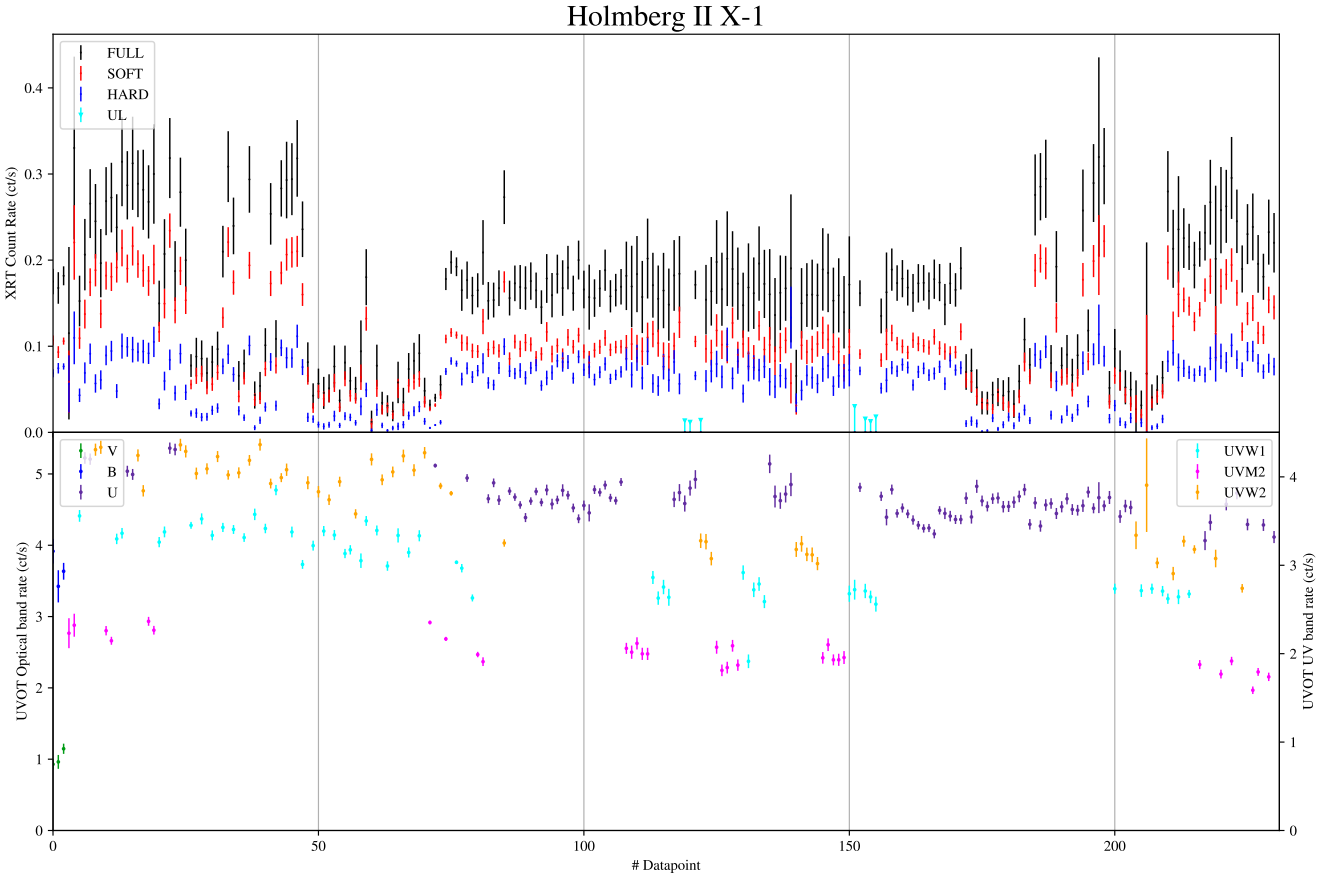
Holmberg II X-1
FULL
SOFT
HARD
UL
XRT Count Rate (ct/s)
V
B
U
UVW1
UVM2
UVW2
UVOT Optical band rate (ct/s)
UVOT UV band rate (ct/s)
Datapoint

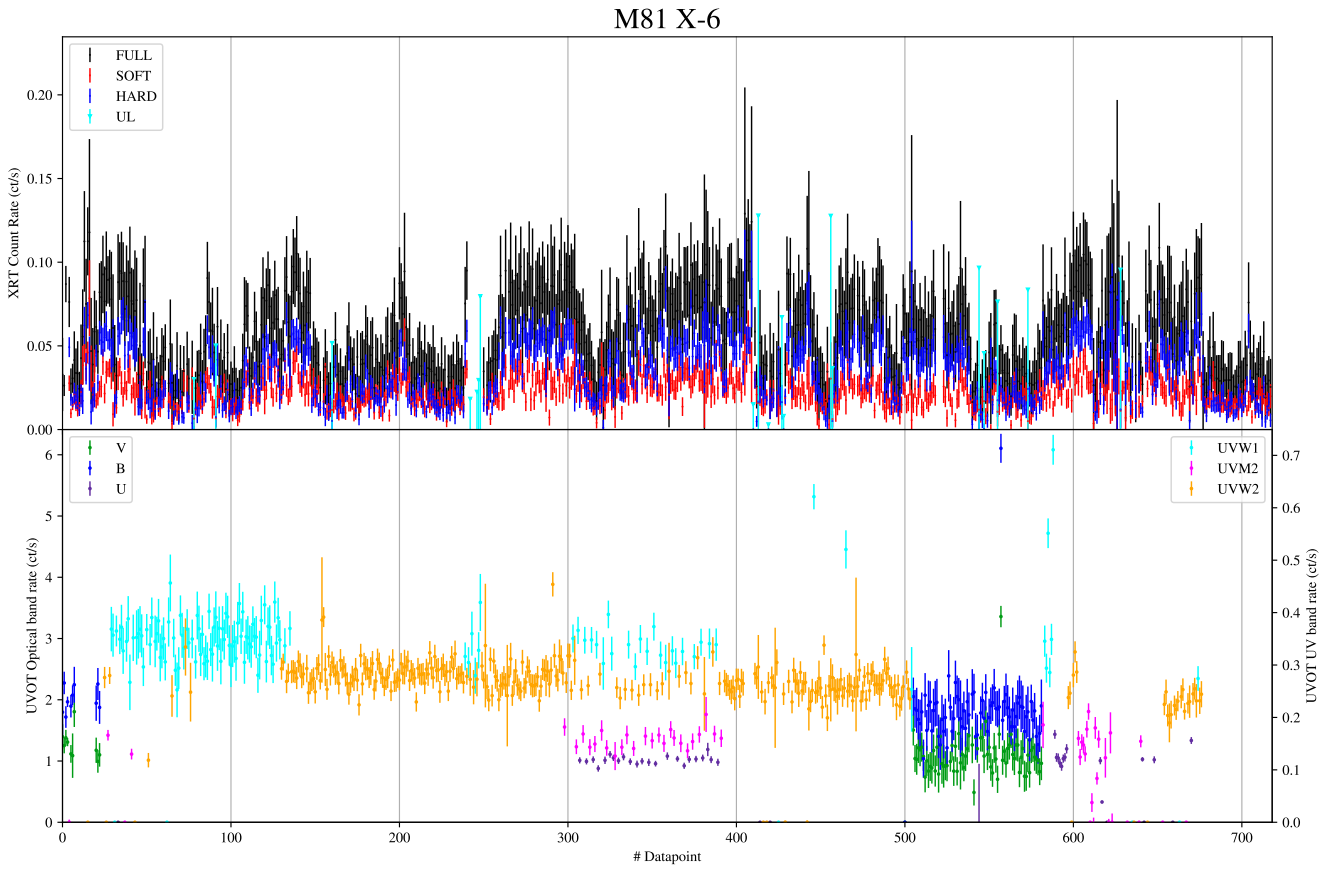
M81 X-6
FULL
SOFT
HARD
UL
XRT Count Rate (ct/s)
V
B
U
UVW1
UVM2
UVW2
UVOT Optical band rate (ct/s)
UVOT UV band rate (ct/s)
Datapoint

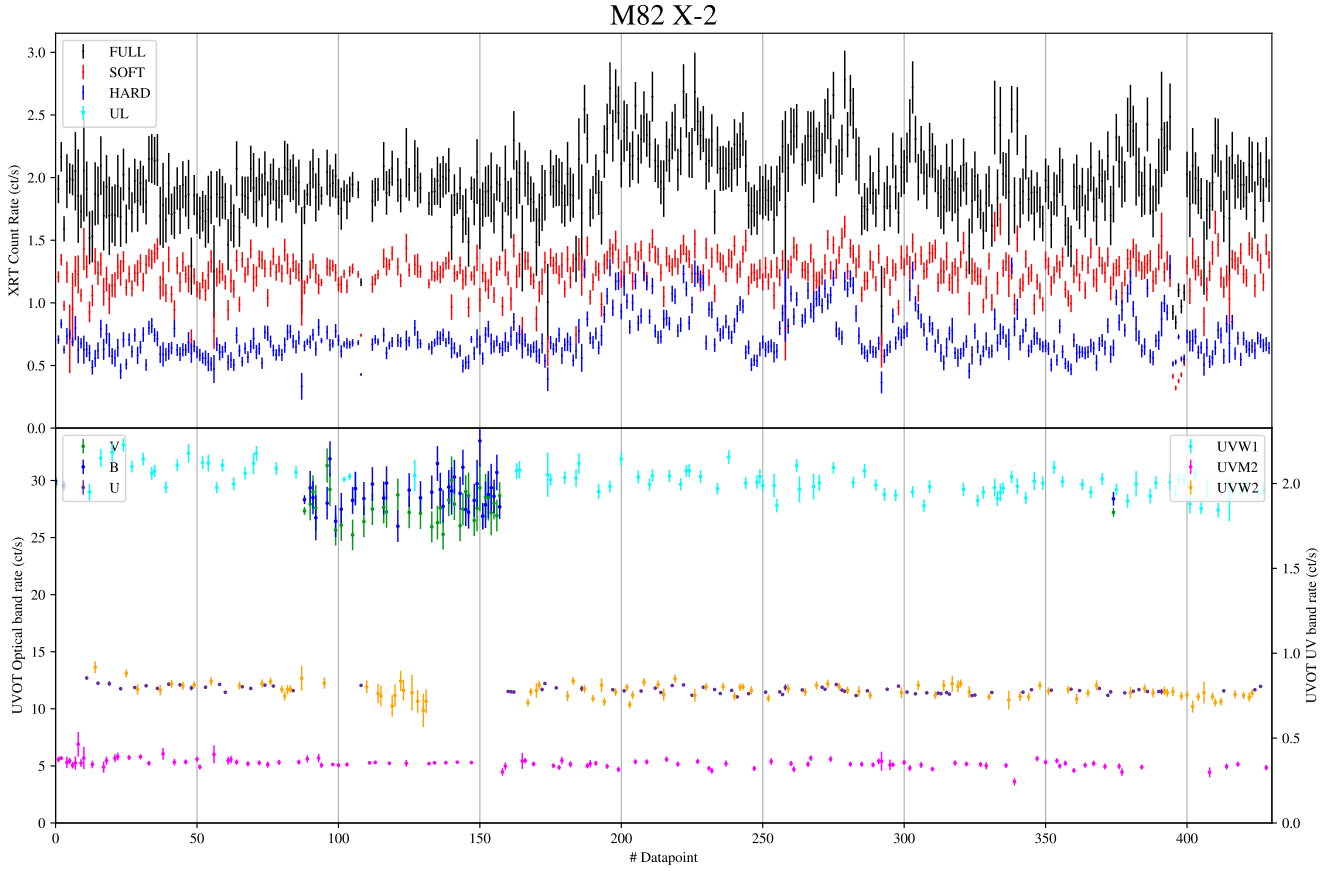
M82 X-2
FULL
SOFT
HARD
UL
XRT Count Rate (ct/s)
V
B
U
UVW1
UVM2
UVW2
UVOT Optical band rate (ct/s)
UVOT UV band rate (ct/s)
Datapoint

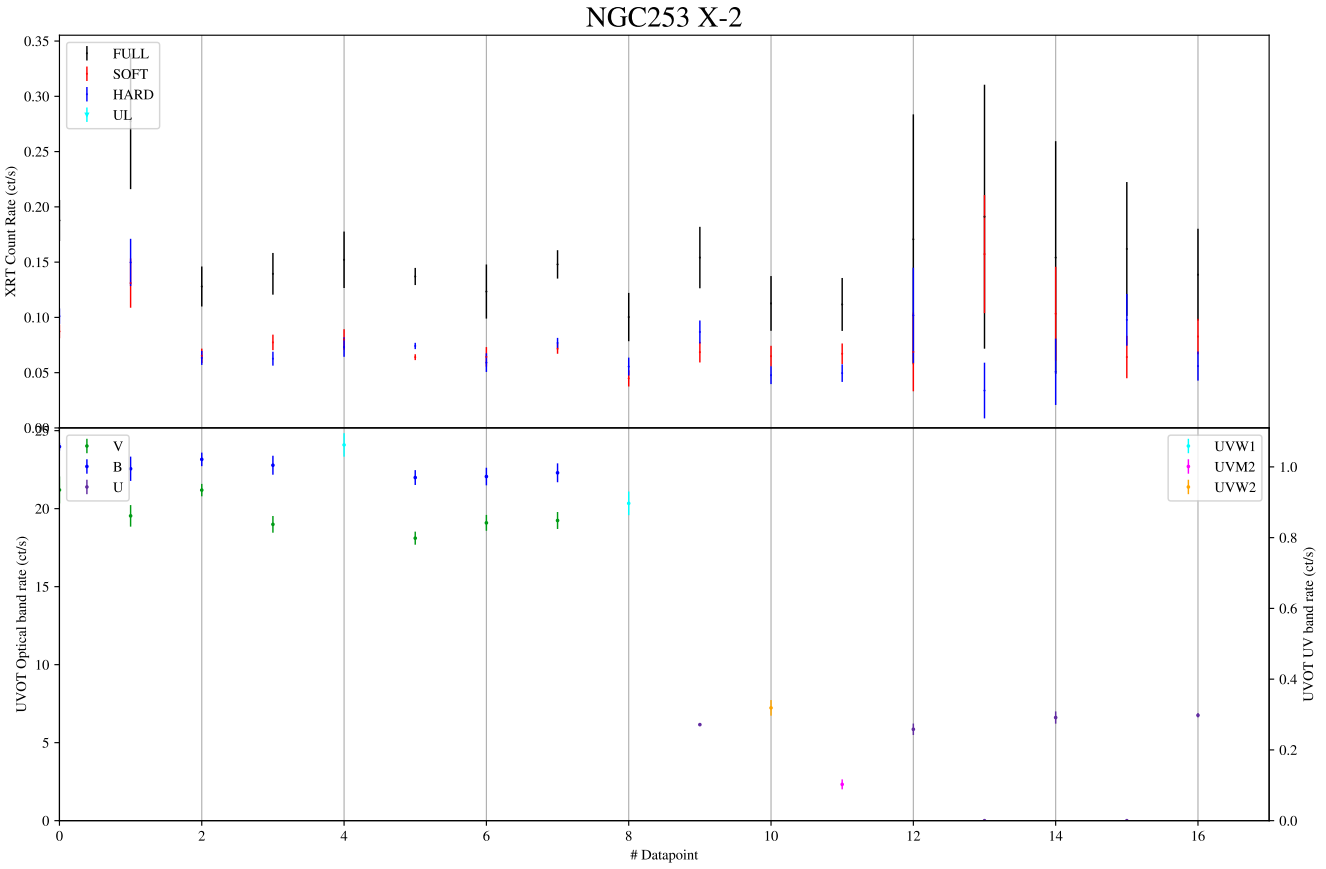
NGC253 X-2
FULL
SOFT
HARD
UL
XRT Count Rate (ct/s)
V
B
U
UVW1
UVM2
UVW2
UVOT Optical band rate (ct/s)
UVOT UV band rate (ct/s)
Datapoint

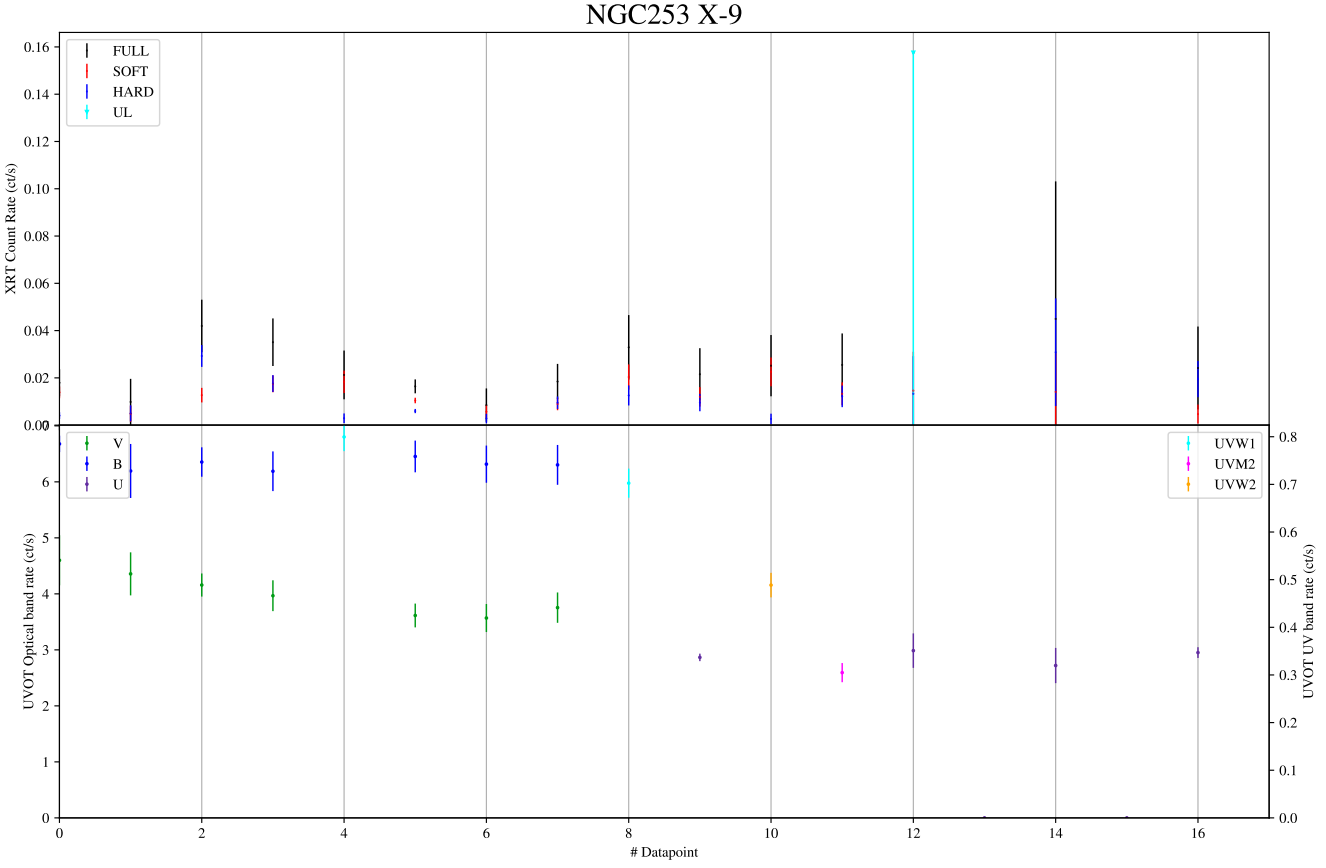
NGC253 X-9
FULL
SOFT
HARD
UL
XRT Count Rate (ct/s)
V
B
U
UVW1
UVM2
UVW2
UVOT Optical band rate (ct/s)
UVOT UV band rate (ct/s)
Datapoint

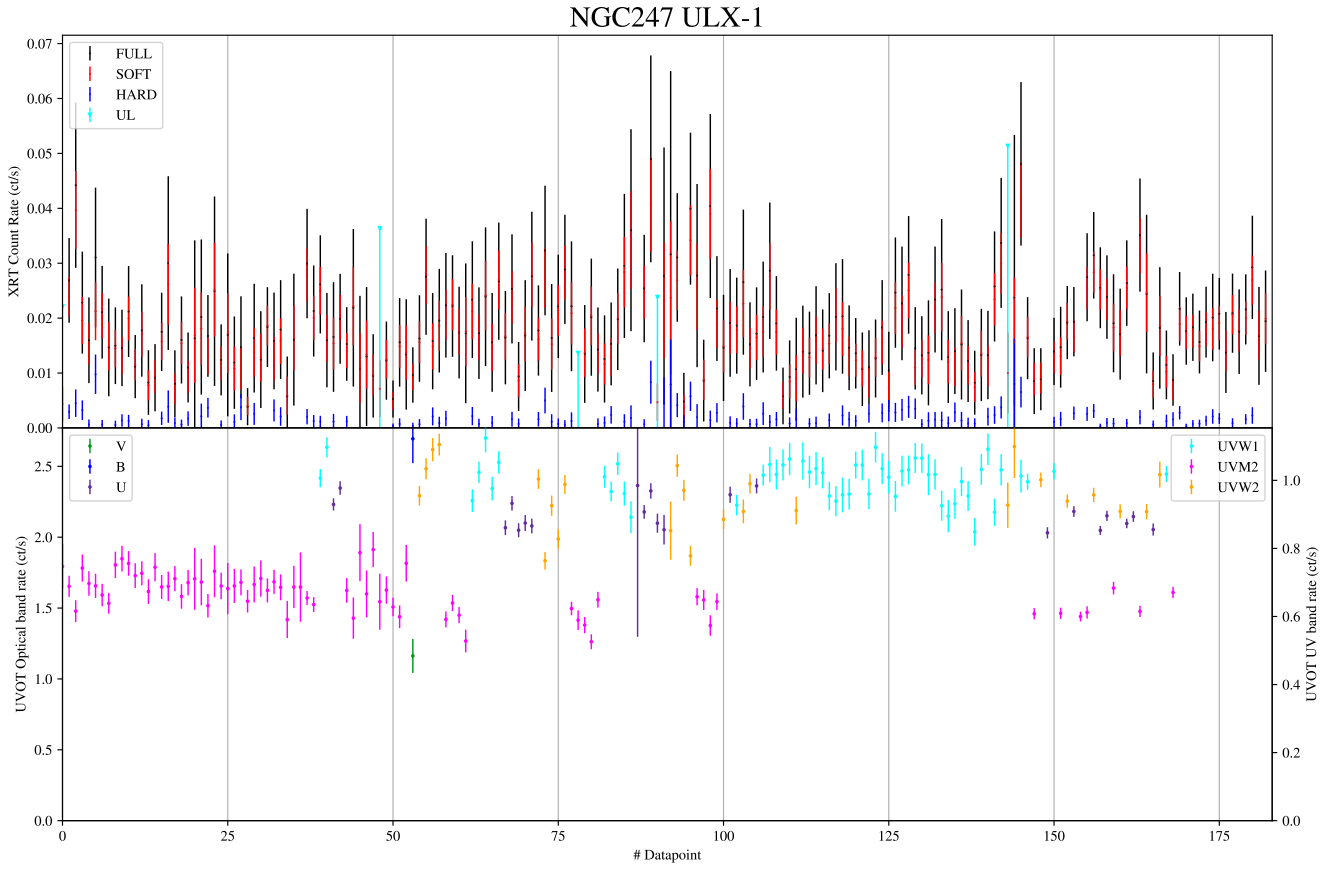
NGC247 ULX-1
FULL
SOFT
HARD
UL
XRT Count Rate (ct/s)
V
B
U
UVW1
UVM2
UVW2
UVOT Optical band rate (ct/s)
UVOT UV band rate (ct/s)
Datapoint

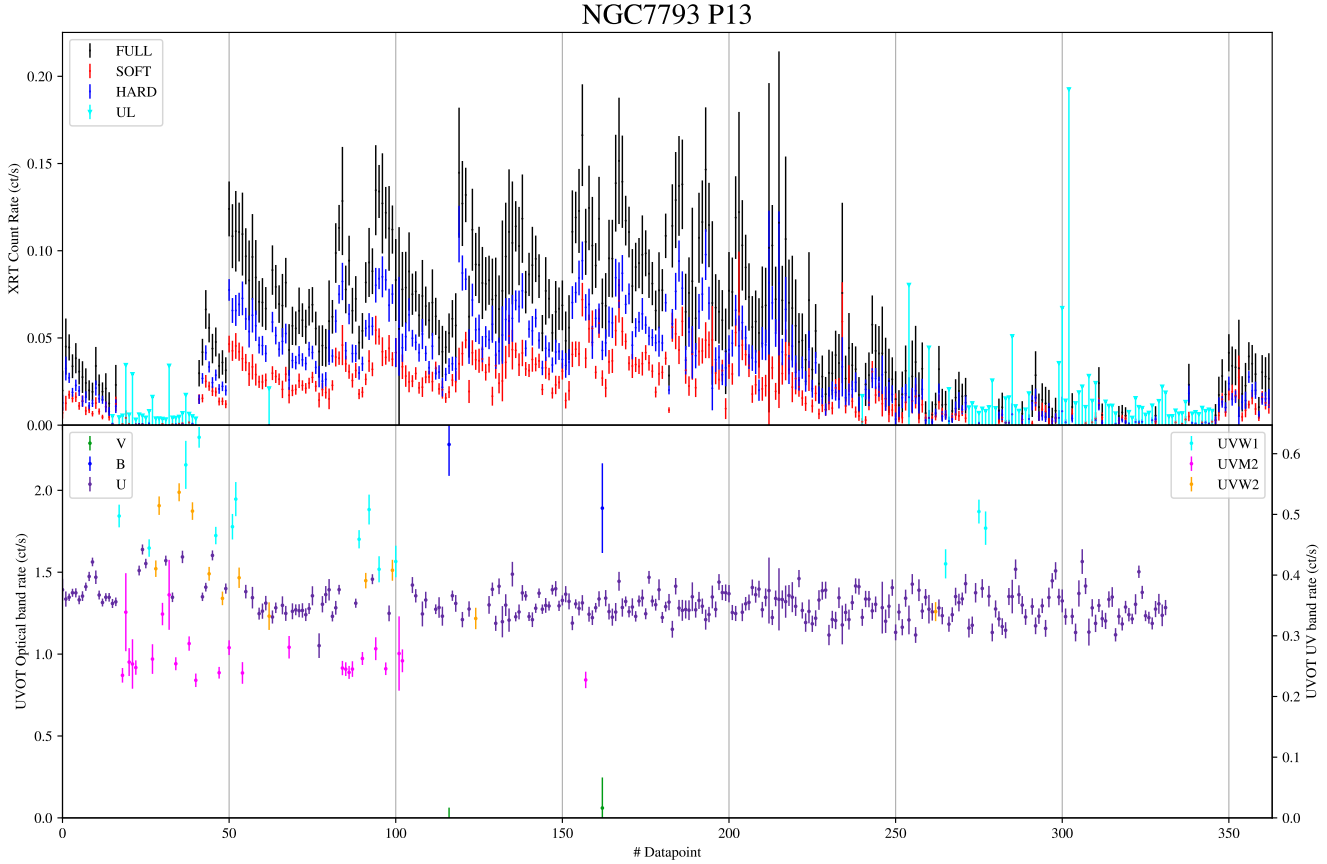
NGC7793 P13
FULL
SOFT
HARD
UL
XRT Count Rate (ct/s)
V
B
U
UVW1
UVM2
UVW2
UVOT Optical band rate (ct/s)
UVOT UV band rate (ct/s)
Datapoint

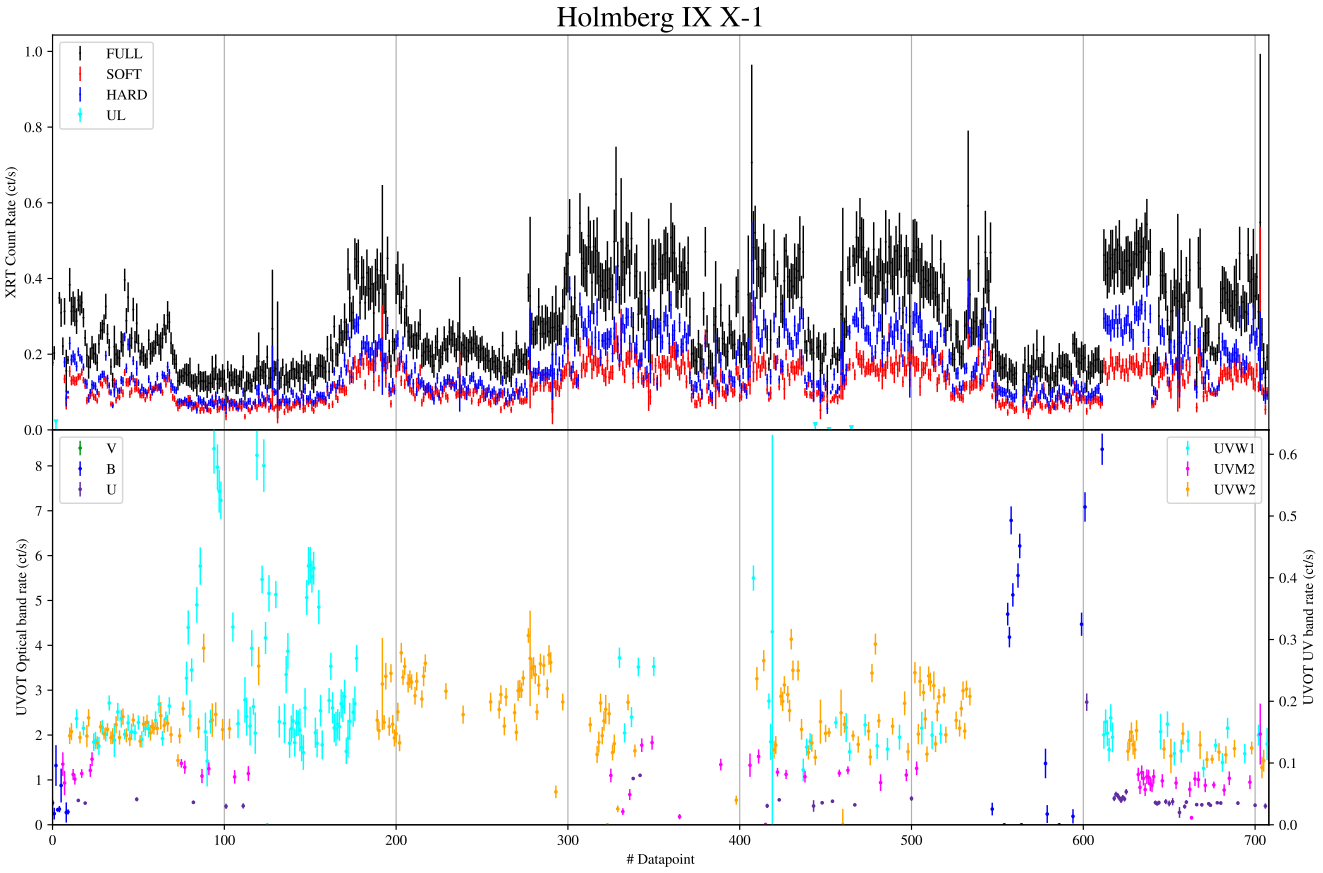
Holmberg IX X-1
FULL
SOFT
HARD
UL
XRT Count Rate (ct/s)
V
B
U
UVW1
UVM2
UVW2
UVOT Optical band rate (ct/s)
UVOT UV band rate (ct/s)
Datapoint

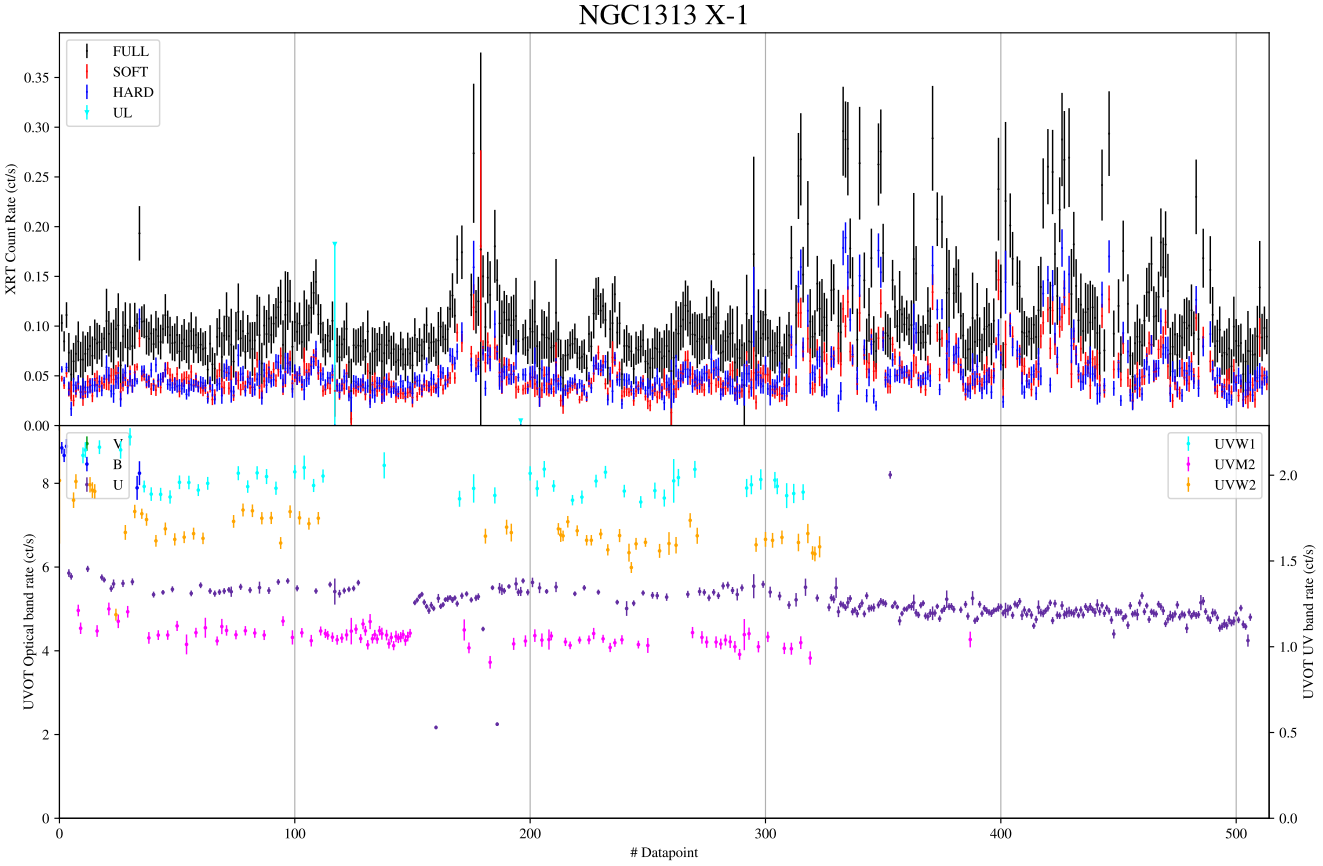
NGC1313 X-1
FULL
SOFT
HARD
UL
XRT Count Rate (ct/s)
V
B
U
UVW1
UVM2
UVW2
UVOT Optical band rate (ct/s)
UVOT UV band rate (ct/s)
Datapoint

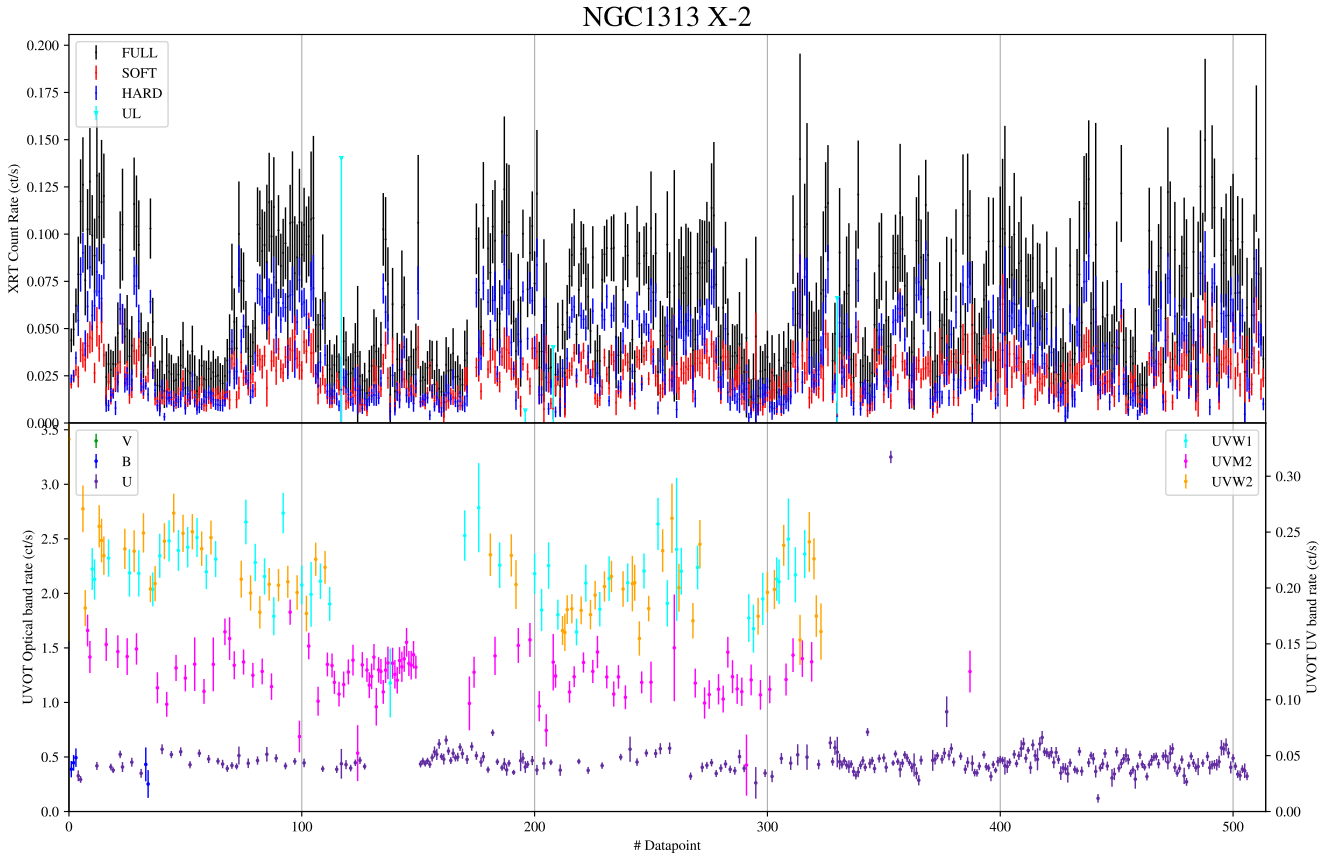
NGC1313 X-2
FULL
SOFT
HARD
UL
XRT Count Rate (ct/s)
V
B
U
UVW1
UVM2
UVW2
UVOT Optical band rate (ct/s)
UVOT UV band rate (ct/s)
Datapoint

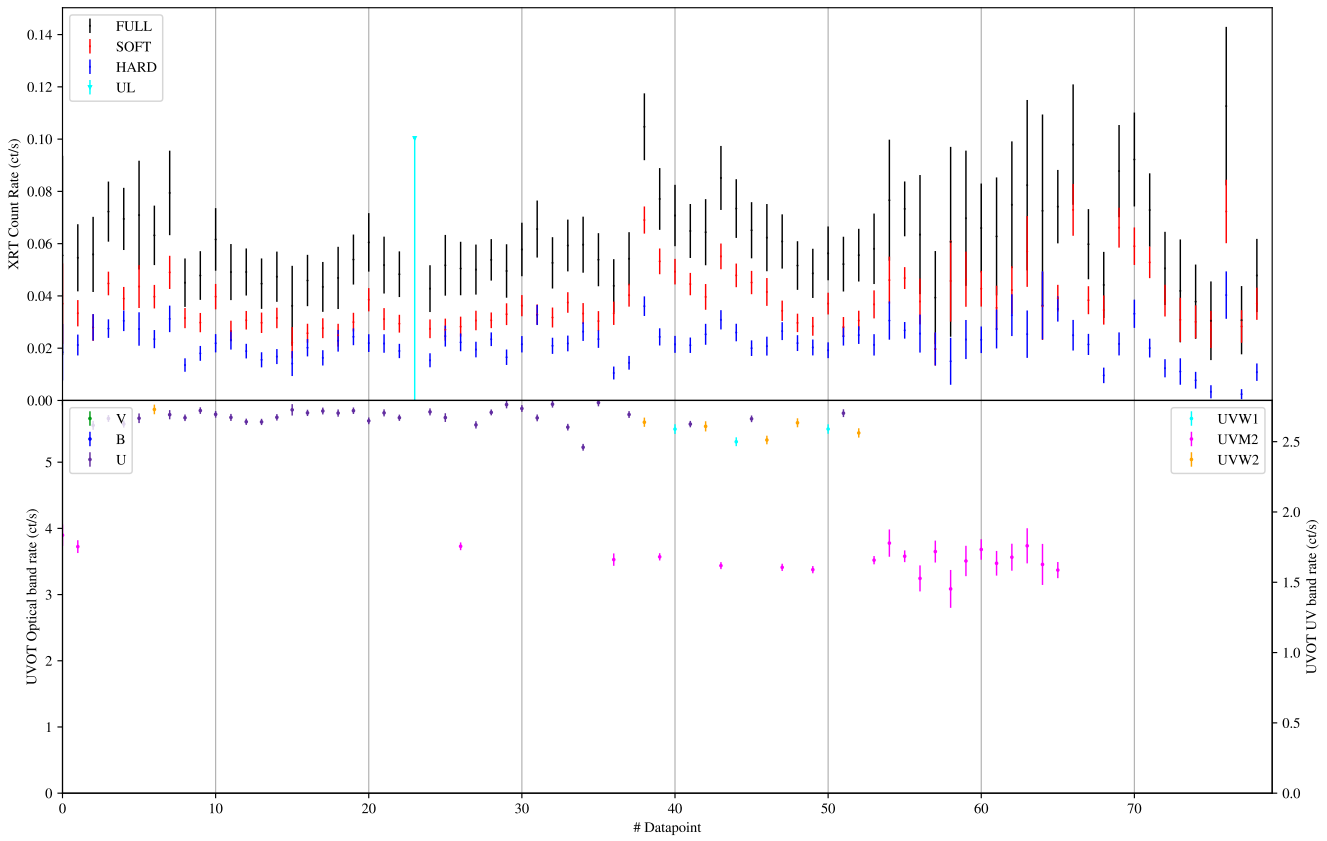
NGC5204 ULX-1
FULL
SOFT
HARD
UL
XRT Count Rate (ct/s)
V
B
U
UVW1
UVM2
UVW2
UVOT Optical band rate (ct/s)
UVOT UV band rate (ct/s)
Datapoint

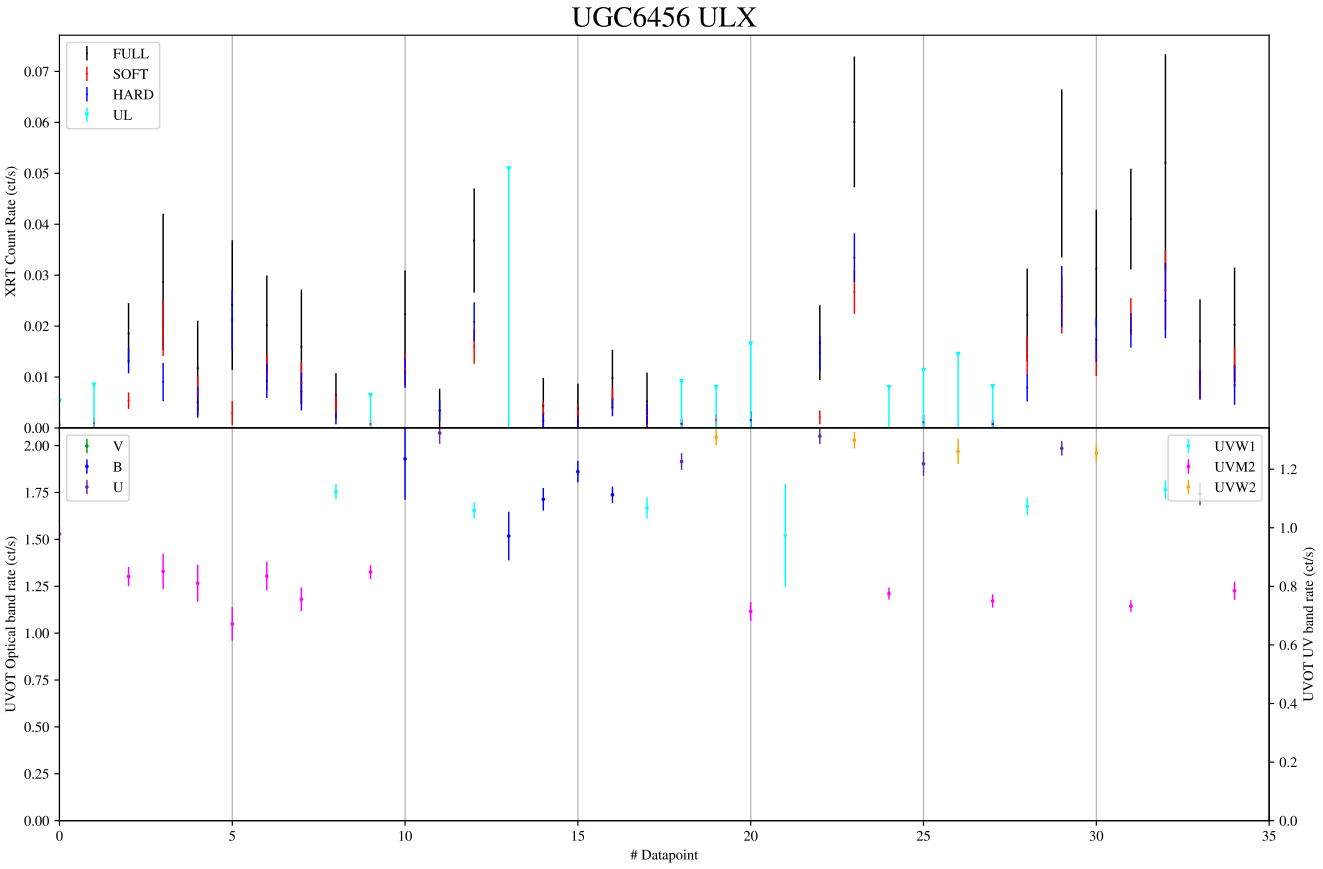
UGC6456 ULX
FULL
SOFT
HARD
UL
XRT Count Rate (ct/s)
V
B
U
UVW1
UVM2
UVW2
UVOT Optical band rate (ct/s)
UVOT UV band rate (ct/s)
Datapoint

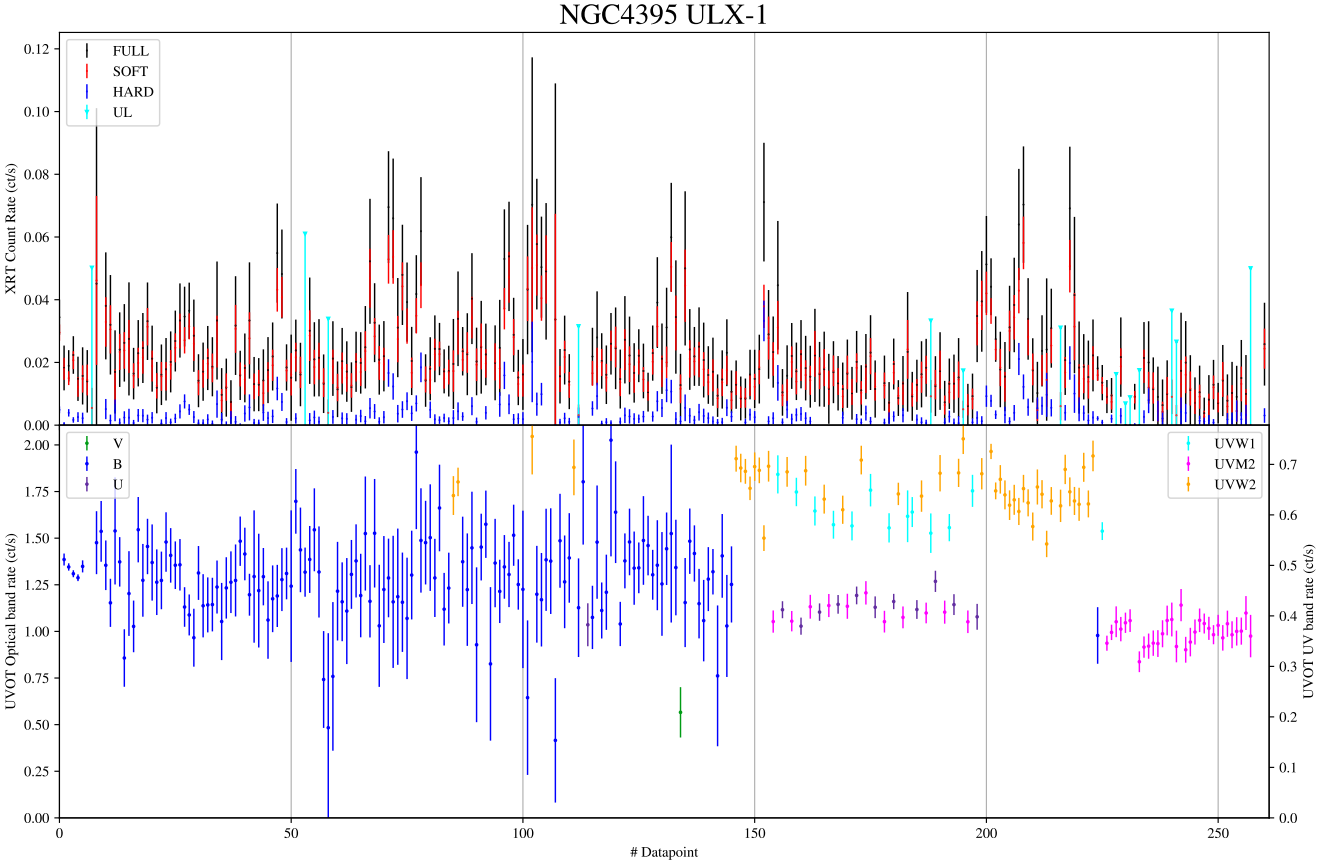
NGC4395 ULX-1
FULL
SOFT
HARD
UL
XRT Count Rate (ct/s)
V
B
U
UVW1
UVM2
UVW2
UVOT Optical band rate (ct/s)
UVOT UV band rate (ct/s)
Datapoint

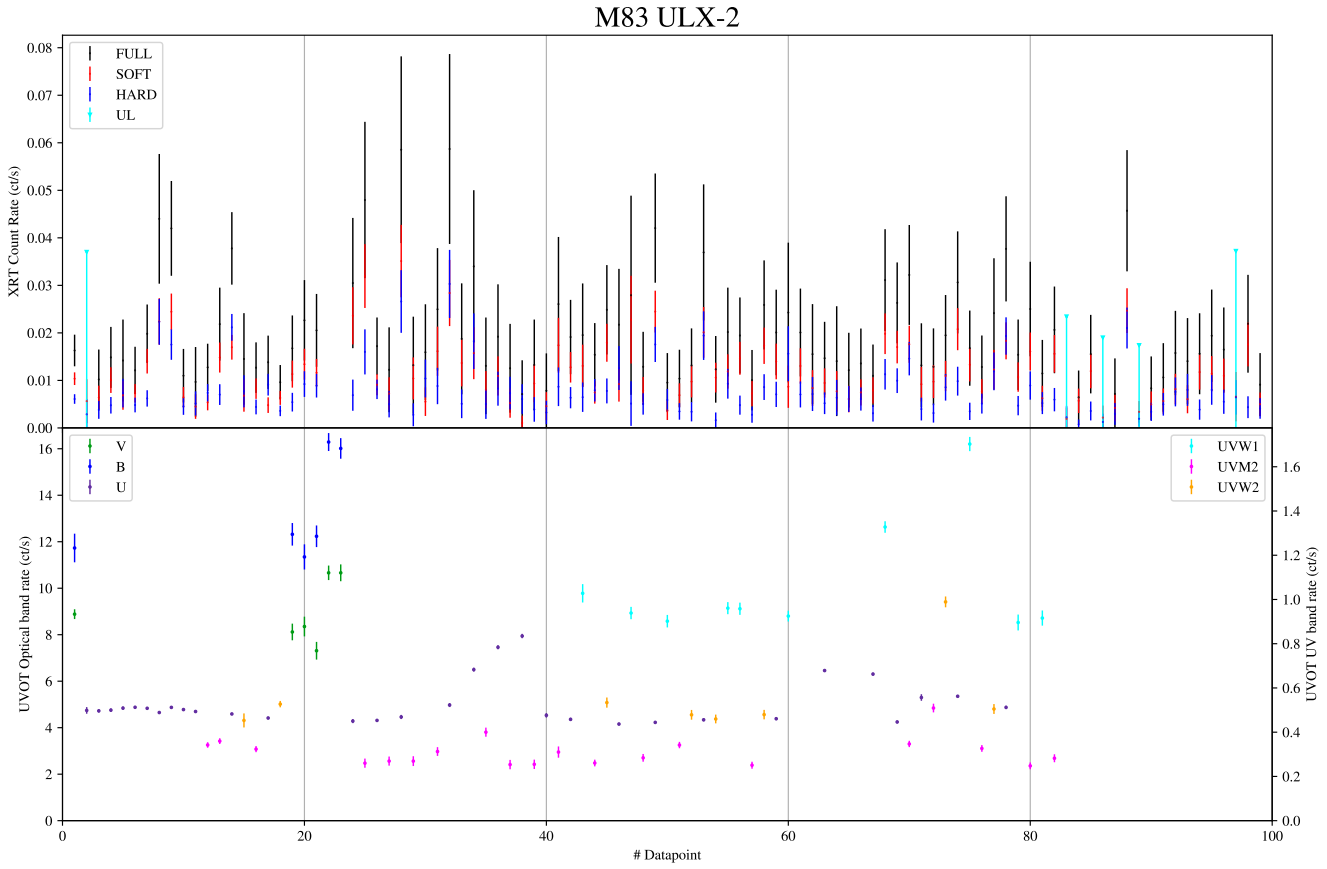
M83 ULX-2
FULL
SOFT
HARD
UL
XRT Count Rate (ct/s)
V
B
U
UVW1
UVM2
UVW2
UVOT Optical band rate (ct/s)
UVOT UV band rate (ct/s)
Datapoint

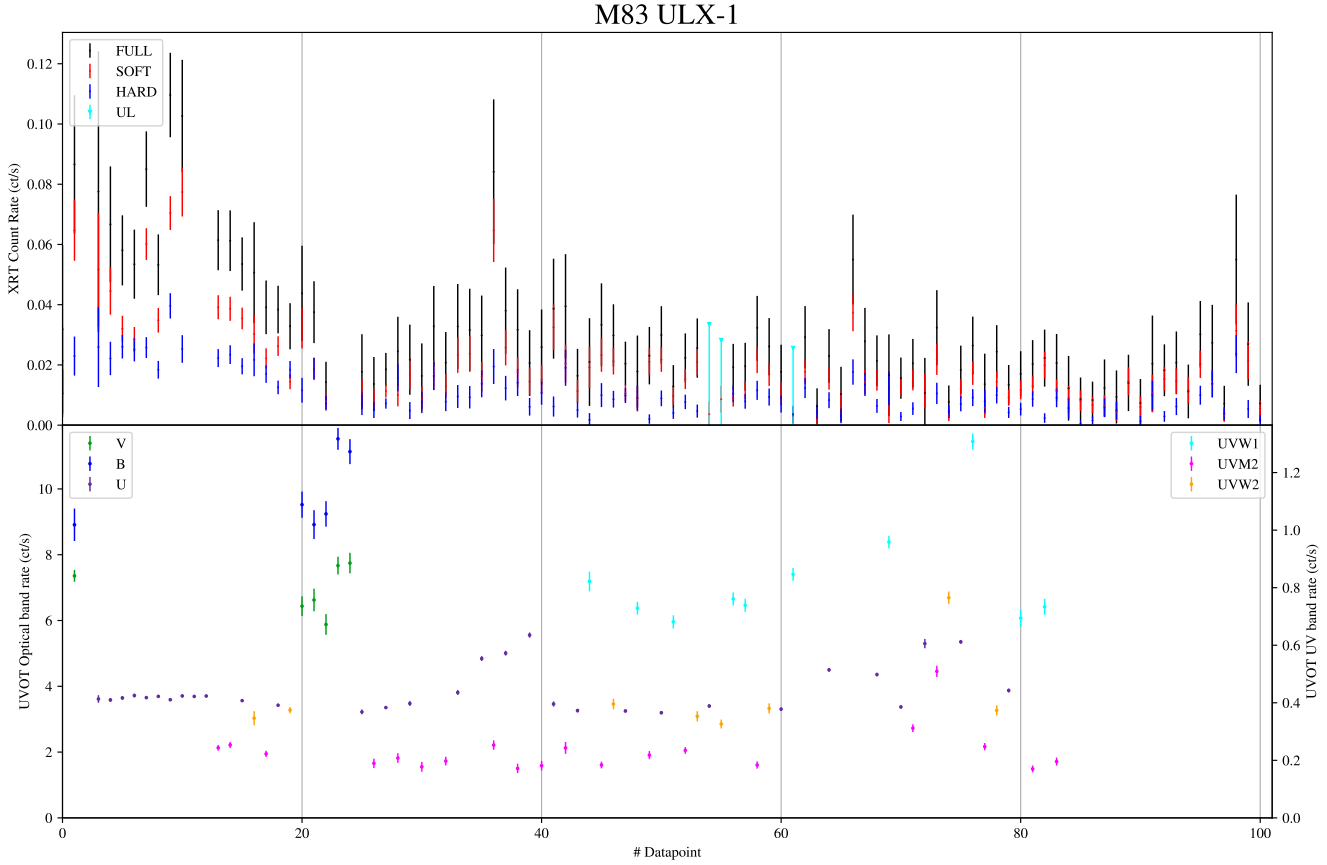
M83 ULX-1
FULL
SOFT
HARD
UL
XRT Count Rate (ct/s)
V
B
U
UVW1
UVM2
UVW2
UVOT Optical band rate (ct/s)
UVOT UV band rate (ct/s)
Datapoint

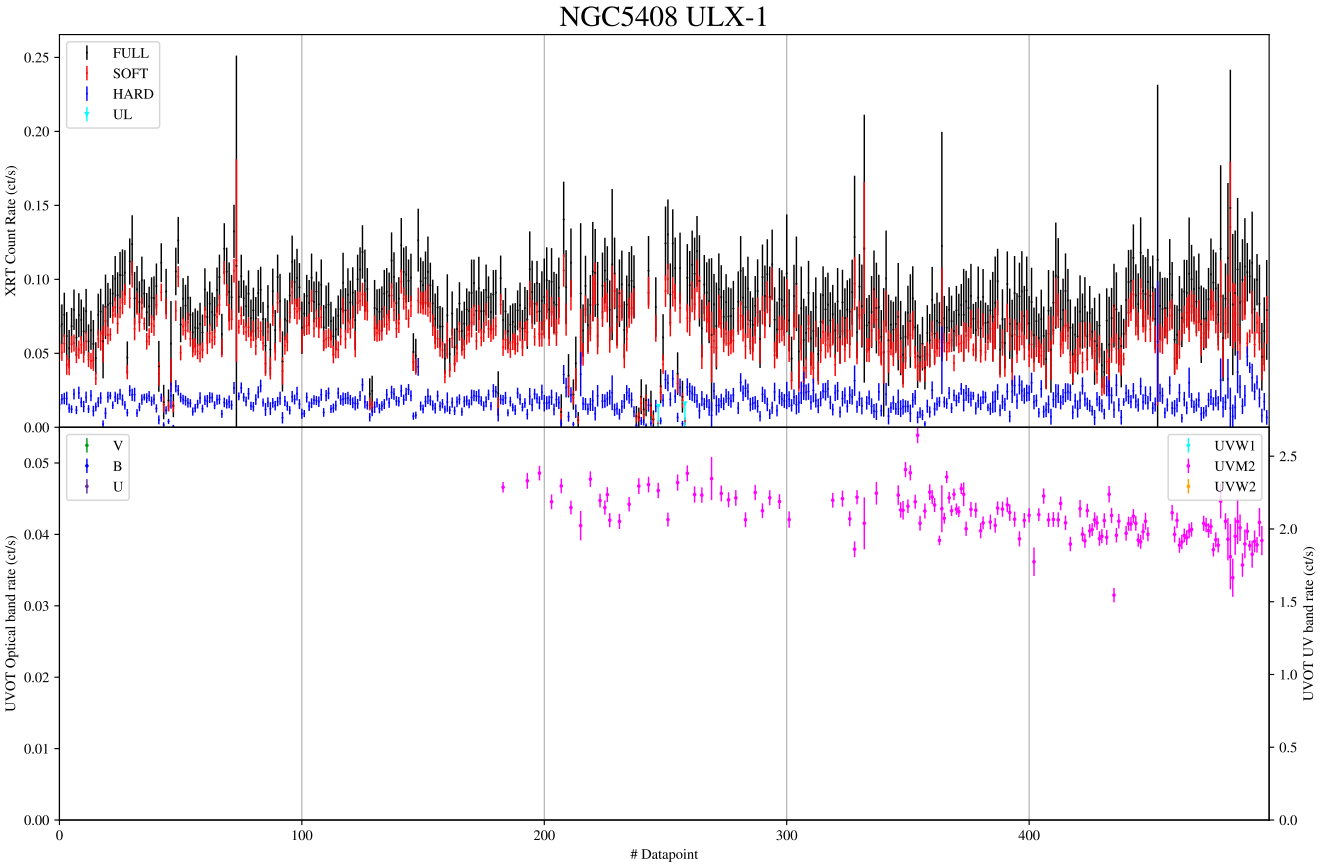
NGC5408 ULX-1
FULL
SOFT
HARD
UL
XRT Count Rate (ct/s)
V
B
U
UVW1
UVM2
UVW2
UVOT Optical band rate (ct/s)
UVOT UV band rate (ct/s)
Datapoint

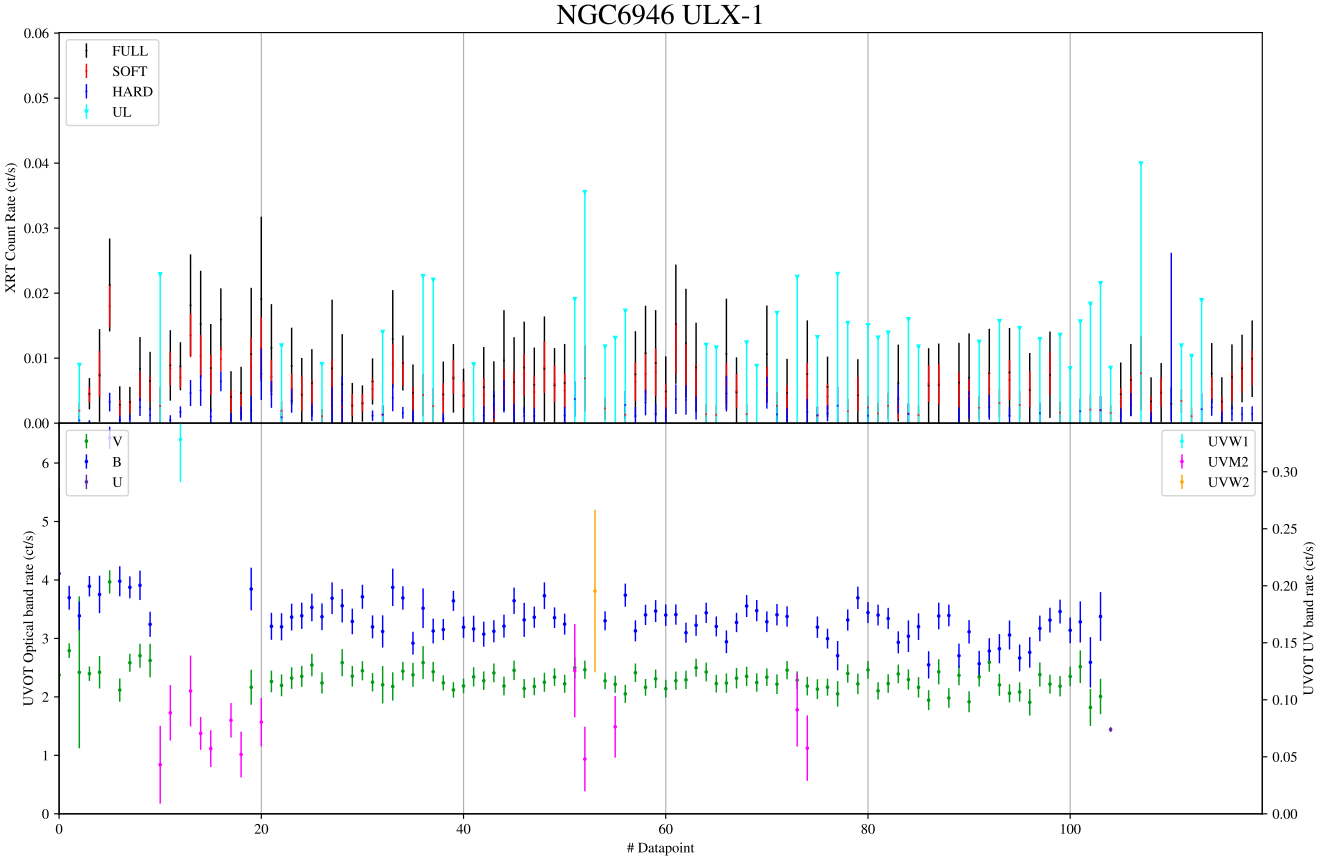
NGC6946 ULX-1
FULL
SOFT
HARD
UL
XRT Count Rate (ct/s)
V
B
U
UVW1
UVM2
UVW2
UVOT Optical band rate (ct/s)
UVOT UV band rate (ct/s)
Datapoint

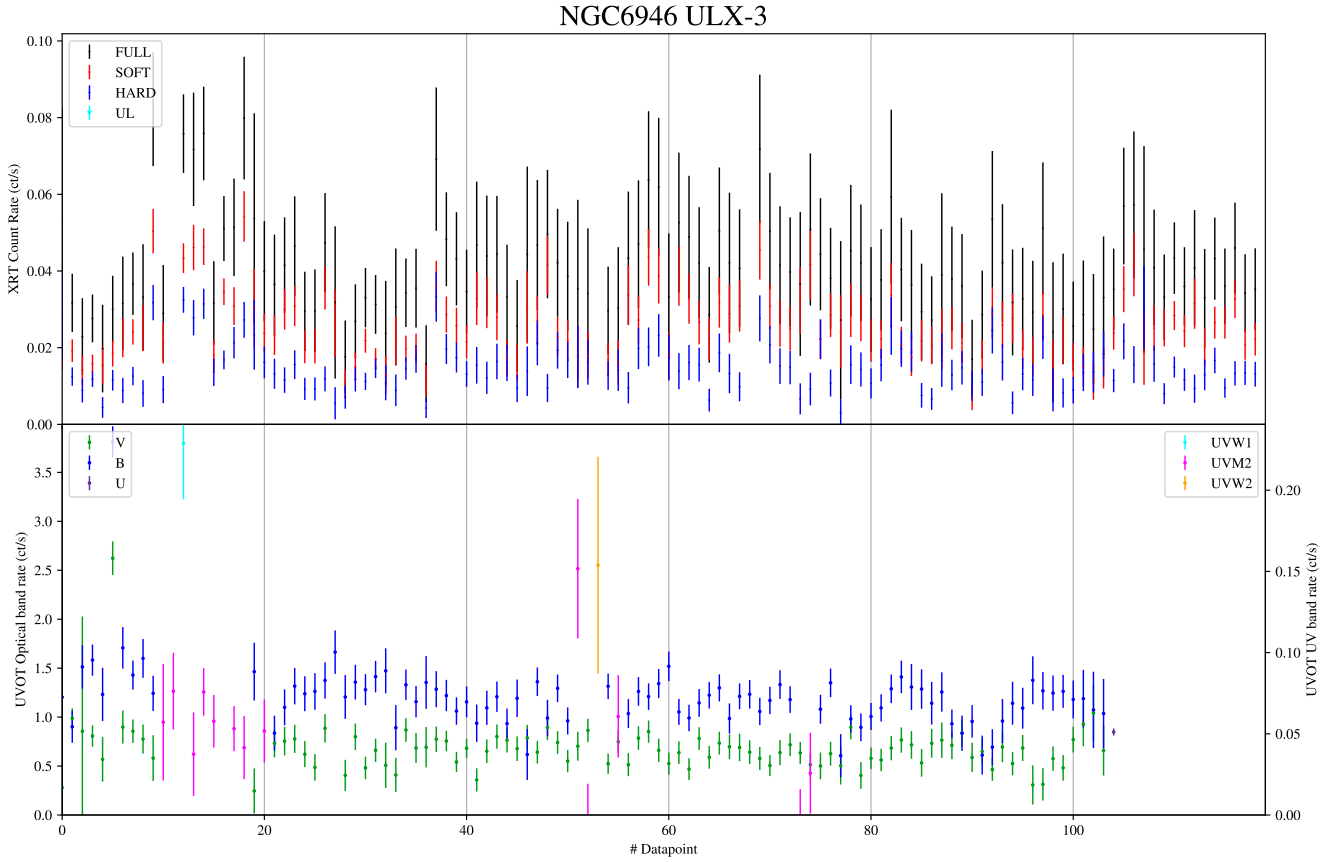
NGC6946 ULX-3
FULL
SOFT
HARD
UL
XRT Count Rate (ct/s)
V
B
U
UVW1
UVM2
UVW2
UVOT Optical band rate (ct/s)
UVOT UV band rate (ct/s)
Datapoint

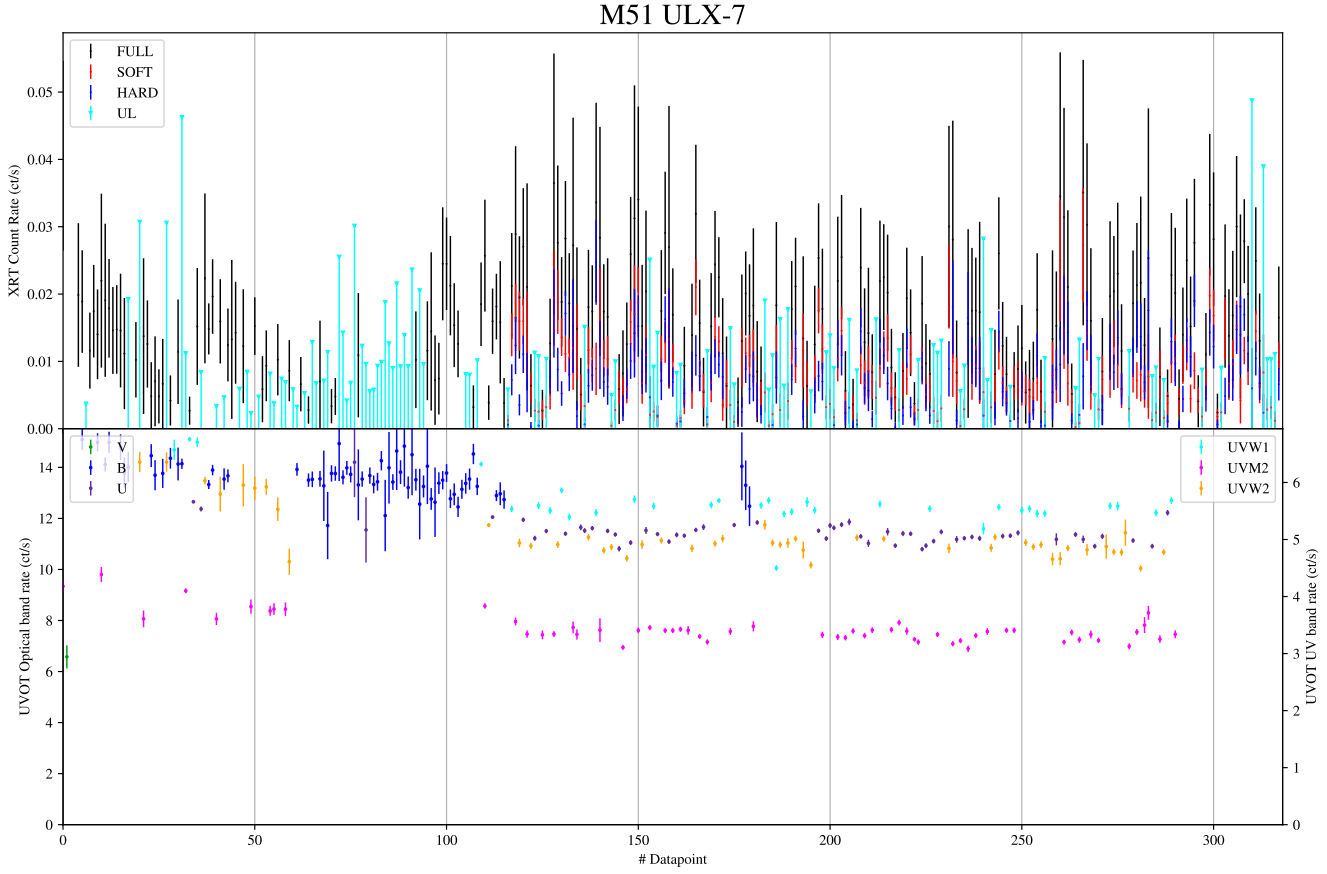
M51 ULX-7
FULL
SOFT
HARD
UL
XRT Count Rate (ct/s)
V
B
U
UVW1
UVM2
UVW2
UVOT Optical band rate (ct/s)
UVOT UV band rate (ct/s)
Datapoint

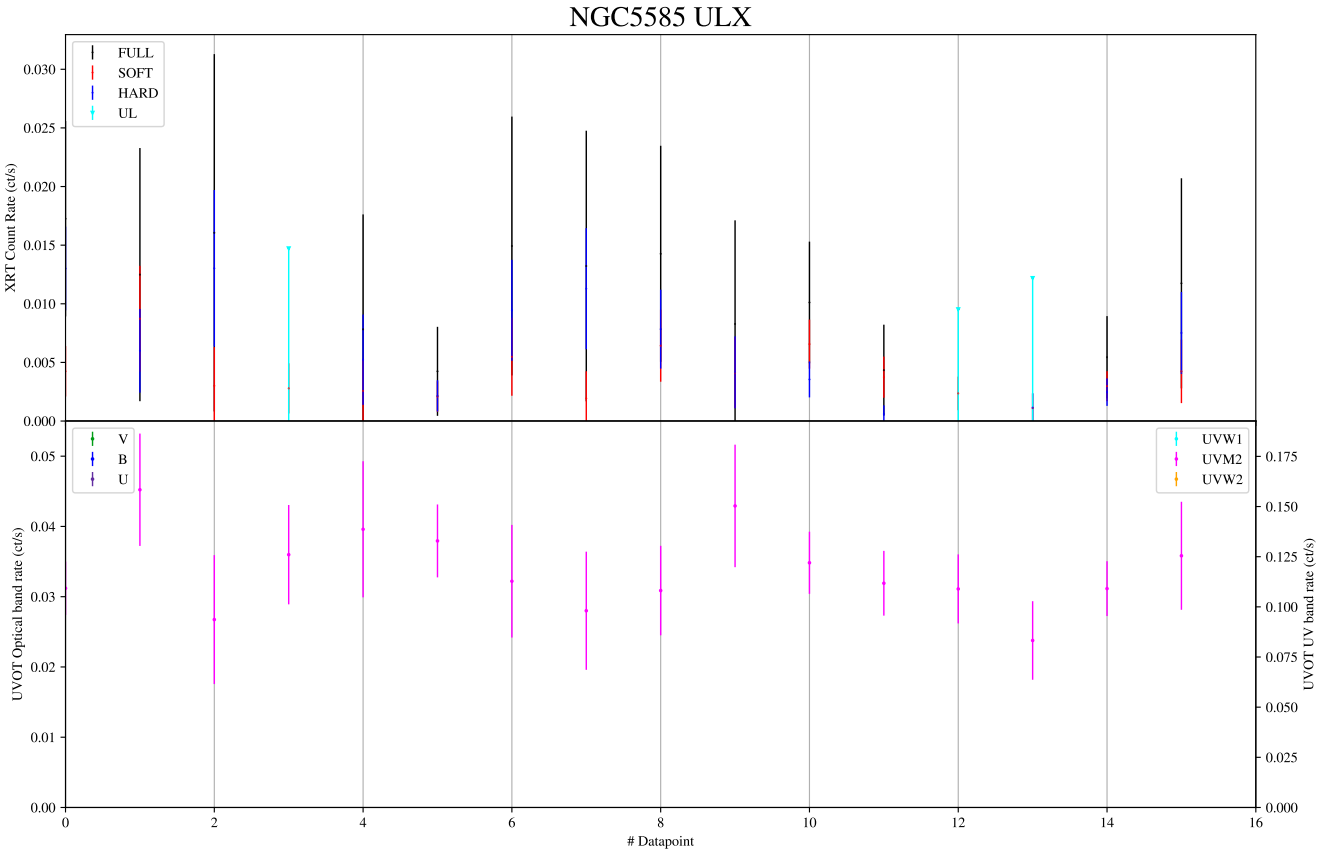
NGC5585 ULX
FULL
SOFT
HARD
UL
XRT Count Rate (ct/s)
V
B
U
UVW1
UVM2
UVW2
UVOT Optical band rate (ct/s)
UVOT UV band rate (ct/s)
Datapoint

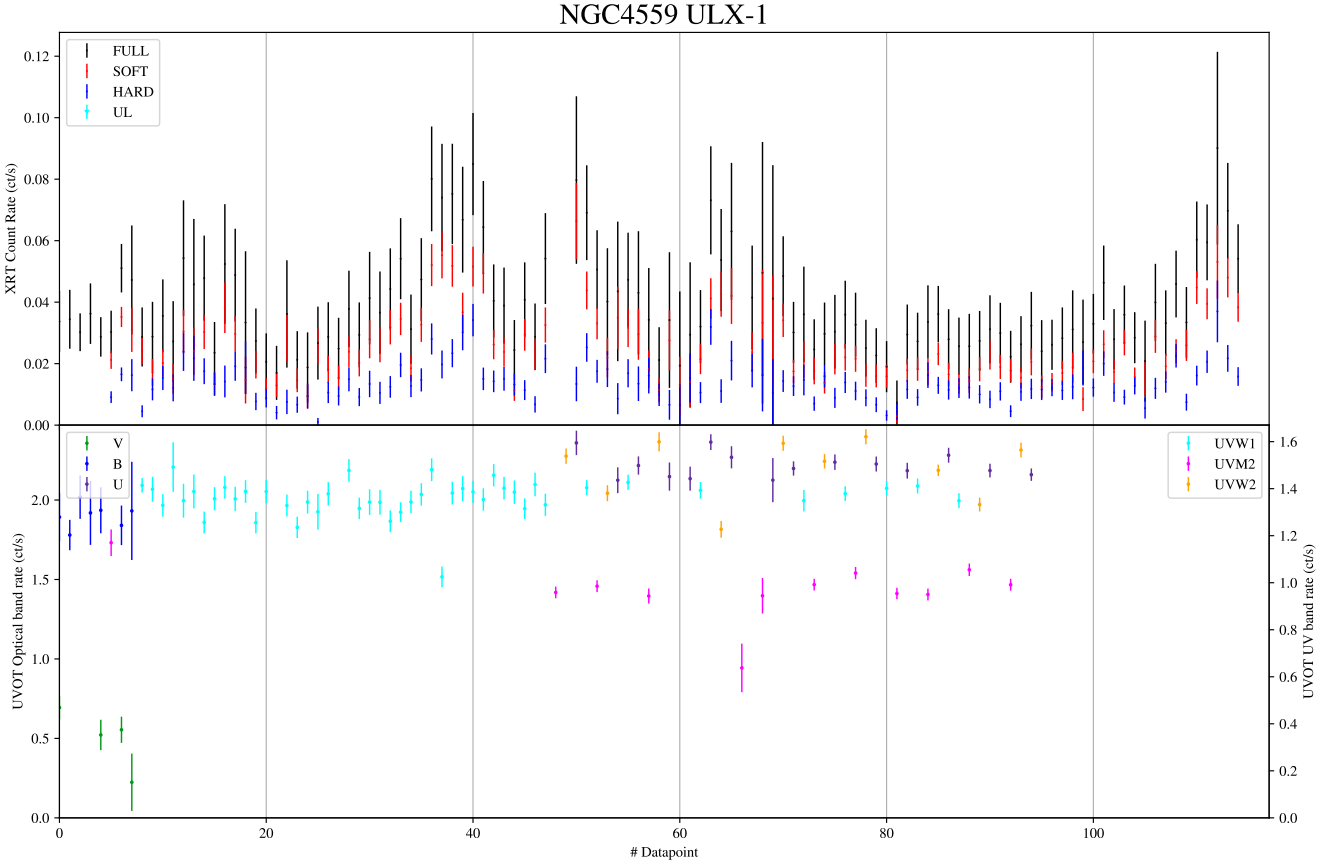
NGC4559 ULX-1
FULL
SOFT
HARD
UL
XRT Count Rate (ct/s)
V
B
U
UVW1
UVM2
UVW2
UVOT Optical band rate (ct/s)
UVOT UV band rate (ct/s)
Datapoint

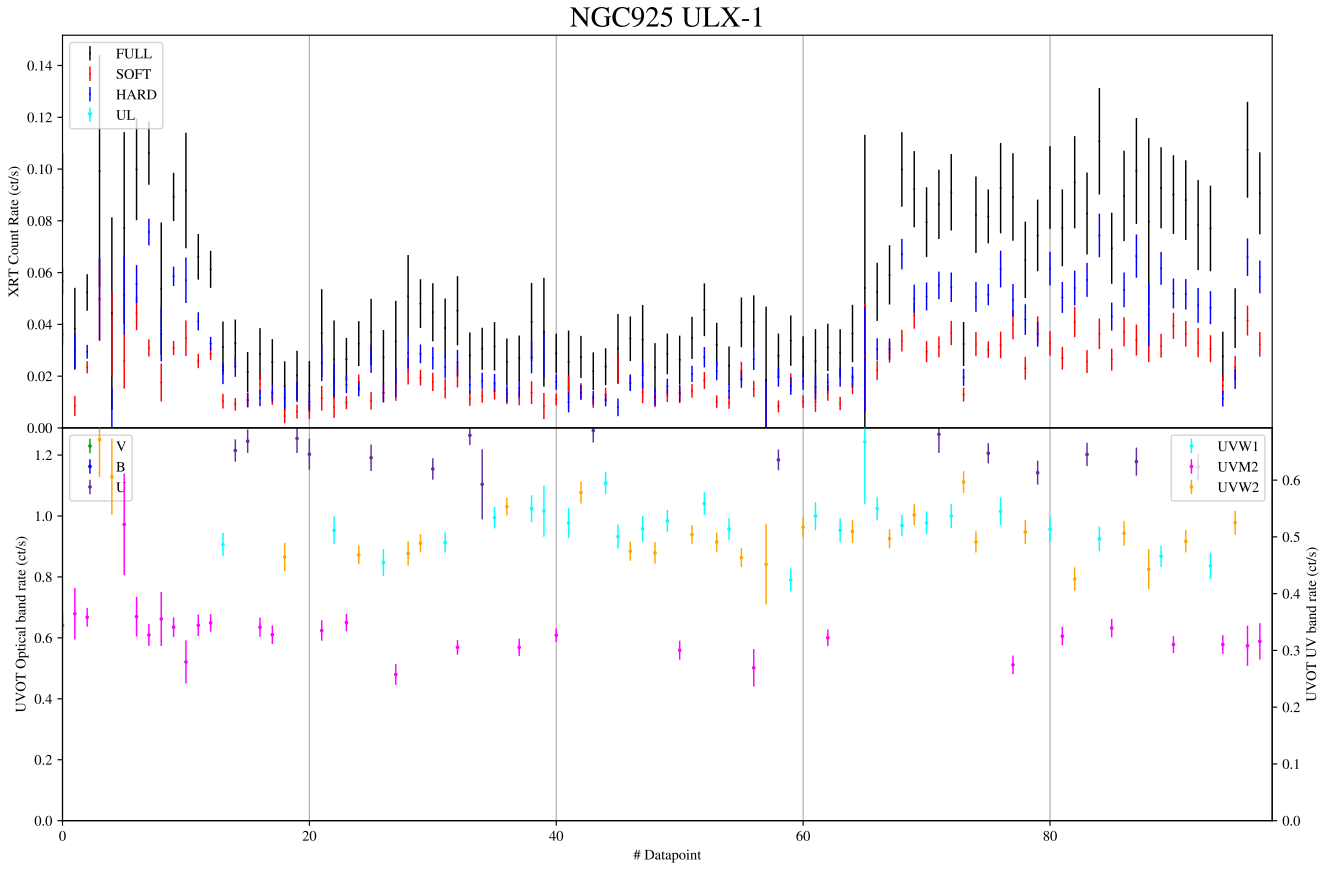
NGC925 ULX-1
FULL
SOFT
HARD
UL
XRT Count Rate (ct/s)
V
B
U
UVW1
UVM2
UVW2
UVOT Optical band rate (ct/s)
UVOT UV band rate (ct/s)
Datapoint

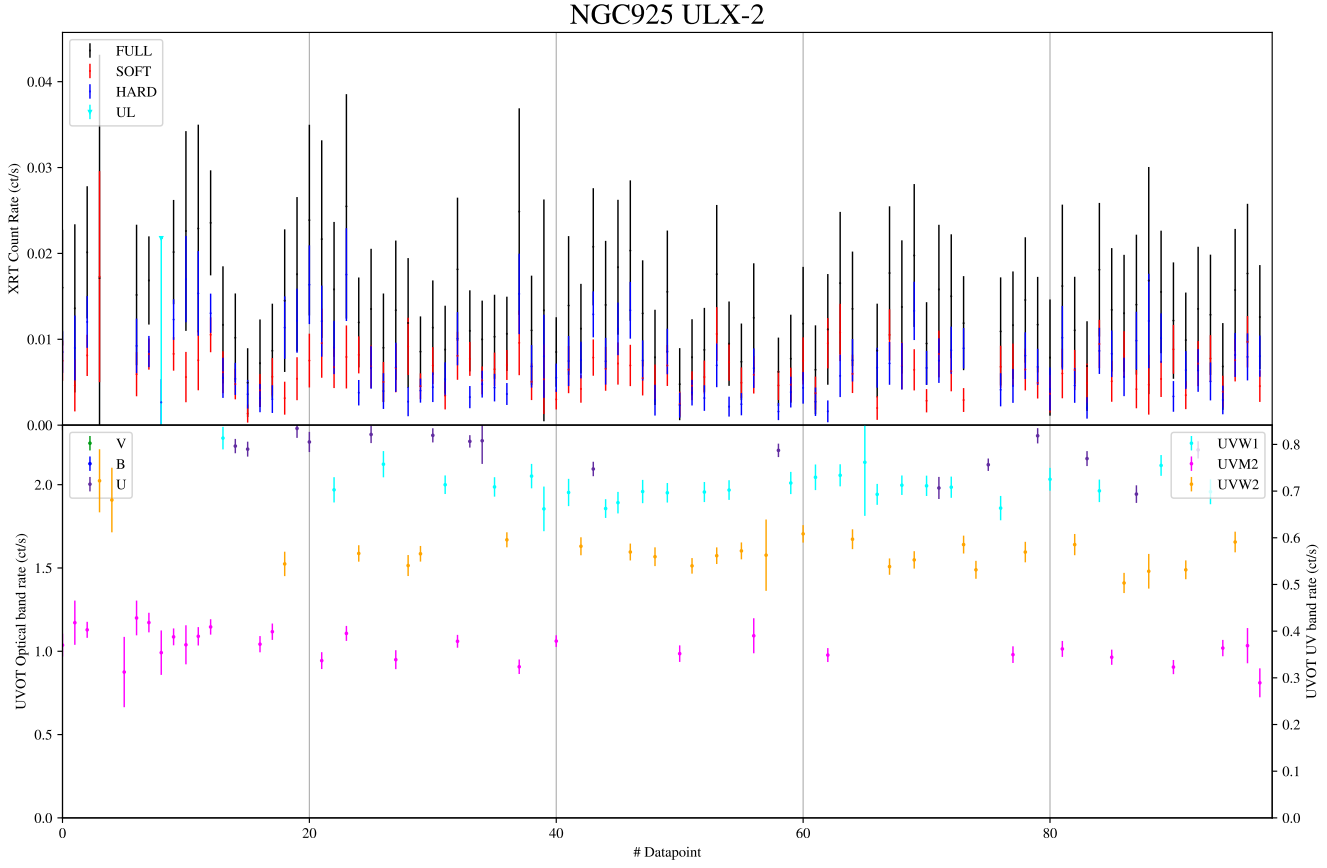
NGC925 ULX-2
FULL
SOFT
HARD
UL
XRT Count Rate (ct/s)
V
B
U
UVW1
UVM2
UVW2
UVOT Optical band rate (ct/s)
UVOT UV band rate (ct/s)
Datapoint

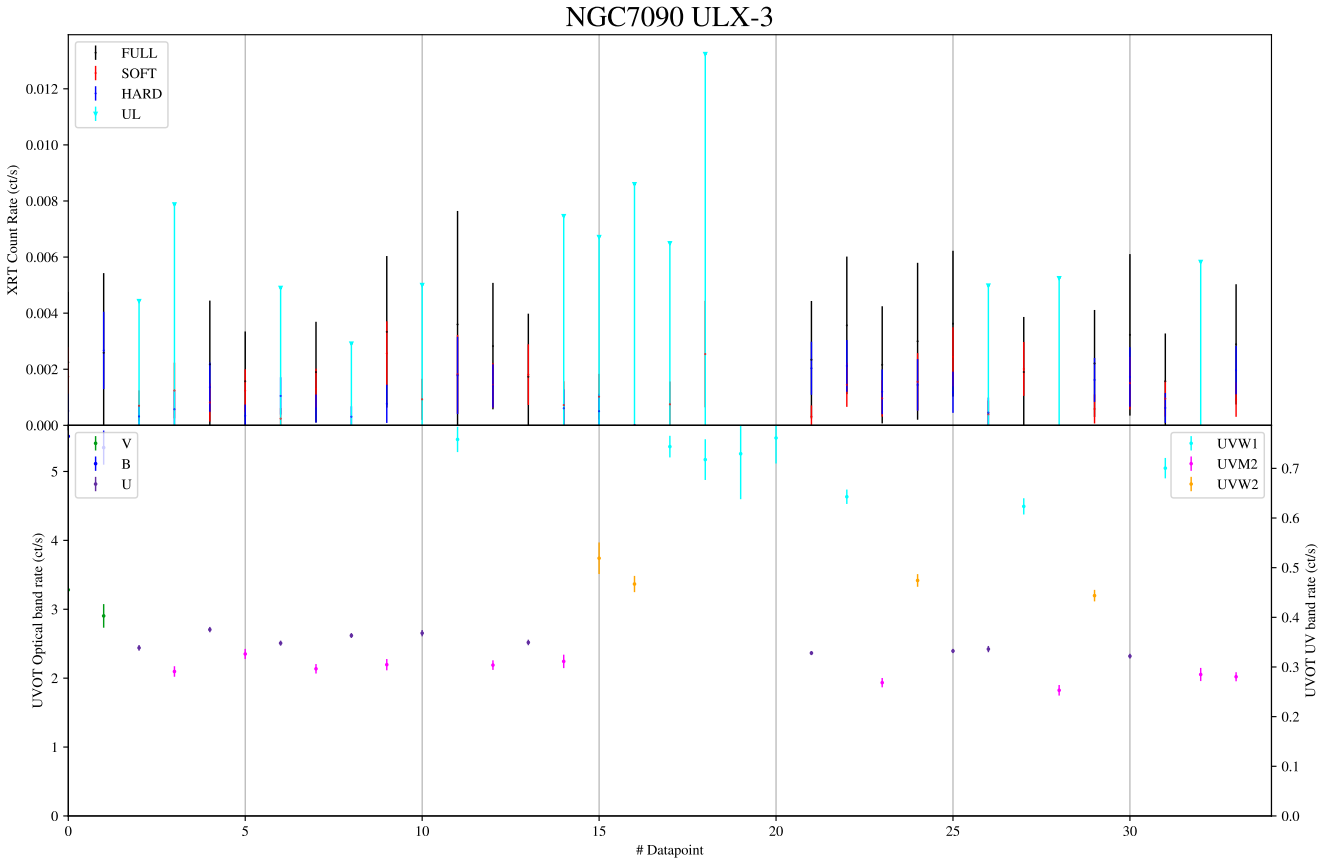
NGC7090 ULX-3
FULL
SOFT
HARD
UL
XRT Count Rate (ct/s)
V
B
U
UVW1
UVM2
UVW2
UVOT Optical band rate (ct/s)
UVOT UV band rate (ct/s)
Datapoint

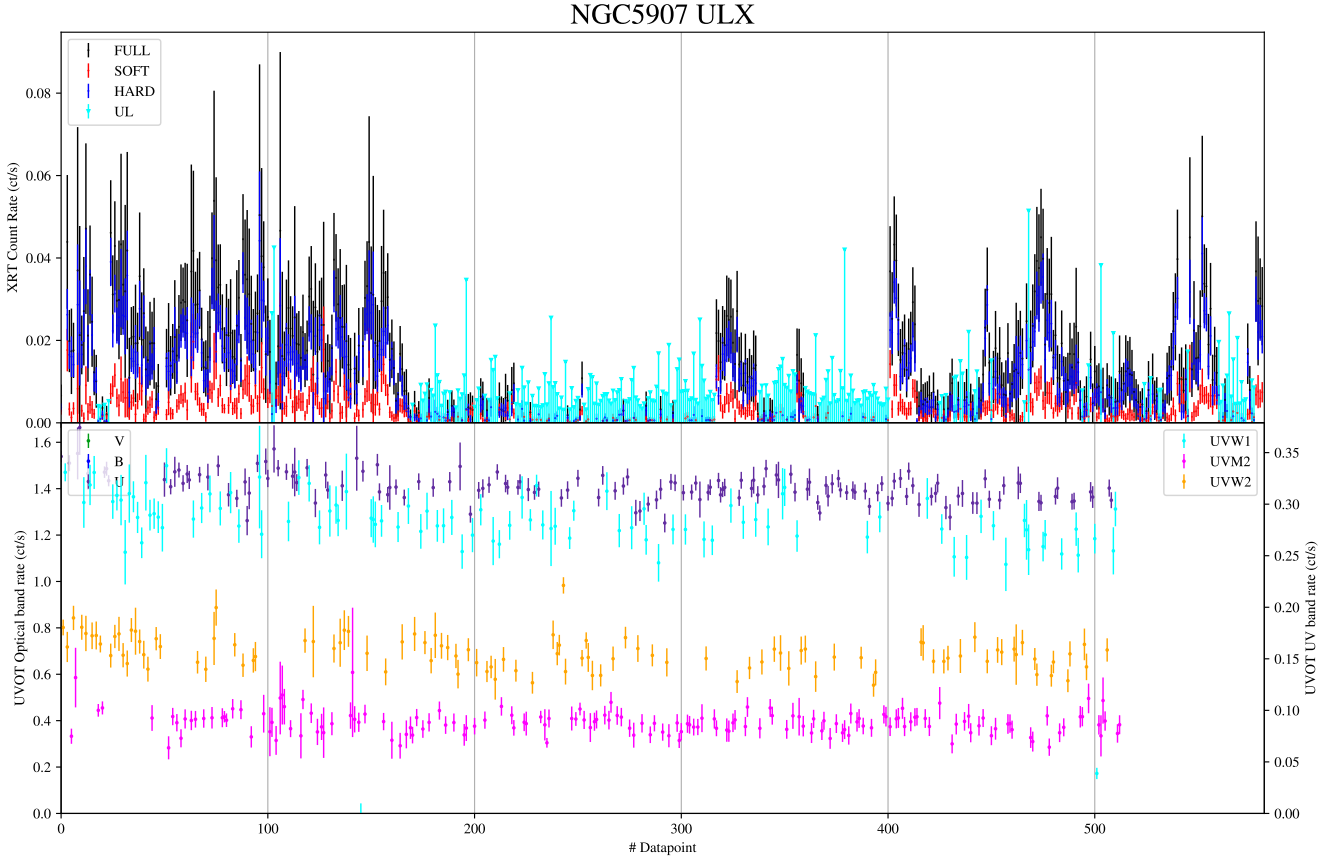
NGC5907 ULX
FULL
SOFT
HARD
UL
XRT Count Rate (ct/s)
V
B
U
UVW1
UVM2
UVW2
UVOT Optical band rate (ct/s)
UVOT UV band rate (ct/s)
Datapoint

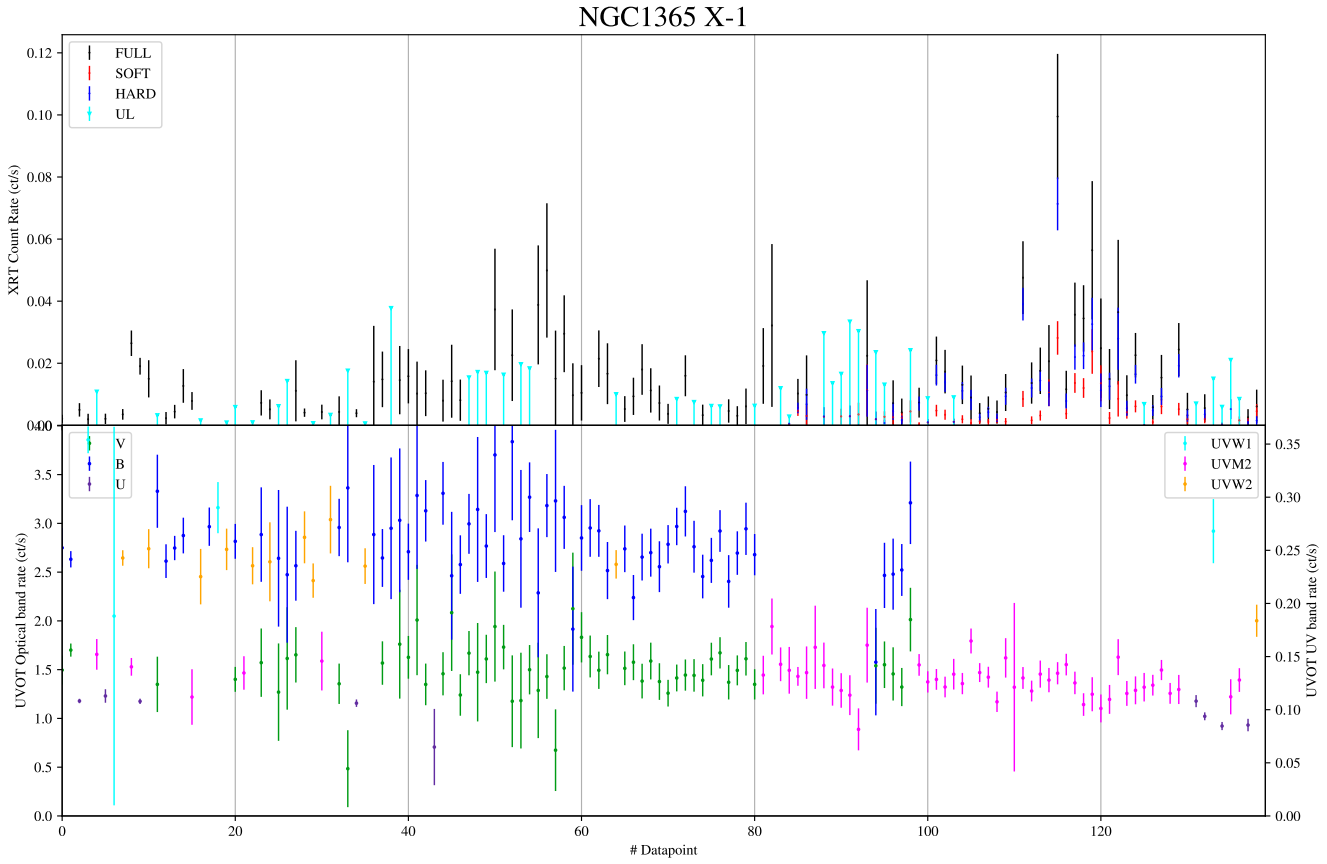
NGC1365 X-1
FULL
SOFT
HARD
UL
XRT Count Rate (ct/s)
V
B
U
UVW1
UVM2
UVW2
UVOT Optical band rate (ct/s)
UVOT UV band rate (ct/s)
Datapoint

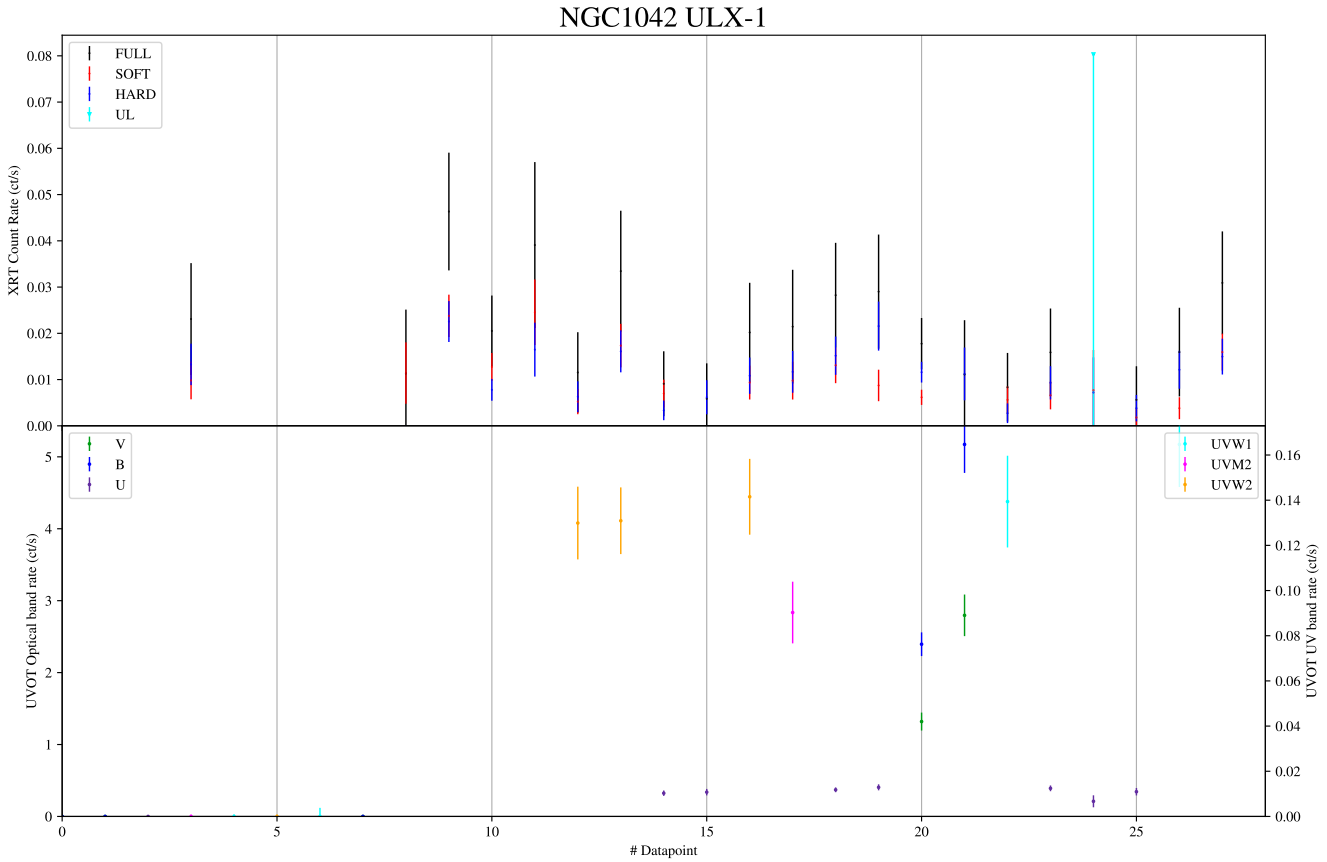
NGC1042 ULX-1
FULL
SOFT
HARD
UL
XRT Count Rate (ct/s)
V
B
U
UVW1
UVM2
UVW2
UVOT Optical band rate (ct/s)
UVOT UV band rate (ct/s)
Datapoint